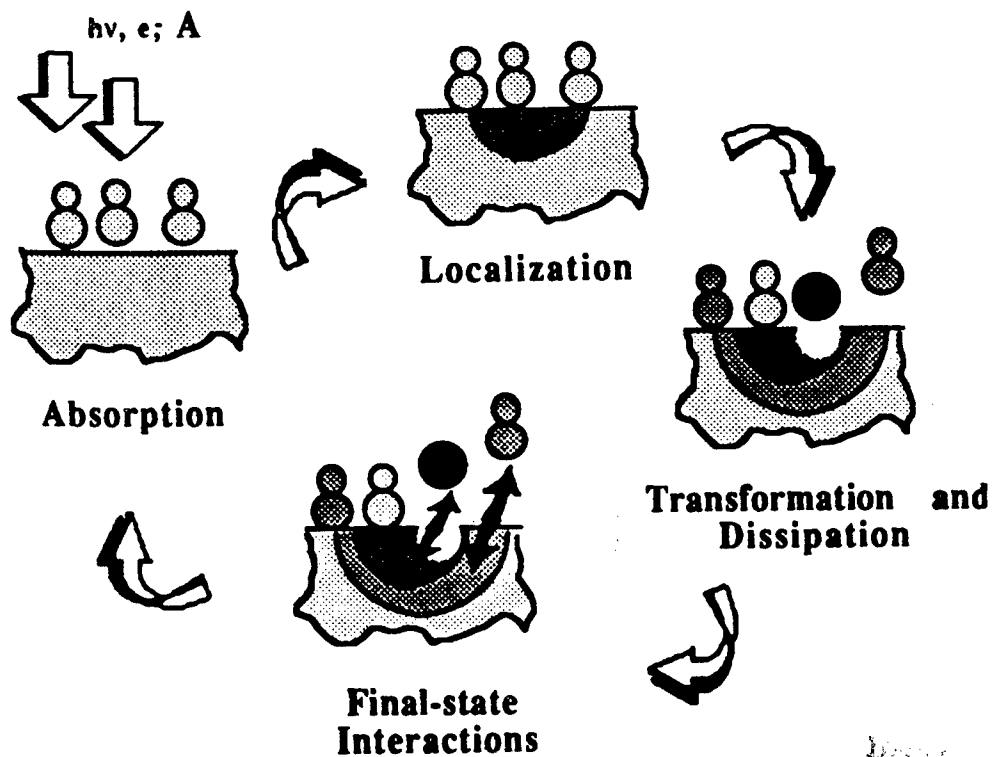
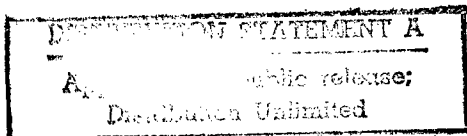


SURFACE REACTIONS IN THE SPACE ENVIRONMENT

1988



19980513 135

DISC Q 114 IMPROVED 4

AIR FORCE OFFICE OF SCIENTIFIC RESEARCH
Air Force Systems Command USAF

401950

PLEASE RETURN TO:

BMD TECHNICAL INFORMATION CENTER
BALLISTIC MISSILE DEFENSE ORGANIZATION
7100 DEFENSE PENTAGON
WASHINGTON D.C. 20301-7100

Accession Number: 1950

Publication Date: Oct 18, 1988

Title: Surface Reactions in the Space Environment; Papers from the Workshop, Vanderbilt U., TN, 17-18 October 1988

Personal Author: Tolk, N.H.; Kinser, D.L.; Nordlander, P.; Tully, J.; et al.

Corporate Author Or Publisher: Vanderbilt University, P.O. Box 1807-B, Nashville, TN 37235

Report Prepared for: Air Force Office of Scientific Research, Bldg. 410, Bolling AFB, Washington, DC 20332-6448

Descriptors, Keywords: Research Space Radiation Temperature Metal Surveillance Environment Surface Physics Chemistry
Reaction Material Damage Fluorescence Design Engineering

Pages: 211

Cataloged Date: Sep 28, 1989

Contract Number: F49620-86-C-0125

Document Type: HC

Number of Copies In Library: 000001

Record ID: 20846

NOT IN DFOZS

REPORT DOCUMENTATION PAGE

Form Approved
OMB No. 0704-0188

1a. REPORT SECURITY CLASSIFICATION			1b. RESTRICTIVE MARKINGS		
2a. SECURITY CLASSIFICATION AUTHORITY			3. DISTRIBUTION/AVAILABILITY OF REPORT Approved for public release; distribution is unlimited.		
2b. DECLASSIFICATION/DOWNGRADING SCHEDULE					
4. PERFORMING ORGANIZATION REPORT NUMBER(S)			5. MONITORING ORGANIZATION REPORT NUMBER(S)		
6a. NAME OF PERFORMING ORGANIZATION Vanderbilt University		6b. OFFICE SYMBOL (If applicable)		7a. NAME OF MONITORING ORGANIZATION AFOSR	
6c. ADDRESS (City, State, and ZIP Code) P O Box 1807-B Nashville, TN 37235			7b. ADDRESS (City, State, and ZIP Code) Bldg 410 Bolling AFB DC 20332-6448		
8a. NAME OF FUNDING/SPONSORING ORGANIZATION AFOSR		8b. OFFICE SYMBOL (If applicable) NC		9. PROCUREMENT INSTRUMENT IDENTIFICATION NUMBER F49620-86-C-0125	
8c. ADDRESS (City, State, and ZIP Code) Bldg 410, Bolling AFB Washington, DC 20332-6448			10. SOURCE OF FUNDING NUMBERS		WORK UNIT ACCESSION NO.
			PROGRAM ELEMENT NO. 61102F	PROJECT NO. 2303	
11. TITLE (Include Security Classification) Surface Reactions in the Space Environment					
12. PERSONAL AUTHOR(S) N. Tolk					
13a. TYPE OF REPORT Technical Report		13b. TIME COVERED FROM _____ TO _____		14. DATE OF REPORT (Year, Month, Day)	
15. PAGE COUNT					
16. SUPPLEMENTARY NOTATION					
17. COSATI CODES			18. SUBJECT TERMS (Continue on reverse if necessary and identify by block number)		
FIELD	GROUP	SUB-GROUP	Surface Reactions in Space		
			Surface Chemistry		
			Surface Physics		
19. ABSTRACT (Continue on reverse if necessary and identify by block number) This report documents presentations given by researchers at the Third Annual Workshop on Surface Reactions in the Space Environment held at Vanderbilt University 17-18 October, 1988. It consists of papers and extended abstracts from each of the presentations.					
20. DISTRIBUTION/AVAILABILITY OF ABSTRACT <input type="checkbox"/> UNCLASSIFIED/UNLIMITED <input type="checkbox"/> SAME AS RPT. <input type="checkbox"/> DTIC USERS			21. ABSTRACT SECURITY CLASSIFICATION UNCLASSIFIED		
22a. NAME OF RESPONSIBLE INDIVIDUAL Larry W. Burggraf, Lt Col, USAF, Editor			22b. TELEPHONE (Include Area Code) (202) 767-4960		22c. OFFICE SYMBOL AFOSR/NC

TABLE OF CONTENTS

SURFACE REACTIONS IN THE SPACE ENVIRONMENT

	Page
Foreword	v
Technical Program Agenda	vi
Participants List	ix
"Introductory Comments on Energy-Solid Interactions" N. H. Tolk and D. L. Kinser	1
"Theory of Alkali Atom Neutralization in Ion-Surface Scattering" P. Nordlander and J. Tully [AT&T Bell Labs]	4
"Effect of Overlayers on Ion Neutralization in Grazing Incidence and Thin Foil Experiments" D. Russell	10
"Ab Initio Study of Excited States of CN ⁻ Stabilized in Point-Charge Lattices" C.S. Ewig and J. Tellinghuisen	17
"Vanderbilt Low Energy Ion and Atom Beam Facility" A. V. Barnes and M. M. Albert	24
"Radiation Induced Charge Storage in a-SiO ₂ " D.L. Kinser, M.H. Mendenhall and R.A. Quarles	32
"Characteristics of the Vanderbilt/SRB 6-meter Toroidal Grating Monochromator at the University of Wisconsin Synchrotron Radiation Center [SRC]" J. Rose	38
"HREM Observations of Electron-Stimulated Damage Processes in NiO" M.I. Buckett and L.D. Marks [Northwestern University]	48
"Laser Induced Desorption and Electron Emission" P.G. Strupp, P.C. Stair and E. Weitz [Northwestern University]	60
"A Quantitative Test of the Kinetic Model of Secondary Ion Emissions" R.A. Weller	70
"Threshold Level Photoablation of Metals: Ejected Ion Kinetic Energy Distributions" H. Helvajian and R. Welle [Aerospace Corporation]	82
"The Interaction of Hydrogen with Alkali Halide Surfaces under Electron Beam Irradiation" L.T. Hudson, A.V. Barnes, M.H. Mendenhall, N.H. Tolk, P. Nordlander, G. Betz, W. Husinsky, E. Wolfrum and P. Wurz	94
"The Role of Core Excitons in the Desorption Process" W. Husinsky, P. Wurz, E. Wolfrum, G. Betz, L. Hudson and N. Tolk	104

"A Time-of-Flight Spectrometer for Medium-Energy Ion Scattering" M. Mendenhall and R. Weller	110
"Surface Electron Spectroscopy" R. Albridge and S. Banna	123
"Interactions of Hypothermal Ions at Metal Surfaces" B.H. Cooper, D.M. Goodstein, G.A. Kimmel, R.L. McEachern [Cornell University]	125
"On the Validity of Reduced Potential Curves" J. Tellinghuisen	140
"Comparison of the Desorption by 9KeV N ₂ and 4.5 KeV N ⁺ on Silicas" P. Wang, R. Haglund, D. Kinser, N. Tolk, R. Weeks	151
"Secondary Electron Emission as a Potential Source in Shuttle Glow" P. Bunton, L. Wang and R. Haglund	159
"UV Responses of GeO ₂ Glasses" R. Magruder III, D. Kinser, J. Jackson and R. Weeks	171
"The Role of Microstructure in Determining Critical Currents in 1:2:3 High Temperature Polycrystalline Superconductors" J. Stark, R. Magruder III and D. Kinser	179
"Ion Implantation Modification of the Surface Region of Silica" G. Whichard, R. Weeks and J. Stark	190
"CN Excited Neutral Desorption from KCl Surfaces" J. Xu, M. Mendenhall, N. Tolk, L. Hudson, D. Russell and J. Tellinghuisen	201
"Anisotropic Neutralization by Thin-Foil Transmission" D. Harper, R. Albridge, D. Russell, P. Savundararaj and N. Tolk	208

SURFACE REACTIONS IN THE SPACE ENVIRONMENT

This program addresses the need for a coherent, systematic research effort to understand the physical and chemical changes which occur when materials interact with ions, atoms and molecules at energies corresponding to orbital velocities. These interactions not only produce electrical and structural damage, but the fluorescent radiation produced interferences with surveillance missions. Understanding these surface reactions is central to design of space systems for effective, long-term operation. The product of this effort will be creation of models for prediction of surface damage and fluorescence. Our goal is to use this understanding to forge a link between atomic-scale models and macroscopic phenomena to improve engineering design of space systems. This research is supported under the AFOSR Chemical and Atmospheric Directorate directed by Dr. Donald L. Ball

Larry W. Burggraf.

LARRY W. BURGGRAF, Lt Col, USAF
Program Manager
Directorate of Chemical and
Atmospheric Sciences

Third Annual Air Force Office of Scientific Research Workshop on
SURFACE REACTIONS IN THE SPACE ENVIRONMENT

Technical Program

Monday, October 17, 1988

SESSION CHAIRPERSON - Norman H. Tolk

- 7:30 Registration
- 8:30 Welcome and Introductions - N.H. Tolk
- 8:35 Remarks - J. Voegeli, Dean, College of Arts & Science
- 8:45 Remarks - L. Burggraf
- 9:00 Program Overview - N.H. Tolk
- 9:30 Atomic Oxygen Effort at Vanderbilt - A. Barnes
- 10:00 Break

SESSION CHAIRPERSON - B. Cooper

- 10:30 Damage Spectroscopies - R.F. Haglund
- 11:00 Damage Susceptibilities on Glass - D. Kinser
- 11:30 Electrons, Photons and Defects in Silica - R. Weeks
- 12:00 LUNCH

SESSION CHAIRPERSON - J. Tellinghuisen

- 1:00 Electronic Transitions in Gas-Surface Dynamics - J. Tully, AT&T Bell Labs
- 1:30 Lifetimes of Excited Hydrogen and Alkali Atoms Near Surfaces - P. Nordlander
- 2:00 Ion Neutralization at Surfaces - D. Russell
- 2:30 Lattice Stabilization of Excited Electronic States of CN^- - C. Ewig
- 3:00 Break

SESSION CHAIRPERSON - D. Kinser

- 3:30 Wisconsin Beamline Progress - J. Rose
- 4:00 Atom Probe Studies of Radiation Damage - D.N. Seidman, Northwestern University
- 4:30 Infra-red FEL Experiments - G. Edwards
- 5:00 Break

5:30 - POSTER SESSION
7:30

"Accelerators at Vanderbilt" - R. Weller, M. Mendenhall

"Comparison of the Desorption by 9KeV N₂ and 4.5 KeV N⁺ on Silicas" - P. Wang, R. Haglund, D. Kinser, N. Tolk, R. Weeks

"Ultrafast Laser Spectroscopy on Desorbed Atoms and Molecules: What Can We Learn?" - X. Li, L. Wang, R. Haglund

"Secondary Electron Emission as a Potential Source in Shuttle Glow" - P. Bunton, L. Wang, R. Haglund

"A Potential Tunable Solid-State Laser Source in the Ultraviolet: CN Negative Ions Embedded in Alkali Halide Surfaces" - R. Haglund, M. Mendenhall, J. Tellinghuisen, N. Tolk

"UV Responses of GeO₂" - R. Magruder III, D. Kinser, R. Weeks

"The Effects of Grain Size on Critical Current Density of Granular YBa₂ Cu₃ O_{7-x} Superconductors" - J. Stark, D. Kinser, R. Magruder IV

"Ion Implantation Modification of the Surface Region of Silica" - G. Whichard, R. Weeks, J. Stark

"Ion-Surface Interactions at Grazing Incidence" - P. Savundararaj, R. Albridge, D. Harper, D. Russell, N. Tolk

"CN Neutral Desorption from KCl Surfaces" - J. Xu, M. Mendenhall, N. Tolk, L. Hudson, D. Russell, J. Tellinghuisen

"Radiation Induced Distortion of Optics" - R. Quarles, D. Kinser, R. Weeks, M. Mendenhall

"Anisotropic Neutralization by Thin-Foil Transmission" - D. Harper, R. Albridge, D. Russell, P. Savundararaj, N. Tolk

"Ion-Induced Electron Emission from Oxygen-Dosed Metal Surfaces" - D. Russell, R. Albridge, D. Harper, P. Savundararaj, N. Tolk, A. Barnes

"Experimental and Theoretical Investigation of Surface Chemistry Induced Direct and Indirect Electronic Excitation of TiO₂" - E. Weitz and R. Gerber

Tuesday, October 18, 1988

SESSION CHAIRPERSON - A. Barnes

- 8:00 Phase Transition and Radiation Damage in Oxides - L.D. Marks & B. W. Wessels,
Northwestern University
- 8:30 Design of an UHV High Resolution Electron Microscope - L.D. Marks and P.C. Stair,
Northwestern University
- 9:00 Laser Induced Desorption and Electron Emission - P.C. Stair and E. Weitz,
Northwestern University
- 9:30 Test of the Kinetic Model of Secondary Ion Emission - R.A. Weller
- 10:00 Break

SESSION CHAIRPERSON - R. Albridge

- 10:30 Threshold Level Laser Ablation of Metals - H. Helvajian, Aerospace Corporation
- 11:00 Electronically Induced Desorption of Hydrogen - L.T. Hudson
- 11:30 The Role of Core Excitons in the Desorption Process - W. Husinsky
- 12:00 LUNCH

SESSION CHAIRPERSON - L.D. Marks

- 1:00 Medium-Energy Ion Scattering for Surface Spectroscopy - M. Mendenhall
- 1:30 Surface Electron Spectroscopy - R. Albridge/S. Banna
- 2:00 Interactions of Hypothermal Ions at Metal Surfaces - B. Cooper, Cornell University
- 2:30 Break

SESSION CHAIRPERSON- R. Weller

- 3:00 Validity of Reduced Potential Curves from Alkali Halide Surface - J. Tellinghuisen
- 3:30 Electric Field Induced Desorption - A.V. Barnes
- 4:00 Concluding Remarks and Adjournment

Third Annual AFOSR Workshop on "Surface Reactions in the Space Environment"
Vanderbilt University, Nashville, TN
October 17-18, 1988

PARTICIPANTS LIST

Dr. Thomas H. Allen
Optical Coating Lab
Northpoint Parkway
Santa Rosa, CA 95407

Dr. Ralph Carruth
NASA - MSFC, EH12
Marshall Space Flight Center
Huntsville, AL 35812

Dr. Royal Albridge
Department of Physics
Vanderbilt University, Box 1807-B
Nashville, TN 37235

Mr. Armond B. Chase
The Aerospace Corp.
Box 92957, Mail Station M2/241
Los Angeles, CA 90009

Dr. Salim Banna
Department of Chemistry
Vanderbilt University, Box 1822-B
Nashville, TN 37235

Prof. Barbara H. Cooper
Dept. of Physics
Cornell University/109 Clark Hall
Ithaca, NY 14853

Dr. Alan Barnes
Department of Physics
Vanderbilt University, Box 1807-B
Nashville, TN 37235

Major Larry P. Davis
AFOSR/NC
Bolling AFB, DC 20332-6448

Dr. Bill Bertrand
Arnold Engineering Development Center
Mail Stop 640, Arnold Air Force Station
Tullahoma TN 37389

Mr. Richard W. DeKalb
TBE
Sanders Road
Hartselle, AL 35640

Dr. Frederick C. Brown
University of Washington
Department of Physics, FM-15
Seattle, WA 98195

Capt. David Doryland
AFWL/ARBD
Kirtland AFB
Albuquerque, NM 87117-6008

Mr. Patrick Bunton
Department of Physics
Vanderbilt University, Box 1807-B
Nashville, TN 37235

Dr. Glenn Edwards
Department of Physics
Vanderbilt University, Box 1807-B
Nashville, TN 37235

Lt. Col. Larry Burggraf
Directorate of Chemical & Atmospheric
Sciences
Bolling AFB
Washington, DC 20332-6448

Dr. Carl S. Ewig
Chemistry
Vanderbilt University, Box 1822, Sta B
Nashville, TN 37235

Dr. Manfred Fink
University of Texas at Austin
Physics Dept., RLM Bldg. 10.214
Austin, TX 78712

Dr. E. J. Friebele
Code 6505
Naval Research Lab
Washington, DC 20375

Mr. Alan Gelb
Physical Sciences, Inc.
Research Park, P.O. Box 3100
Andover, MA 01810

Dr. R. Gerber
Dept. of Chemistry
Northwestern University
Sheridan Road
Evanston, IL 60208

Mr. George A. Graves
University of Dayton Research Institute
College Park, KL 165
Dayton, OH 45469

Dr. Richard Haglund
Department of Physics
Vanderbilt University, Box 1807-B
Nashville, TN 37235

Dr. Joseph H. Hamilton
Department of Physics
Vanderbilt University, Box 1807-B
Nashville, TN 37235

Mr. Doug Harper
Physics & Astronomy
Vanderbilt University, Box 1807 Sta B
Nashville, TN 37235

Dr. Henry Helvajian
Aerospace Corporation,
Laser Chemistry & Spectroscopy Dept.
MS: M5-747, P.O. Box 92957
Los Angeles, CA 90009

Mr. Larry Hudson
Department of Physics
Vanderbilt University, Box 1807-B
Nashville, TN 37235

Dr. Wolfgang Husinsky
Institut fur Allgemeine Physik
Technische Universitat Wien
Karlsplatz 13
Wein AUSTRIA A-1040

Mr. Les Johnson
General Research Corporation
Discovery Drive
Huntsville, AL 35806

Dr. Dan Katayama
AFGL/LIU
Hanscom AFB
Bedford, MA 01731-5000

Dr. Terry Keller
ACUREX CORPORATION
Springfield Pike, Suite 120
Dayton, OH 45431

Dr. David Kerns
Electrical Engineering
Vanderbilt University, Box 1824 Sta B
Nashville, TN 37235

Dr. Don Kinser
Mechanical and Materials Engineering
Vanderbilt University, Box 1689-B
Nashville, TN 37235

Dr. Steven L. Koontz
Johnson Space Center
ES5
Houston, TX 77058

Prof. Andrew C. Kummel
Department of Chemistry B-041
University of California San Diego
La Jolla, CA 92093

Ms. Xiaomei Li
Physics & Astronomy
Vanderbilt University, Box 1807 Sta B
Nashville, TN 37235

Dr. Robert (Bob) Magruder
Mechanical & Materials Engineering
Vanderbilt University, Box 1593, Sta B
Nashville, TN 37235

Dr. Laurence Marks
Department of Materials Science
Northwestern University
Evanston, IL 60201

Mr. Joseph Masso
S-CUBED
Box 1620
La Jolla, CA 92038-1620

Dr. Marcus Mendenhall
Department of Physics
Vanderbilt University, Box 1807-B
Nashville, TN 37235

Dr. Michael J. Meshishnek
The Aerospace Corp.
Box 92957, Mail Station M2/241
Los Angeles, CA 90009

Dr. Edmond Murad
AFGL/PHK
Hanscom AFB, MA 01731

Mr. Tom Nesbit
CAMPS
Vanderbilt University, Box 1807-B
Nashville, TN 37235

Dr. Peter Nordlander
Physics & Astron., Rutgers Univ.
Freylinghuysen Rd., P. O. Box 849
Piscataway, NJ 08855-0849

Dr. Robert Pitz
Mechanical Engineering
Vanderbilt University, Box 54 Sta. B
Nashville, TN 37235

Mr. George E. Pollock
USASDC Attn: CSSD-H-SAV
Box 1500
Huntsville, AL 35807-3801

Mr. Ron Quarles
Mat. Sciece and Engineering
Vanderbilt University, Box 1593-B
Nashville, TN 37235

Dr. Janna Rose
Synchrotron Radiation Ctr.
Schneider Drive
Stoughton WI 535899-3097

Ms. Jacqueline Ruller
Code 6505
Naval Research Lab
Washington, DC 20375

Dr. Dwight Russell
Department of Physics
Vanderbilt University, Box 1807-B
Nashville, TN 37235

Dr. Virgil E. Sanders
Los Alamos National Lab
Mail Stop J 564, P.O. Box 1663
Los Alamos, NM 87545

Mr. Philip M. Savundararaj
Department of Physics
Vanderbilt University, Box 1807-B
Nashville, TN 37235

Dr. D. Seidman
Dept. of Chemistry
Northwestern University
Sheridan Road
Evanston, IL 60208

Dr. Robert W. Shaw
Army Research Office
Research Triangle Park, NC 27709

Dr. Enrique Silberman
Fisk University
Box 15
Nashville TN 37208

Dr. Gary Sjolander
Martin Marietta Space Systems
Box 179, Mail Stop B0630
Denver, CO 80201

Dr. David Skatrud
Physics Division, Army Research Office
Box 12211
Research Triangle Park, NC 27709

Mr. Paul Sonnenberg
Physicon, Inc.
Triana Blvd., Suite A
Huntsville, AL 35805

Dr. Peter C. Stair
Dept. of Chemistry
Northwestern University
Sheridan Road
Evanston, IL 60208

Mr. John Stark
Mechanical and Materials Engineering
Vanderbilt University, Box 1593-B
Nashville, TN 37235

Dr. Joel Tellinghusen
Department of Chemistry
Vanderbilt University, Box 1668-B
Nashville, TN 37235

Dr. Norman Tolk
Department of Physics
Vanderbilt University, Box 1807-B
Nashville, TN 37235

Dr. John C. Tully
AT&T Bell Laboratories
Mountain Avenue
Murray Hill, NJ 07974

Mr. Robert Van Vliet
ACUREX Corp.
Springfield Pike, Suite 120
Dayton, OH 45431

Dean Jacque Voegeli
College of Arts & Science
Vanderbilt University
301 Kirkland Hall
Nashville, TN 37240

Dr. Paul Wang
Physics & Astronomy
Vanderbilt University, Box 1807 Sta B
Nashville, TN 37235

Prof. James Wittig
Materials Science Mech.
Vanderbilt University, 509 Olin Hall
Nashville, TN 37235

Dr. Robert A. Weeks
Mechanical & Materials Eng.
Vanderbilt University, Box 1678-B
Nashville, TN 37235

Dr. Frank Wodarczyk
AFOSR/NC
Bolling AFB
Washington, DC 20332-6448

Dr. E. Weitz
Department of Materials Science
Northwestern University
Evanston, IL 60201

Dr. Paul J. Wolf
DNA/SPSP
Telegraph Road
Alexandria, VA 22310

Dr. Bob Weller
Mechanical & Materials Eng.
Vanderbilt University, Box 1678-B
Nashville, TN 37235

Mr. Jun Xu
Physics & Astronomy
Vanderbilt University, Box 1807 Sta B
Nashville, TN 37235

Prof. Bruce W. Wessels
Department of Materials Science and
Engineering
Northwestern University
Evanston, IL 60201

Mr. Glen Whichard
Mechanical and Materials Engineering
Vanderbilt University, Box 1593-B
Nashville, TN 37235

Dr. Patricia L. White
Battelle Pacific Northwest Laboratories
Box 999 MSIN: K3-59
Richland, WA 99352

Workshop
on
**SURFACE REACTIONS IN THE
SPACE ENVIRONMENT**

October 17-18, 1988

Vanderbilt University - University Club

CENTER FOR ATOMIC AND MOLECULAR PHYSICS AT SURFACES

POSTER SESSION

Monday 5:30 - 7:30 p.m.

"Accelerators at Vanderbilt"

R. Weller, M. Mendenhall

"Comparison of the Desorption by
9KeV N₂ and 4.5 KeV N⁺ on Silicas"

P. Wang, R. Haglund,
D. Kinser, N. Tolk, R. Weeks

"Ultrafast Laser Spectroscopy on Desorbed
Atoms and Molecules: What Can We Learn?"

X. Li, L. Wang, R. Haglund

"Secondary Electron Emission as a
Potential Source in Shuttle Glow"

P. Bunton, L. Wang,
R. Haglund

"A Potential Tunable Solid-State Laser
Source in the Ultraviolet: CN Negative
Ions Embedded in Alkali Halide Surfaces"

R. Haglund, M. Mendenhall,
J. Tellinghuisen, N. Tolk

"UV Responses of GeO₂"

R. Magruder III, D. Kinser,
R. Weeks

"The Effects of Grain Size on Critical
Current Density of Granular
YiBa₂ Cu₃ Og-x Superconductors"

J. Stark, D. Kinser,
R. Magruder IV

"Ion Implantation Modification of the
Surface Region of Silica"

G. Whichard, R. Weeks,
J. Stark

"Ion-Surface Interactions at
Grazing Incidence"

P. Savundararaj, R. Albridge,
D. Harper, D. Russell, N. Tolk

"CN Neutral Desorption from KCl Surfaces"

J. Xu, M. Mendenhall, N. Tolk
L. Hudson, D. Russell,
J. Tellinghuisen

"Radiation Induced Distortion of Optics"

R. Quarles, D. Kinser,
R. Weeks, M. Mendenhall

"Anisotropic Neutralization by
Thin-Foil Transmission"

D. Harper, R. Albridge,
D. Russell, P. Savundararaj,
N. Tolk

INTRODUCTORY COMMENTS ON ENERGY-SOLID INTERACTIONS

N. H. Tolk and D. L. Kinser
Center for Atomic and Molecular Physics at Surfaces
Vanderbilt University, Nashville, TN 37235

The third annual workshop on *Surface Reactions in the Space Environment* sponsored by the Air Force Office of Scientific Research took place October 17 and 18, in Nashville Tennessee on the campus of Vanderbilt University. The workshop was hosted by the Vanderbilt Center for Atomic and Molecular Physics at Surfaces (CAMPS), and focussed on research accomplished in this exciting and fast breaking field during the second year of the AFOSR University Research Initiative (URI) program. The meeting brought together more than 60 workers in the field principally from Vanderbilt and Northwestern University but also from a wide array of university, private sector and government laboratories.

From the beginning, a central goal of this effort has been to establish a coordinated multidisciplinary Center of Excellence program concentrating on the atomic-scale dynamics of surface and near surface bulk reactions in the space environment. The style and content of the meeting was an indication that although much remains to be done, there has been substantial progress made during the past year. The major research focus in the workshop was on the investigation of the ways in which energy deposited by incident atoms, ions, electrons and photons is absorbed and localized to produce bond-making, bond-breaking and other atomic-scale phenomena on surfaces and in the near-surface bulk. Knowledge of the microscopic mechanisms responsible for these phenomena provides detailed clues to the macroscopic processes which manifest themselves as surface erosion, materials modification, charge separation and damage.

Contemporary surface- and bulk-reaction studies must be concerned with the most basic questions of energy absorption, localization and redirection or decay, which are intimately linked to the specific atomic-scale electronic properties of materials. Because of the complexity of the field, effective work in this area must be multidisciplinary involving contributions from material scientists, chemists and physicists at a minimum. In accord with this, the work must not be tied to one technique or even a small number of techniques. This meeting illustrated the importance of these principles and reflected a broad approach to

energy-solid interaction problems. The research discussed in the workshop bears directly on a broad spectrum of questions of significance to the long-term operation of platforms in space, including long-term structural, optical and electronic degradation of materials in the ambient near-earth environment, survivability under and hardening against irradiation from directed-energy weapons, vulnerability in disturbed nuclear atmospheres, and discrimination and sensing techniques based on characteristic radiation (glow) signatures.

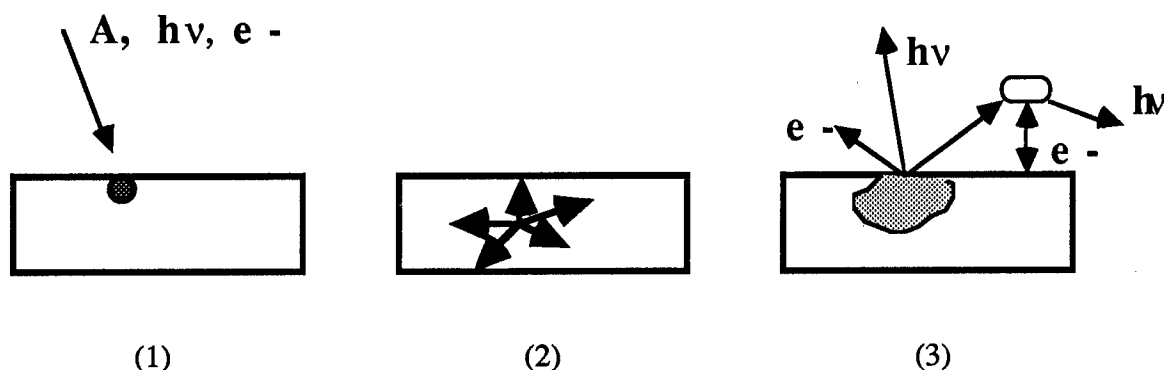


Fig. 1. Schematic representation of the three stages of electronically induced desorption.

In considering the detailed dynamics of electron-, photon- or atom-surface interactions, it has been found to be useful to describe electronically-mediated surface reactions as a three-stage process as shown in Figure 1: (1) the initial deposition of energy through creation of a hole, two holes, an exciton, a defect or some other electronic excitation; (2) the partitioning of energy into any of a number of possible localized states leading to desorption induced by electronic transitions (DIET), luminescence, charge separation, dissociation, bond making, long-lived defects, momentum transfer, or thermal processes; and (3) additional particle-surface interactions (neutralization, Auger transitions, and so on) which ultimately determine the final states of the emitted particles, of the surface and of the bulk.

Following this approach, speakers presented their latest experimental results on a wide variety of related topics including low-energy atomic and ionic oxygen interactions on surfaces, optical damage mechanisms in glass, phase transitions and radiation damage in

metal oxides, electron microscope monitored damage, laser induced desorption, desorption of atomic hydrogen from surfaces, neutralization processes at surfaces, ion solid interactions, and the role of overlayers and dopants in energy partitioning. New and exciting theoretical results were also discussed involving nonadiabatic neutralization at surfaces, lifetimes of excited hydrogen and alkali atoms near surfaces, electronic transitions in gas-surface dynamics, and lattice stabilization of excited electronic states of CN^- . In addition to the talks, there was a poster exhibition which also stimulated extended and excited discussions. The ordering of the papers and extended abstracts in this proceeding generally follows the order of presentation in the workshop with the exception that we have placed the theory papers at the beginning.

We acknowledge the assistance given by others in developing the scientific program, in particular A. V. Barnes, R. F. Haglund and L. Marks. Special acknowledgement is due Tom Nesbit, assisted by Pat Myatt and Bettye Stanley, who were responsible for the administrative and operational aspects of the meeting. In particular, we want to thank Lt. Col. L. Burggraf, AFOSR, for his continued and vigilant support.

In addition to support from Air Force Office of Scientific Research, work presented in this meeting was funded by the Naval Research Laboratory, the Acurex Corporation, National Aeronautics and Space Administration, the Office of Naval Research, Martin Marietta Corporation and the National Science Foundation.

THEORY OF ALKALI ATOM NEUTRALIZATION IN ION-SURFACE SCATTERING

P. Nordlander

Department of Physics and Astronomy
Rutgers University, Piscataway, NJ 08855

J. C. Tully

AT&T Bell Laboratories
Murray Hill, NJ 07974

ABSTRACT

Recent first principle calculations of the broadening of atomic levels near surfaces have shown that such lifetimes can be very long. We discuss the qualitative consequences of this on the interpretation of neutralization processes in ion-surface collisions. We introduce a new model for charge transfer at surfaces. An application to a recent ion surface neutralization experiment shows good agreement between theory and experiment.

THEORY OF ALKALI ATOM NEUTRALIZATION IN ION-SURFACE SCATTERING

The energies and lifetimes of excited atomic states in the vicinity of metal surfaces play an important role in many dynamical processes.¹ In an earlier paper² we presented an accurate and convenient method to calculate lifetimes of excited atomic states near metals. In an application to excited hydrogen and alkali atoms³ physisorbed on free electron-like metals, we have shown that the lifetimes can be several orders of magnitude longer than what earlier estimates have predicted. The purpose of this paper is to investigate how our finding of long lifetimes of atomic states at metal surfaces will affect the interpretation of some recent ion-surface scattering experiments.

A formal expression for the charge state of an atomic level $|a\rangle$ after a surface collision has been derived using the Anderson Hamiltonian.⁴ For simplicity we use a semiclassical approximation derived by Geerlings, et al.⁵

$$\begin{aligned} \langle n_a(\infty) \rangle = & \langle n_a(z_0) \rangle e^{-2\chi(z_0)} + \\ & + 2 \int_{z_0}^{\infty} \frac{dz}{v(z)} f(\epsilon_a(z), T) \Delta(z) e^{-2\chi(z)} \end{aligned} \quad (1)$$

Where z denotes the distance between the atom and the surface, z_0 is some initial point along the trajectory where the charge state $\langle n_a(z_0) \rangle$ is known. The first term is the so-called memory term. The second term is due to nonadiabatic charge transfer at the surface and will be called the nonadiabatic term. The function f is the Fermi Dirac function, $v(z)$ is the normal velocity of the ion, $\epsilon_a(z)$ is the energy shift, T is the surface temperature,

$$\Delta(z) \text{ is the width of the atomic level and } \chi(z) \text{ is defined by } \chi(z) = \int_z^{\infty} \frac{dz}{v(z)} \Delta(z)$$

In previous applications of this formalism the memory term has normally been neglected since the magnitude of χ based on earlier calculations of Δ has been believed to be large.⁶ Our finding of very long lifetimes no longer allows this approximation and the memory term should be included. The unknown quantity is $\langle n_a(z_0) \rangle$, the initial degree of ionization. Outside a perfect metal surface the ionic levels only shift upwards which would cause this term to be zero close to the surface. In the case of alkali adsorption on metal surfaces it has been shown⁷ that there is a strong electrostatic potential induced around the atom. This potential shifts down the ionization

levels in the vicinity of the chemisorbed Cs. We will assume that associated with each chemisorbed Cs atom there is an area of influence, a_0 , such that if the scattered ion passes through the area defined by a_0 at the distance z_0 the ion is neutralized. Thus, the $\langle n_a(z_0) \rangle$ term will be proportional to the Cs coverage, θ_{Cs} , which ranges from 0 for the clean metal surface to 1 for low work functions.

The remaining quantities in Eq. (1) are obtained as follows: $\epsilon_a(z)$ and $\Delta(z)$ are the shifts and lifetimes calculated as described above. The calculations are insensitive to whether the normal velocity, $v(z)$, is taken constant or allowed to vary according to an assumed gas-surface interaction potential.

The work function of the metal is changed by alkali atom (Cs) coadsorption. The strong fields around these atoms will induce a lateral corrugation of ϵ_a . In an earlier application we have shown that the effect of a lateral corrugation of ϵ_a on the neutralization rates of scattered ions can be accounted for by using an effective surface temperature T^{eff} in Eq. 1.

We now consider T^{eff} , a_0 and z_0 as parameters and vary them until a fit with experiment is obtained. We make no claim of prediction. As we will show, it is possible to reproduce all of the experimental data with the same physically reasonable parameters. The key to successfully reproducing the experimental results is our finding of long lifetimes of the atomic levels. This observation means, first, that the memory term in Eq. 1 will be much more important than what has hitherto been assumed, and second, that the charge transfer process will occur so close to the surface that the lateral variation of the surface potential must be taken into account.

The surface temperature, T^{eff} , is estimated by fitting the calculated neutralization yields to the experimental data for Cs scattering. We find that the experimental curve corresponds to a surface temperature of 1500K. This corresponds to a lateral corrugation due to the chemisorbed Cs of 0.2eV at distances 10 a.u. from the surface. Such corrugations are consistent with previous theoretical calculations.⁷ We emphasize that the use of an effective surface temperature T^{eff} in Eq. 1, is a nonthermal effect and only applies in charge transfer reactions.

The second parameter a_0 can most conveniently be determined from the Li scattering since the memory term is largest here due to the high velocity for Li. The Li scattering experiment reveals that below a work function of 3.8 eV, there are no ions emerging. This means that at this coverage⁸ effectively the whole W surface is covered with Cs atoms, causing a very efficient

neutralization of the alkali ions at impact or on their way out from the surface. At the work function of 3.8 eV the Cs coverage is around 0.1^8 which means that the area of influence a_0 of the Cs is approximately 500 a.u.² This value seems high, but since the experiments are performed under almost grazing incidence, the lateral size of the Cs may be effectively enhanced.

The final parameter is the initial perpendicular distance z_0 . A best fit yields $z_0=9.0$ a.u. This same choice of z_0 and the above-mentioned T and area of influence a_0 can reproduce the scattering data for all 3 alkali ions for all work functions considered. The results of the calculation is shown in Fig. 1. Given the approximate theoretical treatment we have employed and the adjustment of parameters, we do not place any importance on the quantitative nature of this agreement. However, the fact that we were able to reproduce the qualitative behavior for the three experimental systems with the same set of parameters is significant, and this agreement could not have been achieved without the long lifetimes computed here.

In conclusion we have shown that our finding of long lifetimes of excited atomic levels near metal surfaces has important implications for the interpretation of ion-surface scattering experiments. In particular, the so-called "memory term" cannot be neglected in high energy ion surface collisions. In addition, charge transfer processes will only be probable close to the metal surface where impurity induced electrostatic fields will introduce a lateral corrugation in the shifts of the atomic levels. We have shown that the presence of such a laterally varying electrostatic potential has approximately the same effect on the neutralization efficiency in ion-surface scattering as an increased surface temperature, and therefore can conveniently be included in the finite temperature charge transfer formalism introduced by Geerlings.⁵

This work was supported in part by an AFOSR University Research Initiative Contract No. F49620-86-C-0125DEF; by the Office of Naval Research under Contract No. N00014-86-K-0735 and by the Air Force Office of Scientific Research under Contract No. AFOSR-86-0150 and by NSF under Contract No. DMR-88-01027.

REFERENCES

1. B. I. Lundquist in "Many-Body Phenomena at Surfaces," eds. D. Langreth and H. Suhl, Academic Press, 1984.
2. P. Nordlander and J. C. Tully, *Phys. Rev. Lett.* *61* (1988) 990.
3. P. Nordlander and J. C. Tully, to appear in *Surface Science*, 1987.
4. R. Brako and D. M. Newns, *Surf. Sci.* *108* (1981) 253.
5. J. J. C. Geerlings, J. Los, J. P. Gauyacq and N. M. Temme, *Surf. Sci.* *172* (1986) 257.
6. M. Remy, *J. Chem. Phys.* *53* (1970) 2487, *Compt. Rend. (Paris)* *287* (1978) 235.
7. J. K. Norskov, S. Holloway and N. D. Lang, *Surf. Sci.* *137* (1984) 65.
8. J. L. Desplat and C. A. Papageorgopoulos, *Surf. Sci.* *92* (1980) 97.
9. J. J. C. Geerlings, L. F. Tz Kwakman and J. Los, *Surf. Sci.* *184* (1987) 305.

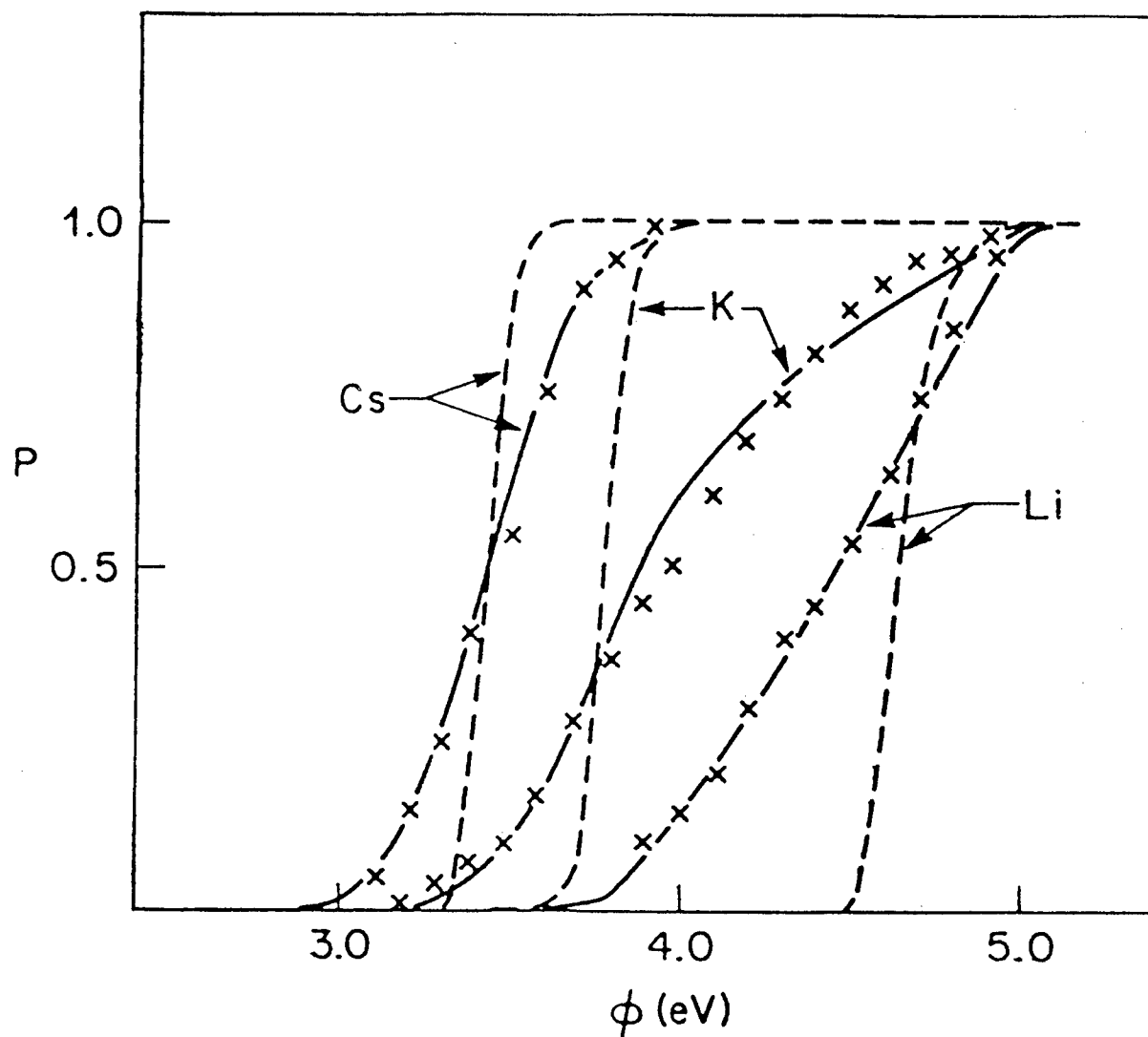


Fig. 1. Calculated fraction of ions $P=1-\langle n_a \rangle$ as function of work function ϕ for Cs, K and Li. The experimental results are indicated with crosses. A calculation⁹ using the shorter lifetimes of Ref. 6 give the dashed lines. The results of the present calculations are shown by the solid lines.

EFFECT OF OVERLAYERS ON ION NEUTRALIZATION IN GRAZING-INCIDENCE AND THIN-FOIL EXPERIMENTS.

D.P. RUSSELL, R.G. ALBRIDGE, A. V. BARNES, D.L. HARPER, P. NORDLANDER,
P.M. SAVUNDARARAJ, and N.H. TOLK

Center for Atomic and Molecular Physics at Surfaces, Department of Physics and Astronomy, Vanderbilt University, Nashville, Tennessee 37235, U.S.A.

and

J. C. TULLY

AT&T Bell Laboratories, Murray Hill, New Jersey 07974, U.S.A.

We report first detailed measurements of the effect of adsorbates on final configuration of electrons after electron pickup by positive ions during grazing-incidence and beam-foil interactions. Positive hydrogen ions incident at grazing angles on metal surfaces are neutralized and coherently excited due to anisotropic electron pickup from the surface. As a result the emitted radiation is strongly circularly polarized and when the scattered ions pass through an external electric field, the Stokes parameters characterizing the polarization oscillate as a function of the electric field strength. These oscillations, quantum beats, arise from quantum mechanical phase interference between participating atomic states. The effect of surface modification on these quantum beats is studied by adsorbing oxygen onto the surface. In addition, we discuss the alignment induced by interactions of a 17-keV H^+ beam passing through thin carbon foils with and without a deposited layer of lithium. The results presented here demonstrate the sensitivity of these techniques to the influence of overlayers on surface conditions and support the idea that future experiments with detailed surface characterization could provide a basis for theories of the sensitivity of electron pickup to surface electronic structure.

1. Introduction

We have completed an initial series of experiments to study the influence of the surface electronic structure on electron pickup in ion-surface interactions. Studies of the dynamics of interactions between surfaces and atoms (or molecules) are of importance to basic science because they provide information about fundamental processes, and are of importance to technology because they contribute to an understanding of phenomena such as catalysis, optical damage, erosion and spaceglow. Measurement of the properties of light emitted during particle-surface interactions is a particularly fruitful means of undertaking such studies. The frequency, intensity, angular distribution, polarization and point of origin of the light are all clues to the nature of the interactions that produce the radiation. Particle-surface interactions initiated by a beam of energetic particles can involve the transmission, reflection or absorption of the particles by the surface; and the origin of the emitted light can be the particles, the surface, or atoms desorbed from the surface. Collisional interactions that involve significant amounts of momentum transfer between the incoming beam and the atoms of the solid are commonly studied, as are

electronic interactions that involve the disruption of electronic structure and/or the exchange of charge with little exchange of linear momentum. We report here on studies involving electron-exchange between a surface and a beam of protons where the exchange takes place as (1) the beam reflects at a small angle from a metal surface, or as (2) the beam exits a thin carbon foil after transmission through the foil. Such electron-exchange interactions can provide information about the electronic structure of the surfaces and about the nature of the electronic interaction between particles and surfaces.

The basic observation in these studies is the measurement of the polarization of the light emitted by the atom after the ion acquires an electron from the surface. The polarization of the light provides information about the state of the electron in the atom at the point of pickup. For example, if the light is emitted from a p-state then circularly polarized light shows in the spherical representation an unequal mix of $m = 1$ and $m = -1$ states while linearly polarized light shows equal amounts of $m = 1$ and $m = -1$ with a differing amount of $m = 0$. Models of the pickup process are based on direct resonance transfer of the electron between the surface and the ion[1] and such models have been successful in explaining general features of the observed polarized light. We are attempting to determine how surface conditions, particularly the surface electronic structure, affect the electron pickup process and to what extent the experimental techniques of grazing-incidence and thin-foil transmission are sensitive to these conditions. To this end we have performed experiments in which adsorbed layers of gases or deposited layers of solids have been added to clean surfaces in order to determine the effect of surface electronic structure modification on the polarization and quantum beats measured. Significant changes are observed.

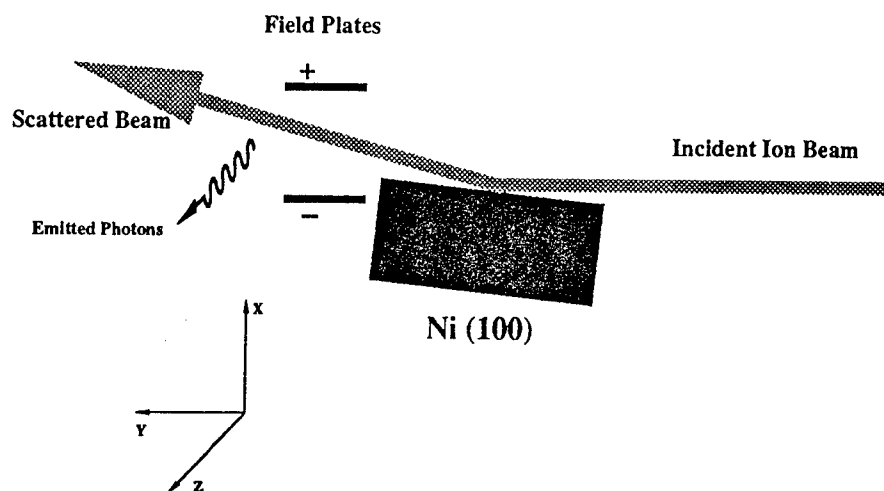


Fig. 1. Schematic diagram of the equipment used for grazing-incidence studies. The grazing-incidence plate is the [100] surface of a single nickel crystal that is cleaned by heating to $\sim 800^\circ\text{C}$ and Ar^+ sputtering in situ. The angle of incidence is $\sim 4^\circ$.

2. Grazing-Incidence Studies

Our studies of ion-surface interactions using grazing incidence were made by means of a 10-keV proton beam incident at $\sim 4^\circ$ onto a nickel crystal (Fig. 1). When a proton picks up an electron the resulting hydrogen atom can leave the surface in an excited state. In such interactions emitted Balmer-Alpha light has been found to be highly circularly polarized indicating an oriented state[2]. For example, in the present work we have measured $\sim 60\%$ circular polarization. In order to extract further information from the excited hydrogen atoms, a uniform transverse electric field (~ 700 V/cm) is applied to the beam downstream from the nickel crystal. This electric field causes Stark mixing of the magnetic sublevels, which in turn modifies the polarization of the light emitted in a manner dependent on the coherent superposition of the atomic sublevels populated by the electron following pickup. The dependence of the polarization on the electric field strength is seen to be oscillatory. The oscillatory structure is due to the quantum mechanical phase interference of the atomic sublevels and is referred to as *quantum beats*. The quantum beats provide certain information that cannot be obtained from zero-field measurements, namely the coherence parameters of mixed parity states [3].

We use reduced Stokes parameters to describe the polarization of the light. These are defined as

$$\frac{S}{I} = \frac{I_R - I_L}{I_R + I_L} \quad \frac{M}{I} = \frac{I_{0^\circ} - I_{90^\circ}}{I_{0^\circ} + I_{90^\circ}} \quad \frac{C}{I} = \frac{I_{45^\circ} - I_{135^\circ}}{I_{45^\circ} + I_{135^\circ}} \quad (1)$$

where each I refers to the intensity of light measured in a particular polarization state[4]. Subscripts identify the particular polarization state. Thus, R refers to right-hand circular, L to left-hand circular and the remaining refer to linear polarized light in directions denoted by angles with respect to the horizontal (Fig. 1). The Stokes parameters completely specify the polarization state of the light. For example, S/I represents the circular polarization giving a value of +1 for right-hand circular polarization, -1 for left-hand circular polarization and zero when no net circular polarization is present in the light. M/I and C/I perform a similar function in characterizing transmission through linear polarizers. Figure 2 shows the electric field dependence of the Stokes parameters (quantum beats) for the clean nickel crystal. Note the high value of S/I at zero field that is characteristic of grazing-incidence neutralization on clean metal surfaces. Our goal is to observe any change in the quantum-beats pattern due to the introduction of an overlayer onto the nickel surface and then to relate this change to the modification in the electronic structure of the surface due to the presence of the overlayers. Adsorbed oxygen is a suitable overlayer because it is known to affect the local electronic structure of surfaces, as is indicated by the fact that the work functions of metals are altered by adsorbed oxygen[5]. Also, the effects of oxygen on the polarization has been observed in earlier hydrogen beam experiments by Tolk *et al* [6], and in argon beam studies by Church *et al* [7]. In the present experiment oxygen was introduced into the UHV system to a partial pressure of 4×10^{-7} Torr; whereas the normal operating pressure with beam on was 2×10^{-8} Torr. Ambient background pressure with beam off was 6×10^{-10} Torr. The quantum-beats pattern recorded for the oxygen overlayer surface is shown in Figure 3. It is evident that this pattern differs from that shown in Figure 2, particularly for S/I . Thus showing that the quantum-beats pattern is sensitive to the modification of surfaces by overlayers.

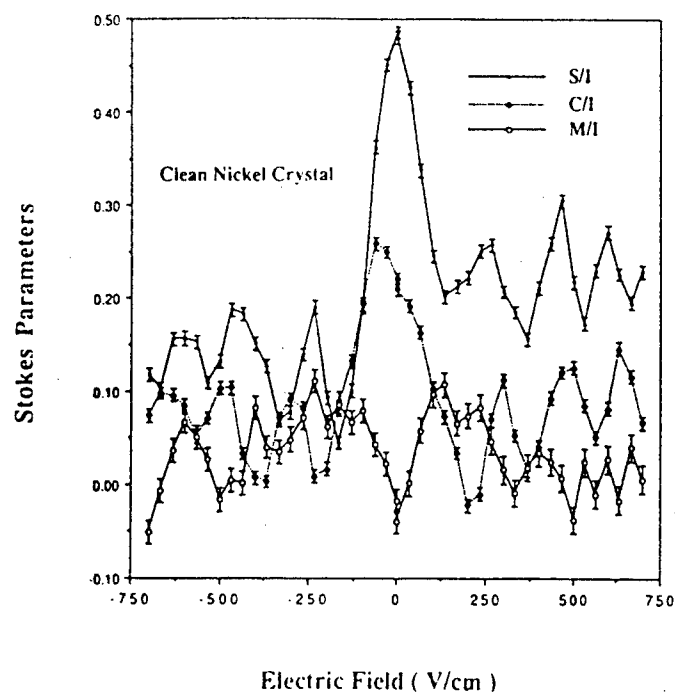


Fig. 2. Stokes parameters as a function of applied electric field for Balmer alpha radiation. The field is applied to hydrogen atoms created by the neutralization of 10 keV protons during a grazing-incidence interaction with a clean nickel crystal.

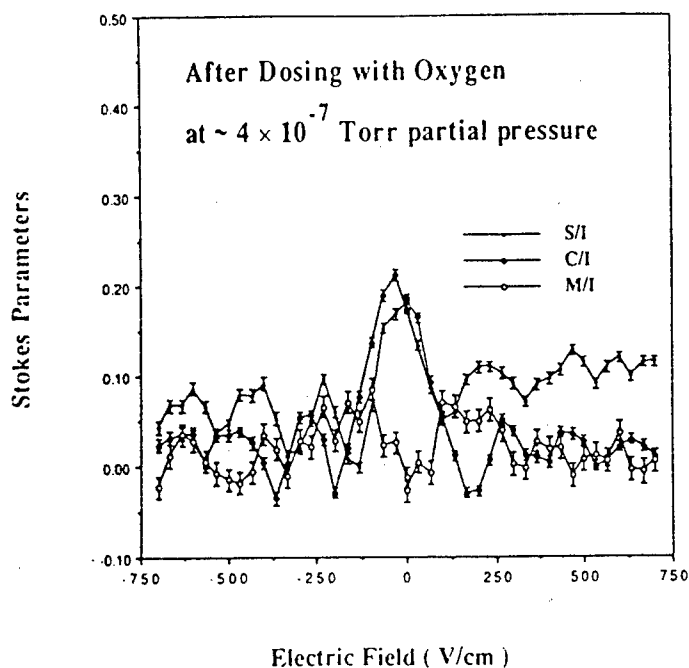


Fig. 3. Stokes parameters as a function of applied electric field for Balmer alpha radiation. The field is applied to hydrogen atoms created by the neutralization of 10 keV protons during a grazing-incidence interaction with a nickel crystal that is overlayered with oxygen.

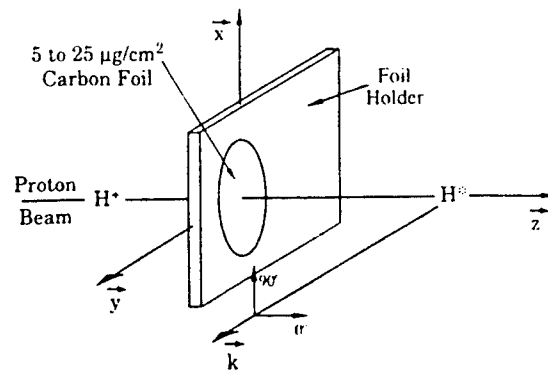


Fig. 4. Schematic diagram of the experimental arrangement for the thin-foil transmission experiments. The proton beam strikes the carbon foil at normal incidence. The measurements of polarization are made downstream from the foil.

3. Thin-Foil Studies

In addition to grazing-incidence studies, we have performed transmission experiments using a 17-keV proton beam incident on thin carbon foils. This is a new program intended to identify bulk and surface effects in final state determination. The beam-foil geometry of these experiments (Fig. 4), with the beam normal to the foil surface, possesses cylindrical symmetry about the beam axis, which results in an alignment of the electron pickup along the surface normal [8]. This alignment is manifest in a non-zero value of M/I for the light emitted from the atom [9]. The goal of this experiment is to modify the exit surface of the foil and observe any change in the value of M/I . The exit surface was modified by dosing to a visibly thick layer of lithium from an SAES doser. The mean values of M/I before and after dosing differ, as shown in Figure 5. In no case are the values of C/I or S/I seen to be different from zero. As in the case of the grazing-incidence studies, we observe that polarization data are sensitive to modifications of the surface.

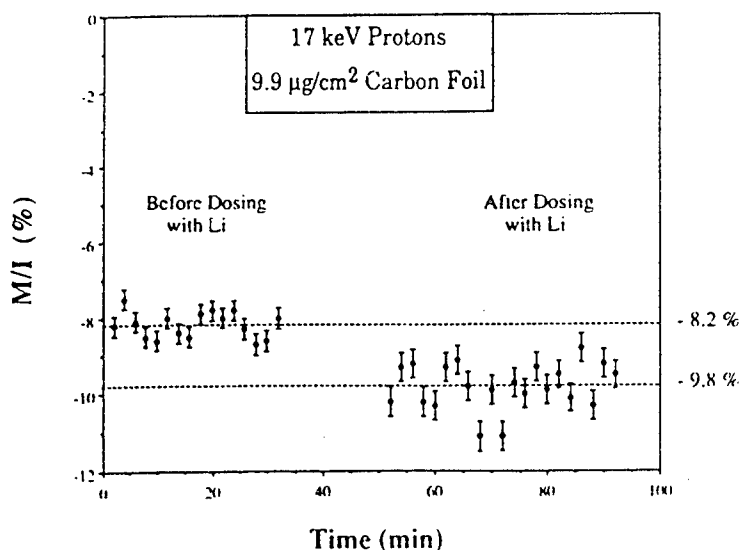


Fig. 5. M/I as a function of time for 17 keV protons incident normally on a $9.9 \mu\text{g}/\text{cm}^2$ carbon foil. Initially the value of M/I was $-8.2 \pm 0.3\%$. After dosing the exit surface of the foil with lithium M/I shifted to $-9.8 \pm 0.6\%$.

4. Discussion

In the grazing incidence data presented in Figures 2 and 3 we see a sensitivity of the quantum beats to changes in the surface composition due to oxygen coverage. These data provide information related to the state of the electron as it leaves the surface. What is ultimately of interest is the influence of the adsorbed oxygen on this state.

Models describing grazing incidence collisions break the atom-surface interaction into two parts. There is a strong-interaction region, near the surface, where, due to the presence of the surface the atomic states are hybridized and have a finite lifetime [10], the electron can transfer between the surface and the atom. There is also a weak-interaction region in which transfer no longer occurs but the quantum mechanical phase of the electron is still evolves due to the electric field interaction at the surface. In calculations based on the Anderson model [1] it is seen that in the strong-interaction region the electron pickup is sensitive to the electronic properties of the surface such as the work function. Thus, the influence of oxygen in the strong-interaction region may be through its change in the surface electronic properties and this will directly affect the atomic states involved in the pickup. Also, the presence of the oxygen can be expected to change the electric fields present in the weak-interaction region this in turn will change the time evolution of the state of the electron on the atom. The boundary between the strong and weak interaction regions is related to the freezing distance. The freezing distance is defined as the distance from the surface at which the electron state decouples from the surface and becomes 'frozen' to the atom. Although at present neither the effects in the strong or weak regions are well characterized one may still ask if they are consistent with the data presented here.

In computing quantum beats patterns from an initial atomic state we use a model, developed by Tully *et al* [2], of the time evolution of the atom through the experimental device. This model allows us to make changes in either the initial state of the electron which represents changes in the pickup process in the strong-interaction region, or to change the electric field at the surface which changes the time evolution in the weak-interaction region. Concentrating on the Stokes parameter S/I we start with an initial electron state and surface field that gives a quantum beat pattern with a large center peak characteristic of the clean nickel surface (Fig. 6a). Also shown in Figures 6b and 6c are results of two more calculations. For Figure 6b we have left the electronic state unchanged but increased the surface

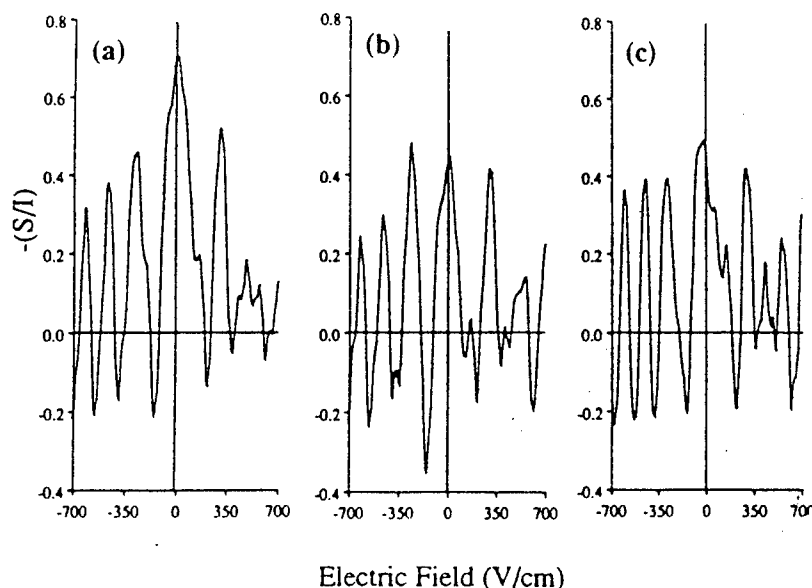


Fig. 6. (a) Calculated S/I dependence reminiscent of experimental data for clean nickel surface. (b) S/I dependence with increased surface field. (c) S/I dependence for modified initial electron state.

field by a factor of 2 and observe a marked reduction in the height of the central peak. Next, we leave the surface field as in Figure 6a and change the initial electronic state again in an attempt to decrease the central peak. The change made is to remove the p-state leaving only s- and d- states. This particular choice for changing the initial electron state is not based on any model calculation and is thus somewhat arbitrary. However as seen in Figure 6c this simple straightforward change in the initial state can also give a reduction in the central peak. It may be appropriate to address these questions in terms of the freezing distance. One can ask what the effect of the presence of oxygen has on the freezing distance (where the electron decouples from the surface). Conventional wisdom suggests that the freezing distance will be nearer the surface for the oxygen covered surface since the oxygen binds the electron more tightly both energetically and spatially. Efforts to calculate this effect are underway.

Although there are some features in the calculation that are not in quantitative agreement with the experimental results this analysis demonstrates the possibility that influences on the electron state on the atom in both the strong and weak interaction regions can be consistent with the most marked experimental feature, i.e. the reduction of the central peak in the quantum beats of S/I.

5. Conclusion

We have demonstrated that polarization data (degree of polarization and quantum beats) for light emitted in thin-foil and grazing-incidence experiments exhibit a sensitivity to the conditions of the surface. Since changes in surface conditions result in changes in the electronic structure of the surface, these results suggest that such experiments may be useful for characterizing the electronic properties of surfaces and for providing experimental tests for models of ion-surface interactions, including the influence of overlayers on those interactions.

At present we are developing an apparatus that will enable us to study quantum beats in the thin-foil geometry. Also, we are developing methods for applying submonolayer coverages.

This work was supported by Martin Marietta Michoud Contract No.A17205, by the University Research Initiative of the Air Force Office of Scientific Research Contract No.F49620-86-C-0125DEF and by the Acurex Contract No.F33615-85-C-5063 Project No.8505.

- [1] R. Brako, D.M. Newns, N.H.Tolk, J.C.Tully and R.J. Morris, *Phys. Lett.* 114A (1986) 327.
- [2] J.C. Tully, N.H. Tolk, J.S. Kraus, C. Rau and R.J. Morris, in *Inelastic Particle-Surface Collisions*, Eds. E. Taglauer and W. Heiland (Springer-Verlag, Berlin, 1981) p. 196.
- [3] J. Burgdörfer, E. Kupfer and H. Gabriel, *Phys. Rev. A* 35 (1987) 4963.
- [4] W.A. Shurcliff, *Polarized Light* (Harvard, Cambridge, 1962) p. 21.
- [5] J.E. Demuth and T.N. Rhodin, *Surface Sci.* 45 (1974) 249.
- [6] N.H. Tolk, J.C. Tully, J.S. Kraus, W. Heiland and S. H. Neff, *Phys. Rev. Lett.* 41, (1978) 643; 42 (1979) 1475.
- [7] D.A. Church, C.S. Lee, and J. Lenoir, *Phys. Rev. Lett.* 53 (1984) 1394.
- [8] H.J. Andra, *Phys. Rev. Lett.* 25 (1970) 325.
- [9] H.G. Berry, in *Inelastic Ion-Surface Collisions* Eds. N.H. Tolk, J.C. Tully, W. Heiland and C.W. White (Academic, New York, 1977) p. 309.
- [10] P. Nordlander and J.C. Tully, *Phys. Rev. Lett.* 61(1988) 990.

Ab Initio Study of Excited States of CN⁻ Stabilized in Point-Charge Lattices

Carl S. Ewig and Joel Tellinghuisen

*Department of Chemistry and Center for Atomic and Molecular Physics at Surfaces
Vanderbilt University
Nashville, Tennessee 37235*

An MCSCF approach is used to study low-lying excited electronic states of CN⁻ and CN both *in vacuo* and in point-charge lattices. The latter simulate the electrostatic potential that renders excited states of CN⁻ stable against autoionization in ionic lattices. The results provide strong support for a $^3\Sigma^+$ assignment for the excited state involved in the UV emission spectrum of CN⁻ in alkali halide substrates.

INTRODUCTION

Under certain circumstances, many of the alkali halides emit a prominent "molecular" band system in the 2200-3600 Å region, following excitation by electrons, ions, or VUV radiation.¹⁻⁷ This spectrum was early associated with a CN species^{2,3} present as an impurity, and subsequent work pointed strongly to CN⁻.^{6,7} According to present interpretations, the emission comes from $v = 0$ of the lowest excited molecular electronic state; and since CN⁻ is isoelectronic with CO, by analogy most authors have adopted the $^3\Pi$ designation for the emitter in CN⁻.

Recent work from this laboratory⁸ has raised questions about the $^3\Pi$ identification of the emitting state, suggesting instead that the analogy is with the isoelectronic N₂ rather than CO, making $^3\Sigma^+$ the first excited state. The principal spectroscopic evidence for this assignment is the large increase (by 0.17 Å) in the internuclear distance R_e on going from the X $^1\Sigma^+$ ground state to the excited state, as deduced from analysis of the Franck-Condon pattern of the spectrum. The idea that the valence electrons of CN⁻ behave more like those in N₂ than those in CO is also supported by Auger studies of alkali cyanides.^{9,10} Furthermore the long lifetime (80 ms) of the emitting state is more in keeping with expectations for $^3\Sigma^+$ than for $^3\Pi$.⁸

Although a number of theoretical treatments of the ground state of CN⁻ have been reported, the work by Ha and Zumofen¹¹ appears to be the only published calculation of excited states. These authors studied only the $^1\Pi$ and $^3\Pi$ excited states. They obtained results which were not consistent with the experimental spectrum (ΔR_e too small) and acknowledged that the actual emitting state might be other than $^3\Pi$. However they calculated structures only for CN⁻ *in vacuo*. The experimentally observed excited state lies 5.6 eV above the ground state, which *in vacuo* would be 1.8 eV above the ionization limit of CN⁻.¹² Thus full optimization of the wavefunction *in vacuo* should lead to CN + e⁻ rather than to a stable excited singlet or triplet state of the anion, which raises questions about the applicability of such calculations to the interpretation of the solid-state spectra. In the alkali halide lattices the ionization potential of CN⁻ is raised to ~ 10 eV,⁹ rendering the low-lying excited states stable against autoionization.

In the present work we report extensive MCSCF calculations for CN^- stabilized in point-charge lattices chosen to mimic the experimental environment. Results have been obtained over a range of internuclear distances for the lowest $^3\Sigma^+$ and $^3\Pi$ states as well as for the $^1\Sigma^+$ ground state. For comparison we have also calculated the first two electronic states in the CN radical. These calculations clearly support the $^3\Sigma^+$ assignment for the emitting state in CN^- and suggest a strong orientational preference for this state in the lattice.

COMPUTATIONAL DETAILS

The *ab initio* computations described herein employed the UEXP2 program,¹³ which uses the exponential-operator unitary-group MCSCF approach for finding total molecular energies.¹⁴⁻¹⁶ The basis set consisted of triple-zeta plus double-polarization and diffuse functions, denoted "6-311+G(2d)".^{17,18} The diffuse functions are particularly important to account for the relatively large radii of charge distributions in anions such as CN^- .¹⁹ This basis set contains 26 functions of σ symmetry, 12 π_x , and 12 π_y . The active space included 5 σ , 3 π_x , and 3 π_y molecular orbitals. All possible single and double excitations were included among the active orbitals of each symmetry, but excitations from the core orbitals were omitted. This procedure resulted in the following numbers of optimized configurations (CSFs) and rows in the distinct row tables: $\text{CN } ^2\Sigma^+ -- 3645$ and 35, $\text{CN } ^2\Pi -- 3123$ and 35, $\text{CN}^- ^1\Sigma^+ -- 2016$ and 39, $\text{CN}^- ^3\Sigma^+ -- 2889$ and 39, $\text{CN}^- ^3\Pi -- 3240$ and 36. The calculations were carried out on an SCS Model 40 mini-supercomputer and required about 24 hours to obtain values for all five electronic states at a single internuclear distance in a particular lattice.

Computations were done for the lowest states of $^2\Sigma^+$ and $^2\Pi$ symmetry in CN and the lowest states of $^1\Sigma^+$, $^3\Sigma^+$, and $^3\Pi$ symmetry in CN^- . All five states were treated in the point-charge lattices, and the three stable states -- CN ($X ^2\Sigma^+$), CN ($A ^2\Pi$), and CN^- ($X ^1\Sigma^+$) -- were calculated *in vacuo* as well. In the lattice calculations the CN or CN^- was positioned at an anion location in an fcc structure having the KCl lattice constant, 3.14 Å. The model lattice included the nearest and next-nearest layers of positive charges (6 and 8, respectively) and the nearest shell of negatives.¹² This lattice is relatively small and has a net charge of +1 (+2 for neutral CN). However, preliminary computations indicated that for the purpose of stabilizing the CN^- excited states, it is adequate to achieve a realistic semblance of the stabilization that occurs in the actual lattice.

We examined two orientations of the CN^- , chosen to maintain the molecular symmetry of the ion *in vacuo* (i.e. to preserve the equivalence of the π_x and π_y orbitals). In the first (lattice A) the CN^- axis was directed toward a nearest positive charge (i.e. in the $\langle 100 \rangle$ or equivalent direction); in the second (B) it was oriented toward a nearest negative charge ($\langle 110 \rangle$ direction).

Energies were obtained at internuclear distances 2.039 – 2.839 a_0 at intervals of 0.1 a_0 . Spectroscopic constants -- T_e , R_e , ω_e , and $\omega_e x_e$ -- were extracted from least-squares fits to Morse functions²⁰ and in some cases to a modification of the Morse function that includes a prefactor, $1 + a(R - R_e)$, designed to correct for skewedness errors often observed in comparisons of the Morse function with RKR potentials.²¹ Tests of this procedure on similar R regions of the known potentials of other molecules have shown that is fully reliable. (However, without additional flexibility, it would not be appropriate for spanning a much larger range of R .)

RESULTS AND DISCUSSION

There have been quite a number of theoretical treatments of CN^- *in vacuo*, dating back at least 20 years; all except ref. 11 (which includes a summary of earlier works) have considered just the ground state, $X^1\Sigma^+$. Only in the more recent works have attempts been made to predict the vibrational and rotational constants for this state. The anion remains uncharacterized experimentally in the gas phase, but its infrared and UV spectra are known in condensed media. The CN radical is of course very well known experimentally; here again most of the serious attempts to predict the spectroscopic properties from *ab initio* calculations have been reported only recently.

Our minimal energies *in vacuo* -- -92.38619 hartree for CN (X) and -92.49225 hartree for CN^- (X) -- are noticeably higher than the best previously reported estimates, -92.52322 and -92.73911 hartree,²³ respectively. In separate calculations using the same program and basis, we obtained minimal SCF energies of -92.20950 (CN) and -92.33617 hartree (CN^-), which are much closer to the lowest available estimates of -92.2103022 and -92.34898 hartree.²⁴ In the latter comparison the discrepancy is appreciably larger for the anion, which suggests that our basis set is still relatively deficient for it, even though diffuse functions have been included. The much larger discrepancies in the correlated energies are partly due to our use of inactive core orbitals. Our resulting estimate of the electron affinity is 0.93 eV below experiment.¹² However, the *ab initio* estimation of molecular electron affinities is a demanding task, and CN a particularly demanding target for this task.^{25,26} As evidence of this difficulty, we note that simple adoption of the lowest available estimated energies for both species leads to a 2.0 eV *overestimation* of the electron affinity.

Table I. Estimated spectroscopic constants (cm^{-1}) for states of CN and CN^- *in vacuo*.

	R_e (Å)	T_e	ω_e	ω_{ex_e}	Reference
CN (X)	1.1718	0	2068.59	13.087	27 (expt.)
	1.183		2116	12.0	28
	1.1903 ^a		2061	12.7	29
	1.1755		2065	13.0	this work
CN (A)	1.2333	9245.28	1812.56	12.609	27 (expt.)
	1.237	11243	1912	11.9	28
	1.246 ^a	8420	1852	11.5	29
	1.2409	12850	1796	12.8	this work
CN^- (X)	1.173	0	2150	11.3	30
	1.198		2132	16.4	11
	1.1804		2080	12.1	31
	1.1772		2082	13.6	23
	1.1852		2047	12.6	this work

^aTabulated points refitted in present work.

Table I above compares recent theoretical estimates of the spectroscopic constants for CN(X), CN(A), and CN⁻(X) with experimental values, where available. Our calculations fare well in this comparison: Our R_e estimates are high by only 0.004 and 0.008 Å, respectively, for the X and A states of CN; and our vibrational constants for these two states are the best theoretical estimates reported to date. If the error trends in our results for CN can be extrapolated to CN⁻(X), we can expect the true R_e to be 1.177–1.180 Å and ω_e to be 2065–2075 cm⁻¹. These values are consistent with the recent estimates in refs. 23 and 31. On the other hand a scaling procedure for SCF values³² has yielded a prediction quite close to our calculated value. The one disappointment in these comparisons is the 3600 cm⁻¹ error in our estimate of T_e for CN(A).

Our results for all five states *in vacuo* and in the two lattices are collected in Table II below.

Table II. *Ab initio* spectroscopic constants (cm⁻¹) of CN⁻ and CN from present work.^a

	R_e (Å)	T_e	ω_e	$\omega_e x_e$	lattice
CN ⁻ (X) ^b	1.185	0	2047	12.6	<i>in vacuo</i>
	1.187		2033	12.6	A
	1.184		2053	12.5	B
CN ⁻ (³ Σ ⁺) ^c	1.377	47600	1240	18	A
	1.358	45300	1320	14	B
CN ⁻ (³ Π)	1.28	59000	1610	4	A
	1.28	57400	1640	7	B
CN (X) ^d	1.176	23280	2065	13.0	<i>in vacuo</i>
	1.173	102950	2081	12.8	A
	1.175	101280	2059	13.3	B
CN (A) ^e	1.241	36130	1796	12.8	<i>in vacuo</i>
	1.244	114690	1776	12.9	A
	1.242	114110	1787	13.0	B

^aAll energies for each "lattice" are referenced to CN⁻ (X) for that lattice.

^bExperiment: $R_e = 1.18$ Å³³, $\omega_e = 2125$ cm⁻¹ in KCl and NaCl.

^cExperiment: $R_e = R_{eX} + 0.17$ Å, $T_e = 45350$ (adjusted for smaller ω_e of present work).

^dExperimental values in Table I. T_e *in vacuo*, relative to CN⁻ (X), is the electron affinity, 30820 cm⁻¹, ref. 12.

^eExperiment: $T_e = 40060$ relative to CN⁻ (X) *in vacuo*.

By comparison with the other states, the CN⁻ excited states exhibited noticeably slower convergence, which was reflected in higher residuals in the fits used to extract the spectroscopic constants. However, the latter were still significant to the indicated digits. The main result is that the ³Σ⁺ state is 1.5 eV lower than ³Π, with precisely the right internuclear distance (in lattice B) to account for the observed spectral intensity pattern. The energy of ³Σ⁺ is also remarkably close to the observed experimental T_e ; but in view of the errors in the electron affinity and in T_e for CN(A), this may be fortuitous. However, we consider the R_e comparison definitive evidence that the state responsible for the UV

emission spectrum is indeed $^3\Sigma^+$ rather than $^3\Pi$. Furthermore the calculated energy separation of these two states is large enough to trust as an indicator of their relative positions, meaning that the emitting state is also the lowest excited state, as is expected on physical grounds.⁸

Relative to $\text{CN}^-(X)$ the states of CN show the expected electrostatic upshift in the lattice. The magnitude of this shift is about 0.7 eV larger than would be estimated from the Madelung energy; but this error is actually very close to the error in the Madelung energy for our truncated lattice.³⁴ None of the states of CN^- or CN show dramatic sensitivity to lattice in their spectroscopic properties; however, the $\text{CN}^- ^3\Sigma^+$ state is more sensitive than the others, with a 0.02 Å spread in R_e values, 80 cm^{-1} in ω_e , and 2400 cm^{-1} in T_e . It is noteworthy that all of the excited states show lower T_e for lattice B than for lattice A, which may indicate a real preference for the $\langle 110 \rangle$ orientation over $\langle 100 \rangle$ (see below).

In a check on the role of the lattice constant, we repeated the lattice A calculations at $R_e = 1.185$ Å using the larger lattice constant of KCN, 3.25 Å. All of the states were raised in energy, as anticipated, but the energies of the excited states dropped relative to that of $\text{CN}^-(X)$. The decrease amounted to 200 cm^{-1} for $\text{CN}^- (^3\Sigma^+)$ which is consistent in both direction and magnitude with the experimental observations for NaCl and KCl.⁸ The relative energies of $\text{CN}(X)$ and $\text{CN}(A)$ dropped by about 2600 cm^{-1} , which is roughly as predicted from the change in the Madelung energy for our truncated lattice.

Our calculations place the $\text{CN}^- ^3\Pi$ state about 10000 cm^{-1} higher than estimated from *in vacuo* calculations by Ha and Zumofen.¹¹ As we noted at the outset, there is a question about the validity of such calculations for electronically unstable excited states. To check this point we conducted the following test calculation: First the energies of all five states under consideration here were calculated *in vacuo* at $R = 1.185$ Å using the basis set described above. Then the exponents on the diffuse functions in the basis were changed from 0.0438 (C) and 0.0639 (N) to 0.01 (both), and the calculations were repeated. This change led to slight increases in the energies of the CN states (300 cm^{-1}), a somewhat larger increase for $\text{CN}^-(X)$ (2400 cm^{-1}), but dramatic *decreases* (13000-14000 cm^{-1}) for the excited states of CN^- . The moderate increase for $\text{CN}^-(X)$ is evidence of the need for optimized diffuse functions for this state, but the large decreases for the excited states of CN^- show that such results are meaningless for these unstable states *in vacuo*.

Although our estimated ω_e for $\text{CN}(X)$ *in vacuo* is quite close to experiment, for $\text{CN}^-(X)$ in lattices our estimates are still 70-90 cm^{-1} below experiment.⁸ We attribute this disparity to deficiencies in our point-charge model. Fowler and Klein³⁵ have noted that to obtain reliable estimates of spectroscopic properties, it is important to retain realistic charge distributions for at least the nearest neighbors in the lattice. The overlap compression of the central anion by "real" positive ion nearest neighbors in place of point charges might be expected to increase ω_e for the anion. We are presently extending our calculations to check this point.

CONCLUSIONS

The results of the present study provide solid support for the earlier conjecture⁸ that the excited electronic state responsible for the UV emission spectrum of CN^- is $^3\Sigma^+$ rather than $^3\Pi$. We have also shown that simple point-charge lattices can model the electrostatic

stabilization that prevents the excited states from autoionizing in actual lattices. Without such stabilization, optimized *ab initio* calculations must generally yield ambiguous results.

Although our theoretical estimates of the energy and internuclear distance of the $^3\Sigma^+$ state agree very well with experiment, our estimate of the vibrational frequency in the ground $^1\Sigma^+$ state is less satisfactory. We tentatively attribute this shortcoming to deficiencies in the point-charge model. Another weakness of this model is its prediction of absolute energies: Our calculations place the ground state of CN^- 2200 cm^{-1} lower in lattice A than in lattice B, whereas experimentally CN^- is essentially a free rotor in KCl at room temperature, with a preference for the $\langle 111 \rangle$ orientation that is so slight that it is only evident at very low temperatures.³⁶ On the other hand, the relatively large difference in the calculated T_e values for the CN^- excited states in the model lattices may indicate a real and much stronger orientational preference in the excited states. Such an effect might be expected for the larger internuclear distances and more diffuse electron distributions in the excited states and should be experimentally identifiable.

Another possible problem with the point-charge model is that in the optimization of the excited states, it may offer an unphysical opportunity for the electronic charge to relocate on what are effectively fixed H nuclei. The slow convergence observed for the $^3\Pi$ and $^3\Sigma^+$ states may have been signaling this effect, and preliminary calculations for the still-higher $^1\Pi$ state have shown even more such difficulty. We are currently attempting to extend the calculations to check on these possibilities.

ACKNOWLEDGMENT

We want to thank Dr. Ron Shepard for assistance in implementing and using the UEXP2 program. This work was supported by the Air Force under grants AFOSR-86-0146 and AFOSR-F49620-86-C-0125 to Vanderbilt University. The SCS computer was acquired with the assistance of SCS Corporation, Vanderbilt University, and NSF Grant CHE-8808018.

REFERENCES

- ¹ E. von der Heyden and F. Fischer, *Phys. Stat. Sol.* **69b** (1975) 63.
- ² A. I. Bazhin, E. O. Rausch and W. E. Thomas, *J. Chem. Phys.* **65** (1976) 3897.
- ³ W. A. Metz and E. W. Thomas, *Nucl. Instr. Methods* **194** (1982) 505.
- ⁴ N. H. Tolk *et al.*, *Phys. Rev. Lett.* **46** (1981) 134.
- ⁵ D. Cherry *et al.*, *Nucl. Instr. Methods B* **13** (1986) 533.
- ⁶ A. B. Henrique and J. P. von der Weid, *Solid State Commun.* **56** (1985) 571.
- ⁷ A. B. Henrique and J. P. von der Weid, *J. Phys. C* **19** (1986) 1071.
- ⁸ M. Mendenhall *et al.*, *Chem. Phys. Lett.* **147** (1988) 59.
- ⁹ H. Pulm *et al.*, *Chem. Phys.* **92** (1985) 457.
- ¹⁰ H. Pulm, C.-M. Liegener and H.-J. Freund, *Chem. Phys. Lett.* **119** (1985) 344.
- ¹¹ T.-K. Ha and G. Zumofen, *Mol. Phys.* **40** (1980) 445.
- ¹² R. Klein, R. P. McGinnis, and S. R. Leone, *Chem. Phys. Lett.* **100** (1983) 475.
- ¹³ R. Shepard, UEXP 2.00 (Argonne National Laboratory, 1980).
- ¹⁴ R. Shepard and J. Simons, *Int. J. Quantum Chem. Symp.* **14** (1980) 211.
- ¹⁵ R. Shepard, I. Shavitt, and J. Simons, *J. Chem. Phys.* **76** (1982) 543.
- ¹⁶ F. B. Brown, I. Shavitt, and R. Shepard, *Chem. Phys. Lett.* **105** (1984) 363.

- 17 R. Krishnan, J. S. Binkley, R. Seeger, and J. A. Pople, *J. Chem. Phys.* **72** (1980) 650.
- 18 M. J. Frisch, J. A. Pople, and J. S. Binkley, *J. Chem. Phys.* **80** (1984) 3265.
- 19 C. S. Ewig and J. R. Van Wazer, *J. Phys. Chem.* **90** (1986) 4360.
- 20 G. Herzberg, *Spectra of Diatomic Molecules* (Van Nostrand, Princeton, 1950).
- 21 J. Tellinghuisen, S. D. Henderson, D. Austin, K. P. Lawley, and R. J. Donovan, *Phys. Rev. A* (in press).
- 22 P. J. Bruna, H. Dohmann, and S. D. Peyerimhoff, *Can. J. Phys.* **62** (1984) 1508.
- 23 K. A. Peterson and R. C. Woods, *J. Chem. Phys.* **87** (1987) 4409.
- 24 D. Sundholm, P. Pyykko, and L. Laaksonen, *Mol. Phys.* **56** (1985) 1411.
- 25 J. Baker, R. H. Nobes, and L. Radim, *J. Comput. Chem.* **7** (1986) 349.
- 26 R. H. Nobes, J. A. Pople, L. Radim, N. C. Handy, and P. J. Knowles, *Chem. Phys. Lett.* **138** (1987) 481.
- 27 K. P. Huber and G. Herzberg, *Constants of Diatomic Molecules* (Van Nostrand, Princeton, 1979).
- 28 H. Ito *et al.*, *Chem. Phys.* **98** (1985) 81.
- 29 H. Lavendy, J. M. Robbe, and G. Gandara, *J. Phys. B: At. Mol. Phys.* **20** (1987) 3067.
- 30 P. R. Taylor, G. B. Bacskay, N. S. Hush, and A. C. Hurley, *J. Chem. Phys.* **70** (1979) 4481.
- 31 P. Botschwina, *Chem. Phys. Lett.* **114** (1985) 58.
- 32 T. J. Lee and H. F. Schaefer III, *J. Chem. Phys.* **83** (1985) 1784.
- 33 J. M. Rowe, D. G. Hinks, D. L. Price, S. Susman, and J. J. Rush, *J. Chem. Phys.* **58** (1973) 2039.
- 34 C. Kittel, *Introduction to Solid State Physics* (Wiley, New York, 1966).
- 35 P. W. Fowler and M. L. Klein, *J. Chem. Phys.* **85** (1986) 3913.
- 36 H. U. Beyeler, *Phys. Rev.* **B11** (1975) 3078.

Vanderbilt Low Energy Ion and Atom Beam Facility

A.V. Barnes and M.M. Albert

*Center for Atomic and Molecular Physics at Surfaces
Vanderbilt University
Nashville, Tennessee*

Abstract: We report on the construction status of the low energy facility and present preliminary data from low energy ion bombardment of an Al(Li) sample.

1. Low Energy Neutral Beam Design

The Vanderbilt low energy neutral beam facility is a new design concept based on grazing incidence neutralization of positive ions. This has the advantages of producing neutral beams from almost any positive ionic species and working over a broad range of energies. The full system design is outlined in figure 1. It consists of a positive ion source, a beam transport system, a decelerator, a neutralizer, and a target chamber.

The initial ion beam is produced in a Colutron G2 ion source. This is a plasma discharge source with a small beam energy spread ($\pm 0.2\text{eV}$) and a low emittance. The ions are extracted from the plasma through a small orifice and focused using a simple Einzel lens geometry. It is then velocity selected using a Wien filter (crossed electric and magnetic fields). In operation the source chamber pressure is on the order of 10^{-6} Torr. This character of the source demands a good differential pumping section and a bend to get rid of gaseous charge exchange neutrals formed in this region. The bend also prevents the light from the plasma discharge from reaching the experimental chamber.

After these elements of the G2 source the beam enters an inhouse designed electrostatic beam transport system. The beam is bent and focused through a tube to provide differential pumping. The vacuum in this section is about 3×10^{-9} Torr. The beam is then bent back parallel to but slightly offset from its original direction. Any neutrals formed by gaseous neutralization in the source or by grazing incidence neutralization in the tube will be lost from the beam at this point. The beam then passes through a second Einzel lens where it is focused onto the decelerator and grazing incidence devices.

The decelerator and neutralizer in this device are combined. The neutralization is performed by passing the beam through a metallic plate with small holes in it. The holes are arranged at an angle such that there is no line of sight transmission and a maximum one bounce transmission. The deceleration field is produced by a holding this neutralizer plate at the desired potential and transporting the beam as close to the plate as possible before it feels the field. The beam is decelerated in a very short distance and then enters the small holes of the neutralizer. This very short transport of the low energy ions alleviates most of the space charge effects which hamper systems with separate function decelerators and neutralizers. To perform low energy ion measurements the neutralizer is replaced by the target.

2. Low Energy Beam Status

The systems described above are all in the process of being acquired and constructed. The Colutron G2 source is presently operating and producing a low energy ion beam. The vacuum chamber, chamber mounting stand and electrostatic elements for the transport system are completed but have not yet been assembled and tested.

3. Data Taken with the Low Energy Ion Source

We have been using the low energy source to investigate the desorption of excited species from an Al(Li) alloy. These excited states are measured with a McPherson 918 monochromator. The geometry of the source, target and the monochromator is shown in figure 2. The source is connected to the experimental chamber through a small tube to provide differential pumping. The pressure in the experimental chamber was 1×10^{-8} Torr for these measurements. The beam was extracted from the source at 2010 volts and decelerated by changing the potential of the target. Under 2 keV ion bombardment we observe emission spectra such as the one in figure 3. The strong emission lines correspond to the lithium doublet at 6707Å (Li*) and the aluminum doublet at 3944Å, 3961Å (Al*). We investigated how the intensities of these lines change as we go to lower energies with several bombarding species.

3.1 Argon Ions

A separated Ar⁺ beam of about 900 nanoamperes was extracted from the source. Figure 4 shows the yield of Li* and Al* as a function of energy. The constant Al* yield at low energies is caused by a high energy neutral contamination in the beam. Note the qualitative difference in the yields. As the energy falls below 200 eV the Al* signal becomes constant (all from high energy contamination) while the Li* signal remains strong. The point labeled "2p hole" corresponds to the energy in the lab where the center of mass energy in the argon-aluminum system corresponds to the 73 eV needed to remove a 2p electron from the aluminum atom. Also note the break in the Li* yield at around 100 eV. We have not yet found a good explanation for these behaviors.

3.2 Nitrogen Ions

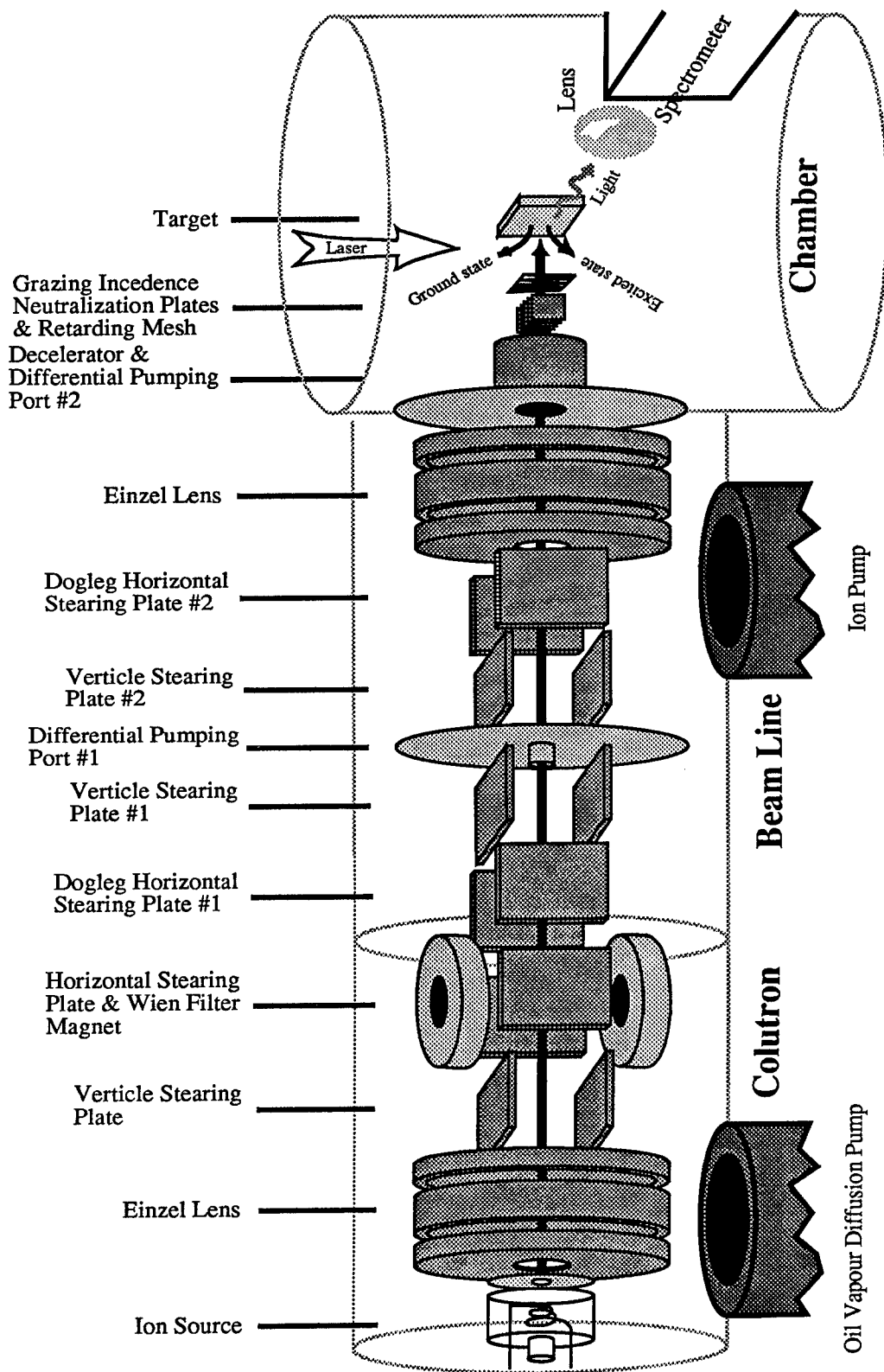
A separated N⁺ beam of about 100 nanoamperes was extracted from the source and used to measure the yields as a function of energy. Figure 5 shows the energy dependence of the observed Li* signal. Note that this signal does not go to zero at zero energy. This is due to a contamination of the beam by high energy neutrals formed by grazing incidence neutralization at the differential pumping tube. Figure 6 shows the ratio of the Al* yield to the Li* yield. These were collected during the same energy scan. The Al* yield goes to zero at about 115 eV. At the same energy the Li* yield changes slope. The point labeled "2p hole" again indicates the energy in the laboratory frame where the center of mass energy in the nitrogen-aluminum frame equals the energy required to remove a 2p electron from the aluminum atom.

3.3 Oxygen Ions

A separated O⁺ beam of about 10 nanoamperes was extracted from the source and maintained for several hours. During that time we made the yield measurement shown in figure 7. Note the sharp fall off in the yield as the energy decreases. This fall off is at a much higher energy than with either Ar⁺ or N⁺.

4. Future Measurements

We plan to expand these measurements by running different ions and by measuring the ground state neutrals using laser induced fluorescence. By investigating the relative yields in many systems we hope to uncover specific mechanisms which are responsible for the excited state emissions.



Low Energy Neutral Source

Under Construction at Vanderbilt University

Figure 1

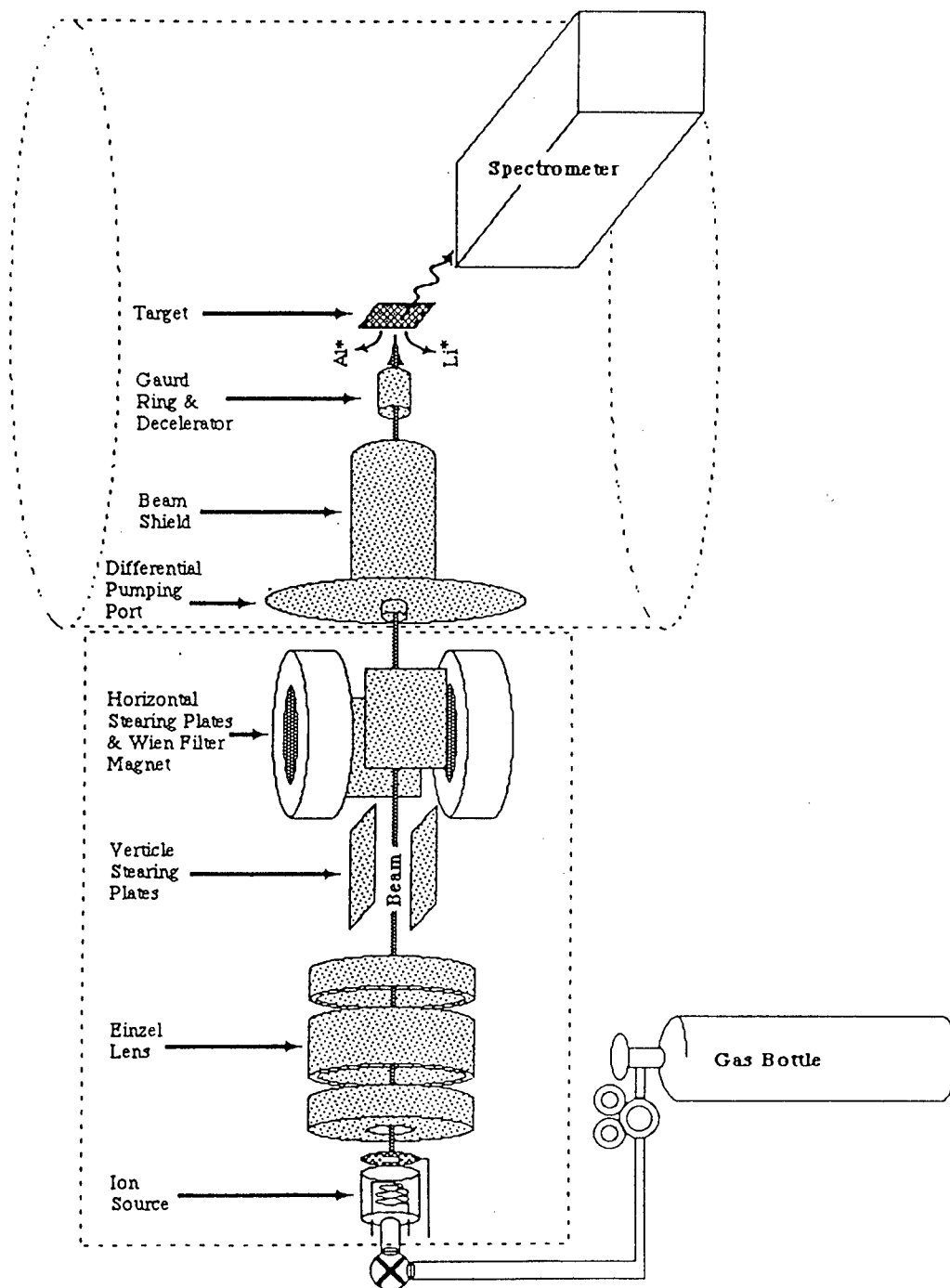


Figure 2

Spectrum from 2KeV Ar+ on 230°C Al(Li)

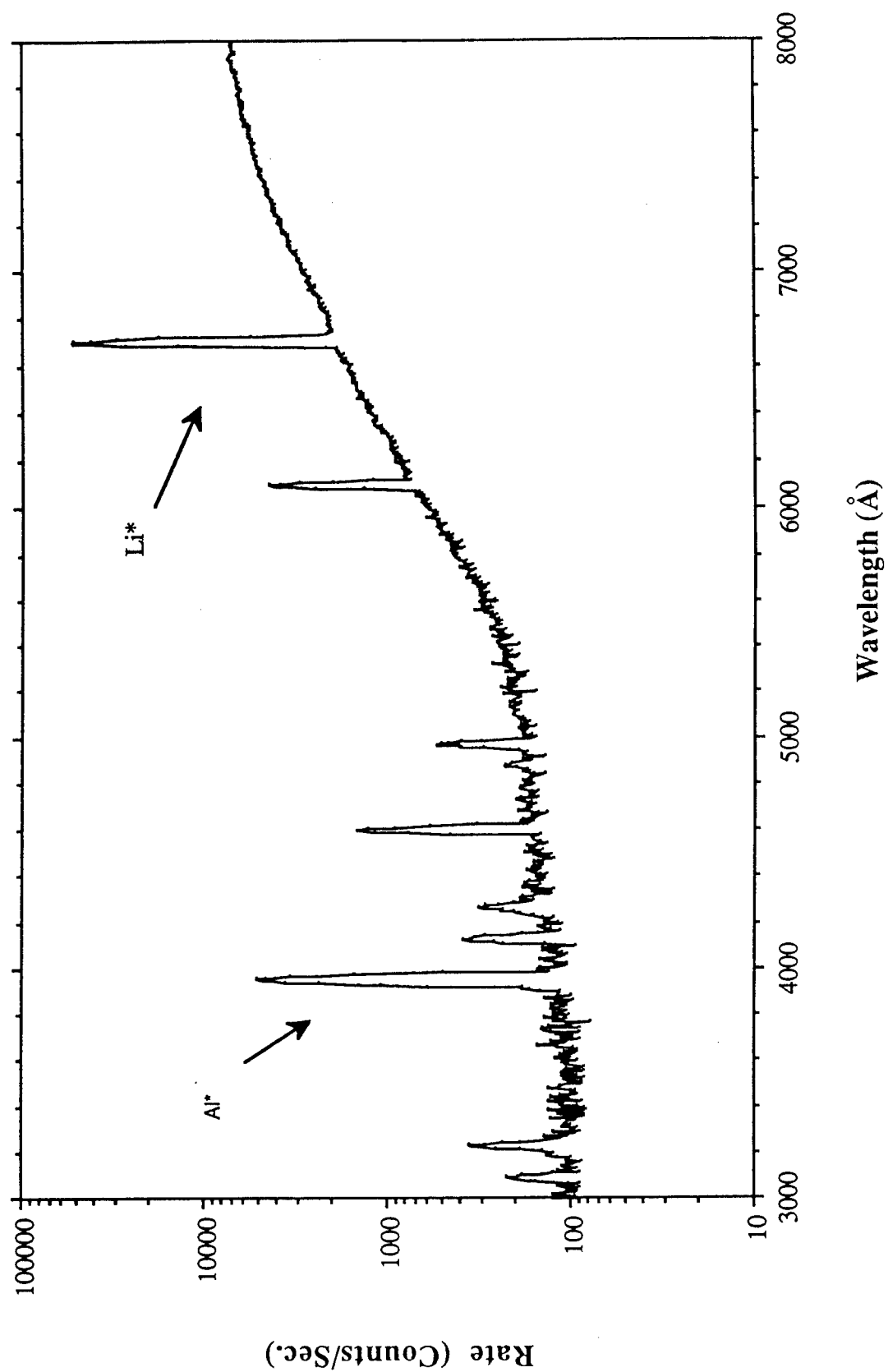


Figure 3

Li* & Al* vs. \sqrt{E} of Ar+ on Al(Li)

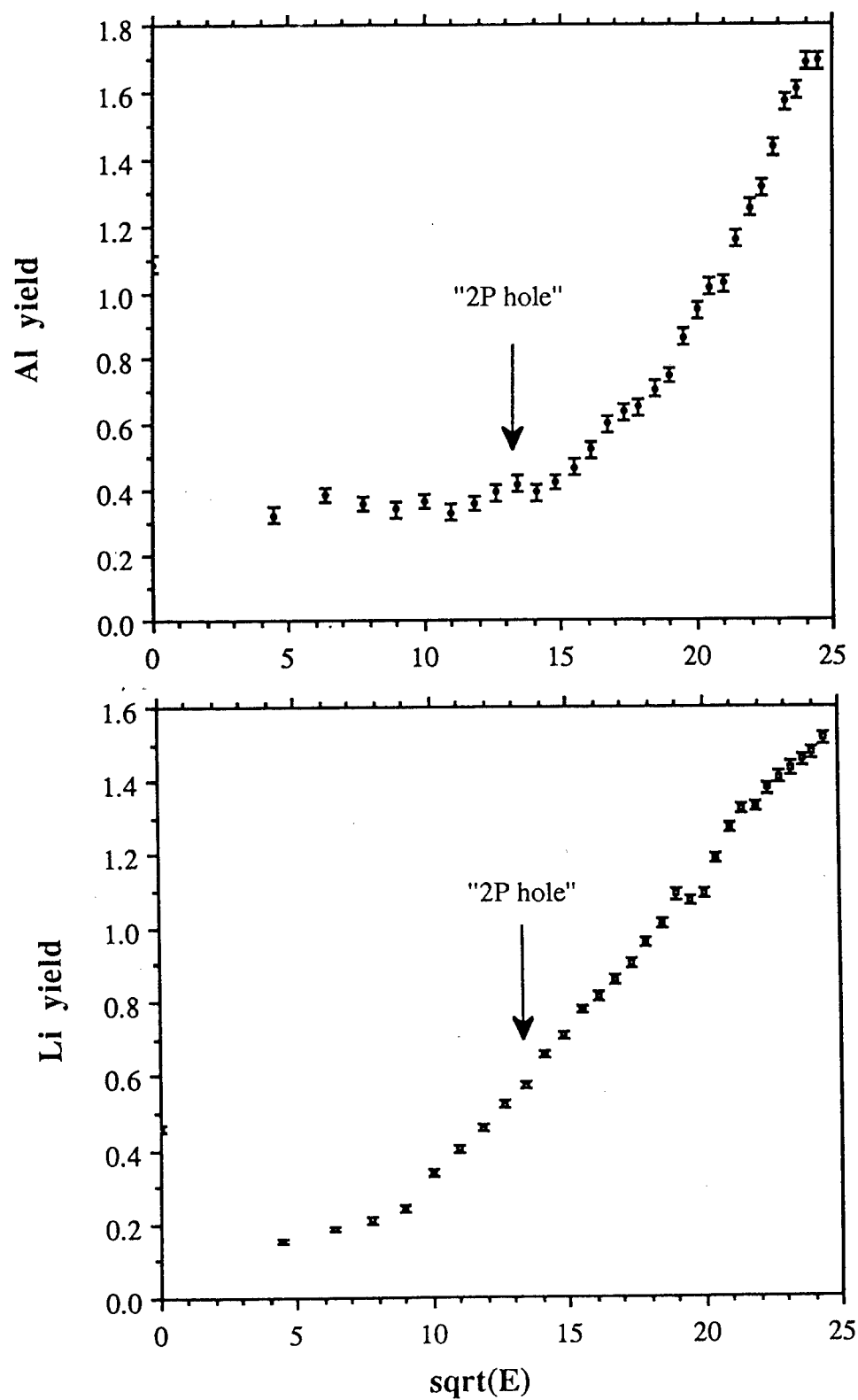


Figure 4

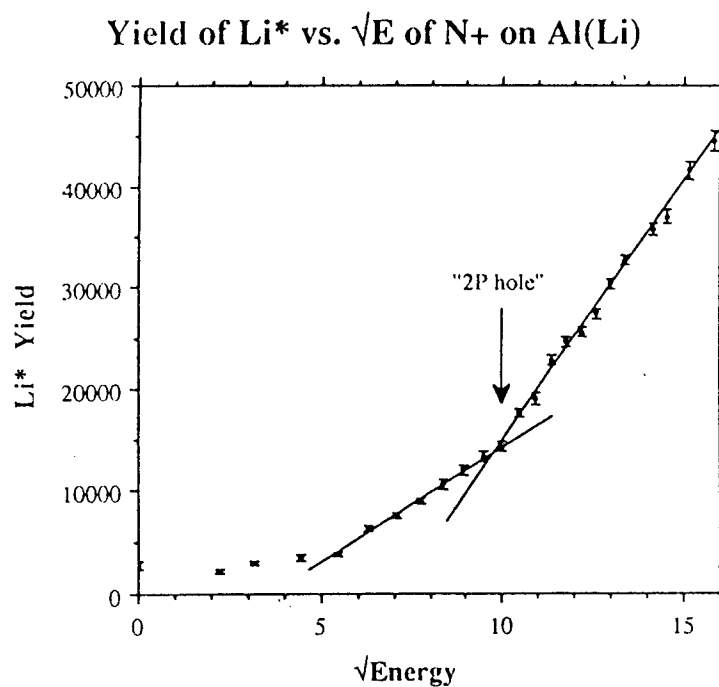


Figure 5

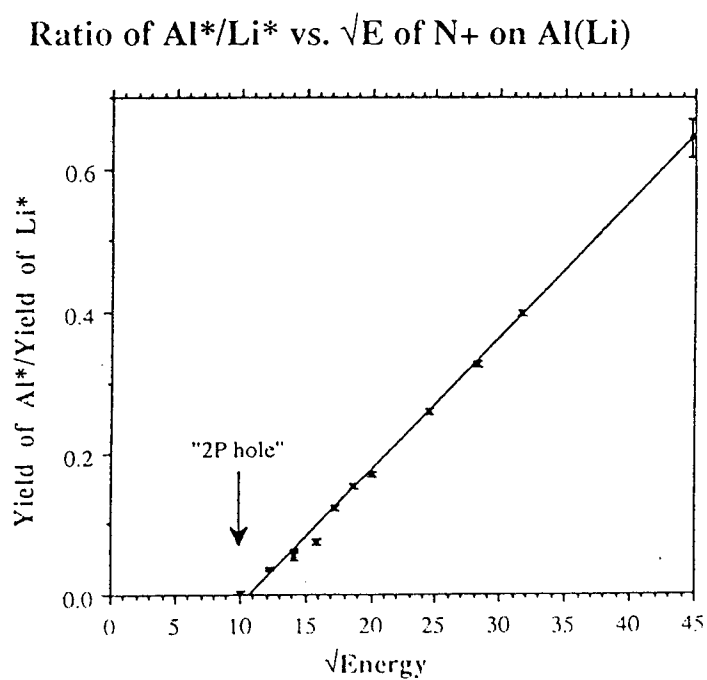


Figure 6

Al* Yield from Al(Li) under O+ Bombardment

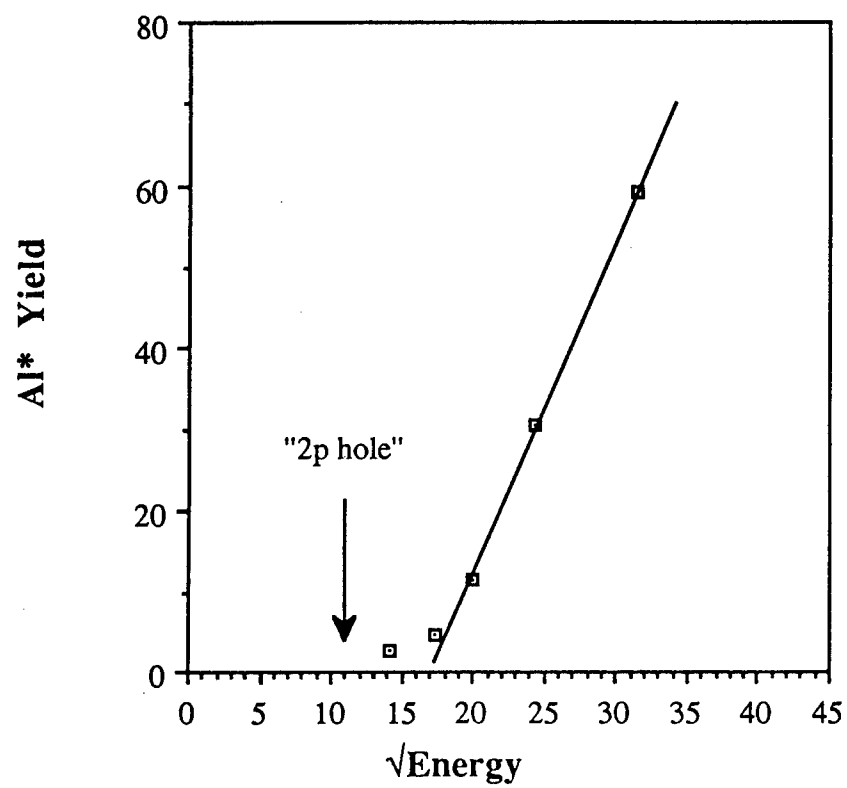


Figure 7

RADIATION INDUCED CHARGE STORAGE IN a-SiO₂

Kinser D. L.^{*}, Mendenhall M. H.⁺, and Quarles R. A.^{*}

^{*}Department of Materials Science and Engineering

⁺Department of Physics and Astronomy

Center for Atomic and Molecular Physics at Surfaces

Vanderbilt University, Nashville, Tennessee, 37235, USA

Abstract

The displacement of charge in glasses by electron, particle and gamma radiation has been known for a number of years but quantitative measurements of charge storage and mechanical displacement resulting from the Coulombic forces have not been reported. The charge stored and mechanical distortion of types II, III, and IV high purity SiO₂ glasses have been measured after exposure to ¹³⁷Cs gamma radiation. The type IV a-SiO glasses store the largest charge and display the largest distortions.

Introduction

The storage of charge in dielectrics has been known since the observations of Lichtenberg /1/ whilst radiation induced storage was first reported by Culler in 1959 /2/. Many studies on radiation effects in glasses have concentrated on the atomic-scale structural defects induced by radiation /3/. The majority of such studies were conducted after irradiation in cylindrically symmetric radiation sources /4/ which result in isotropic damage and no net charge displacement. Thermally stimulated discharge current measurements on lead-silicate glasses were reported by Hong, et al. /5/. The results of those measurements indicated that charge storage appeared to be influenced by the microstructure of the phase separated glass. The charge storage sites in a-SiO₂ are almost certainly not related to the microstructure of the glass but are rather point defects arising from either structural or chemical disorder within the glass. The work of Dutta, et al. /6/ reports an observation of polarization of intrinsic defects in a-GeO₂ and it appears that such defects are the sites where displaced charge is stored in those glasses.

This work examines the macroscopic effects of anisotropic ¹³⁷Cs radiation. Compton electrons which are isotropically displaced in most experiments are anisotropically displaced in these experiments hence new effects arise from the macroscopic displacement of charge. This research quantitatively characterizes the charge displaced and elastic distortion arising from the Coulombic forces acting on the solid.

Experimental Procedure

Thermally Stimulated Discharge Current (TSDC). TSDC measurements were made on samples of type /7/ II, III, and IV high-purity silica samples after anisotropic radiation to a dose of 1.5×10^5 rad. Samples were gold coated on both faces before irradiation. Contrary to normal procedures for measurement of TSDC, no external voltage was applied to the sample at any time before or during these experiments. The discharge currents reflect the polarization induced by Compton scattering during the gamma irradiation. The measurement apparatus employed has been previously described /8/.

He-Ne Laser Interferometry. Samples examined were 1 mm thick, 30 mm diameter discs polished to less than 10 wavelengths per inch aperture. The face of the sample exposed to the radiation source was coated with gold to increase its reflectivity thus enhancing the interference from the surface of interest. The interferometer employed is schematically depicted in Figure 1. He-Ne laser interferograms ($\lambda=632$ nm) were photographically recorded before and after irradiation. The interferograms were analyzed by measuring distances between successive fringes in two orthogonal diameters of the sample as illustrated in Figure 2. The measurement before and after irradiation were made along the same diameters as referenced to a fiduciary mark on the gold coating.

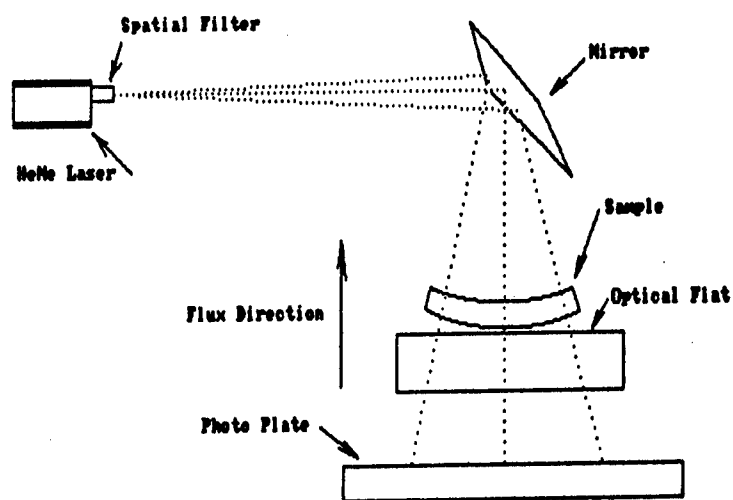


Figure 1: Experimental setup of the interferometer showing the direction of irradiation with respect to the optical flat.

Results

A representative result from the TSDC measurements is shown in Figure 3. The current released from this sample appears in two temperature ranges ($\sim 320^\circ\text{C}$ and $\sim 500^\circ\text{C}$). This curve was integrated to give the total charge stored in the irradiated sample. The results of these measurements for the six samples examined are tabulated in Table 1. TSDC measurements were conducted on the samples as summarized in Table 1. For the ^{137}Cs radiation dose of 1.5×10^5 rad, the charge stored rises from 7.2×10^{-9} in the type II glass to 1.5×10^{-5} Coulombs in the type IV glass. The charge stored at equivalent radiation dose thus varies by a factor of 10^4 for the samples examined in this work.

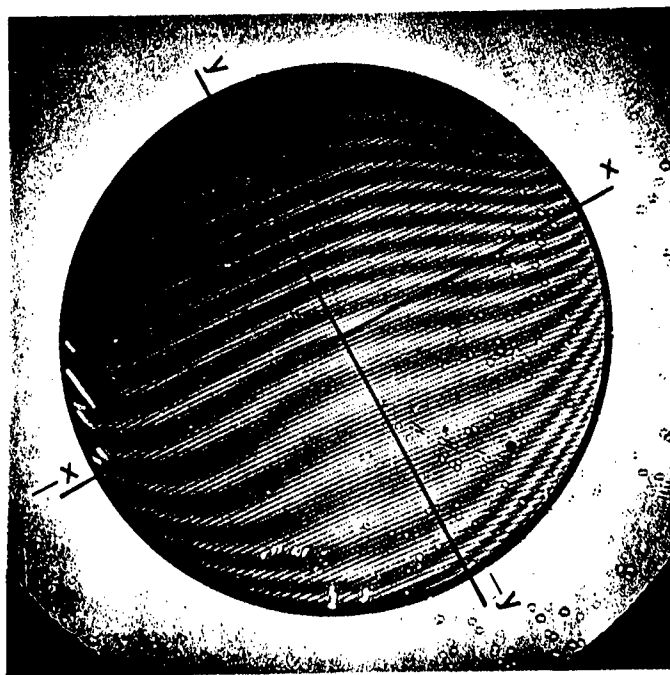


Figure 2: Interferogram of Optosil (type II) irradiated to 1.5×10^5 rad ^{137}Cs . Distortion measurements were performed by measuring the distances between fringes along the orthogonal diameters marked "X" and "Y".

Table I

Glass Type	Manufacturing Process	Trade Name	Maximum Deflection (nm)		Charge Storage for
			1.5×10^4 Rad	1.5×10^5 Rad	1.5×10^5 Rad
II	Electromelted Natural Quartz	Optosil	400*	400	$7.2 \times 10^{-9}\text{C}$
III	Flame Hydrolysis SiCl_4	Spectrosil	250	250	$1.3 \times 10^{-7}\text{C}$
		Suprasil I	400	250	$1.5 \times 10^{-7}\text{C}$
		Corning ULE	350	400	
IV	Plasma Oxidized SiCl_4	Spectrosil WF	450	1200	$1.5 \times 10^{-5}\text{C}$
		Suprasil W1	500	900	$1.4 \times 10^{-5}\text{C}$
Glass/Ceramic	Conventional Melting	Zerodur	<50	<100	

*Readability of He-Ne laser interferometer = 100nm

Results of these measurements are presented in Figures 4-6 for samples of types II, III and IV a-SiO₂. Examination of these results reveals that the samples were not initially optically flat but distortion induced by the radiation is nevertheless evident. The results for type II glass (Optosil) indicate that the outer edge of this glass is deflected approximately 400 nm by the 1.5×10^4 rad radiation dose employed. The corresponding results for type III (Spectrosil) shown in Figure 5 indicate that this glass is distorted slightly less (~250 nm) for a corresponding dose. Similar measurements on another type III (Suprasil) a-SiO₂ result in a maximum displacement of 400 nm at equivalent dose. The results for a type IV glass

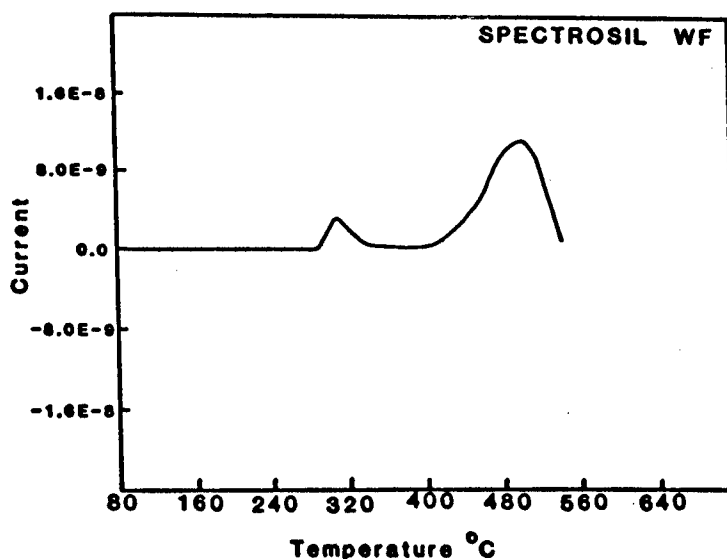


Figure 3: Thermally stimulated discharge current measurement for Spectrosil WF (type IV) subjected to anisotropic dose of 1.5×10^5 ^{137}Cs . Integration of this curve yields the total charge stored as tabulated in Table 1.

(Spectrosil WF) are shown in Figure 6. These results indicate that the displacement of the surface exceeds 1500 nm at a dose equivalent to the types II and III samples discussed above. The peculiar shape of the displacement as a function of distance for this sample is a consequence of buckling which locally reversed the original curvature of the sample.

The results presented are measurements made on orthogonal directions of the sample with the maximum distortion. It should be noted that different samples were used for the 1.5×10^4 and 1.5×10^5 rad doses. This explains the differences in initial shapes amongst the unirradiated glasses. These differences in shape are especially prominent in Figure 5, a type III (Spectrosil).

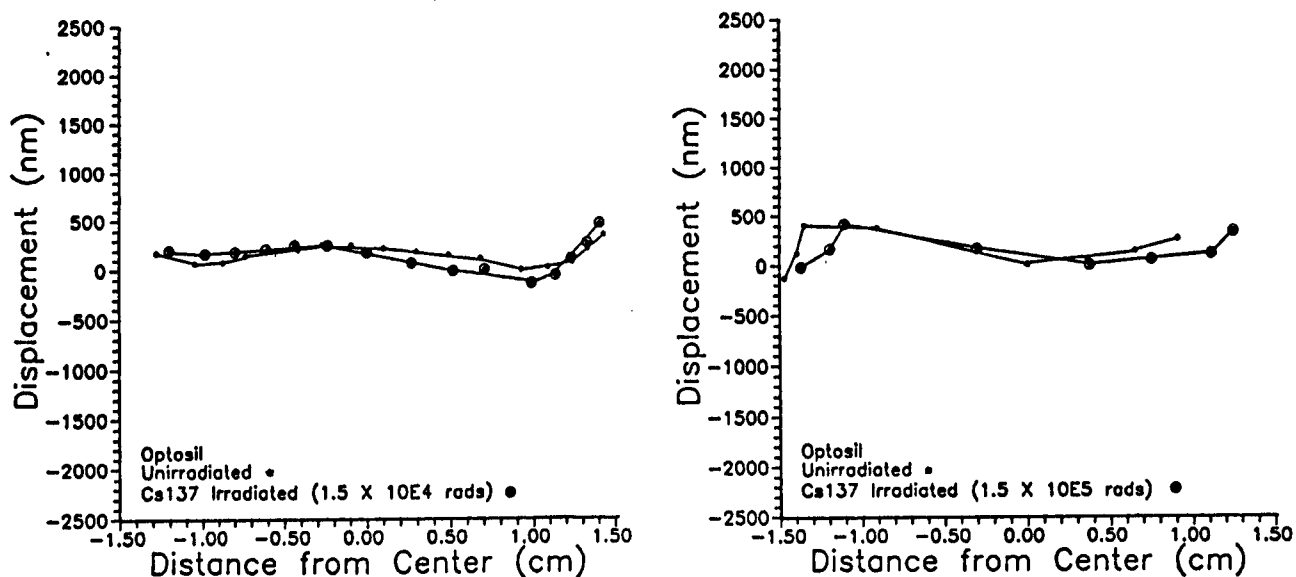


Figure 4: Displacement curves for Optosil (Type II) a-SiO₂ for ^{137}Cs dose of 1.5×10^4 rad (left) and 1.5×10^5 rad (right).

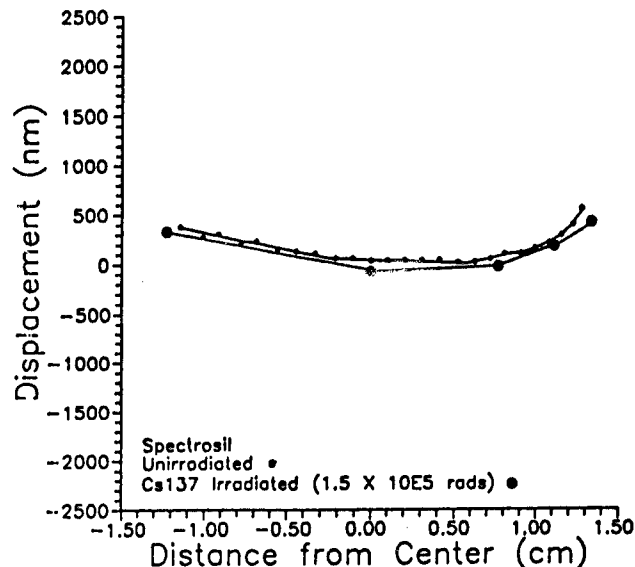
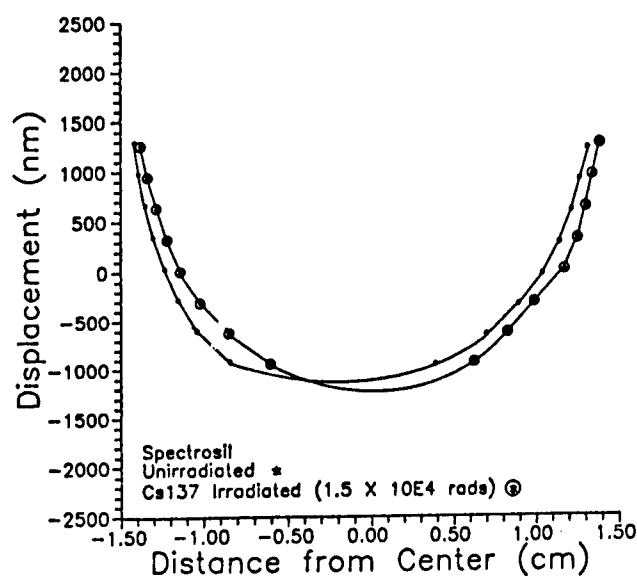


Figure 5: Displacement curves for Spectrosil (Type III) for ^{137}Cs dose of 1.5×10^4 rad (left) and 1.5×10^5 rad (right). Note the difference in shape of the unirradiated samples arises from the different initial surface profiles.

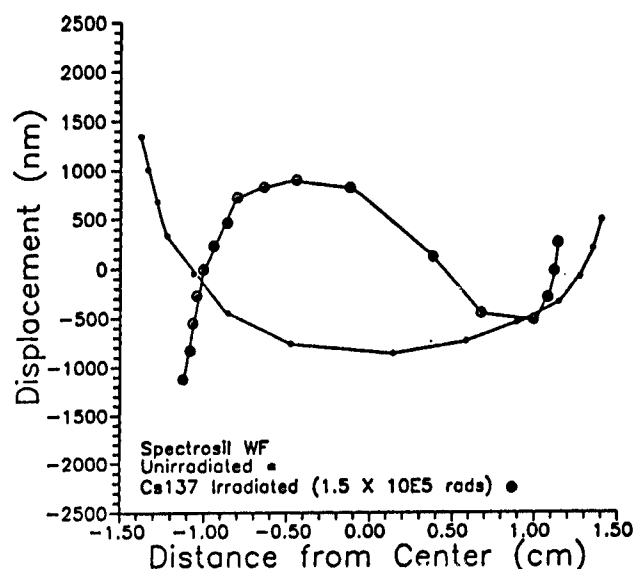
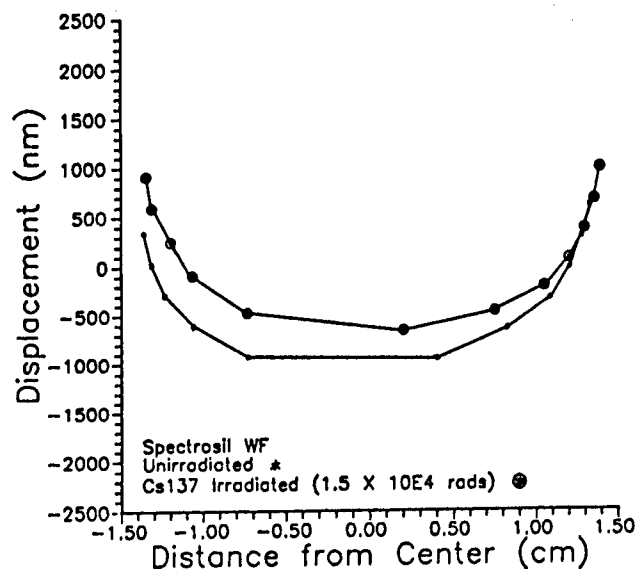


Figure 6: Displacement curves for Spectrosil WF (type IV) a-SiO₂. Distortion saturation was not achieved after 1.5×10^4 rad (left) resulting in increased distortion and buckling after 1.5×10^5 rad (right).

Discussion

The charge displaced by anisotropic gamma radiation in a-SiO₂ varies over four orders of magnitude with glass type for a fixed radiation dose. This observation indicates that the charge storage and charge bleed-off processes are sensitive to glass processing variables. This is consistent with the radiation induced E' and oxygen hole center production rates ^{/9/} in similar glasses which are also markedly sensitive to glass preparation processes.

Anisotropic ^{137}Cs gamma irradiation has been observed to distort high purity silica optical materials. This distortion of the material is a consequence Coulombic forces arising from charge stored in the samples which requires storage of electrons and/or holes at preexisting trapping sites. We conclude that the trapping sites are preexisting because their

ability to trap charge depends upon the type a-SiO₂ or prior thermal processing of the glass. The Coulombic interaction of the macroscopically displaced charge results in a mechanical stress which leads to distortion of the glass shape. The magnitude of this distortion depends upon prior glass processing because the charge which produces the distortion is stored in trapping sites whose concentration is dependent upon prior glass processing.

The radiation induced mechanical distortions have saturated at the lowest dose level (1.5×10^4 rad) employed in current studies of type II and III silicas. These glasses show the minimum observed charge storage and the smallest shape distortions.

Type IV silica glasses were observed to store the largest charge and also had the largest shape distortions. The displacement in these glasses was not saturated at 1.5×10^4 rad as the distortion doubled when the radiation dose was increased to 1.5×10^5 rad, but no additional distortion occurred as the dose was increased to 1.5×10^6 rad.

CONCLUSIONS

1. The charge released from an anisotropically irradiated a-SiO₂ sample correlates positively with the radiation induced distortion in the glass.
2. The quantity of charge stored in a-SiO₂ glasses is sensitive to glass processing variables hence the mechanical distortion of the glass depends upon processing variables.

Acknowledgements

The authors gratefully acknowledge the financial support of this research program under Naval Research Laboratories contract number N00014-86-C2546.

References

1. Lichtenberg G.C. // De nova metodeo naturam ac motum electrici fluidi investigandi commentatio posterior. 1779. Gottingen. University of Gottingen. P. 1-16.
2. Culler V. // Proceedings of the 7th Hot Lab and Equipment Conference. 1959. P. 120-131.
3. Griscom D.L. // Mat. Res. Soc. Symp. Proc. 1986. Vol. 61. P. 213-221.
4. Barton J., Ghormley J.A., and Hochandel C.J. // Nucleonics. 1955. Vol. 13. P. 74-77.
5. Hong C.M., Day D.E., Weeks R.A., and Kinser D.L. // J. Non-Cryst. Solids. 1981. Vol. 46. P. 389-404.
6. Dutta B., Kinser D.L., Magruder III R.H., and Weeks R.A. // J. Non-Cryst. Solids. 1987. Vol. 95-96. P. 389-396.
7. Hetherington G. // J. of British Ceram. Soc. 1966. Vol. 3. P. 595-598.
8. Jackson J.M., Dutta B., and Kinser D.L. // Rev. Sci. Instrum. 1987. Vol 58. P. 1003-1008.
9. Weeks R.A., Kinser D.L., Kordas G., Magruder R., and Wells M. // Journal de Physique. 1982. Vol. C9. P. 149-153.

Characteristics of the Vanderbilt/SRC 6-meter
Toroidal Grating Monochromator at the University of
Wisconsin Synchrotron Radiation Center (SRC)

Janna L. Rose

Department of Physics and Astronomy and
Center for Atomic and Molecular Physics at Surfaces
Vanderbilt University, Nashville, TN 37235

Abstract

The Vanderbilt University/Synchrotron Radiation Center 6-meter toroidal grating monochromator (TGM) was commissioned the first of March 1988. The general layout of the beamline and the characteristics of individual components are given. Extensive resolution measurements have been done using transitions of the inert gases. The experimentally determined resolution is compared with theory for the medium energy grating. Finally, it is shown that by masking the outer portions of the grating that the resolution can be improved significantly.

The University of Wisconsin Synchrotron Radiation Center storage ring is normally run at 800MeV with injected currents of 200mA. There are nine beamlines that are owned and maintained by the Synchrotron Radiation Center, in addition, there are eight beamlines that are owned and maintained by participating research teams. Vanderbilt University and the Synchrotron Radiation Center are co-owners of a 6-meter toroidal grating monochromator commonly referred to as a 6-meter TGM. The beamline was officially commissioned the first of March 1988. The TGM is a high flux, relatively high energy monochromator. The general layout of the beamline is shown in figure 1. The light enters from the left in the figure and is focused by the first mirror on the entrance slit. After passing through the entrance slit the light hits the grating. The light is then focused by the grating on the exit slit and then passed through a chamber containing an array of filters. The next component along the beamline is a beam chopper (not shown in figure 1). Finally, the beam is refocused by the exit mirror to a point 17.5 inches from the exit valve.

The characteristics of the first mirror are shown in table 1. The mirror is located 1800 mm from the source and has a minus 5° tilt. The entrance and exit slits are continuously adjustable between 8 μ m and 5000 μ m. In addition, the slit assemblies have a series of horizontal apertures to reduce the width of the image at the slit. The gratings are composed of a silicate substrate with ion-etched holographic rulings coated with platinum or gold. The grating characteristics are shown in table 2. There are three 6-meter toroidal gratings (low, medium and high energy) mounted on a revolving carousel. The useable energy range and the theoretical resolution for each of the three gratings is given in table 2. The gratings can be used outside the given energy range but the flux is fairly low.

The resolution of a TGM with a stationary exit slit is dependent on the wavelength since the slit coincides with the Rowland Circle at only two points during the rotation of the grating. Consequently, as the grating is rotated the light is focused on the exit slit at only two positions of the grating. So the resolution of the TGM not only depends on the slit width but also on the wavelength. The theoretical resolution for the medium energy grating is shown in figure 2. Only at the two energies corresponding to the minima of the curve is the light focused on the exit slit. The resolution can be improved at the non-optimal wavelengths by masking the outer portions of the grating. By masking the grating the amount of scattered light is reduced and hence one may observe an improvement in the resolution. Transitions of He, Xe, Ar and Ne in the gas phase have been used to experimentally determine the resolution at various energies. Shown in figure 2 are some of the experimentally determined resolution values for Ar, Ne and He at various slit widths. For Ne the resolution was improved at 300 μ m slits with masking of the grating. In figure 3 absorption versus energy is plotted for a transition of He in the gas phase at 300 μ m entrance and exit slits, 100 μ m slits and 100 μ m slits with the grating masked. There is a substantial increase in the resolution

due to masking of the grating. Figures 4 and 5 show the improved resolution as a function of slit width for a transition of Ar and Xe respectively in the gas phase.

One of the characteristics of holographic gratings is their large contribution of higher order components. While doing the resolution experiments it was found that the second order component was as much as 50% and orders as high as 8th were observed. The large contribution from higher order components explains the necessity of a filter array. In table 4 the proposed filter array is given. Presently only the LiF and Al filters are installed, however the Sn and In filters have been ordered and should be installed by December 1988. Also present in the filter chamber are a Au diode and a Ni mesh. These are used to measure the intensity as a function of energy for each of the three gratings (figure 6). The characteristics of the exit mirror are very similar to the entrance mirror characteristics given in table 1.

The experiments that have been done recently on the Vanderbilt/SRC beamline include photon stimulated desorption of D from a D₂ rich KCl crystal and the emission of secondary electrons from NaCl, LiF, KCl and KBr. The spectrum of a KCl crystal while dosing with D₂ between 2000 Å and 8000 Å is shown in figure 7. The most prominent features are the bulk fluorescence from KCl, D α , D β , OD and K*. The H layer experiments will be continued the first of December.

The Vanderbilt/SRC 6-meter TGM has met if not exceeded all previous expectations. The flux and resolution are very close to the theoretically predicted values. Vanderbilt as well as other users have been pleased with the overall performance of the monochromator.

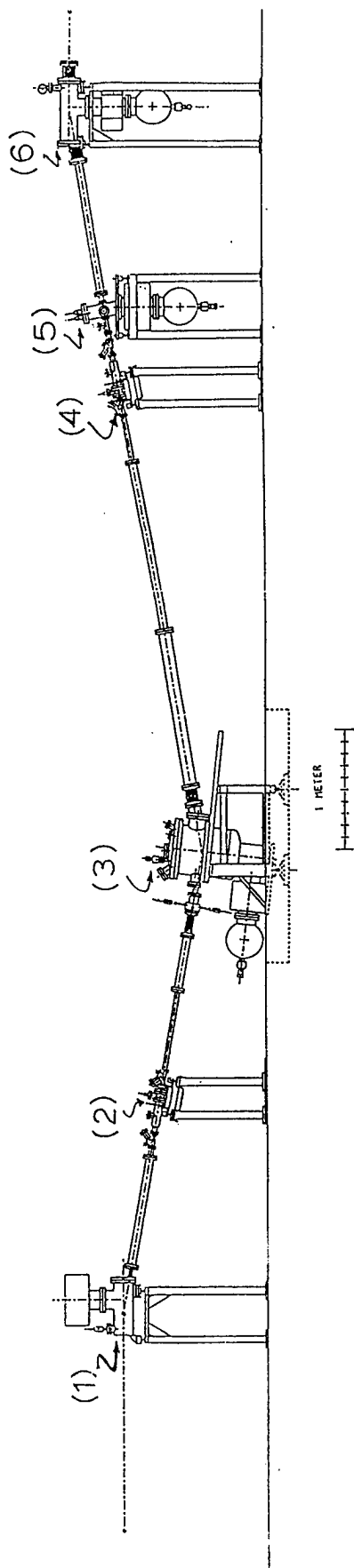


Figure 1: 6-meter toroidal grating monochromator; (1) first mirror,
 (2) entrance slit, (3) grating chamber, (4) exit slit,
 (5) filter chamber, (6) exit mirror.

Table 1: Entrance Mirror Characteristics

Figure Type	ELIPSOIDAL
Dimensions	80 mm <i>by</i> 40 mm
Magnification	1 : 1
Deflection Angle	-10.0°
Acceptance Angle	22 mrad _x 3.9 mrad _y
Coating	Gold
Surface Roughness	46 Å(rms)
Supplier	Research Optics

Table 2: Grating Characteristics

GRATINGS I

Figure Type	TOROIDAL
Dimensions	135 mm <i>by</i> 45 mm
Magnification	1 : 1.84
Deflection Angle	+20.0°
Rulings	Holographic / Ion Etched
Coating	Platinum or Gold
Supplier	Jobin-Yvon

GRATINGS II

Grating	Low Energy (LEG)	Medium Energy (MEG)	High Energy (HEG)
Groove Density	288 /mm	822 /mm	2400 /mm
Useful Range	1650 – 500 Å 7.5 – 24.8 eV	600 – 175 Å 20.6 – 70.9 eV	190 – 65 Å 65.2 – 191 eV
Optimal Resolution	.61 Å @ 1378 Å 4 meV @ 9 eV	.18 Å @ 476.9 Å 10 meV @ 26 eV	.055 Å @ 165.3 Å 25 meV @ 75 eV

OBSERVED RESOLUTION, MEG

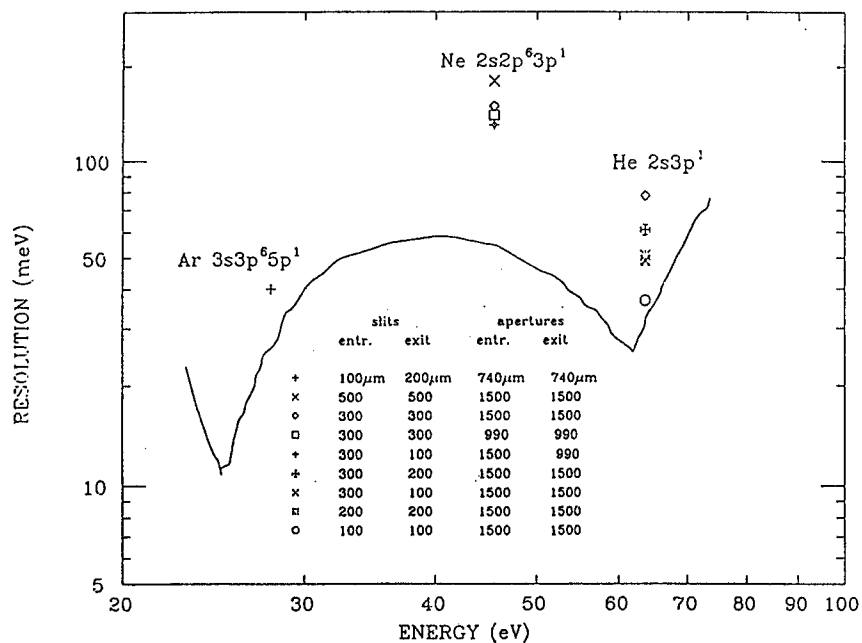


Figure 2: Theoretical¹ and Observed Resolution for Medium Energy Grating
1. P. Thiry, et al., N. I. M., 222, 85 (1984).

HELIUM RESOLUTION

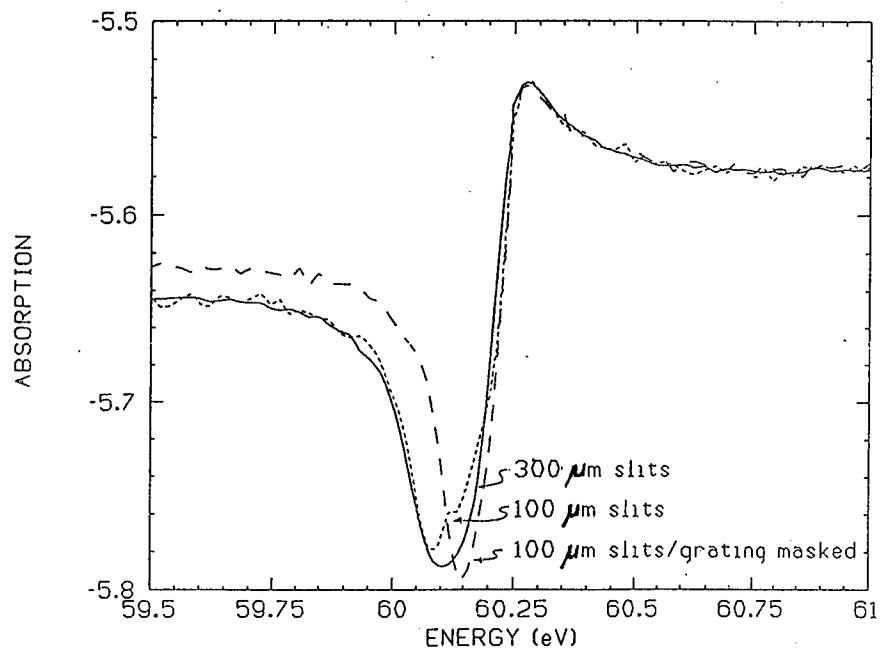


Figure 3: Helium Resolution; 300 μ m and 100 μ m entrance and exit slits

ARGON RESOLUTION

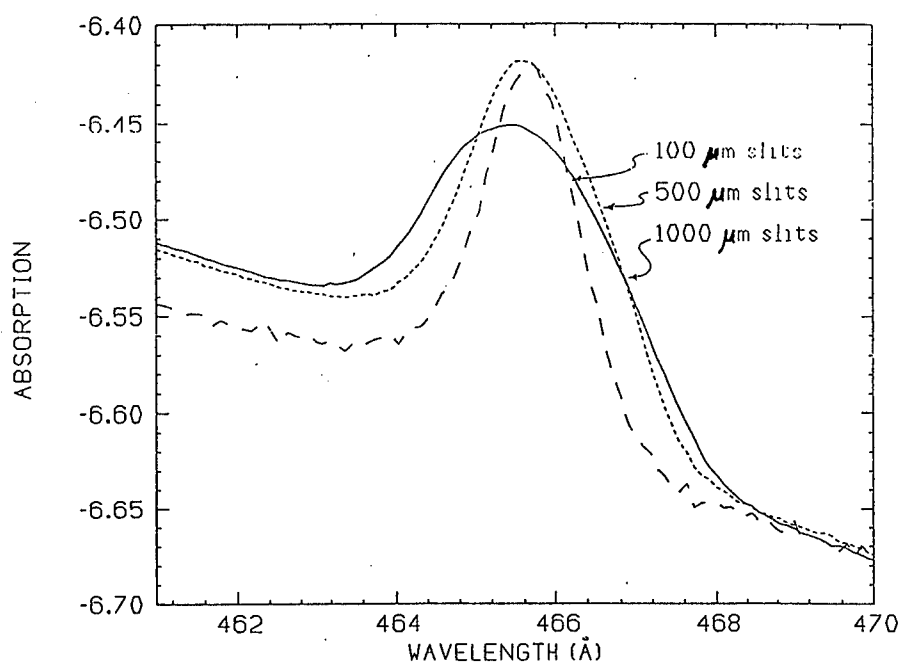


Figure 4: Argon Resolution; 1000μm to 100μm entrance and exit slits

XENON RESOLUTION

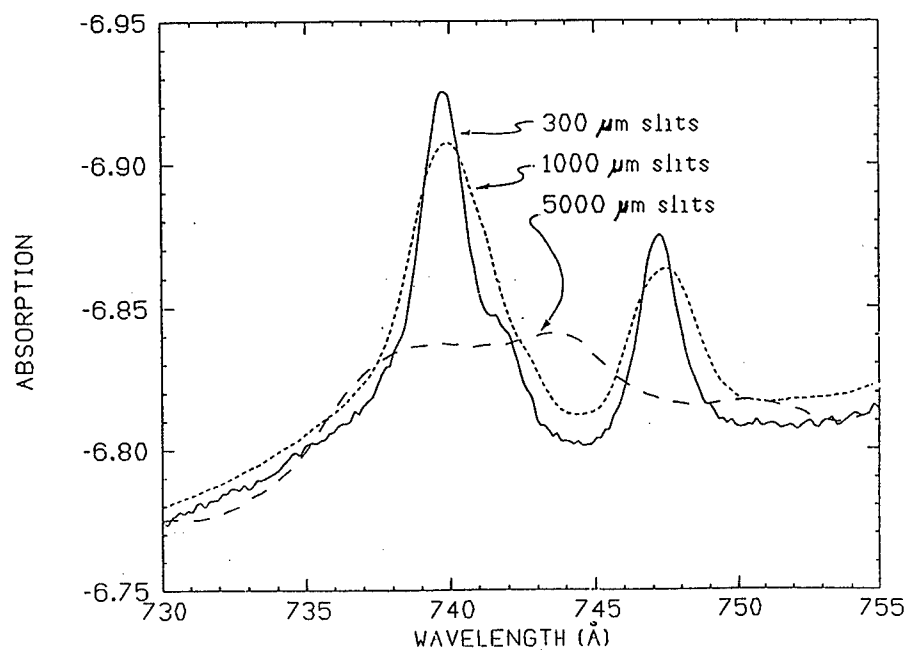


Figure 5: Xenon Resolution; 5000μm to 300μm entrance and exit slits

FILTER ARRAY

LiF	6 – 12 eV	Al	36.5 – 73 eV
In	11.8 – 16.4 eV	Be	55.7 – 111.5 eV
Sn	15.5 – 23.9 eV	C	142.1 – 284.2 eV
Mg	24.6 – 49.2 eV	OPEN	
OPEN		Gold Diode	
Supplier		SRC	

Table 3: Proposed filter array

6 m TGM

I₀ SCANS

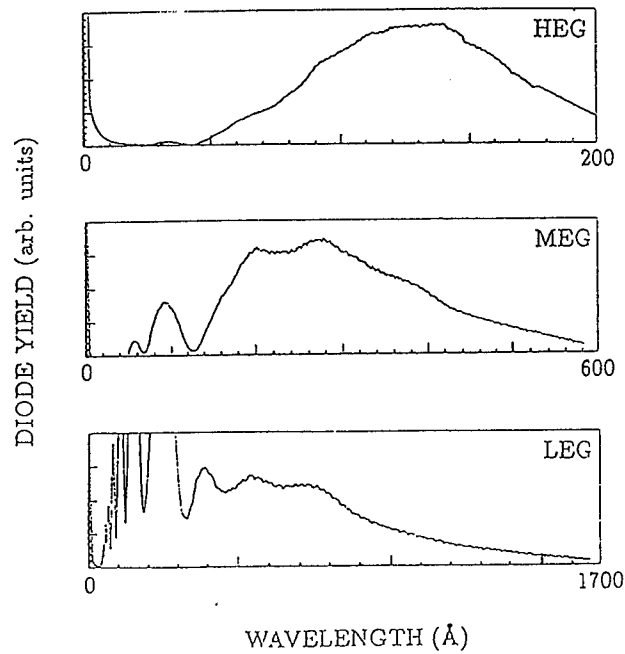


Figure 6: Intensity versus Wavelength for the three gratings

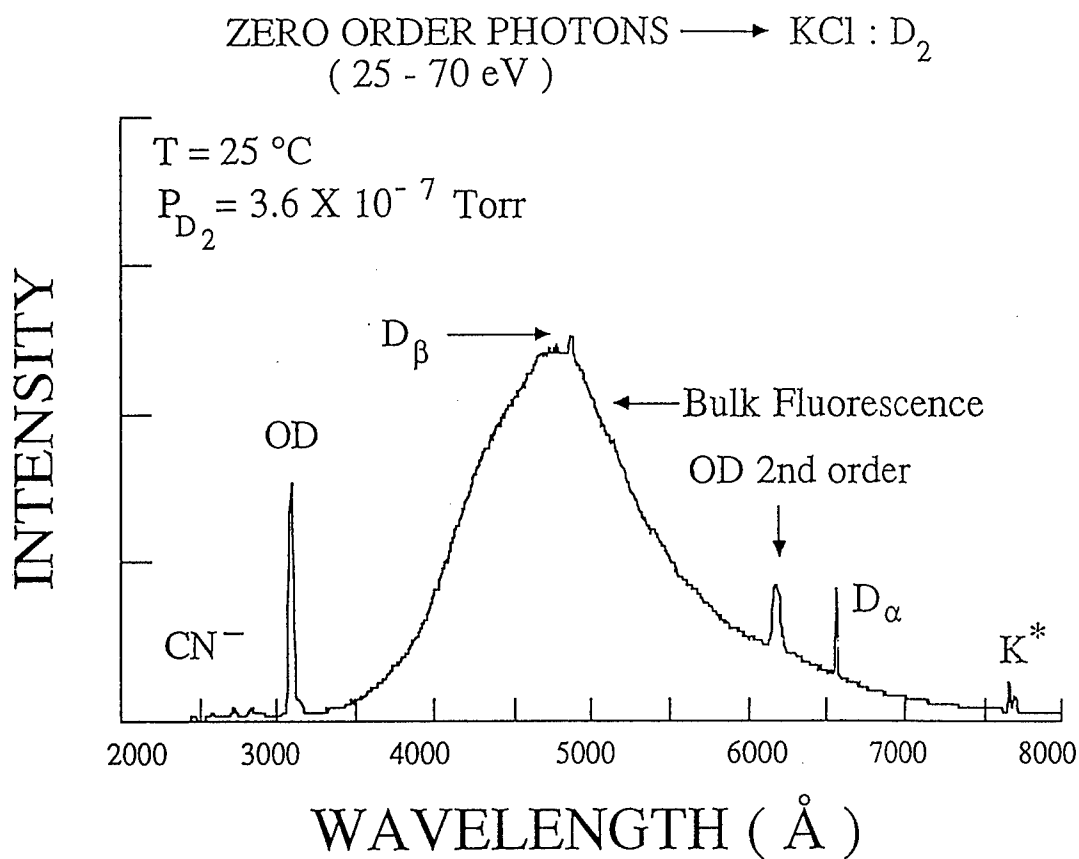


Figure 7: Intensity versus Wavelength for KCl while dosing with D₂.

HREM Observations of Electron-Stimulated Damage Processes in NiO

M. I. Buckett and L. D. Marks, Dept. of Materials Science and
Engineering, Northwestern University, Evanston, IL 60208

Beam-induced structural and chemical changes in materials which occur during observation in the electron microscope may be classified as radiation effects or more specifically, radiation damage. The various mechanisms by which these occur include ballistic (knock-on), radiolysis or electron-stimulated desorption (ionization), and thermal (beam heating) processes. These processes may be initiated either in the bulk or on the surface and are inherently specimen, beam energy, dose and/or flux dependent. Further effects of specimen preparation and surface environment are also important considerations, especially for surface-initiated processes. It has recently been shown that high resolution electron microscopy (HREM) can be a complementary technique to surface science studies.¹⁻³ In this paper, we wish to show that this is the case for the electron-stimulated damage processes in NiO.

It is now well-established from the surface science literature that electron-stimulated desorption (ESD) of oxygen occurs from maximum valence transition metal (TM) oxide systems, such as TiO_2 , WO_3 , and V_2O_5 ,⁴ as well as systems of chemisorbed oxygen on metal surfaces under low energy electron bombardment. These results have been supported by HREM investigations which report the formation of a 'metallized' surface layer during electron irradiation in a number of TM oxide systems.^{3,5} The

desorption mechanism (specifically the observance of O⁺ desorption) from maximum valence TM oxides has been successfully described by Knotek and Feibelman ⁶ (the K-F mechanism); whereas more general descriptions of the desorption mechanism from metal surfaces, covalently bonded solids, as well as several other systems have been proposed by a number of authors, the most notable being attributed to Menzel and Gomer ⁷ and Redhead ⁸ (the MGR mechanism) and Antoniewicz. ⁹

ESD in NiO remains a controversial subject in that conflicting observations of O⁺ desorption ^{10,11} and the lack of O⁺ desorption ^{6,12} have both been reported. It should be noted that NiO is not a maximum valence TM oxide and therefore is not a classic K-F material. Previous HREM investigations of NiO have contributed a number of interesting observations but, unlike the results obtained for TiO₂, ^{13,14} V₂O₅, and WO₃, ¹⁴ have not shown conclusive evidence revealing the nature of ESD processes in this material. Smith, et al., reported the recrystallization of a (100) NiO surface and the formation of holes. ¹⁵ Luzzi, et al., observed the formation of Ni islands, and measured a beam energy threshold of 115±5 keV for ballistic damage in NiO. ¹⁶ Observations of Ni islands have also been reported by Ostyn and Carter for ion-milled NiO for a beam energy of 125 kV ¹⁷ and by Liu and Cowley for beam energies of 100 and 200 keV ¹⁸. Liu and Cowley further reported on the apparent melting of NiO under an intense beam.

In this study, beam-induced structural and chemical changes occurring in-situ in the electron microscope were observed and classified under various operating conditions and sample preparations. Our results indicate that ESD is not a predominant damage mechanism in NiO. Clean NiO is fairly

stable in the electron beam and suffers primarily from ballistic damage as shown in Figure 1. Electron-stimulated reaction (ESR) processes, however, do occur in this material and are observed under conditions where the surface is heavily defective and/or covered with adsorbed gases, e.g. - as a result of sample preparation, or if the surface is contaminated with a reactive carbon layer. Under these circumstances, two prevalent reactions are observed as described below.

In specimens free of carbon contamination, an electron-stimulated oxidation reaction occurs at the NiO surface which results in the formation of a Ni_3O_4 spinel phase as shown in Figure 2. In specimens where reactive carbon contamination is present, a vigorous reduction reaction occurs at the NiO surface which varies in extent from the formation of Ni islands (Figure 3) to more extensive bulk structural changes such as recrystallization, spontaneous disintegration, or apparent melting. The reactions occur more vigorously at lower incident electron energies, as can be seen in Figure 5.

It has been confirmed that the radiation damage mechanisms are primarily surface-initiated by encapsulating the surface with an unreactive graphitic layer. In this encapsulated condition, the ESR processes were completely quenched and the ballistic processes were greatly retarded. The effect of encapsulation on beam damage is illustrated in Figure 6. This sample surface was only partially encapsulated, resulting in a significant difference in the rate at which the exposed versus unexposed surfaces degraded.

The dependence of radiation damage on electron beam energy, flux, and crystal orientation has also been investigated. Results are summarized in

Table I. The energy dependence was determined simply by varying the operating voltage of the microscope. Two flux conditions, low and high, were utilized. In the low flux condition, the incident electron flux was on the order of 10^2 A/cm². In the high flux condition, the flux was on the order of 50 times higher. Three specific crystal orientations were investigated: the (001), (110), and (111) zones. 'Clean' samples indicate freshly prepared surfaces with essentially contamination free initial surfaces. 'Dirty' samples indicate the presence of a carbon layer on the initial surface. These samples were usually left in air for 1 day to 2 weeks prior to insertion into the microscope.

Conclusion

The behavior of NiO surfaces during electron irradiation has been shown to be quite varied and complex. It involves both electronic and ballistic processes which depend on the condition of the surface and the surface environment, as well as electron beam energy, flux, and crystal orientation. It has also been shown that high resolution electron microscopy - with which definite structural observations of surfaces can be obtained - can serve to complement other surface science techniques where direct structural information can only be inferred.

References

- 1 L.D. Marks, Phys. Rev. Letters 51 (1983) 1000.
- 2 L.D. Marks and D.J. Smith, Surface Sci. 143 (1984) 495.
- 3 D.J. Smith and L.A. Bursill, Ultramicroscopy 17 (1985) 387.
- 4 See articles in Desorption Induced by Electronic Transition DIET I
ed: N.H. Tolk, M.M. Traum, J.C. Tully, and T.E. Madey, Springer-Verlag
Berlin (1983).
- 5 D.J. Smith, et al., Ultramicroscopy 23 (1987) 299.
- 6 M.L. Knotek and P.J. Feibelman, Phys. Rev. Letters 40.14 (1978) 964.
- 7 D. Menzel and R. Gomer, Journ. Chem. Physics 41.11 (1964) 3311.
- 8 P.A. Redhead, Canadian Journ. Physics 42 (1964) 886.
- 9 P.R. Antoniewicz, Phys. Rev. B, 21.9 (1980) 3811.
- 10 H.H. Madden, J. Vacuum Sci. Technol. 13 (1976) 228.
- 11 H.C. Gerritsen, et al., Surface Sci. 139 (1984) 16.
- 12 H. Niehus and W. Losch, Surface Sci. 111 (1981) 344.
- 13 J.W. Strane, M.S. Thesis, Northwestern University (July 1988).
- 14 D.J. Smith, M.R. McCartney, and L.A. Bursill, Ultramicroscopy 23
(1987) 299.
- 15 D.J. Smith, et al., Surface Sci. 175 (1986) 673.
- 16 D.E. Luzzi, et al., Mat. Res. Soc. Symp. Proc. vol.100 (1988) 635.
- 17 K.M. Ostyn and C.B. Carter, Electron Microscopy 1982, vol. 2. p. 191.
- 18 J. Liu and J.M. Cowley, Proc. of EMSA (1987) 176.

Table I
Summary of Electron Irradiation Damage in NiO

Incident Electron Energy = 300 kV

<u>Sample Orientation</u>	<u>Clean</u>		<u>Dirty</u>	
	<u>High Flux</u>	<u>Low Flux</u>	<u>High Flux</u>	<u>Low Flux</u>
(100)	Ballistic erosion of surface, scarce traces of Ni_3O_4 (Figure 1a)	Ballistic erosion of surface, competing Ni_3O_4 formation (Figure 2a)	Spontaneous disintegration	Spontaneous reaction to form Ni islands, Recrystallization, Spontaneous disintegration
(110)	Ballistic erosion of surface, scarce traces of Ni_3O_4 (Figure 1b,c)	Ballistic erosion of surface, competing Ni_3O_4 formation (Figure 2b)	Spontaneous disintegration	Spontaneous reaction to form Ni islands (Figure 3a,b), Recrystallization, Spontaneous disintegration
(111)	—	Ballistic erosion of surface, competing Ni_3O_4 surface phase formation	—	—

Incident Electron Energy = 100 kV

<u>Sample Orientation</u>	<u>Clean</u>		<u>Dirty</u>	
	<u>High Flux</u>	<u>Low Flux</u>	<u>High Flux</u>	<u>Low Flux</u>
(100)	—	—	Recrystallization, Disintegration	—
(110)	—	Formation of Ni_3O_4 surface phase (Figure 4)	—	—
(111)	—	—	Spontaneous Disintegration (Figure 5)	—

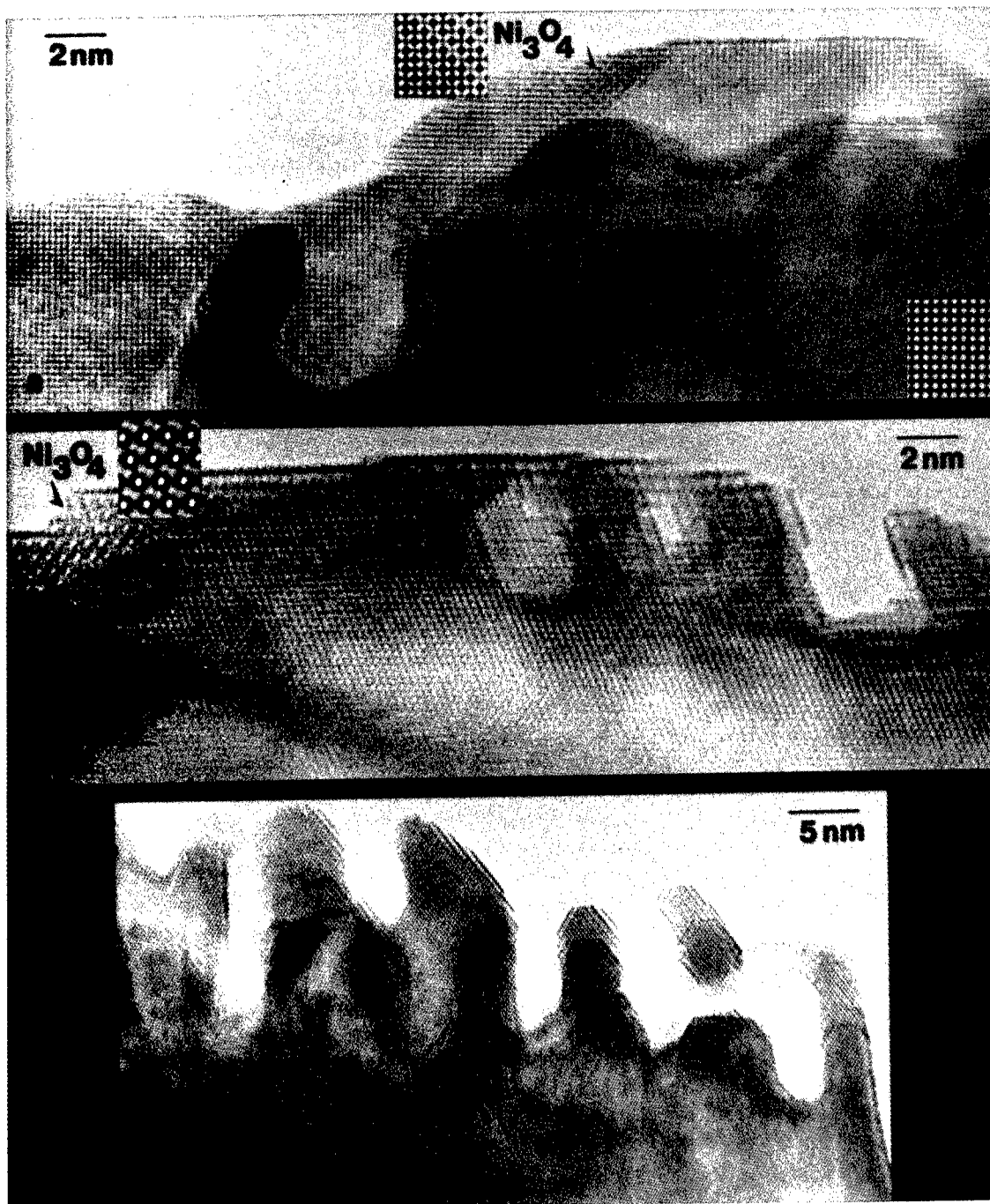


Figure 1. a) NiO(100) after 1 hr. of high flux irradiation at 300 kV. Ballistic damage in the form of surface erosion was evident by the slow etching and grooving of the initially smooth surface.
 b) NiO(110) after 1 hr. of high flux irradiation at 300 kV. As in a), ballistic damage is prevalent along with trace isolated areas of the Ni_3O_4 spinel phase. Computer simulation is inset.
 c) Same sample as in b), after 2.5 hr. of high flux irradiation at 300 kV.

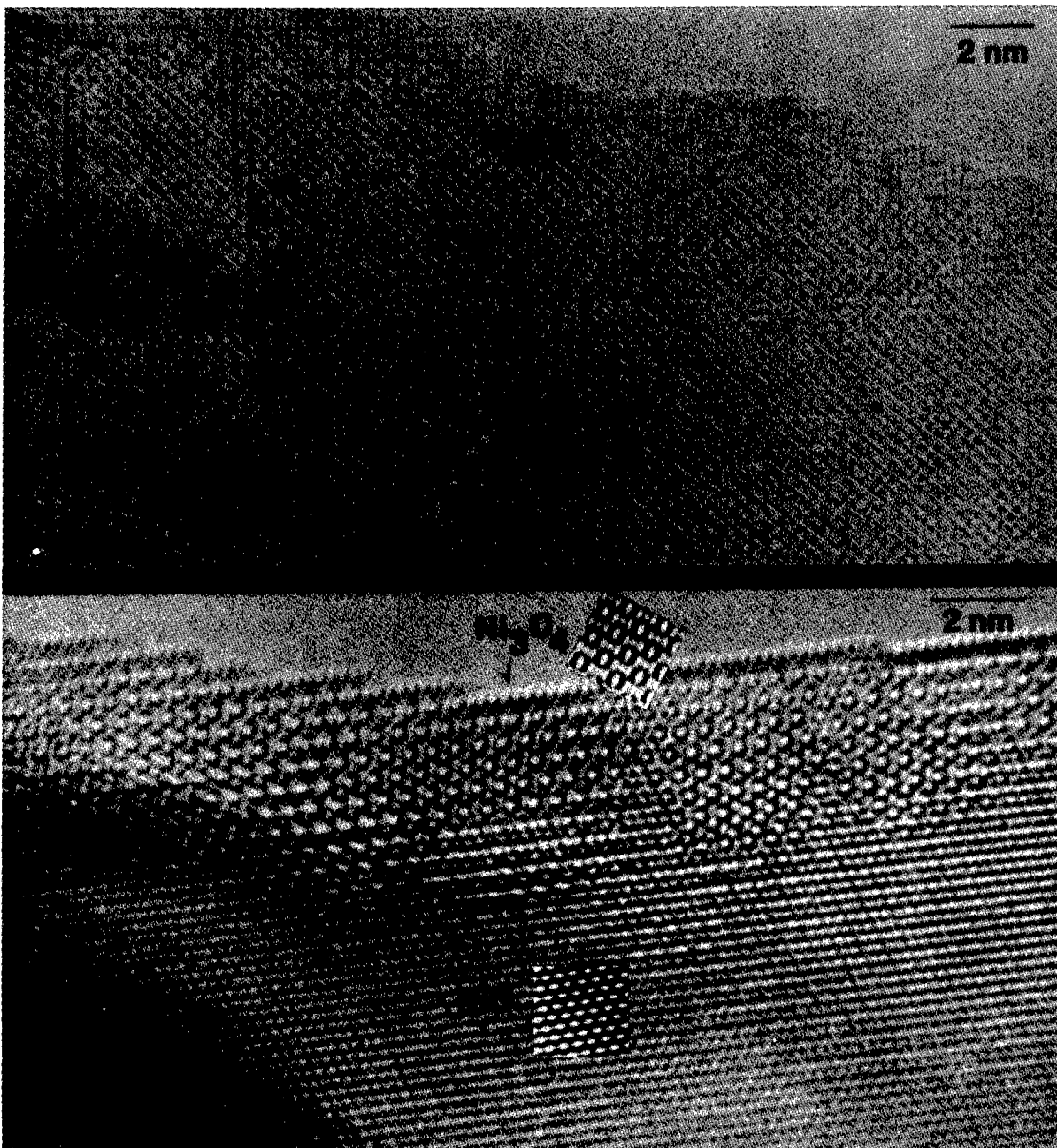


Figure 2. Surface-initiated Ni_3O_4 spinel phase formation in NiO after short time (<0.5 hr.) at 300 kV. Computer simulations are inset. a) NiO(100). b) NiO(110).

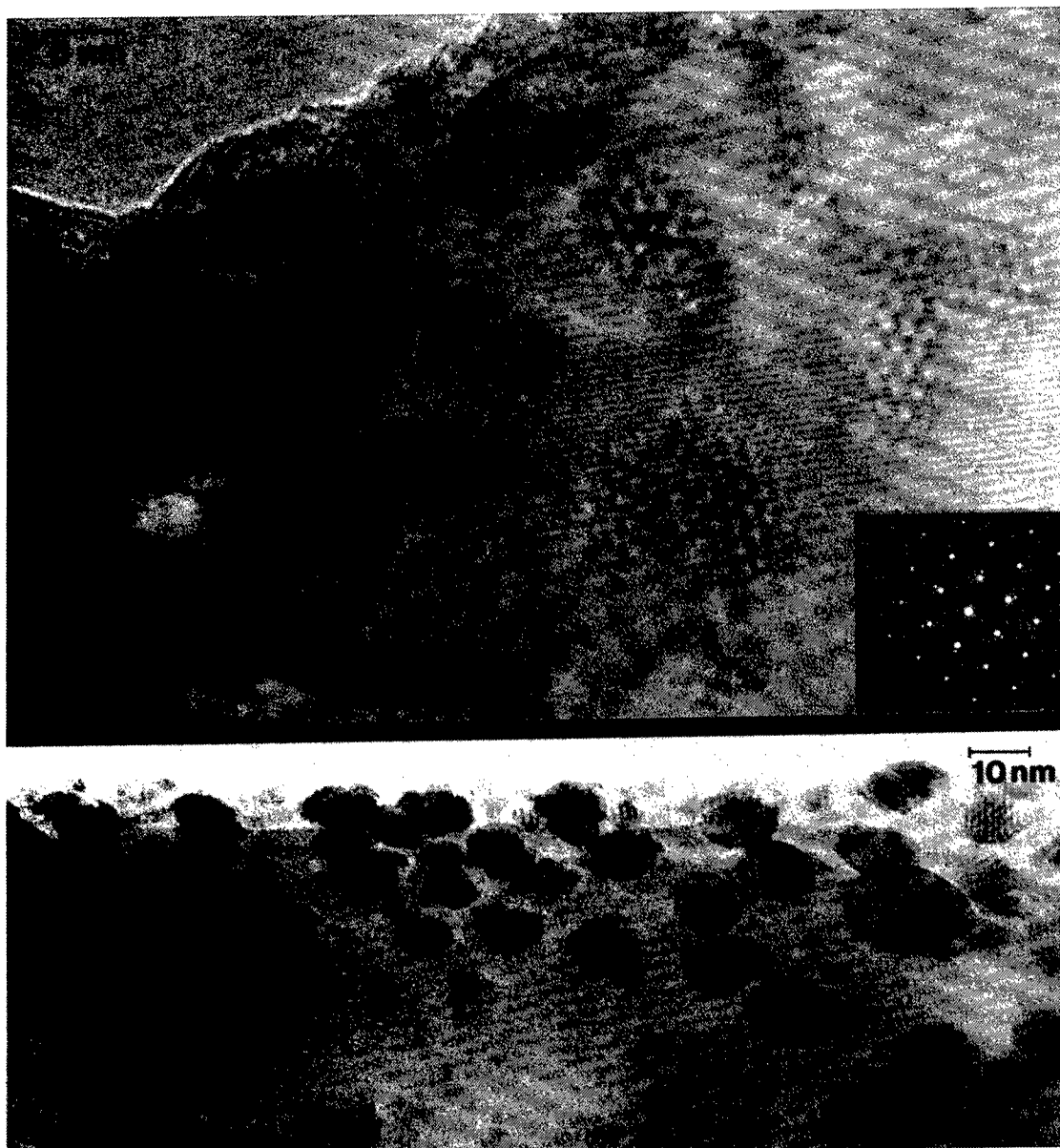


Figure 3. a) and b). 'Dirty' NiO(110) samples which, at the onset of irradiation at 300 kV, had undergone spontaneous reaction to form Ni islands on all exposed surfaces.

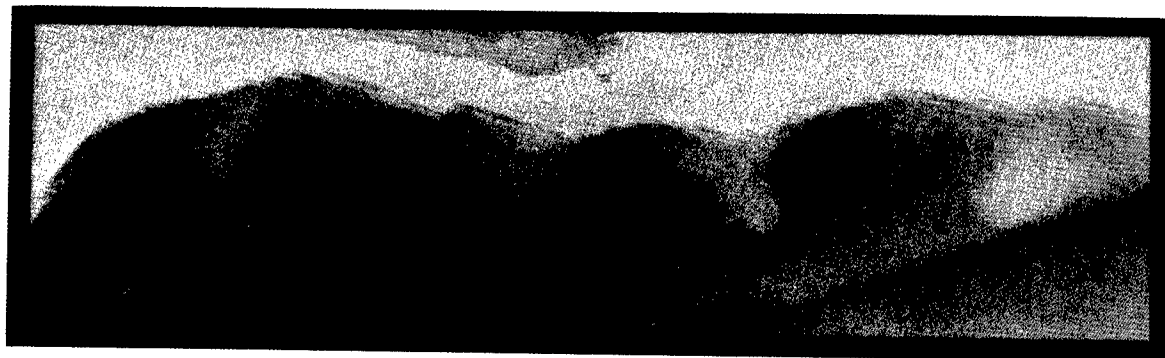


Figure 4. NiO(110) irradiated for a short time at 100 kV. The characteristic surface fringes correspond to Ni₃O₄ formation.

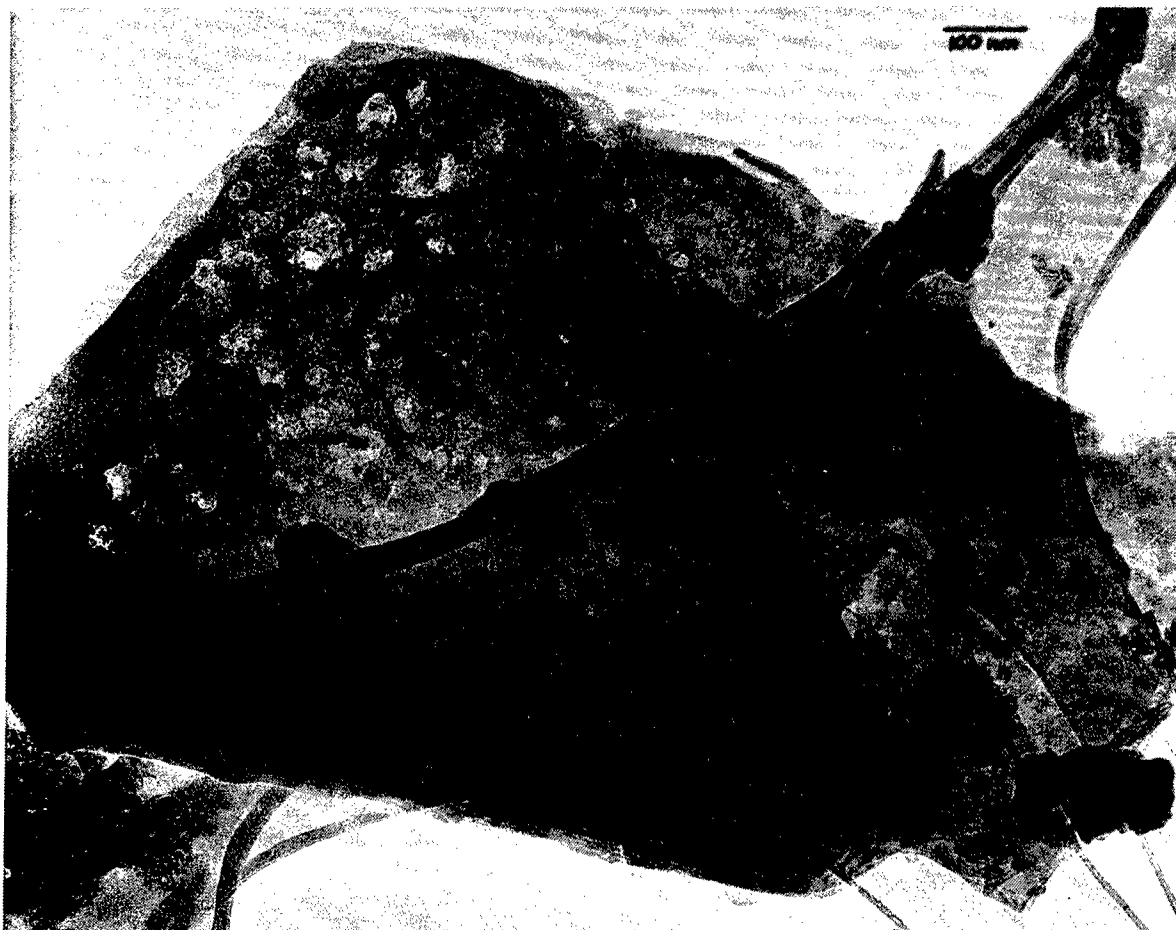


Figure 5. NiO(111) particle which, at the onset of irradiation at 100 kV, had undergone spontaneous disintegration.

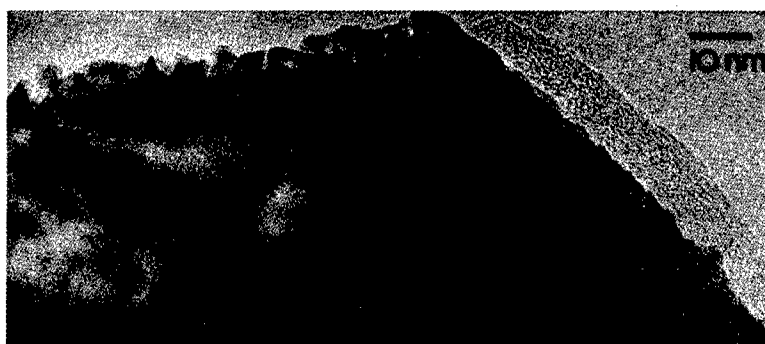


Figure 6. A partially encapsulated NiO(110) surface. Encapsulated regions undergo no apparent beam damage, whereas exposed regions are being eroded away.

LASER-INDUCED DESORPTION AND ELECTRON EMISSION

Paul G. Strupp
Peter C. Stair
Eric Weitz

Department of Chemistry
Northwestern University
Evanston, Illinois 60208

Introduction

The subject of this paper is an experimental investigation of the laser-induced emission of electrons and ions from a clean Cu(100) single crystal surface in ultrahigh vacuum. Electron emission produced by a three photon excitation process is observed for wavelengths in the range 575 nm to 640 nm at absorbed laser intensities from 10 to 50 Mw/cm². At laser intensities of approximately 75 Mw/cm² the electron emission flux increases dramatically. Since the threshold for this giant electron emission was observed to depend upon sample temperature, the process is clearly thermally assisted. Emission of copper ions from the surface is also observed with a laser intensity threshold at approximately the same value as measured for the thermally assisted electron emission. The ion kinetic energy distribution is clearly nonthermal suggesting that the mechanism for ion emission is not simply sublimation of copper due to laser-induced heating.

Experimental

The copper surface in ultrahigh vacuum ($P \sim 5 \times 10^{-11}$ torr) was prepared in a clean state by a combination of argon ion bombardment and annealing. The surface composition and structure were characterized by Auger electron spectroscopy and low-energy electron diffraction, respectively. Radiation from an excimer pumped, tunable dye laser was directed on the surface at an angle of 45° from the surface normal. The pulse energy was measured and

recorded for each laser shot using a photodiode. Time resolved charged particle emission, either electrons or ions, was measured for each laser shot by feeding the output of a 75 mm diameter microchannel plate array charged particle multiplier into a charge sensitive preamplifier and thence into a transient recorder/microcomputer (see Fig. 1). The detector subtends a cone angle of 60° above the sample. Both the copper sample and a set of grids in front of the microchannel plate array could be electrically biased in order to collect particles whose trajectories would otherwise fall outside the active area of the detector. The biasing was also used to discriminate ions from electrons as well as emission due to the sample from stray emission sources elsewhere in the vacuum chamber.

Results

Three Photon Photoemission

Fig. 2 presents a log-log plot of the measured electron emission signals as a function of the absorbed laser power density produced by irradiation at 590 nm with the sample at 300 K. Each point in the figure represents a single laser shot. The data falls on a straight line with a least-squares slope of 2.8, consistent with a three photon excitation mechanism.

The three photon excitation mechanism was confirmed by retarding potential measurements of the electron kinetic energy distribution. The experiments were performed by recording the electron emission intensity with the retarding grids shown in Fig. 1 at a series of negative voltages. The measured signals, shown in Fig. 3, are due to electrons with kinetic energies in excess of the applied potential between the copper sample and the retarding grids. The high energy threshold for the data in Fig. 3, at 2.2 eV kinetic

energy, is indicative of emission originating at the Fermi level. The total energy of these electrons above the Fermi level, ~ 6.6 eV, (equal to the sum of their kinetic energy and the Cu(100) work function, 4.4 eV) is consistent with expectations for a three photon process.

Examination of the copper bulk band structure [1] suggests a likely transition for the three photon excitation process. The λ_1 to λ_1 transition at the L point in the bulk Brillouin Zone is dipole allowed and of the proper energy to explain the measured kinetic energies. An angle resolved emission experiment is required to identify the states involved in the three photon process.

Thermally Assisted Electron Emission

At higher absorbed laser powers the electron emission flux begins to roll over as a function of increasing laser power density. This is interpreted as arising from space charge effects due to large electron densities just above the surface. At still higher laser power densities the electron emission flux increases dramatically, approximately 100-fold. Fig. 4 shows two sets of data which differ in the sample temperature. For the sample at 300 K the emission flux "jumps" from approximately 1000 electrons per laser shot to 50,000 to 100,000 electrons per laser shot. The "jump" in emission flux depends upon sample temperature as shown by comparing the data obtained at 160 K and 300 K. The electron fluxes at laser power densities from 75 to 100 Mw/cm² are much lower at the lower temperature indicating that the excitation process has a thermal component. On the other hand, calculations using the Richardson Equation [2] indicate that surface temperatures in excess of 1700 K would be required to produce the observed electron fluxes by purely thermionic emission

(see Fig. 5). Temperatures in this range are substantially in excess of the melting point of copper, but no evidence for sample melting was observed. Thus we hypothesize that the giant electron emission fluxes are due to thermally assisted photoemission as described by Lin and George [3].

Copper Ion Emission

Copper ion emission from the surface was detected at absorbed laser power densities above 50 Mw/cm^2 (see Fig. 6). The emission flux vs. absorbed laser power density follows a linear log-log relationship with a slope of ~ 9.5 . In the early literature on laser-induced electron emission from surfaces a slope above 2-3 was interpreted as evidence for thermal emission [4]. However, the ion kinetic energy distribution, measured by the retarding field method, peaks at $\sim 0.75 \text{ eV}$. This is much too large to be explained by purely thermal excitation via laser-induced heating. Furthermore, sample temperature did not effect the yield of ions. At the present time we have no mechanism which explains the ion emission.

References

1. J.F. Janak, A.R. Williams, and V.L. Moruzzi, Phys. Rev. B11 (1975) 1522.
2. C. Herring and M.H. Nichols, Rev. Mod. Phys. 21 (1949) 185.
3. J.-T. Lin and T.F. George, J. Appl. Phys. 54 (1983) 382.
4. E.M. Logothetis and P.L. Hartman, Phys. Rev. 187 (1969) 460.

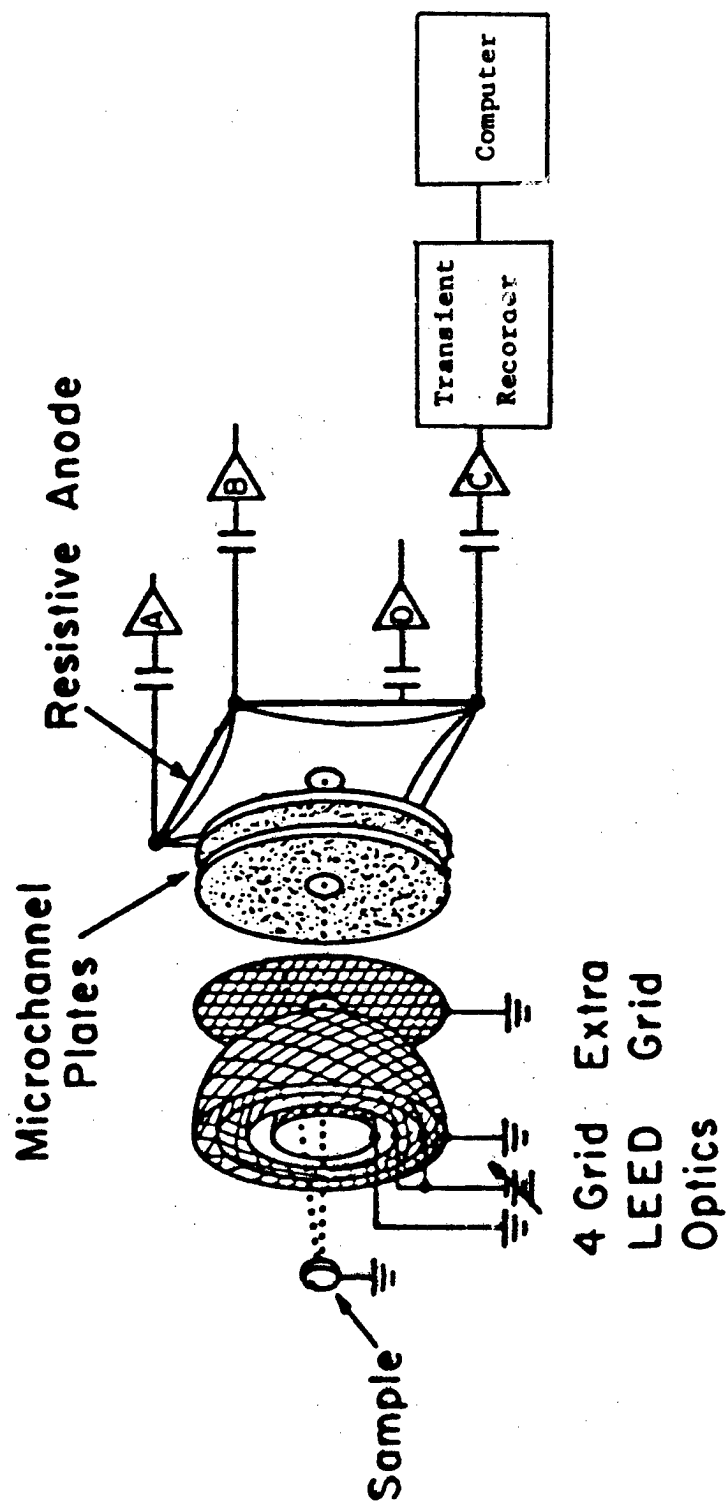


Fig. 1

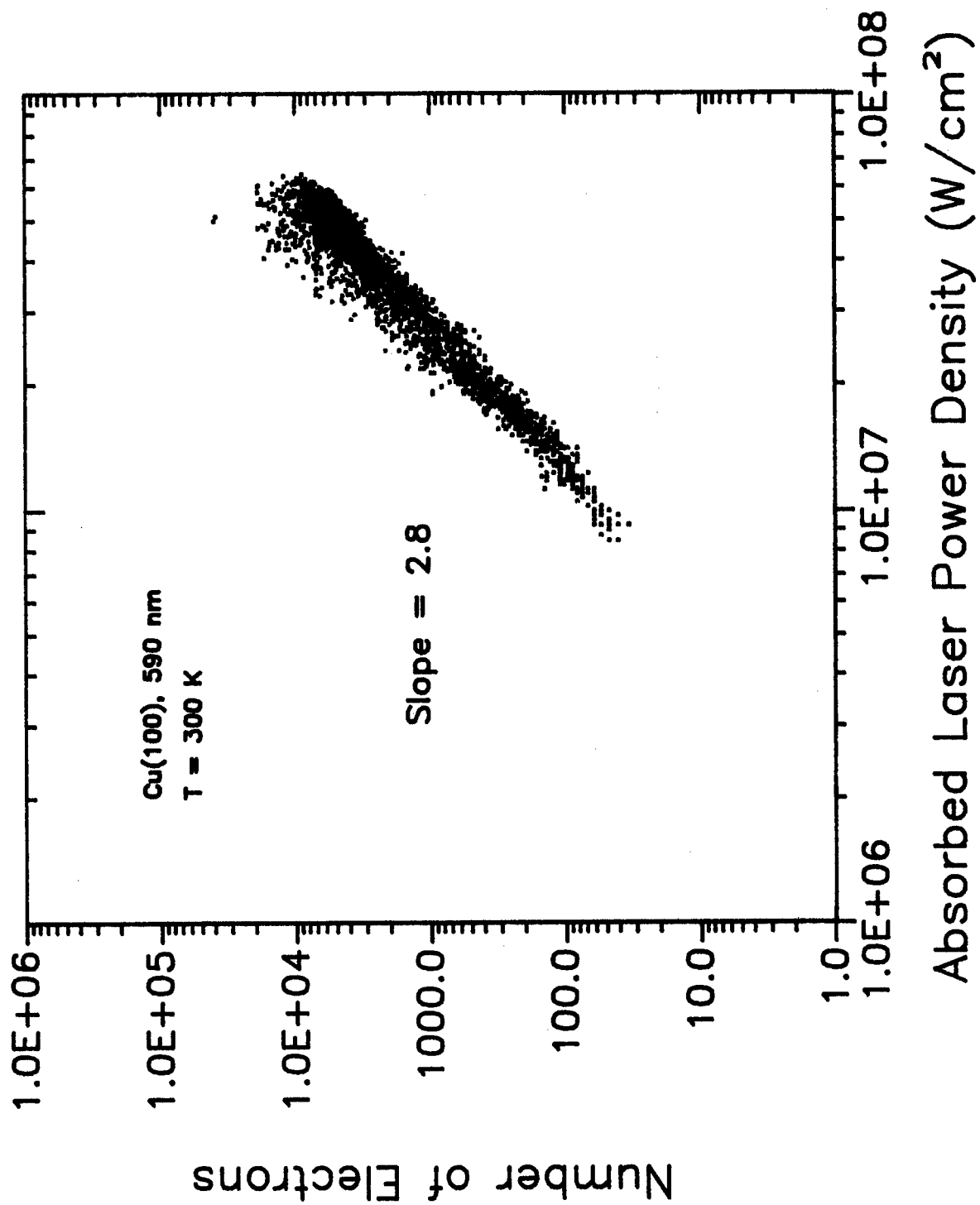


Fig. 2

KINETIC ENERGY DISTRIBUTION

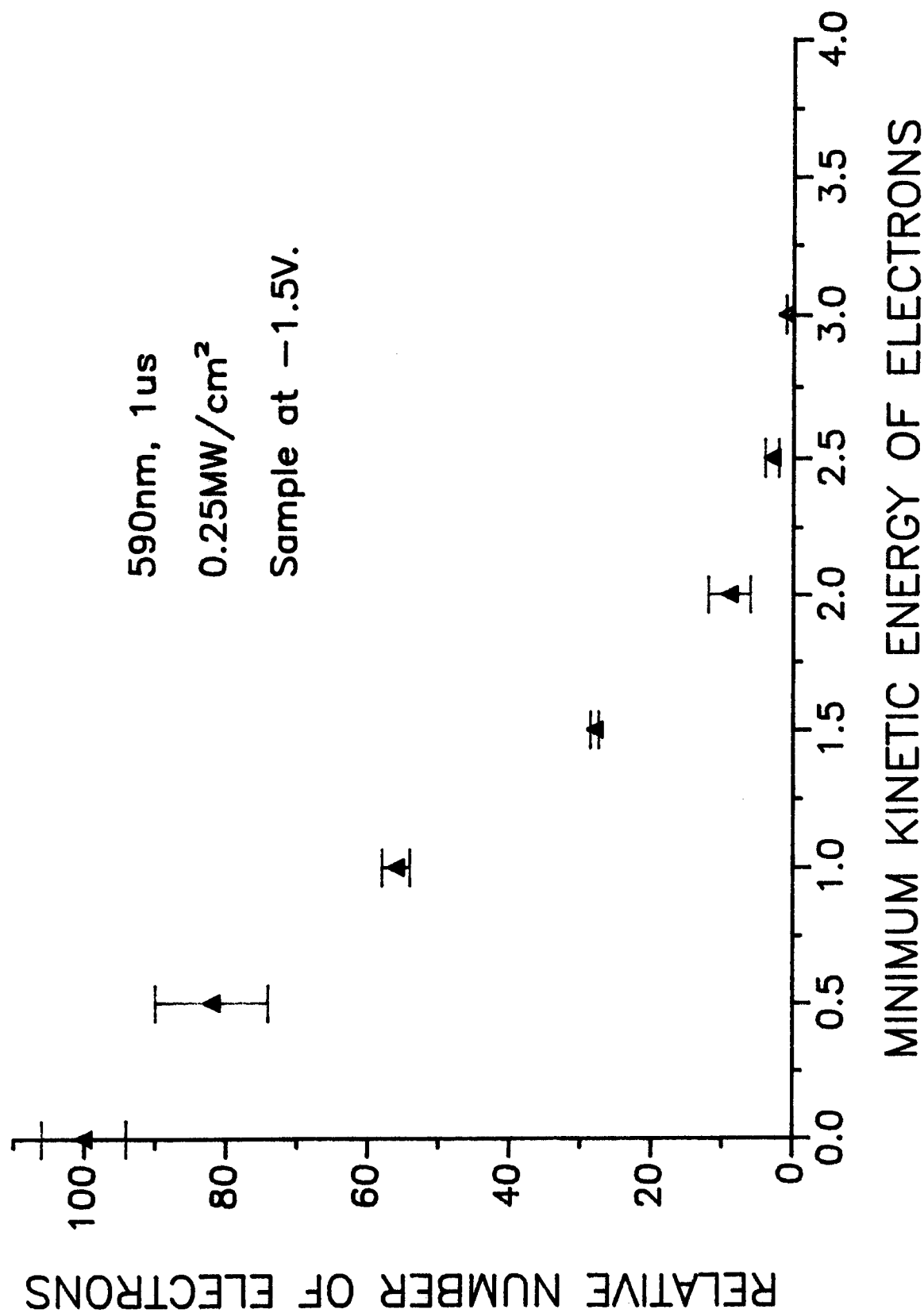


Fig. 3

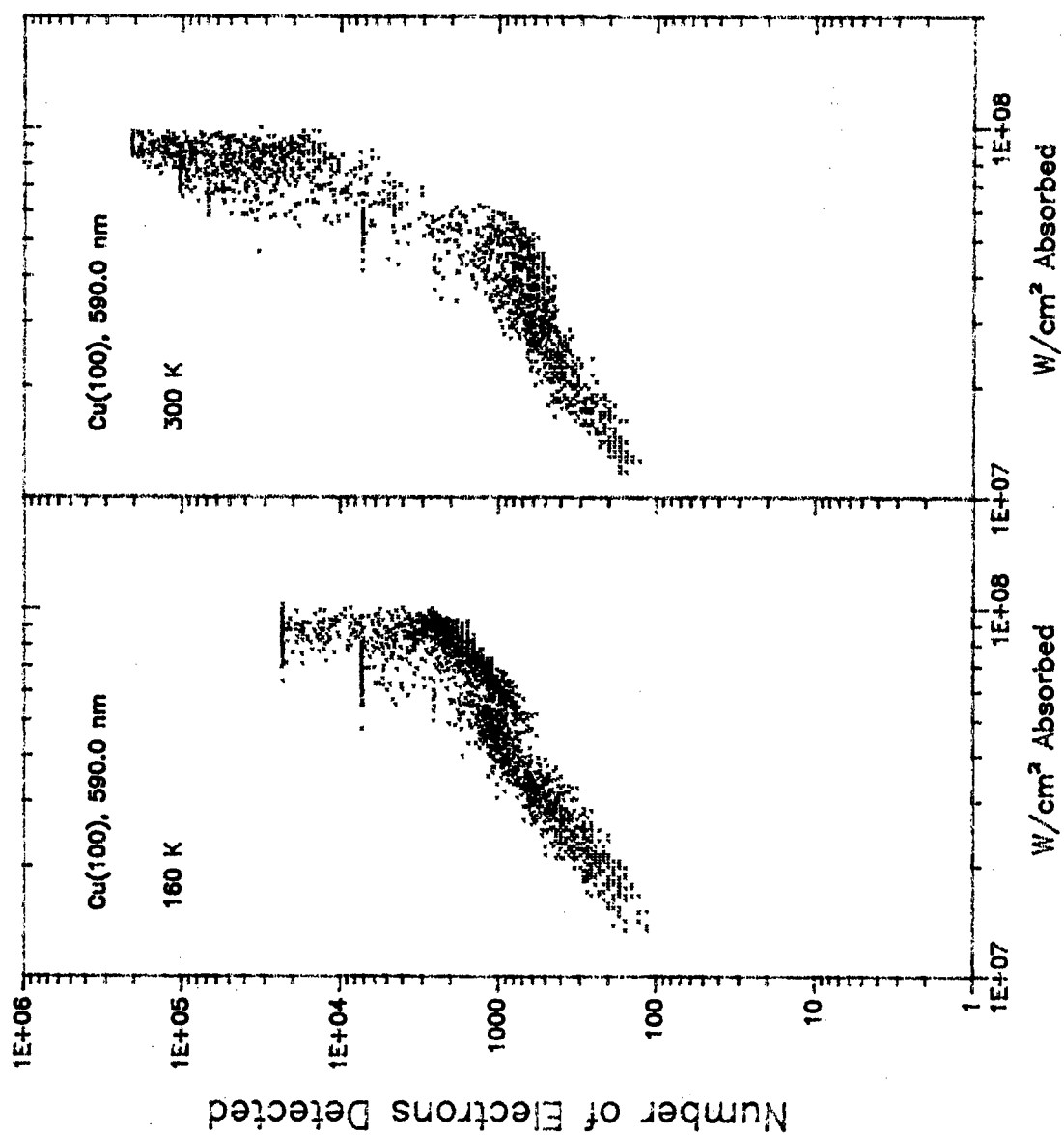


Fig. 4

Calculation of the Laser-Induced Thermionic Electron Emission Flux From Copper

Richardson Equation:

$$j = A T^2 \exp(-e\phi/kT)$$

A is a universal constant equal to 120 amps/cm²-T²

$e\phi/k = 1.1604 \times 10^4 \phi$ where ϕ is in volts

For a laser irradiated area of 0.0023 cm² and a pulse duration of 10⁻⁸ sec. the number of electrons emitted per laser shot is given by:

$$N = A (6.25 \times 10^{18} \text{ elec/coul}) (0.0023 \text{ cm}^2) (10^{-8} \text{ sec}) T^2 \exp(1.1604 \times 10^4 \phi/T)$$

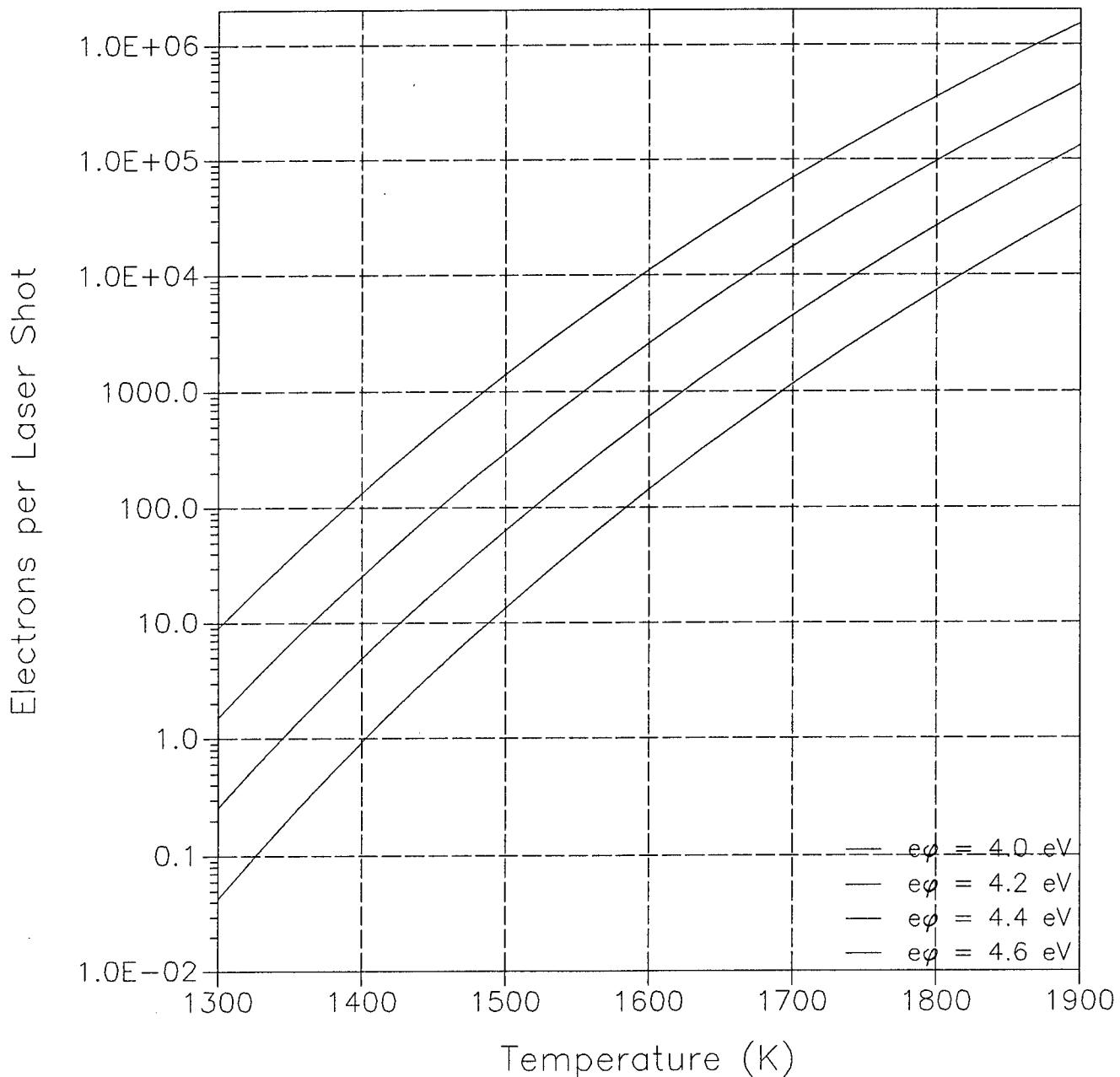


Fig. 5

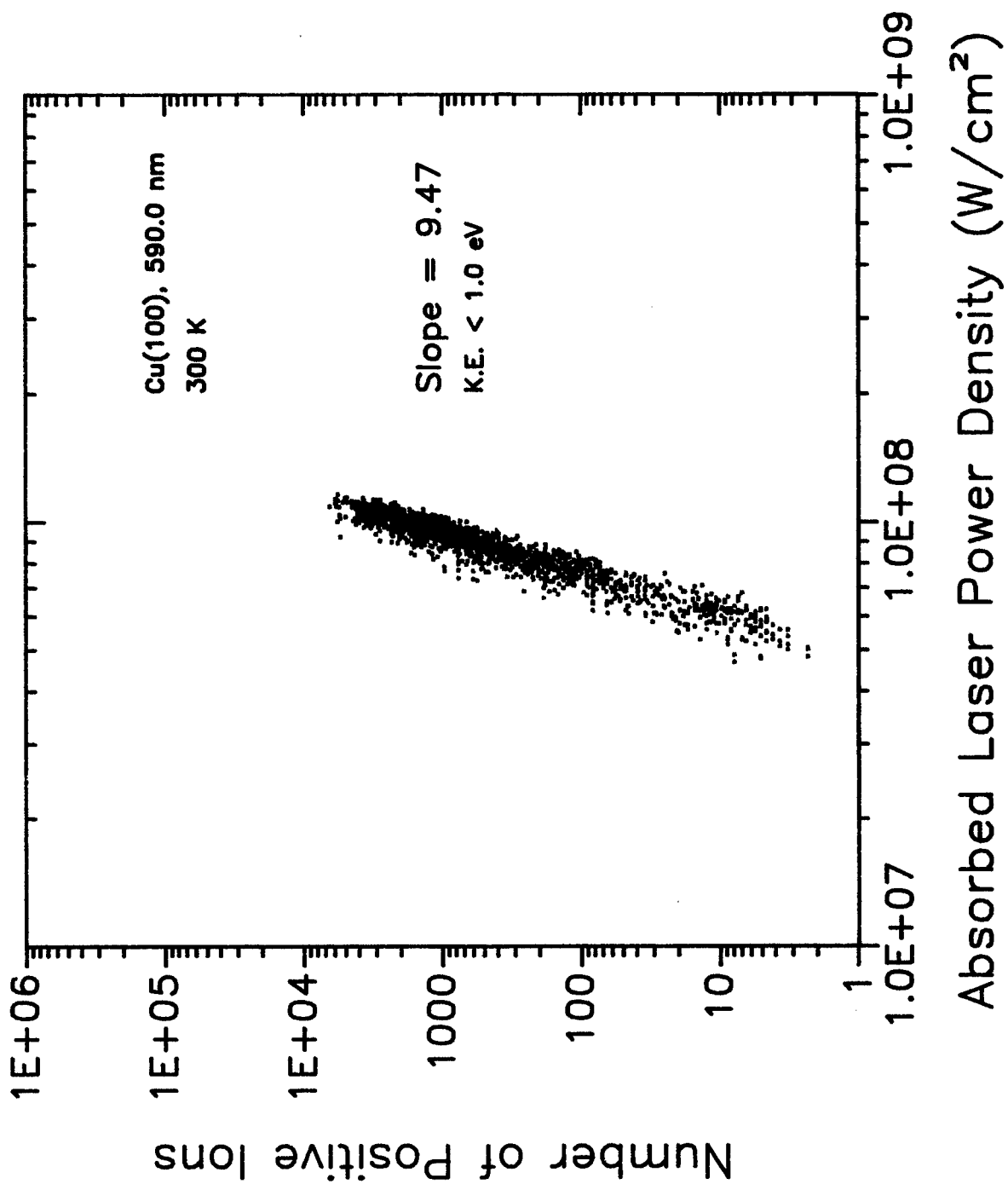


Fig. 6

A Quantitative Test of the Kinetic Model of Secondary Ion Emission

Robert A. Weller

Department of Materials Science and Engineering

and

Center for Atomic and Molecular Physics at Surfaces

Vanderbilt University

Nashville, Tennessee 37235

Abstract

The kinetic model of secondary ion emission has been used as the basis for an extensive set of calculations of the yield of secondary Al^+ ions as a function of primary ion energy. These computations have been compared with the recently published results of measurements of the intensity of Al^+ and Al^{2+} secondary ions produced by 15-275 keV Ar^+ ion bombardment. The theory as presently formulated does not adequately reproduce the variation of secondary ion intensity with primary ion energy, suggesting that the collision sequence leading to the ejection of an excited Al atom has not been properly identified. In particular, the data are inconsistent with the assumption that the crucial excitation occurs in the later stages of a well developed collision cascade.

1. Introduction

The complexity of secondary ion emission has thus far prevented the development of a general quantitative theory of ion yields even for emission from simple elemental targets. The essence of the problem is that ionization of an atom is a quantum phenomenon requiring a fully quantum mechanical description, while atomic motion in a solid is usually adequately described by classical mechanics. Thus, sputtering theories based upon classical transport theory and sputtering models based upon classical molecular dynamical calculations cannot be readily generalized to explain the sputtering of ions. Since the fully quantum mechanical description of a collision cascade is not (and may never be) a practical alternative, it is reasonable to construct a theory in which the internal states of atoms are treated quantum mechanically, their center-of-mass motions are treated classically, and a mechanism is provided for the two motions to be coupled. The kinetic model of secondary ion emission is such a theory.

The kinetic model was devised by Joyes [1-3] in order to explain data of Hennequin [4,5] and has been further refined by Veksler [6-8]. Its distinguishing feature is that it uses the concept of electron promotion developed by Fano and Lichten [9] as the mechanism which couples center-of-mass motion into internal excitation. Collisions in the solid are assumed to be binary and in other respects identical to collisions of isolated atoms. In the collisions, some fraction of colliding atoms are excited and these excited atoms continue to participate in the collision cascade until they are sputtered. Those which have not previously reverted to the ground state then relax to the ground state by Auger electron emission and, in so doing, become ions.

The kinetic model is supported by several experimental observations. In one of the most striking, Brochard and Slodzian [10] showed that the yield of Al^{2+} ions increases quadratically with increasing Al concentration in a Cu-Al alloy. The implication of this observation is that the excitation which precedes the creation of sputtered ions involves collisions of Al atoms with other Al atoms. It is well known that in the electron promotion model such symmetric collisions are

most effective in producing excitation. Thus, this experiment is regarded as evidence that electron promotion is the mechanism for Al excitation. A supporting observation was made by comparing the results of bombardment of a pure Al and an Al_2O_3 target [11].

The purpose of this paper is to report the results of a calculation of the variation of the yield of secondary Al ions with primary beam energy and to compare these results with recent measurements. The calculation has been made using the formalism of Veksler [8]. For the case of Al bombardment, this formulation contains only two parameters that may be reasonably regarded as adjustable and one of these is a trivial overall normalization. Thus, an arguably decisive test of the assumptions that underlie the model can be made. The following section contains the details of the calculation.

2. Calculation

In the kinetic model, the energy distribution of sputtered ions after refraction by the (planar) surface binding potential is assumed to be given by the following expression:

$$n_i^*(z, E_0) = \left[\frac{z}{z+z_b} \right] \int_{z_t}^1 dz' n(z') w(z') \int_{z+z_b}^{z'} dz'' g(z', z'') w_s(z'', z+z_b) \exp(-t_m''/\tau) \quad (1)$$

Here E_0 is the incident beam energy, z is the secondary ion energy, E , in units of E_0 ($z = E/E_0$), and $n_i^*(z, E_0)$ is the energy spectrum of sputtered ions. The function $n(z')$ is the energy spectrum of atoms moving in the solid, $g(z', z'')$ is the probability that a collision between an atom with energy z' and an atom at rest will give the latter an energy z'' , $w(z')$ is the probability that in a collision between an atom with energy z' and one at rest the latter will be excited, and $w_s(z'', z)$ is the probability that the excited atom will slow down to the energy z . The dimensionless surface binding energy is obtained as, $z_b = E_b/E_0$. The time t_m'' is the mean time for slowing from energy z'' to energy $z+z_b$ and τ is the lifetime of the excitation. The dimensionless parameter z_t which appears in the limit of the outer integral is $z_t = E_t/E_0$, where E_t is the minimum energy for which an

excitation of an atom in collision is possible. The value of E_t for aluminum has been quoted on page 161 of ref. 12 to be 888 eV. This value was used in all calculations. A value of 3.39 eV was used as the surface binding energy, E_b , for Al.

Veksler assumes that $n(z)$ consists of two parts, one associated with the moving incident ions and one associated with the moving target atoms. Thus, he writes:

$$n(z) = n_s(z) + n_d(z) = 2K_s z + 2z_b S/z^2 \quad (2)$$

Here the first term, $n_s(z)$, represents the spectrum of scattered incident projectiles and the second, $n_d(z)$, the familiar Thompson spectrum of moving target atoms [13]. S is the sputtering yield and K_s is a parameter. Since the experimental evidence cited above suggests strongly that only symmetric collisions between target atoms are responsible for excitation, and since numerical tests indicated that the results are relatively insensitive to the value of K_s , the parameter K_s has been taken to be zero in all calculations presented here.

The function $g(z', z'')$ is assumed to be that which is appropriate to hard sphere collisions. Thus, $g(z', z'') = 1/z'$. The function $w_s(z'', z)$ is found after a brief argument [8] to be $w_s(z'', z) = 2G(z)/z''$, where $G(z)$ is defined below. Finally, t_m'' is taken so that

$$t_m''/\tau = \epsilon^{1/2} [(E+E_b)^{-1/2} - (E'')^{-1/2}], \quad (3)$$

where ϵ is effectively a parameter of the theory. Physically, ϵ is proportional to the energy of an excited Al atom which moves one mean free path in the solid in one mean lifetime of the excitation; ϵ has units of energy. Finally, the excitation probability $w(z)$ is given by $w(z) = w_0[1 - (z_t/z)^2]$. The parameter w_0 , which Veksler takes to be about 0.1, effects only the overall normalization of the result and is the only other adjustable parameter in the theory.

With these assumptions and a few pages of algebra it is possible to demonstrate that the expression (1) can be evaluated explicitly. The result is:

$$n_i^*(z, E_0) = 4 \left[\frac{zz_b}{z+z_b} \right] w_0 SG(z+z_b) e^{-\kappa} \{ \eta_t [Ei(\kappa) - Ei(\kappa_t)] + H(\kappa, \chi, \kappa_t) - H(\chi, \chi, \kappa_t) \} \quad (0 \leq z \leq z_t - z_b)$$

or

$$n_i^*(z, E_0) = 4 \left[\frac{zz_b}{z+z_b} \right] w_0 SG(z+z_b) e^{-\kappa} \{ H(\kappa, \chi, \kappa_t) - H(\chi, \chi, \kappa_t) \} \quad (z_t - z_b \leq z \leq 1 - z_b)$$

Where:

$$H(\kappa, \chi, \kappa_t) = a[\kappa^{-2}(\kappa+1)e^\kappa - 2\kappa_t^{-4}R_1(\kappa)] + \chi^{-4}[R_3(\kappa) - (2\kappa_t^4)^{-1}R_7(\kappa)] + (b-a)Ei(\kappa)$$

$$R_m(\kappa) = (-1)^m m! e^\kappa \sum_{n=0}^m \frac{(-1)^n \kappa^n}{n!} \quad G(z) = (1-z^2) \left[\frac{1}{2} (1-z^2) - (\beta-1)z^2 \ln(z) - \beta z^2 (1-z) \right]^{-1}$$

$$a = \beta \chi^2 / 2 \quad \eta_t = [(1 + z_t)^2 / 2 z_t^2 + \beta](1 - z_t)^2 \quad b = \beta(1 + z_t^2) - 1 + z_t^2 / 2$$

$$\beta = 2K_s / z_b S \quad \kappa = \chi(z+z_b)^{-1/2} \quad \kappa_t = \chi z_t^{-1/2} \quad \chi = (\epsilon/E_0)^{1/2} \quad (4)$$

In this set of equations $Ei(\kappa)$ is the exponential integral given by equation 5.1.2 of Abramowitz and Stegun [14]. Its numerical value has been computed according to the procedures given by Cody and Thacher [15,16]. Note that the definition of $R_m(\kappa)$ differs slightly from the one given by Veksler [8]. The two are, in fact, numerically equal since, for this problem, only odd values of m are present in the solution [17].

The results of the calculation are presented in figs. 1-3. Fig. 1 shows the predicted energy distribution, n_i^* , of secondary ions for $E_0=100$ keV and ϵ values of 0.04 keV, 0.4 keV and 4.0 keV. In general, smaller values of ϵ result as the assumed lifetime τ of the 2p excitation of the Al atom is increased. Intuitively, one expects a longer lifetime to lead to more low energy sputtered ions and this is confirmed by the calculation. Note also that the distributions are quite broad. This is a general feature of the kinetic model which has been regarded as one of its strengths [18].

The measured quantity which is the object of our comparison is not, however, the energy distribution of the secondary ions but, rather, the variation of the secondary ion yield within a narrow energy band as the primary ion energy is varied. The results of ref. 19 were obtained by measuring the yield of secondary ions in a band about 3 eV wide centered at about 5 eV. In order to match these experimental conditions the average value of n_i^* within this energy band was computed for values of E_0 in the range 2-300 keV. The results of this computation are shown in fig. 2 for the same three values of the parameter ϵ . Finally, fig. 3 presents a superposition of the measured [19] and calculated yields of Al^+ and the sputtering yield S calculated by the formula of Matsunami et al. [20].

3. Discussion

It is clear from fig. 3 that the calculated Al^+ ion yield does not agree well with the measurement. Similar disagreement is found when a comparison is made with the yield of Al^{2+} ions which, in this case, have the same variation with E_0 as do Al^+ ions [21]. An examination of equation 4 reveals that the principal dependence of $n_i^*(z, E_0)$ on E_0 is through the sputtering yield S . Indeed, as may be seen in fig. 3, to a reasonable approximation, the calculated ion yield is simply proportional to the sputtering yield. Since this dependence appears in the definition of $n_d(z)$, the most reasonable hypothesis for the failure of the model is that the assumption of excitation in the later stages of a collision cascade is incorrect. A similar conclusion has been reached by Hennequin et al. [18]. They propose that the excitation which leads to the emission of an excited neutral atom occurs as a result of the collision of a primary recoiling atom with a surface atom. Another interesting observation has been made by Blaise and Nourtier [22]. Arguing that the lifetime of the 2p excitation is too short for slowing down of an excited atom (about 10^{-14} s for Al), they conclude that kinetic emission is essentially a surface effect and not a collision cascade phenomenon.

In summary, a prediction of the variation of the intensity of 5 eV secondary ions as a function of incident projectile energy, based upon the kinetic model of secondary ion emission as formulated by Veksler, does not agree with experiment. Joyes's fundamental hypothesis of excitation by electron promotion and subsequent Auger decay of a sputtered neutral is supported by numerous experiments and is not presently being questioned. However, the assumptions which have been made to produce a numerical result appear to be inadequate. In subsequent calculations the function $n_d(z)$ of equation (2) should be replaced by a form derived from a consideration of the first few atomic collisions in the solid and the function $g(z',z'')$ should be derived from an interatomic potential which is more realistic than the hard-sphere potential. Furthermore, accepting the reasoning of Blaise and Nourtier, the function $w_s(z'',z)$ should probably be taken to be the Dirac delta function $\delta(z''-z)$.

Acknowledgment

The author would like to thank P.G. Blauner for providing the experimental data for fig. 3 in a convenient form and M.R. Weller for suggesting that an apparent inconsistency in ref. 7 could be resolved by the redefinition of β [17].

References

1. P. Joyes, J. Physique **29** (1968) 774.
2. P. Joyes, J. Physique **30** (1969) 243.
3. P. Joyes, J. Physique **30** (1969) 365.
4. J.F. Hennequin, J. Physique **29** (1968) 655.
5. J.F. Hennequin, J. Physique **29** (1968) 1053.
6. V.I. Veksler, Fiz. Tverd. Tela. (Leningrad) **24** (1982) 1751.
7. V.I. Veksler, Sov. Phys. Solid State **24** (1982) 997.
8. V.I. Veksler, Vacuum **33** (1983) 159.
9. U. Fano and W. Lichten, Phys. Rev. Let. **14** (1965) 627.
10. D. Brochard and G. Slodzian, J. Physique **32** (1971) 185.
11. P. Joyes, Rad. Effects **19** (1973) 235.
12. V.I. Veksler, Rad. Effects **51** (1980) 129.
13. M.W. Thompson, Phil. Mag. **18** (1968) 377.
14. M. Abramowitz and I. Stegun, ed., Handbook of Mathematical Functions, Dover Publications, 1965, p. 228.
15. W.J. Cody and H.C. Thacher, Jr., Math. Comp. **22** (1968) 641.
16. W.J. Cody and H.C. Thacher, Jr., Math. Comp. **23** (1969) 289.
17. The reader is also cautioned that equation 6 of ref. 8 is only true when $g(z',z'')$ is independent of z'' and that in refs. 6 and 7 the parameter β is incorrectly defined as $2h_1K_s/z\lambda S$. The correct value is $h_1K_s/z\lambda S$. This error is corrected in ref. 8.
18. J.F. Hennequin, R.L. Inglebert and P. Viaris de Lesegno, in SIMS V, ed. A. Benninghoven et al., Springer Series in Chemical Physics **44** (1986) 60.
19. P.G. Blauner and R.A. Weller, Phys. Rev. B **35** (1987) 1492.
20. N. Matsunami et al., At. Data Nucl. Data Tables **31** (1984) 1.
21. The kinetic model is usually only applied to doubly charged ion emission since singly charged ion yields are so sensitive to the presence of surface oxygen. See ref. [19] and references therein for a discussion of this.
22. G. Blaise and A. Nourtier, Surface Science **90** (1979) 495.

Figure Captions

Figure 1. The calculated energy distribution n_i^* of sputtered Al^+ ions for $E_0 = 100 \text{ keV}$ and three values of the parameter ϵ , $\epsilon = 0.04 \text{ keV}$ (upper curve), 0.4 keV (middle curve), and 4.0 keV (lower curve).

Figure 2. The calculated intensity of ion emission at 5 eV , $n_i^*(5 \text{ eV}/E_0, E_0)$, as a function of E_0 for three values of ϵ , $\epsilon = 0.04 \text{ keV}$ (upper curve), 0.4 keV (middle curve), 4.0 keV (lower curve).

Figure 3. The calculated ($\epsilon = 0.04 \text{ keV}$) and measured intensities of Al^+ ions at 5 eV as a function of Ar^+ bombarding energy E_0 . A fifth-order polynomial fit to the data is shown as a guide to the eye. Also shown is the calculated total sputtering yield S which for readability has been scaled by a constant [20]. The data are from ref. 19.

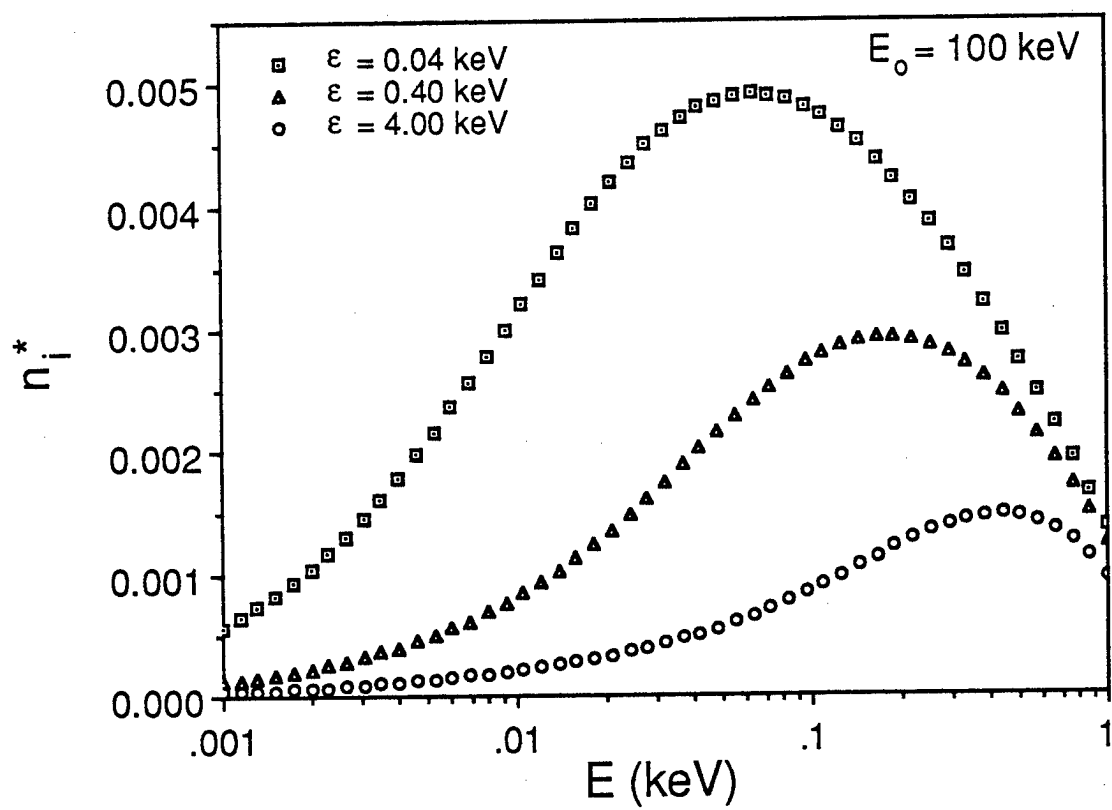


Figure 1

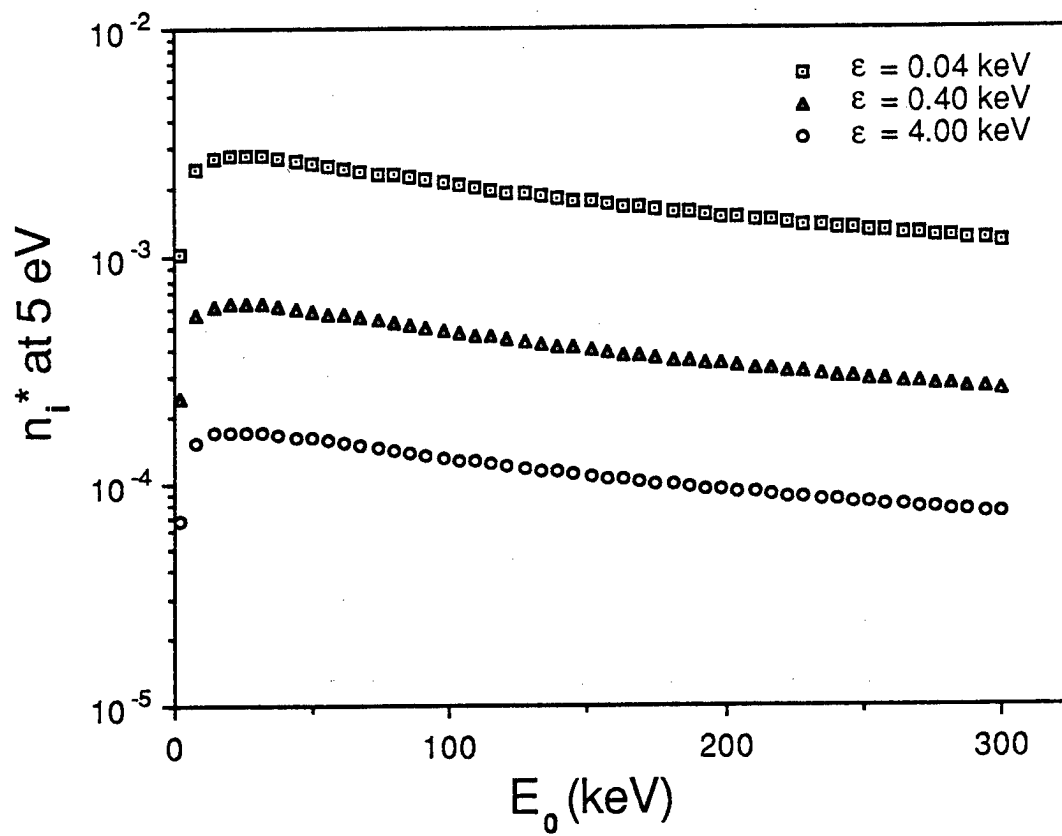


Figure 2

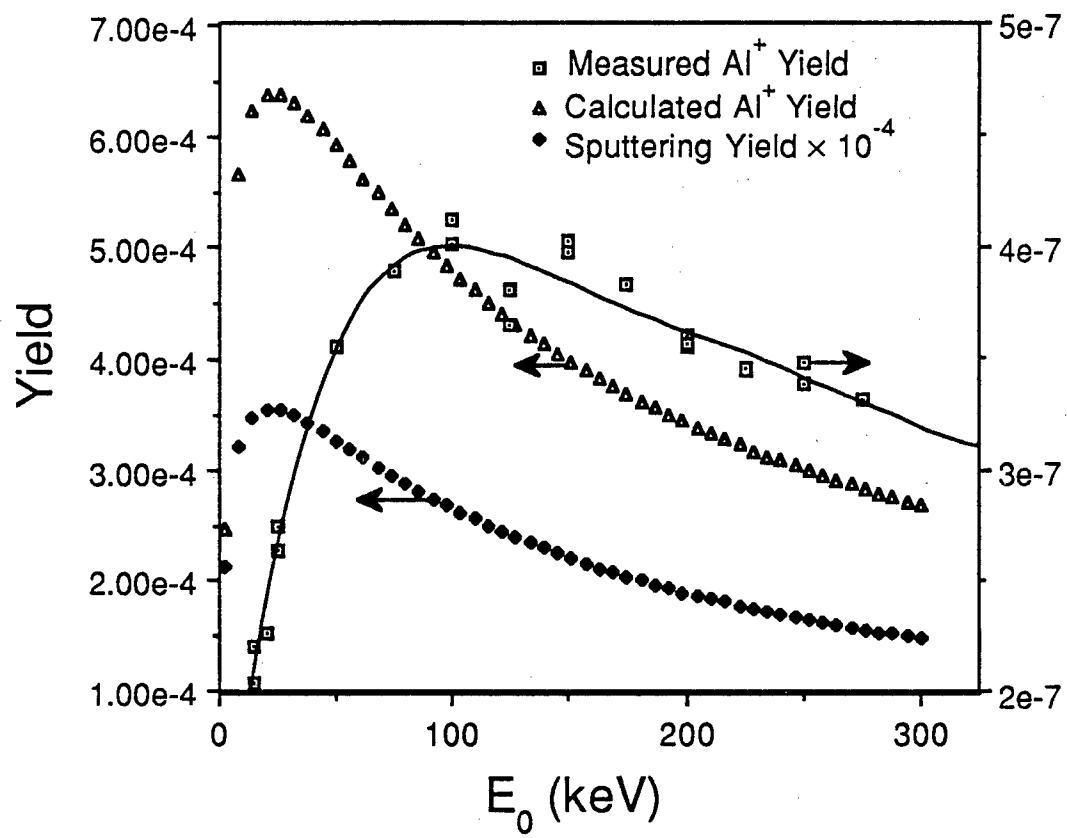


Figure 3

THRESHOLD LEVEL PHOTOABLATION OF METALS: EJECTED ION KINETIC ENERGY DISTRIBUTIONS*

H. Helvajian and R. Welle
Laser Chemistry and Spectroscopy Department
Aerophysics Laboratory
Aerospace Corporation
P. O. Box 92957
Los Angeles, California 90009-2957

ABSTRACT

We have measured, at laser fluence threshold, the ion product kinetic energy (KE) distributions from the single shot UV laser (351 nm and 248 nm) ablation of crystalline metal targets (silver, and aluminum). Under UHV conditions, we use calibrated time-of-flight mass spectrometry to measure the product ion distributions and their KE as a function of laser fluence. At ion production threshold, our results show that for a silver target, the ejected ions (adsorbed (Fe^+) or substrate (Ag^+ , Ag_2^+) species) have a mean kinetic energy equal to 9 eV regardless of mass. The kinetic energy distribution which is independent of the laser intensity ($10 - 50 \text{ MW/cm}^2$) is 3 eV FWHM at threshold. For the aluminum target, preliminary data also show the production of fast ions at threshold. Compared to the silver data, the Al^+ KE distribution is asymmetric and much broader (10 eV FWHM) with the fastest ions having 15-16 eV of kinetic energy. Among the number of possible mechanisms for explaining the data, the process whereby ion desorption is induced by electronic transitions (DIET) has the most merit.

* This project is sponsored by the Aerospace Sponsored Research Program (ASR)

INTRODUCTION

In vacuum, pulsed lasers can create a plasma above a target surface when the intensity exceeds $10\text{MW}/\text{cm}^2$. The plasma is the result of ionization of the ablated products via the inverse Bremsstrahlung mechanism[1]. With further increase in the laser intensity, the amount of energy transfer to the surface and hence removal of the material is solely governed by the photoinitiated above surface plasma. In this intensity regime, plasma hydrodynamic equations and a thermodynamic equilibrium model adequately describe both the gas dynamics and the net mass flow[2]. The early motivation for doing laser ablation experiments, albeit at intensities, was based on developing laser fusion and understanding laser bulk damage. However, with the increase in the use of lasers for processing, especially in semiconductor technologies, the current emphasis has shifted to more understanding of the fundamental processes in the laser/surface interaction. In this spirit, we have developed an experimental technique to measure, at threshold, the ablated product kinetic energy distributions. Our interest is to measure products resulting from the intrinsic photo-induced excitation and ablation, and to more closely reflect the nascent KE distributions produced, our measurements are taken near product formation threshold. In this paper we present our results from the UV laser (351 nm and 248 nm) ablation of crystalline metal targets (silver and aluminum).

EXPERIMENTAL

The experimental setup includes an ultra high vacuum chamber (10^{-10} torr), which has multiple ports, and holds a target sample. The sample can be positioned, via remote control, relative to the incident laser beam and the mass spectrometer. A laser with uniform intensity distribution is brought in to the chamber through a window and for most experiments strikes the surface at 45 degrees to the surface normal. A second tunable laser, aligned parallel to the surface, probes the ejected species. The TOF mass spectrometer provides a real time mass spectrum of the ejected charged species. In addition, a photomultiplier tube is positioned perpendicular to the laser beam axis and monitors emission from electronically excited species.

When monitoring the ablated ion distributions, the signals from the TOF microchannel plate detector (Galileo; response time 1 ns) are amplified (Lecroy; 200 MHz Bandwidth) and then digitized by a fast transient recorder (Transiac 100MHz). For each laser firing, data from the transient digitizer is recorded by the computer along with the TOF voltages and the incident laser energy. It was necessary to develop the capability for single-shot diagnostics as it would be expected that the surface morphology would change with continued laser ablation. With this capability, it becomes possible to monitor the ablation products as surface material is removed layer by layer. Figure 1 shows a low resolution TOF mass spectrum of 100 individually acquired signal traces. The traces record the UV (248 nm) laser ion ablation of a crystalline silver target. The measured Fe^+ signal results from Fe being an adsorbed impurity. The presentation of the data as seen in Fig. 1, is not suitable for analysis in detail. Necessary to our experiment is the capability for measuring a TOF mass spectrum at threshold fluences. We have found that if we analyze the topography of a data set (a number of acquired signal traces) rather than individual amplitude levels, the sensitivity to capturing threshold level signals increases. By the use of contour type plots, we can collect signals with the laser fixed at much lower fluences.

RESULTS

Figure 2 shows a contour plot of 600 individual TOF traces of the ablated ion Ag^+ taken under higher resolution. In this figure the laser fluence was first held constant and then programmed to slowly increase. Under the higher mass resolution, the kinetic energy (KE) distribution at the time of ablation can be calculated from the width in the TOF arrival times. The figure shows that the KE distribution broadens as the laser fluence is increased 20% above threshold. Similarly, by controlling the ablation laser fluence (e.g. fixed energy, and uniform intensity profile) and the target surface morphology (clean, smooth surface), it is possible to obtain consistent ablation product distributions. At the higher laser fluence levels, it can be shown that the KE distributions fit a "hot" Maxwellian distribution. Figure 3 shows three high resolution TOF mass spectra of the substrate ions Ag^+ , Ag_2^+ , and the adsorbed species Fe^+

taken with the laser fluence fixed at the ion production threshold. Each spectrum is a sum of 300 individually acquired laser shots. The two silver isotopes (107, 109 amu) and the three main isotopes of iron (54, 56, 57 amu) are resolved with the ratio of the peak heights as found in natural abundance. Also shown in the upper scale is the ejected ion kinetic energy calculated for a specific mass isotope from the corresponding arrival times. The data show that at threshold laser fluence the ablated ion species regardless of mass and surface binding (substrate/adsorbed) character have a mean kinetic energy $\langle KE \rangle$ of 9.0 eV with a narrow distribution (3 ± 1 eV FWHM). Similarly, Fig. 4 shows a high resolution TOF mass spectrum of the laser ablation from a crystalline aluminum target. The laser fluence was also maintained at ion production threshold while the spectrometer was tuned to monitor the ablated atomic Al^+ (aluminum) ion. The spectrum shows that the KE distribution for the ablated Al^+ is much broader (10 eV FWHM) than that measured in the silver ablation. We are as yet not sure if the width in the KE distribution is intrinsic to the ion desorption or if it has broadened due to long range interactions in the ablation process. The figure also shows that the fastest ions have kinetic energies close to 16 eV. This value also corroborated with the results of a retarding potential experiment.

DISCUSSION

The observation of hypervelocity ions in moderate fluence laser ablation of solid targets is not uncommon [3]. The average kinetic energy tends to be a function of the laser intensity[4], with the energy distribution being very broad. To our knowledge, our results are the first to show that threshold laser ablation of silver, where plasma effects are negligible, results in hypervelocity ions with very narrow KE distributions.

For a specific crystalline metal target (silver and aluminum), the kinetic energy of the ejecta do not vary with wavelength (248 nm and 351 nm), nor with the ion product mass, and within limits are independent of the incident intensity. These results cannot be explained within the framework of a number of potential mechanisms such as a) laser photolysis of an

adsorbate, b) field ionization of an adsorbate or evaporated substrate species, and c) supersonic expansion following laser ablation. If the hypervelocity product ions are formed via laser photolysis of an adsorbed precursor, then we would expect variations in the ejected kinetic energy with wavelength as well as some dependence on the differences in binding potentials between physisorbed and lattice bound species. Laser field ionization of thermally desorbed species followed by coulombic repulsion is also difficult to rationalize. At the laser power densities used in this experiment, the electric field strength near the surface ($2-9 \times 10^{-3}$ V/nm) is orders of magnitude lower than that used in field ionization TOF mass spectrometry (10V/nm)[5]. In addition, a kinetic energy deficit is observed in the TOF mass spectrum by laser field ionization. The energy deficit is due to the ionization of the species at a critical distance above the surface which is laser field dependent[6]. Our results show a kinetic energy enhancement rather than a deficit, and we do not see variation of the kinetic energy with laser fluence near threshold. Finally, in a free jet expansion, similar to that produced in pulsed molecular beams, one expects from conservation of enthalpy to find the ablated species with a common velocity rather than a common kinetic energy[7].

It is known that the laser fluence threshold for electron desorption is far below that for ion desorption [8]. Given this fact, our results could be explained by an electrical acceleration mechanism if a sheath of electron density exists above the surface. Two of our experimental results provide evidence contrary to the existence of an electron sheath. In the laser ablation of the Ag target, we observed the same KE distribution at both laser wavelengths, even though the photon energy at 248 nm is above the silver work function. Similarly, we do not see any change in the KE when the laser fluence is increased up to 20% above threshold. One could argue that the electron density in the sheath is space charge limited, it seems that would give KE energy distributions broader than what is measured. We are attempting to model the effects of electron space charge on the ion KE distributions.

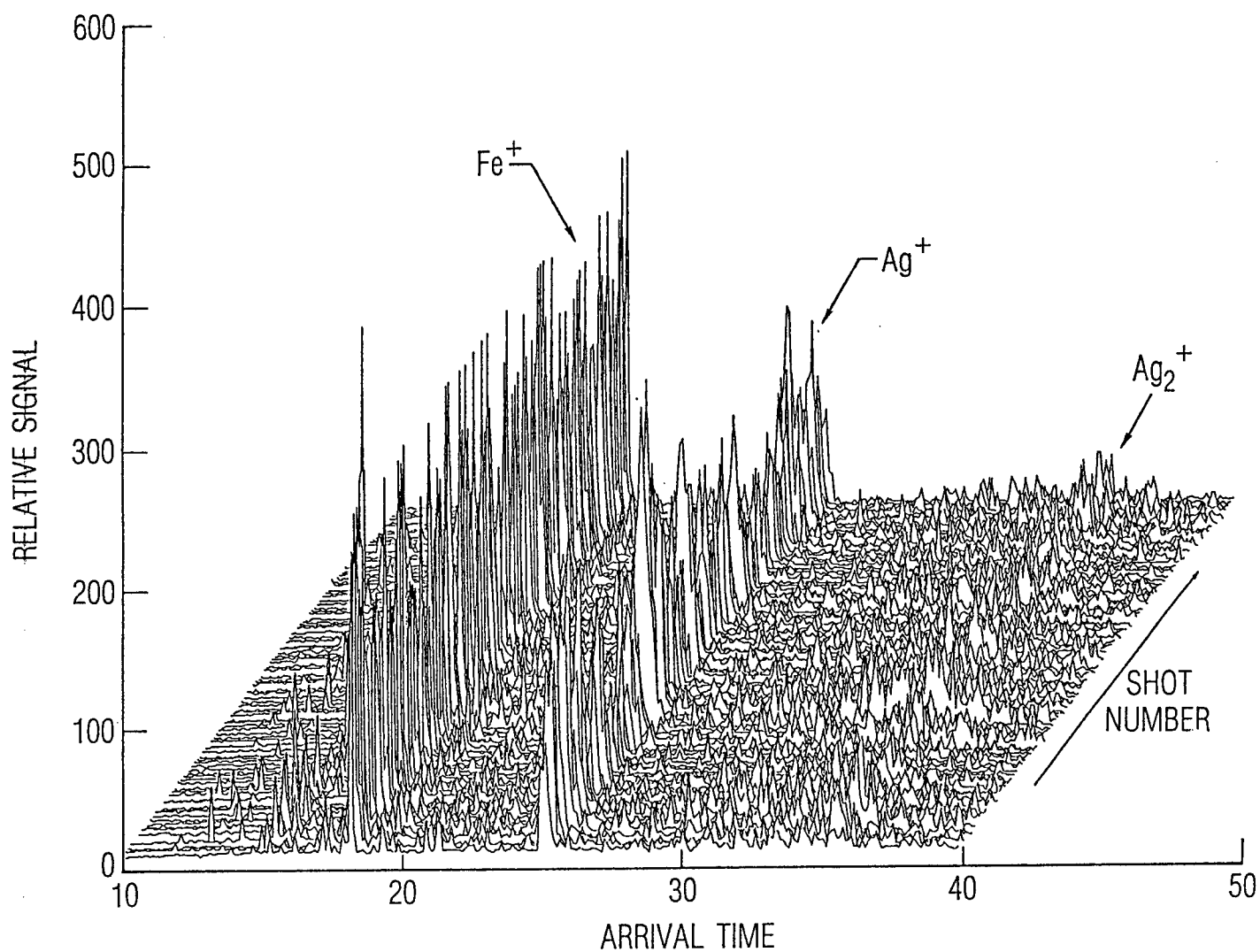
At laser fluence threshold, our observation of hypervelocity ions with narrow kinetic energy distribution suggest that a fraction of the absorbed energy must remain localized to

permit ion desorption, and furthermore for those ions desorbing, the product channel has constraints on the KE. The specific mechanisms by which the ion is actually formed and ejected are not yet fully apparent from our experimental results. However, we have some supporting evidence that the ion formation and the ejection process is induced via an electronic excitation in the solid. The production of ions at the relatively low laser fluences ($10 - 50 \text{ mJ/cm}^2$) might be the result of electronic resonances in the solid or due to surface impurities. The impurity concentration at the surface was minimized during the target preparation cycle. Prior to taking data, roughly 30K laser shots are fired at the test area to remove adsorbed contamination. A small amount of contamination could still be present which may artificially lower the threshold for ion production. A LEEDS or an Auger analysis would help in assuring surface purity. The KE distribution of all ejected ions from a properly prepared surface is the same and very specific to the target (silver, aluminum). This similarity in the ejected kinetic energy distribution, regardless of mass, along with the results that for both laser ablation wavelengths (351 nm 3.5 eV, and 248 nm 5.0 eV), an average of 58-62 eV is absorbed per ejected ion suggests that the initial energy absorption process is through an electronic excitation in the solid. Further support is the fact that the $N_1(4p_{3/2})$, $N_2(4p_{1/2})$ core excitation energies for silver are at 58.5 eV and 64.5 eV respectively. An electronic core excitation does not necessarily lead to ion ejection. It can however create ions through a mechanism originally outlined by Knotek and Feibelman [9]. Given that our photon energies are only a few eV, the creation of a core hole in silver requires a multiple photon absorption process. Recently, it has been suggested that electronic surface states due to defects may help, through resonance enhancement, the absorption of multiple photons [10]. We are now planning experiments where we will measure the KE distributions as a function of laser wavelength and temporal pulse shape. What is not immediately clear to us is the mechanism by which this electronic excitation is converted to atomic motion. It is known that two and three hole Auger final states decay at a much lower rate, essentially trapping the excitation at a particular site [11]. It is also known that in an Auger decay process bulk plasmons can be excited [12]. The values we measure for the ion KE have a fortuitous correlation with the bulk (longitudinal) plasmon fre-

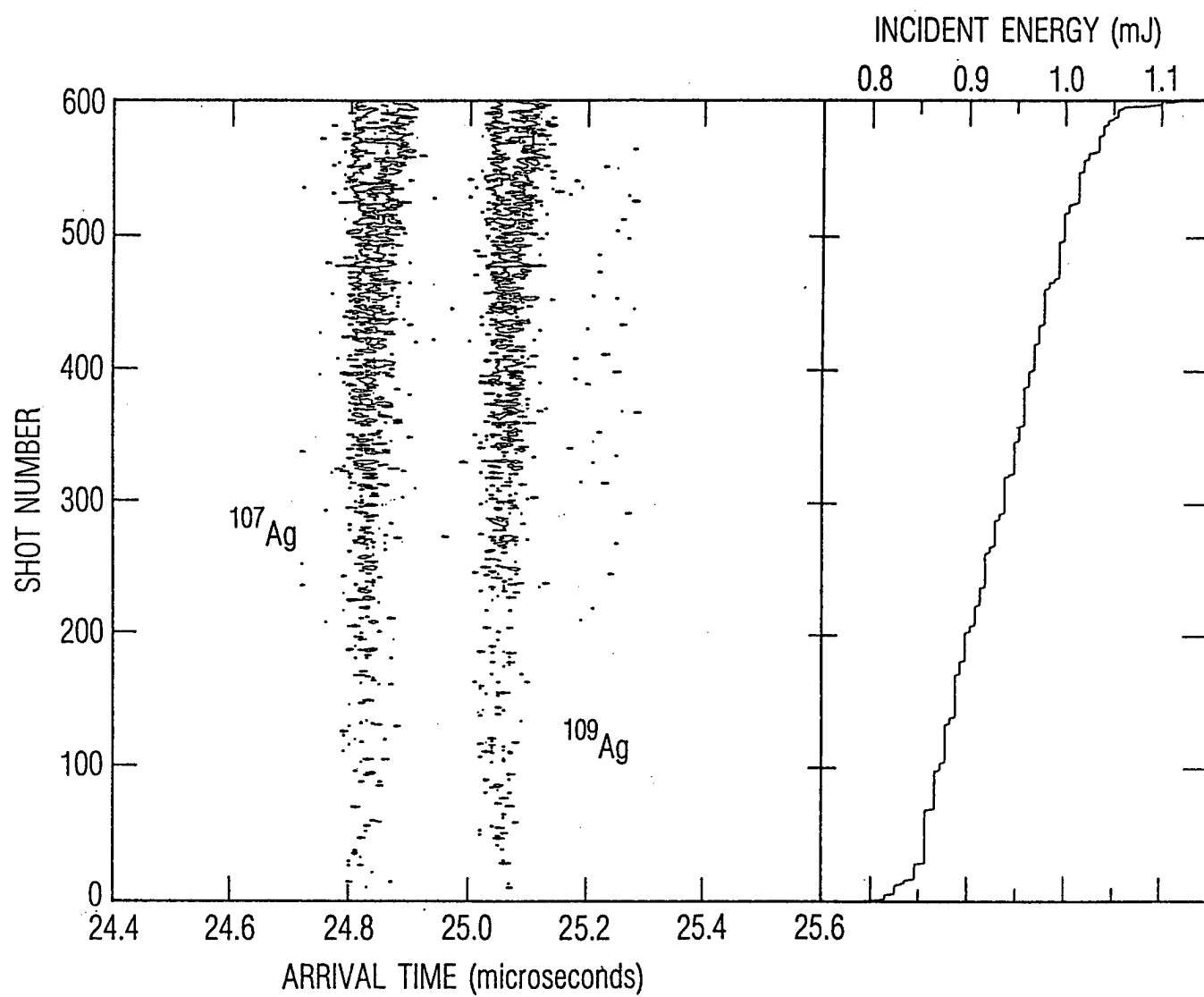
quency of the target metal. Using the free electron metal model, the calculated plasmon frequency for silver and aluminum are 9.0 and 15.8 respectively [13]. The experimentally measured frequencies are 3.78 eV and 8.0 eV for silver [14], and 15.3 eV for aluminum [15]. Our results show that ions are ejected from silver with 9 ± 1 eV of KE and with 15 - 16 eV of KE from aluminum. If in fact our measurements are related to the plasmon frequency, then it is not clear why we do not measure ion KE corresponding to the 3.78 eV bulk plasmon. Otto et al. [14] have concluded from their spectroscopy on silver that the 3.78 and 8.0 eV absorption corresponds to the out and in phase oscillations between the free conduction band electrons and the bound d band electrons. Perhaps the in phase oscillation can more readily promote ion acceleration. Clearly more experiments along with a theoretical model are needed to pin down the underlying mechanisms. We are now preparing experiments to see if this correlation holds with other targets as well, and to see if the predicted laser polarization effects could be observed [16].

REFERENCES

- [1] K. Buchl, J. Appl. Phys. **43**, 1032 (1972).
- [2] V. A. Batanov, F. V. Bunkin, A. M. Prokhorov, and V. B. Fedorov, Soviet Phys. JETP. **36**, 311 (1973).
- [3] M. R. Bedilov, Yu. A. Bykovskii, D. Kuramatov, A. Kholbaev, and K. Khaitbaev, Sov. J. Quantum Electron. **17**, 1068 (1987).
- [4] V. A. Batanov, F. V. Bunkin, A. M. Prokhorov, and V. B. Fedorov, Zh. Eksp. Teor. Fiz. **63** 1240 (1972).
- [5] E. R. McMullen, and J. P. Perdew, Phys. Rev. B **36**, 2598 (1987).
- [6] T. T. Tsong, W. A. Schmidt, and O. Frank, Surf. Sci. **65**, 109 (1977).
- [7] J. B. Anderson, and J. B. Fenn, Phys. Fluids, **8**, 780 (1965).
- [8] P. G. Strupp, J. L. Grant, P. C. Stair, and E. Weitz, J. Vac. Sci. Technol. **A6** 839 (1988).
- [9] M. L. Knotek, and P. J. Feibelman, Phys. Rev. Lett. **40** 964 (1978).
- [10] H. B. Nielsen, J. Reif, E. Matthias, E. Westin, and A. Rosen to be published.
- [11] D. R. Jennison, *Desorption Induced by Electronic Transitions DIET I*, Eds. N. H. Tolk, M. M. Traum, J. C. Tully, and T. E. Madey (Springer Series in Chem. Phys. # 24; Springer-Verlag, New York, 1983).
- [12] J. W. Gadzuk, *Desorption Induced by Electronic Transitions DIET I*, Eds. N. H. Tolk, M. M. Traum, J. C. Tully, and T. E. Madey (Springer Series in Chem. Phys. # 24; Springer-Verlag, New York, 1983).
- [13] C. Kittel, *Introduction to Solid State Physics*, 5th Ed. (John Wiley & Sons, New York, New York) 1976.
- [14] A. Otto, and E. Petri, Solid State Commun. **20**, 823 (1976).
- [15] C. J. Powell, and J. B. Swan, Phys. Rev. **115**, 869 (1959).
- [16] A. R. Melnyk, and M. J. Harrison, Phys. Rev. B. **2**, 835 (1970).

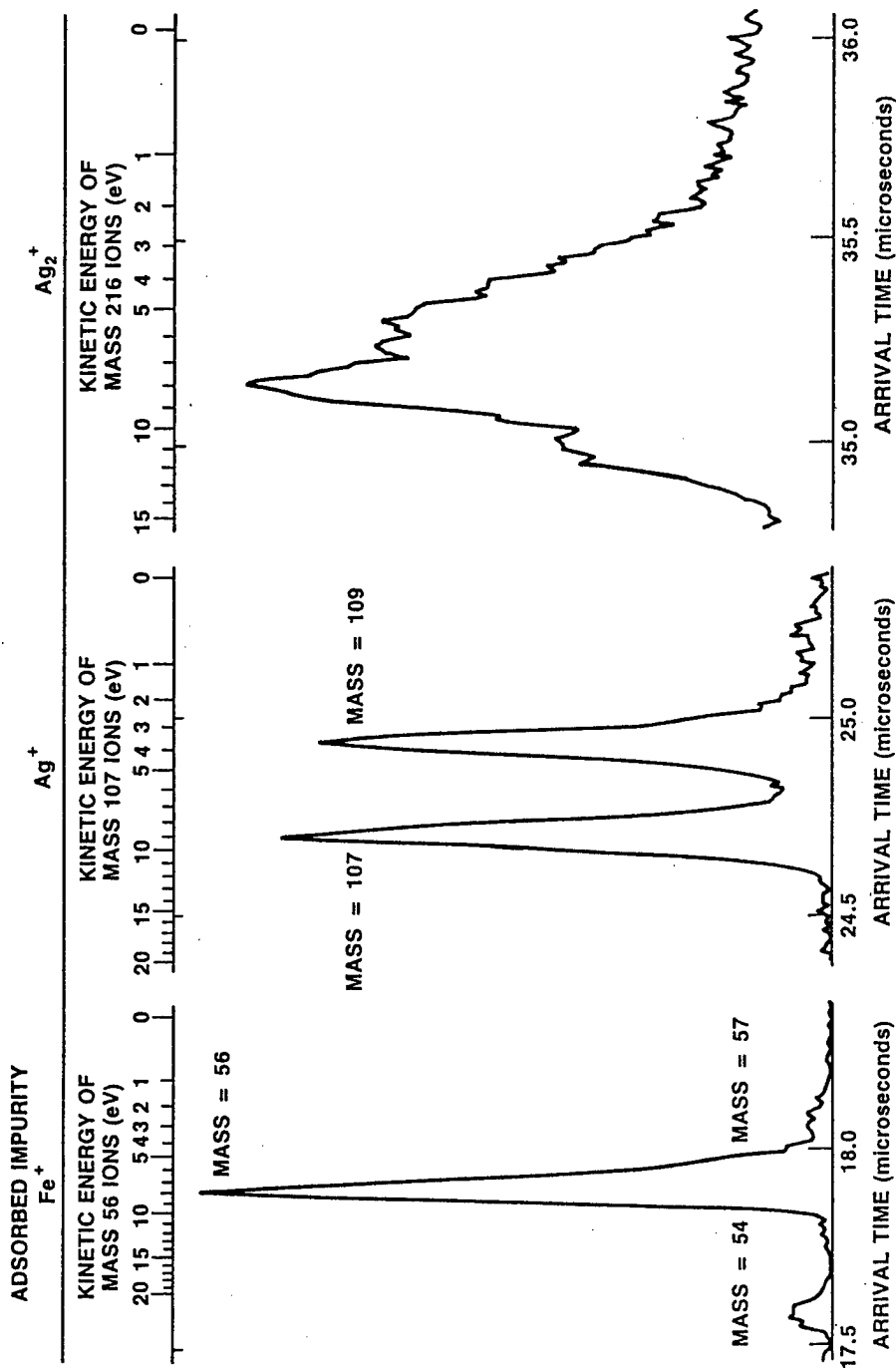


[1] Figure 1: Three dimensional representation of a series of 100 single shot mass spectra of 248 nm laser ablation of silver; only major ions are identifiable.

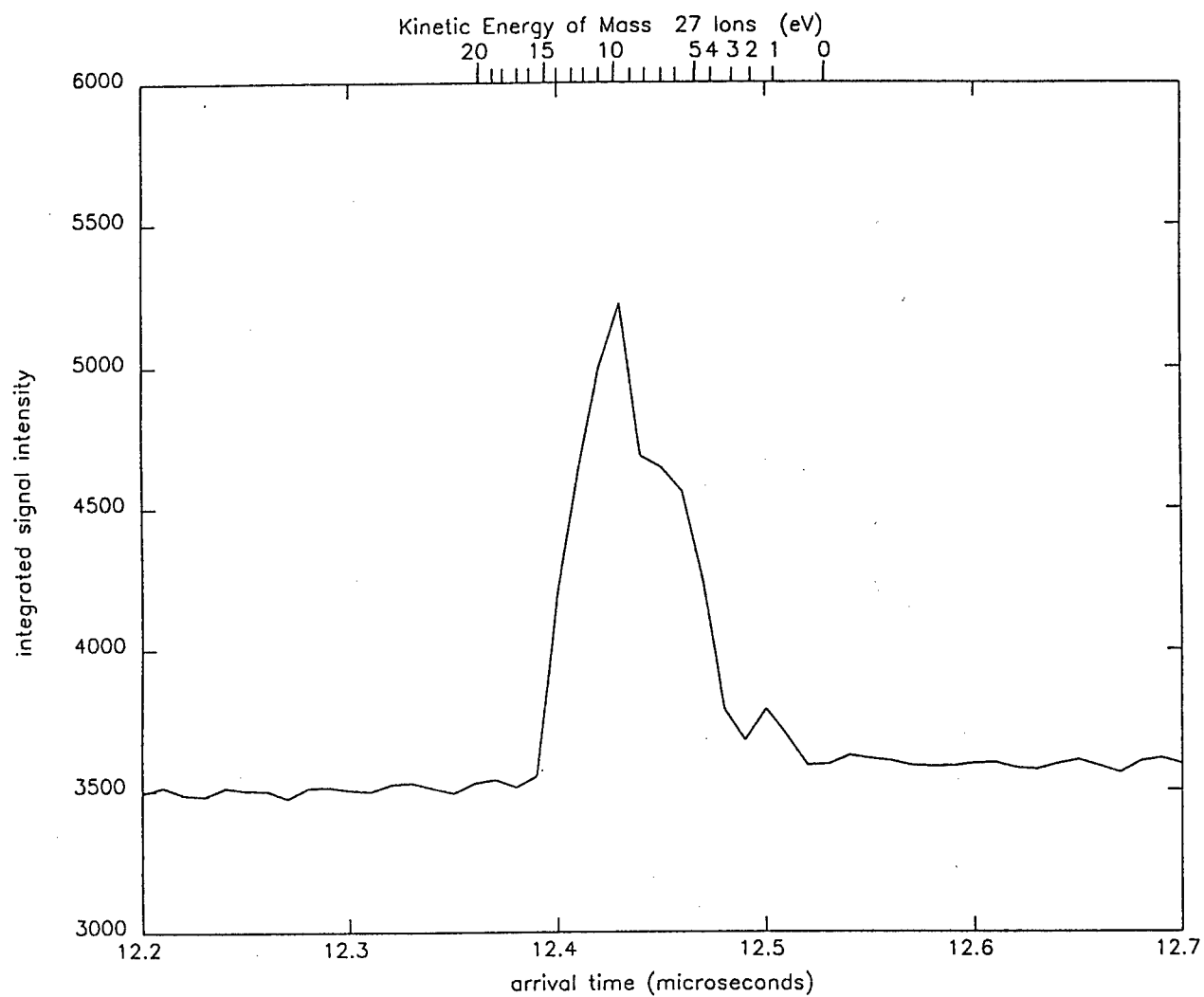


[2] Figure 2: Contour plot of a series of 600 mass spectra of silver monomer ablated at 248 nm.

The spectra are sorted for incident laser energy, which is plotted on the right.



[3] Figure 3: A high resolution 300 shot sum mass spectrum of 248nm laser ablation from a crystalline silver target with adsorbed Fe. The figure shows the three major ablated ions measured at threshold. The kinetic energy for a specific isotope is given in the upper scale.



[4] Figure 4: A high resolution 300 shot sum mass spectrum of 351 nm laser ablation of a crystalline aluminum target. The spectrometer is tuned to Al^+ .

The Interaction of Hydrogen with Alkali Halide Surfaces under Electron Beam Irradiation

L. T. Hudson, A. V. Barnes, M. H. Mendenhall, N. H. Tolk
Center for Atomic and Molecular Physics at Surfaces
Vanderbilt University Physics Department
Nashville, TN 37235

P. Nordlander
Rutgers University Physics Department
Piscataway, NJ 08855-0849

G. Betz, W. Husinsky, E. Wolfrum and P. Wurz
Technische Universität Wien, Institut für Allgemeine Physik
Wiedner Hauptstraße 8-10, A-1040 Wien, Austria

ABSTRACT

First measurements have been made of the energy, temperature and time dependent yields of Balmer and Lyman radiation from excited hydrogen atoms desorbed from alkali halide surfaces by electron impact. These surfaces are dosed *in situ* with molecular hydrogen. Initially, no desorbed H^* is observed from electron irradiation of clean and stoichiometric alkali halide surfaces. As bombardment continues, however, the surface grows metal and defect rich, at room temperature, and H^* fluorescence signals emerge. The data suggest incident molecular hydrogen is dissociated on this surface; surface migration of atomic hydrogen allows the formation of its desorption precursor: bonding to a surface halogen atom.

Hydrogen near a well characterized surface constitutes the model system in the study of the static and dynamic behavior of atoms and molecules interacting with surfaces. Analysis of desorbed excited state neutral atom yields by optical techniques, including beam energy, target temperature and time dependent yields, provides information on the dynamics of bond breaking and making processes at surfaces, leading toward a detailed atomic scale understanding of these fundamental phenomena. Molecular and atomic hydrogen as point defects in the bulk of alkali halides has been well documented¹, but very little work to date has dealt with the desorption of hydrogen from alkali halide surfaces. Tolk *et al.*² observed Balmer hydrogen lines during electron irradiation of alkali halide surfaces, but the precursor state of this desorbate has long been an open question. We address this issue by measuring the desorption energy thresholds and temperature dependence of desorbed H*.

The experimental apparatus consists of a low energy electron gun (5 to 300 eV) and an ultrahigh-vacuum chamber which sustains a base pressure of 10^{-10} Torr. Photons are collected at 90° to the incident electron beam and focused into a 0.3 m f/5.3 grating spectrometer. The target materials used in these studies were the (100) faces of single crystal KCl, LiF and KBr which were cleaved in air and cleaned by heating to 500°C in vacuum. To minimize effects due to sample charging during the low energy threshold measurements, the samples were tilted 45° toward the spectrometer to reduce the angle of incidence of the electron beam.³ Further, the crystal faces were overlaid with a fine (80% transmission) molybdenum mesh which was electrically grounded. During these measurements, the partial pressure of H_2 was maintained at 10^{-7} Torr. Production of Balmer radiation from electron bombardment of gas phase H_2 at this pressure and these currents ($<100\ \mu\text{A}$) would be of negligible intensity.⁴

A fluorescence spectrum from electron bombardment by $22\ \mu\text{A}$ at 60 eV of KCl is shown in the foreground of Figure 1. We observe the first resonance lines of potassium at 7665 Å and 7699 Å and the intrinsic cathodoluminescence of KCl centered around 4500 Å.⁵ A partial pres-

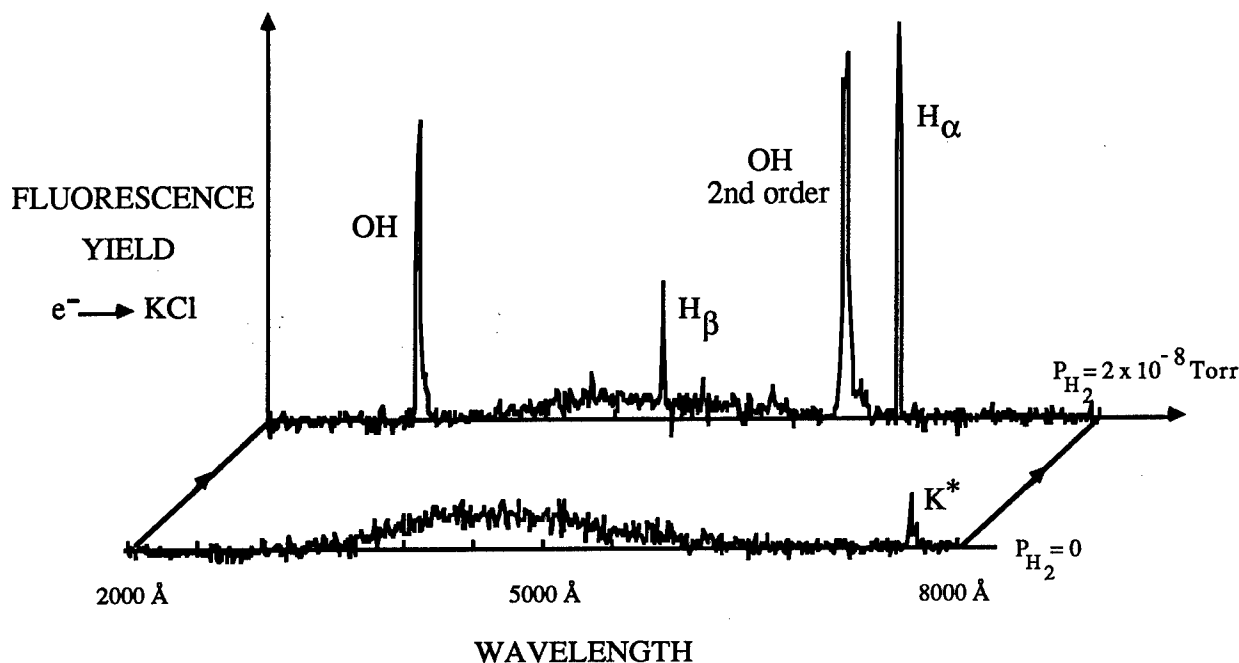


Figure 1. Spectral scans with and without hydrogen dosing.

sure of 2×10^{-8} Torr of H_2 was then admitted. A second spectrum, taken after five minutes of dosing and electron irradiation, reveals a quenching of the excited potassium emissions, replaced by the Balmer lines of atomic hydrogen and the 0-0 and 1-1 emissions of the hydroxyl radical OH ($A^2\Sigma^+ \rightarrow X^2\Pi$) in first and second order (Figure 1). Further measurements are scheduled to determine whether potassium desorption is inhibited or excitation of potassium is quenched. The appearance of OH suggests that some dissociation of H_2 may occur at oxygen containing impurity sites which persist on several alkali halide surfaces even after baking.⁶ Another possible source of OH is discussed below.

At elevated temperatures and currents, the hydrogen signals are diminished and the potassium fluorescence reappears. The variation of Lyman alpha (Ly_α) emissions from $e^- \rightarrow KCl:H_2$ (2×10^{-7} Torr) as a function of temperature is displayed below in Figure 2. The sample holder is resistively heated and the abscissae represent the output of a chromel-alumel thermocouple attached to the copper sample holder. This measurement was made over a three

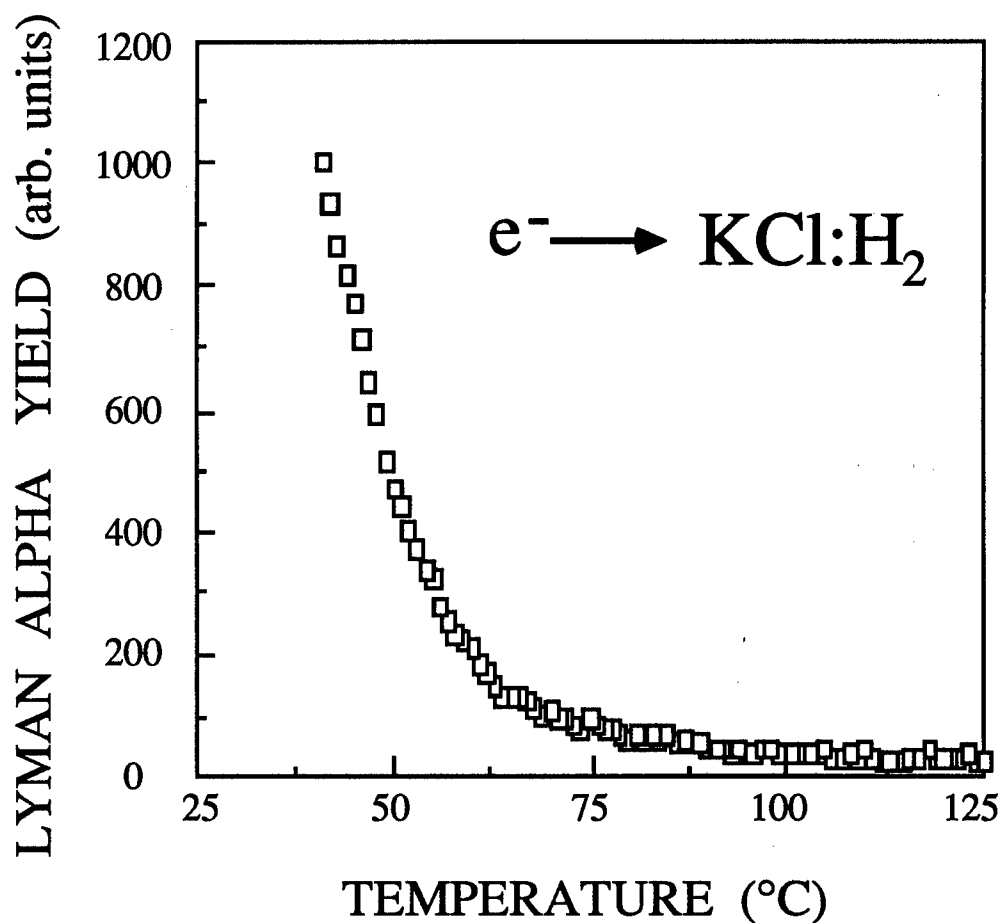


Figure 2. *Temperature dependence of desorbed excited state hydrogen.*

hour period to insure near thermal equilibrium between the sample and holder. Monitoring the Ly_α signal (1216 Å) with a 2m f/4.5 windowless UV spectrometer and channeltron has the advantage of insensitivity to heater or bulk fluorescence background signals which are themselves temperature dependent. The electron beam was maintained at 77 μA and 300 eV. In another experiment, the sample was chilled from room temperature to -145°C . The hydrogen Balmer emissions increased in intensity by about a factor of two.

As a fresh alkali halide surface is irradiated by electrons, surface and bulk defects are created which lead to the fast ejection of halogen atoms leaving excess alkali atoms to desorb

thermally from the surface.⁷ The surface stoichiometry becomes alkali metal rich on a time scale of several minutes. Tokutaka *et al.*⁸ have monitored the time evolution of Auger peaks of potassium and chlorine during electron bombardment of KCl. The surface reaches a metal rich steady state after about thirty minutes. As the sample temperature is increased, the excess metal vapor pressure is raised and the K and Cl signals approach their initial relative values.⁸ For the case of electron irradiation of NaCl, Szymonski *et al.*⁹ find a decrease in the ratio of Na and Cl Auger signals with increasing temperature, leveling off around 150°C. Since the vapor pressure of potassium is a little higher than sodium, this relationship for the potassium halides would be shifted somewhat to lower temperatures. For the lithium halides, one would expect a significant shift towards higher temperatures.

All of our measurements of H^* yields in time and temperature correlate well with the degree of metallization of the surface. Initially, no H^* is observed upon electron irradiation of a fresh, clean crystal under constant H_2 dosing. On a time scale of several minutes, however, an emission appears, grows and equilibrates. We hypothesize the temperature dependence of H^* (Figure 2 and the refrigeration experiment) reflects the degree of metallization of KCl as the sample temperature is varied. As would be expected, it is shifted slightly lower in temperature than the metallization vs. temperature curve for NaCl. No systematic temperature dependence of H^* from LiF has yet been performed, but H^* has been seen in spectra of $e^- \rightarrow LiF:H_2$ at 200°C. This is consistent with the lower vapor pressure of lithium.

Note that these temperature desorption measurements are inconsistent with the removal of a source of surface hydrogen from either a physisorbed or chemisorbed state by purely thermal means. Physisorbed H_2 cannot be a significant precursor of the observed excited hydrogen emissions. Physical binding energies for H_2 on LiF, NaF, NaCl and KCl are 25-40 meV.¹⁰ Binding in these potential wells at room temperature and 10^{-7} Torr background pressure of H_2 implies a residence lifetime of less than one picosecond. Assuming unit sticking efficiency,

these incident electron currents would create negligible H^* intensity. Interpretation of Figure 2 in the context of thermal dissociation of a chemical bond is also problematical. It would be surprising if chemisorbed hydrogen could be removed so easily by such a small change in temperature.

These measurements suggest that the degree of metallization of the surface determines the amount of incident molecular hydrogen which may be dissociatively adsorbed. Because of the difficulties in preparing clean and characterized alkali metal surfaces, few adsorption studies have been performed on these simple metals.¹¹ In fact, this technique may provide a novel approach to *in situ* creation of a surface adequate for such studies. Alkali metals are known to decompose water, forming the hydroxide and evolving hydrogen.¹² This could explain the OH emissions if our H_2 source contained water. Even if dissociative adsorption of H_2 on a perfect alkali surface is an activated process, we believe that under electron bombardment there are ample highly reactive defect sites which provide efficient dissociative adsorption of H_2 . After all, these surfaces are metal rich in the sense that surface halogen atoms have been desorbed exposing alkali atoms of lower atomic planes. "Metal rich" therefore necessarily implies a profusion of step and kink defect sites. This defect-driven, dissociation mechanism is observed, for example, in the H_2 -platinum system. Dissociative adsorption of H_2 on Pt (111) is an activated process ($\cong 1$ kcal/mol), but at step sites H_2 (bond strength = 104 kcal/mol) is atomized and at kinks even CO (257 kcal/mol) is dissociated.¹³ Further motivation for suggesting molecular hydrogen dissociates on electron beam modified alkali halide surfaces is provided by the energy dependent yields of atomic hydrogen and is discussed below.

We now turn to the question of the desorption precursor of excited state atomic hydrogen. Figure 3 shows the incident electron energy thresholds of Balmer alpha (H_α) radiation from excited hydrogen atoms desorbed from the surfaces of LiF and KCl. The integrated peak area above a fit to the background and normalized to collected current is plotted against incident electron

energy. The excitation functions exhibit thresholds at 23 eV for LiF and 20 eV for KCl. These are the minimum incident electron energies at which a resonance could be seen at 6563 Å (H_{α}) in the spectra and are accurate to within an electron volt. Further, H^* exhibits an excitation threshold

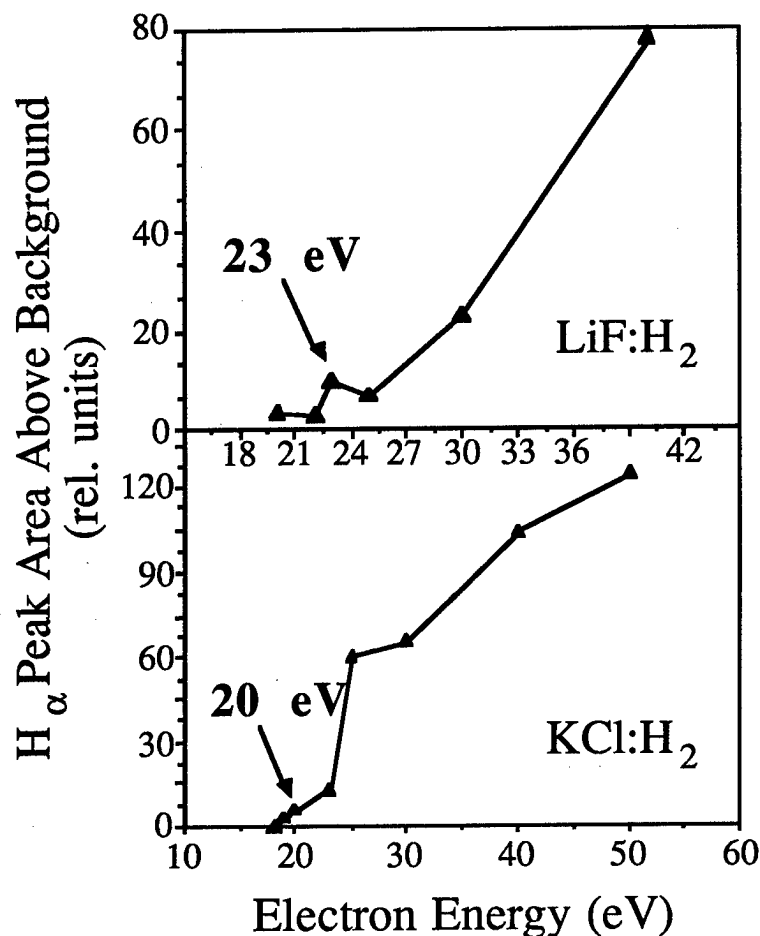


Figure 3. Energy dependence of Balmer yields from different alkali halide substrates.

from KBr at 21 eV. These thresholds are remarkably similar to those of gas phase dissociative excitation of hydrogen halides by electron impact. The primary threshold for production of H_{β} from dissociative excitation of gas phase HCl is 20 eV, yielding fragments with translational kinetic energy of 2.5 eV.¹⁴ A secondary threshold occurs at 25 eV with kinetic energies from 4

to 6 eV. The energy dependence of H_{α} from HF (gas) exhibits a primary and two secondary thresholds: 18, 23 and 40 eV with translational energies of 0.3, 5.2 and 6.5 eV respectively.¹⁵ Möhlman and DeHeer¹⁶ have measured the cross section for the production of H_{α} from electron impact of HBr. Their data were taken in 10 eV increments and show a primary energy threshold between 20 and 30 eV.

Comparison with gas phase energy thresholds suggests chemisorption to a surface halogen atom as the desorption precursor of the observed excited state hydrogen. The desorption threshold of H^* from KCl is the same as that of gas phase HCl. The primary threshold from a LiF surface is the secondary threshold from gas phase HF studies. We propose the suppression of the 18 eV threshold from HF is due to resonant ionization or de-excitation of final state H^* . The energies of H^* overlap the empty conduction band of LiF and the relatively low translational energy of this fragment (0.3 eV) greatly enhances the probability of such a resonant process. Finally, the threshold from the surface of KBr is consistent with the literature on HBr.¹⁵ We also note that the hydrogen halide bond strength is generally twice that of the alkali hydride, providing an energetics argument for mobile hydrogen on alkali metal to terminate its random walk on a nearby halogen.

On occasion we observe H^* emissions before dosing the sample with H_2 . We attribute this to a source of H_2 incident to the surface from within the crystal. Hydrogen is a common impurity in alkali halides and wanders freely through the bulk at room temperature.¹⁷ Our model predicts, as before, that dissociation occurs at the surface followed by adsorption to and desorption from a halogen surface atom. Under continued electron irradiation, the hydrogen signal diminishes and becomes negligible. However, after dosing continuously under electron bombardment, this source term is probably replenished.

Further insight into the H^* production mechanism is provided by high resolution spectroscopic measurements, which reveal the Doppler lineshape. Doppler lineshape

measurements on the $H\beta$ line from KCl reveal a broadening for observation parallel to the surface and both a broadening and a shift for observation near the surface normal. This Doppler shift shows that the emission is from atoms in the gas phase, all moving rapidly away from the surface with energies greater than 4 eV. The line shape is consistent with that of electron dissociative excitation of HCl in the gas phase by 300 eV electrons¹⁴ which results in H^* fragments, as stated above, of 4-6 eV.

To account for these observations we propose the following adsorption-desorption sequence: (1) molecular hydrogen is thermally incident upon an inert alkali halide surface, (2) electron irradiation creates a highly reactive, metal rich surface with a profusion of defect sites, (3) dissociative adsorption of the molecular hydrogen occurs at metal defect sites, (4) atomic hydrogen migrates along the surface, (5) then chemisorbs to a halogen atom, and finally (6) the electron beam dissociates the hydrogen halide molecule with the departing H fragment in an excited state. Furthermore, as the sample is heated and the surface is thereby returned toward its original stoichiometry, less and less H_2 may be dissociated, adsorbed and consequently desorbed. This model could also describe the emission of ground state hydrogen atoms.

Desorption of excited state hydrogen by electron impact of alkali halide surfaces has been investigated by measuring temperature, time and energy dependent yields. These results provide important new information toward a microscopic picture of the interaction dynamics of molecular and atomic hydrogen with the electron modified surface of alkali halides.

The authors would like to gratefully acknowledge helpful discussions with R. S. Freund, R. F. Haglund, Jr., J. B. Tellinghuisen and J.C. Tully. This work was funded by the AFOSR University Research Initiative Contract No. F49620-86-C-0125DEF, the Air Force Office of Scientific Research under Contract No. AFOSR-86-0150, the Office of Naval Research under Contract No. N00014-86-K-0735, the National Science Foundation and NASA grant NGT-50132.

REFERENCES

- [1] A. S. Marfunin, *Spectroscopy, Luminescence and Radiation Centers in Minerals* (Springer-Verlag, Berlin, 1979) p. 267.
- [2] N. H. Tolk, L. C. Feldman, J. S. Kraus, K. J. Morris, M. M. Traum and J. C. Tully, *Phys. Rev. Lett.* **46**, 134 (1981).
- [3] C. G. Pantano and T. E. Madey, *App. of Surf. Sci.* **7**, 115 (1981).
- [4] R. S. Freund, J. A. Schiavone and D. F. Brader, *J. Chem. Phys.* **64**, 1122 (1976).
- [5] A. I. Bazhin, E. O. Rausch and E. W. Thomas, *Phys. Rev. B* **14**, 2583 (1976).
- [6] T. E. Gallon, I. G. Higginbotham, M. Prutton and H. Tokutaka, *Surf. Sci.* **21**, 224 (1970).
- [7] P. D. Townsend, R. Browning, D. J. Garland, J. C. Kelly, A. Mahjoobi, A. J. Michael and M. Saidoh, *Rad. Eff.* **30**, 55 (1976).
H. Overeijnder, R. R. Tol and A. E. DeVries, *Surf. Sci.* **90**, 265 (1979).
- [8] H. Tokutaka, M. Pruton, I.G. Higginbotham and T.E. Gallon, *Surf. Sci.* **21**, 233 (1970).
- [9] M. Szymonski, J. Ruthowski, A. Poradzisz, Z. Postawa and B. Jørgensen, *Desorption Induced by Electronic Transitions (DIET II)*, eds. W. Brenig and D. Menzel (Springer-Verlag, Berlin, 1985) pp. 160-168.
- [10] H. Hoinkes, *Rev. Mod. Phys.* **52**, 933 (1980).
- [11] J. Harris, S. Andersson, C. Holmberg and P. Nordlander, *Physica Scripta.* **T13**, 155 (1986).
- [12] *CRC Handbook of Chemistry and Physics*, R. C. Weast, ed. (CRC Press, Inc., Boca Raton, 1988) p. B-29.
- [13] G. A. Somorjai, *Chemistry in Two Dimensions: Surfaces* (Cornell University Press, Ithaca, 1981) pp. 488-91.
- [14] M. Higo and T. Ogawa, *Chem. Phys.* **44**, 279 (1979).
- [15] M. Ohno, N. Kouchi, K. Ito, N. Oda and Y. Hatano, *Chem. Phys.* **58**, 45 (1981).
- [16] G. R. Möhlman and F. J. DeHeer, *Chem. Phys.* **40**, 157 (1979).
- [17] M. de souza and F. Lüty, *Phys. Rev. B* **12**, 5866 (1973).

The role of core-excitons in the desorption process

W. Husinsky, P. Wurz, E. Wolfrum and G. Betz
Technische Universität Wien, Institut für Allgemeine Physik,
Wiedner Hauptstraße 8-10, A-1040 Wien, Austria

L. Hudson and N. Tolk
Center of Atomic and Molecular Physics at Surfaces,
Vanderbilt University, Nashville, TN, USA

The desorption process from alkali-halides is initiated by electronic excitations caused by the bombarding radiation. In this paper recent results on the desorption of excited alkali atoms are reported. The results indicate, that core-excitons are the first step in the desorption process leading to the desorption of excited alkali atoms.

We have investigated the thresholds for the generation of desorbed excited alkali atoms under electron bombardment for LiF, KCl and KBr in the energy range from 10 to 200 eV from room temperature up to 450 °C. Although the desorption of neutral ground-state atoms is quite well understood (valence excitation mechanism) ^{1 2 3 4} there exists no general agreement about the generation of excited atoms and ions in the literature ^{5 6 7}.

A 10 eV to 200 eV electron beam with currents up to 30 μ A was used to bombard alkali-halide single crystal surfaces. The electron beam axis was incident on the target under 45 °. The bombarding area had dimensions of approximately 2 by 4 mm. Careful investigations have been done to measure the profile of the electron beam. Radiation of excited states was collimated by a MgF₂ lens into a high resolution one meter grating monochromator viewing the crystal surface perpendicularly. The UHV-system maintained a base pressure of less than 3×10^{-10} mbar during the measurements. All investigated crystals have been cleaved in air and cleaned in the UHV-system by baking at 200 °C overnight. The sample temperature was varied between 20 °C and 450 °C. Sample charging, which is a crucial problem with insulators especially at low temperatures, was largely reduced by placing a Mo-mesh with a transmission of 80% over the crystal surface and by using low current densities. Nevertheless, special care had to be taken when changing the electron energy, as the signal reached a steady-state value only after a few minutes. This was ascribed to the migration time of previously produced defects to the surface. Background radiation originating from bulk luminescence from the crystal, from the sample-furnace and from the electron gun filament was measured carefully for each data point and subtracted from the absolute count-rates. Uncertainties in the electron energy are due to the work-function of the cathode and the work-function of the crystal ⁸.

Dealing with the desorption of excited atoms one has to understand the desorption of neutral ground state atoms first, as these generally dominate the desorbed particle flux. It, therefore, seems to be justified to regard the desorption of excited atoms as a second order effect, which is strongly dependent on the situation created by the desorption of the majority ground state atoms. As far as alkali halides are concerned, the target temperature determines the desorption of neutral ground state alkali atoms in a dominant way, resulting in different surface conditions. According to the valence excitation mechanism, which leads to desorption of halogen atoms, excess metal atoms accumulate on the alkali-halide crystal surface. Therefore, two temperature regimes can be distinguished. a) Below a certain temperature the evaporation rate is too low to cause significant desorption and an excess metal layer is produced. b) The evaporation rate is high enough that each excess metal atom evaporates immediately ⁹. The vapor pressure is governed by the crystal temperature and changes by several orders of magnitude in the investigated temperature range.

Unfortunately the vapor pressure of K^{10} is so high that considerable evaporation already occurs at room temperature ¹¹. For K there are no excess metal atoms on the surface above 100 °C. Only the vapor pressure for Li is low enough to allow a surface enrichment of Li on a LiF crystal up to 250 °C ¹².

In the following the experimental findings are described. As a consequence of the desorption behavior of the alkali ground state atoms as a function of the target temperature, we could study both temperature regimes only for LiF. For KCl and KBr cooling of the target below room temperature would be necessary. Therefore, LiF offers the possibility to study two regimes, where in principle different mechanisms for the desorption of excited alkali atoms could be identified. In fact, in a temperature regime, where desorption of ground state atoms usually accompanied by secondary electron emission is taking place, gas phase excitation of neutral atoms is a possible source for excited atoms. In a temperature regime where no neutral ground state atoms are desorbed, this possibility can be excluded and an intrinsic surface excitation mechanism has to be assumed.

LiF targets: This correlation of the yield of neutral ground-state Li atoms by ESD from LiF with the vapor pressure of the Li metal has been shown previously ¹³. The ESD yield follows the evaporation rate giving a detectable amount of neutral ground-state atoms above 250 °C and rising exponentially until 400 °C, where the desorption of ground-state Li is only governed by the electron flux and not limited by the evaporation rate anymore. Below 250 °C no neutral ground-state desorption of Li was found under electron bombardment. In contrast to the Li ground-state emission, the yield of desorbed excited Li atoms in the temperature range from room temperature to 250 °C under electron bombardment is considerable. Fig.1 shows the comparison between our measurement of the temperature dependence of the excited Li atoms and the temperature dependence of ground-state Li atoms measured by Haglund et al. under electron bombardment. With a rough estimate of the detection efficiency we obtain a yield of 10^{-8} excited Li atoms per incoming electron at 150 °C. Even above 250°C no convincing similarities between both investigated species can be seen.

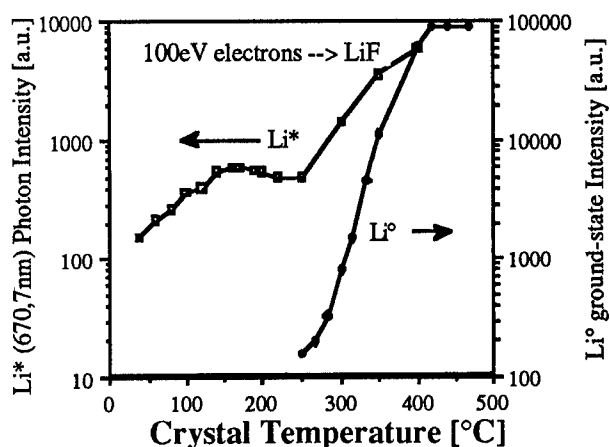


Fig.1: The dependence of the Li* (670.7nm) yield upon the crystal temperature is compared with the Li° yield, for electron bombardment with 100 eV and 500 eV, respectively.

The energy dependence of the desorption yield of excited Li atoms has been measured for both temperature regimes and is shown in Fig.2. Within the accuracy of our measurement the yield-electron energy curves are identical for both temperature regimes, which suggests that there is only

one underlying physical process over the whole investigated temperature range. Most important, an onset for desorption at around 60 eV has been found for both temperature regimes. Due to time dependent surface modifications and defect creation the absolute desorption yield above threshold is subject to variations, which explain the discrepancies.

The observed threshold correlates well with the Li^+ core-exciton levels of $\text{Li}^+(1s'2s)$ at 60.8 eV and for $\text{Li}^+(1s'2p)$ at 61.9 eV of Li in LiF¹⁴. No enhancement of the yield of excited Li atoms is observed at energies corresponding to the core-hole levels $\text{F}^-(2p)$ at 14.2 eV and $\text{F}^-(2s)$ at 38.2 eV. For comparison, a pronounced peak in the excited Li atom emission under photon irradiation at a photon energy of 61.5 eV has been found.

Based on these findings we propose a Knotek-Feibelman like¹⁵ mechanism for the desorption of excited Li atoms from LiF initiated by Li core electron excitations (core-excitons). During the inter-atomic Auger transition following the core exciton, the hole is filled by an electron from the valence band. The alkali ion, which desorbes from the surface, captures an electron into an excited state. This process will be explained in more detail.

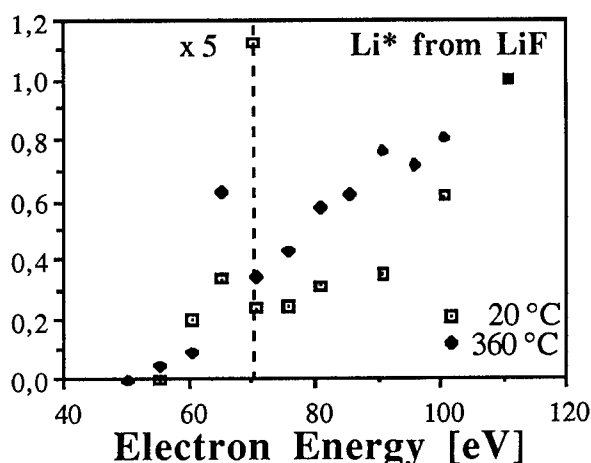


Fig.2: The dependence of desorbed Li^* from LiF on the electron energy is plotted. A clear onset is observed around 60 eV. Li^+ core-exciton levels are known: $\text{Li}^+(1s'2s)$ at 60.8 eV and for $\text{Li}^+(1s'2p)$ at 61.9 eV for Li in LiF.

In the temperature range up to 250°C the emission of excited Li atoms is sufficiently explained by this model. Above 250°C there are two possible explanations. Firstly, the alkali metal enrichment on the crystal surface is not a homogeneous layer, but the excess metal atoms aggregate to three-dimensional islands above the melting point of the alkali metal, i.e. 180°C for Li. Only on a clean crystal between these islands emission of particles due to the Knotek-Feibelman mechanism is possible. Therefore, the emission of excited atoms is prohibited in the area covered by these islands. With increasing temperature more and more pure alkali-halide crystal surface is exposed, because of increased evaporation and increased aggregation of Li atoms above the melting point of the alkali metal. Thus, the desorption yield of excited atoms is enhanced at higher temperatures.

As one impinging electron is sufficient for the desorption of an excited alkali atom, a linear dependence of the yield of excited Li atoms on the current density is expected.

Secondly, the evaporation increases the density of ground-state Li atoms in front of the crystal. These additional atoms could be excited by secondary electrons in the gas phase. The creation of secondary electrons and the evaporation as a consequence of defect generation are not correlated, but both depend on the current density. Therefore, the yield of excited Li atoms should increase proportionally to the square of the current density, at least in the temperature regime where evaporation is not limiting the desorption process. We have, however, found in both cases a linear dependence on the current density up to $1.3 \mu\text{A}/\text{mm}^2$ followed by saturation of the yield of excited Li atoms at higher current densities. Saturation will occur when all available sites for core excitation in the surface region are excited. As the number of these sites per surface area is a property of the crystal and does not change with temperature, the current density value, for which saturation is reached ($1.3 \mu\text{A}/\text{mm}^2$) is temperature independent. This is additional evidence that there is only one mechanism involved for the generation of excited states by ESD in the whole temperature range.

KCl and KBr: As the vapor pressure for K is high in the investigated temperature range, there is always considerable evaporation. Although our measurements were performed at different temperatures all are located in the second regime. For KCl and KBr the energy dependences of the excited K atoms are shown in Fig.3. Again a desorption threshold is observed. The value of 35 eV for both materials correlates with the $\text{K}^+(3s)$ core-exciton at 35.8 eV¹⁶. The K^+ core-exciton limit for $\text{K}^+(3p)$ at 7.16 eV seems to have no effect on the yield of excited K atoms. Also no correlation is found with Cl^- core-holes, $\text{Cl}^-(3p)$ at 9.3 eV and $\text{Cl}^-(3s)$ at 26.0 eV and the Cl^- exciton limits at 7.16 eV and 23.9 eV, respectively. The onset of the excited K atom yield at 35 eV is in sharp contrast with previous measurements. For the desorption yield of excited K atoms Pian et al. found an onset at 100 eV and further increase in the range of 180 - 200 eV, apparently not correlating with K core-excitations.

For KCl the dependence of the excited alkali atoms on the current density, again, is linear, equal to Li from LiF. The formation of three-dimensional islands was also found for KCl and KBr to occur above the melting point of the alkali metal.

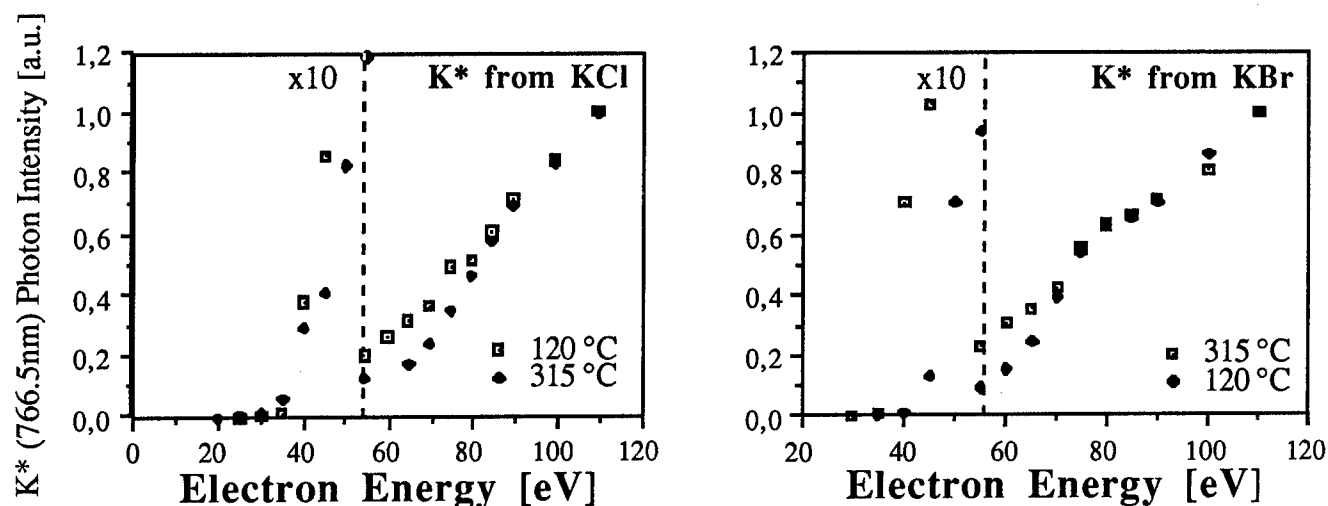


Fig.3: The dependence of desorbed K^* from KCl and KBr on the electron energy is plotted for 120 °C and 315°C. The desorption

onset is observed at 35 eV. The value of 35 eV for both materials correlates with the $K^+(3s)$ core-exciton at 35.8 eV.

Finally, it has to be mentioned that all energy dependent measurements were carried out using current densities well below the saturation regime. Furthermore, the linear current dependence is in contrast to the quadratic current dependence of the yield of excited alkali atoms found by Walkup et al. ⁶ and by Postawa et al. ⁵. A possible explanation for this discrepancy is that these authors used much higher electron energies in their measurements resulting also in a higher penetration depth and generally stronger surface modification and defect creation.

‡ Based on our experimental results we propose the following generation mechanism for excited alkali atoms. In this mechanism the deposition of energy and the subsequent channeling of the energy and converting into kinetic energy evolves in several steps:

. Provided that the primary electron has sufficient energy, the incident electron creates a core-exciton on the alkali-ion lattice site.

. This core-exciton decays via an interatomic Auger transition from a neighboring anion. Consequently, the anion is left in a singly or multiply positively charged state, as the excess energy is used for the release of valence electrons originally located on the anion. The electron itself, which was bound to the core-hole, can be i) released into the conduction band ii) trapped in a surface exciton iii) trapped in a surface state.

. On the surface the alkali ion captures an available electron, presumably from a location mentioned above, into an excited state or the ground state.

. Therefore the ionic bond to the crystal does not exist anymore, and the excited alkali atom leaves the surface.

In conclusion, the experimental results we have obtained show that a direct correlation exists between the creation of core-excitons on the alkali atom in an alkali lattice and the desorption of excited alkali atoms. The linear current dependence is further evidence for an intrinsic process for the desorption of excited atoms. Due to the complexity of the materials involved, in particular their tendency to surface charging, surface modifications, defect creation and the influence of prebombarding conditions contributions via different energy channels cannot fully be excluded and further investigations are needed.

The authors would like to acknowledge financial support by the Österreichische Fonds zur Förderung der wissenschaftlichen Forschung (project Nrs. 5833, 5577), the National Science Foundation (NSF) and the Office of Naval Research (under contract Nr. N00014-86-C-2546).

¹ P.D.Townsend, R.Browning, G.J.Garland, J.C.Kelly, A.Mahjoobi, A.L.Michael, M.Saidoh, Rad. Effects 30, (1976), 55-60

² N.Itoh, Nucl. Instr. Meth. B27, (1987), 155-166

³ M.Szymonski, Rad. Effects, 52, (1980), 9-14

⁴ J.P.Biersack, E.Santner, Nucl. Instr. Meth. 198, (1982), 29-32

- ⁵ Z.Postawa, J.Rutkowski, A.Poradzisz, P.Czuba, M.Szymonski, Nucl. Instr. & Meth. B18, (1987), 574-581
- ⁶ R.E.Walkup, Ph.Avoiris, A.P.Gosh, Phys. Rev. Lett. 57, (1986), 2227-2230
- ⁷ T.R.Pian, N.H.Tolk, J.Kraus, M.M.Traum, J.Tully, W.Collins, J.Vac. Sci. Technol., 20, (1982), 555-558
- ⁸ P.J.Feibelman, M.L.Knotek, Phys.Rev. B18, (1978), 6531-6539
- ⁹ G.M.Loubriel, T.A.Green, N.H.Tolk, R.F.Haglund Jr., J.Vac.Sci. Technol. B5, (1987), 1514-1518
- ¹⁰ R.E.Honig, RCA Review 23, (1962), 567-586
- ¹¹ W.Husinsky, P.Wurz, K.Mader, E.Wolfrum, B.Strehl, G.Betz, R.F.Haglund Jr., A.V.Barnes, N.H.Tolk, Nucl.Inst.&Meth. B33, (1988), 824-829
- ¹² P.Wurz, C.H.Becker, submitted in Surf. Sci.
- ¹³ R.F.Haglund Jr., R.G.Albridge, D.W.Cherry, R.K.Cole, M.H.Mendenhall, W.C.B.Peatman, N.H.Tolk, D.Niles, G.Margaritondo, N.G.Stoffel, E.Taglauer, Nucl.Instr. & Meth. B13, (1986), 525-532
- ¹⁴ A.Zunger, A.J.Freeman, Physics Letters 60A, (1977), 456-460 ;
A.Zunger, A.J.Freeman, Phy. Rev. B 16, (1977), 2901-2923
- ¹⁵ M.L.Knotek, P.J.Feibelman, Phys.Rev.Lett. 40, (1978), 964-967;
- ¹⁶ P.H.Citrin, T.Darrah Thomas, J.Chem.Phys. 57, (1972), 4446-4461

A Time-of-Flight Spectrometer for Medium Energy Ion Scattering

Marcus H. Mendenhall, Department of Physics and Astronomy, and

Robert A. Weller, Department of Materials Science and Engineering

Center for Atomic and Molecular Physics at Surfaces

P. O. Box 1807 B, Vanderbilt University, Nashville TN 37235

Abstract

We are developing a new time-of-flight particle energy spectrometer for use in the 10-200 keV/u range. This spectrometer is designed as a detector for Medium Energy Ion Scattering (MEIS) surface analysis. MEIS, when applied to the charged component of scattered particles, has been demonstrated to be a useful complement to Rutherford backscattering analysis (RBS) and low energy ion scattering (LEIS) in the elemental and structural analysis of surfaces and thin films. However, despite its demonstrated advantages, it has never come into widespread use because of the difficulty of energy analyzing uncharged particles in the relevant energy range of 10-250 keV. Our detector will be equally sensitive to both scattered ions and neutrals and calculations indicate that it will enable MEIS to rival conventional RBS in precision, speed and ease of use and to surpass it in sensitivity, surface specificity and depth resolution.

Introduction

The four most widely used tools for determining the composition of a surface are Auger electron spectroscopy (AES), secondary ion mass spectrometry (SIMS), low energy ion scattering (LEIS), also called ion scattering spectrometry (ISS), and Rutherford backscattering analysis (RBS). In each of these techniques, a probe beam of particles is directed onto the surface to be investigated. The interaction of one of these primary particles with the atoms of the material causes either the emission of a particle or the reflection of the primary particle. The analysis of this secondary particle's properties gives information about the surface.

Of the techniques noted, RBS most directly provides reliable quantitative information about the composition of the surface under study. (1,2) This is because in RBS the fundamental interaction is the Coulomb interaction between the nucleus of the primary ion and that of the surface atom with which it collides. This makes RBS much less sensitive to the chemical environment of the surface than the other techniques, all of which depend upon atomic phenomena for their effectiveness.

The literature on medium energy ion scattering (MEIS) through the mid 1970s has been reviewed by Buck.³ A significant motivating factor for much early MEIS work was the need to understand neutralization in scattering in order to interpret the results of data obtained with electrostatic analyzers. A significant advance in developing a spectroscopy uniting the advantages of RBS and LEIS has been made by Saris's group at the FOM Institute for Atomic and Molecular Physics in the Netherlands⁴ following earlier work by van Wijngaarden *et al.*⁵ and Feuerstein *et al.*⁶ The intrinsic lower limit of primary beam energies for which RBS retains its quantitative accuracy is determined by the deviation of the true cross section from the Rutherford value. For an incident beam of protons this limit is around 30 keV. However, the effective limit is set by the resolution of the detector used. The only detectors which are common today are solid state Si surface barrier detectors. These devices are simple, accurate and inexpensive, but even the best have α particle energy resolutions of about 10 keV. This relatively high value sets a lower limit on the energy of the beam of several hundred keV. The Dutch group avoids this difficulty by using a large electrostatic spectrometer which can analyze scattered ions when the incident projectile is typically 50-200 keV.⁷

In this paper a new detector is described which preliminary calculations indicate will lead to reliable ion scattering analyses using proton beams with energies as low as 20-40 keV. It is based upon a time-of-flight technique which was developed for use in nuclear physics^{8,9} and which more recently has been applied in heavy ion RBS.¹⁰⁻¹⁵ In our detector, the start pulse is produced by a microchannel plate detecting the secondary electrons from a 1 $\mu\text{g}/\text{cm}^2$ carbon foil, and the stop pulse is produced by the impact of the backscattered particle on another microchannel plate.

The time-of-flight technique will be superior to the current procedure using electrostatic analyzers in two very important respects. First, the time-of-flight method will be sensitive to both scattered neutrals and ions whereas the electrostatic analysis detects only ions. This becomes increasingly important as the energy of the beam is decreased. Second, the time-of-flight technique is inherently capable of analyzing the flight time of each particle that enters the sensitive solid angle and will be much faster (or, equivalently, less invasive) than single channel detectors such as electric and magnetic sectors. When compared with conventional RBS, it is also expected to be more surface specific (since the range of the primary ions in the target is shorter and the stopping power higher), and to have a depth resolution of perhaps as little as 0.6 nm. [van Wijngaarden, ref. 5] In addition, using 50 keV protons it will be about 400 times more sensitive than conventional RBS with 2 MeV He^+ because of the larger cross section at lower energies.

Spectrometer Design

A schematic diagram of the prototype of the Mark I spectrometer is shown in Fig. 1a. This prototype is currently being constructed at Vanderbilt. Ions which have been scattered from the target surface in the direction of the detector pass through the first of two grids held at ground potential and then through a $1 \mu\text{g}/\text{cm}^2$ self-supporting carbon foil which is at a potential of -1 to -5 kV. As the backscattered ion exits the foil it causes the emission of secondary electrons which are accelerated by the electric field between the foil and the second grid. The electrons subsequently strike the microchannel plate detector and generate a start pulse. Meanwhile, the backscattered ion continues past the second grid to be stopped by collision with a second microchannel plate which generates a stop pulse. The time interval between the start and stop pulses is measured by a time to digital converter and a time-of-flight spectrum is accumulated by the data acquisition computer. Our spectrometer will have a 50 cm ion flight path and a 15 cm electron flight path. The electrons will be accelerated to a transport energy of 3 keV. Because of the short flight distance of the electrons, no electrostatic focussing will be needed to assure that they strike the microchannel plate detector. We are using Galileo FTD-2003 microchannel plates (a

chevron plate designed for saturated pulse operation) with their special 50Ω anode designed for fast timing applications. The data acquisition will be performed by an Apple Macintosh II computer driving a CAMAC crate through an IEEE-488 bus.

Figure 1b shows the design for the Mark II detector which we will test when we have completed construction of the mark I version. The Mark II design will dispense with off-axis electron detection, which is used in the Mark I to allow the electron detector to be close enough to the foil so that it subtends a large enough angle to permit collection of all of the emitted electrons. Instead, the electrons will be transported over the same path as the heavy particles, and will be confined by a weak electrostatic lens. This design will substantially simplify the spectrometer, but does require careful design of the electron optics. The lens used must be as weak as possible so that it does not significantly affect the trajectories of the heavy particles, since not all of the particles will be charged and any electric fields could destroy the insensitivity of our system to charge state. In the design of our system, the electrons being transported will have energies no greater than 5 keV, and the heavy particles will have energies typically in excess of 50 keV; thus, a lens sufficiently strong to confine the electrons should not strongly influence the higher energy heavy particles.

For most particle scattering spectroscopies, three important figures of merit are the energy resolution of the detector, the solid angle of the detector, and the scattering cross section. For the MEIS technique, the scattering cross section σ is quite large compared with the cross sections typically encountered in MeV He scattering. What a new detection scheme must provide is a large solid angle and good energy resolution. For typical MeV particle scattering systems, an energy resolution of about 1% (15 keV at 1.5 MeV) is considered very good, and solid angles of around 10^{-3} sr are typical. Our detector should, without difficulty, be capable of subtending a solid-angle $d\Omega$ of order 10^{-4} , and a $\sigma d\Omega$ (hence total sensitivity) exceeding substantially that of MeV He scattering. The remaining parameter to be addressed is, then, the resolution.

The resolution of the system we are building will be affected by a number of variables: the acceleration time of the secondary electrons; the flight time of the secondary electrons; the intrinsic timing resolution of the electron detector; the energy loss of the particle traversing the carbon foil; the intrinsic timing resolution of the ion detector; and the intrinsic timing resolution of the pulse amplifiers, discriminators and time-to-digital converter. The apparent flight time t_f of a particle in the system is

$$t_f = \frac{L}{\sqrt{2(E_0 - \Delta E)/m_1}} - t_e$$

where t_e is the electron flight time, E_0 is the scattered particle kinetic energy, ΔE is the energy lost by the particle in the carbon foil, m_1 is the scattered ion mass (assumed exact), and L is the flight distance.

$$E_0 = \frac{m_1 L^2}{2 (t_f + t_e)^2} + \Delta E$$

Thus, the fractional energy resolution is

$$\left\{ \frac{\delta E_0}{E_0} \right\}^2 = 4 \left\{ \frac{\delta L}{L} \right\}^2 + \frac{4}{(t_f + t_e)^2} \{ (\delta t_f)^2 + (\delta t_e)^2 \} + \left\{ \frac{\delta \Delta E}{E} \right\}^2$$

where $\delta \Delta E$ is the rms energy straggling in the foil, δt_f is the rms uncertainty in the stop pulse time, δt_e is the rms uncertainty in the start pulse time, and δL is the rms uncertainty in the flight path length. For the Mark I spectrometer, the uncertainty in flight path is dominated by the difference in flight path due to the angle Θ between the start foil and the stop detector. A simple integration yields an rms value $\delta L = \frac{r}{2} \sin \Theta$ where r is the radius of the start foil aperture. In the Mark II model, the foil is parallel to the detector, so the only uncertainty is due to real flight path differences, which are insignificant.

We calculate, based on simple kinematics for the electrons and on the specified timing resolution of our electronics, that the system will have a timing resolution δt_c for the start pulse of about 150 picoseconds. When this is combined with the uncertainty due to straggling in the foil, we get energy resolutions $E/\Delta E$ which range from around 200 to around 400, depending on the species scattered. Thus, the technique has a resolution greatly exceeding that available with Si surface barrier detectors, which have maximum resolutions of about $E/\Delta E=100$ for 2 MeV Helium ions and much lower resolutions at lower energies and with heavier ions.

The resolution of a scattered particle detector affects its ability to measure a number of different properties of a surface. First, it will affect the depth resolution attainable, although this resolution is often limited by factors other than the detector. Second, it will affect the mass resolution, *i.e.* the ability of the system to distinguish the masses of the species on the surface from which the particle was scattered. The energy lost by a particle in a single binary collision is

$$\Delta E = E_i \frac{4 m_1 m_2}{(m_1 + m_2)^2} \sin^2(\Theta/2)$$

where m_1 is the mass of the scattered particle, m_2 is the mass of the target particle, and Θ is the center-of-mass scattering angle. When $m_2 \gg m_1$, ΔE is small so one finds that for a given energy resolution, mass resolution decreases with increasing mass. Thus, a figure of merit for mass resolution is the highest mass at which $\Delta m=1$ can be distinguished. Referring back to the above formula, one can convert a given mass resolution into an energy resolution. This can then be related through velocity to the intrinsic timing resolution of the spectrometer and the energy spread of the scattered particles produced by their passage through the foil in the detector. In the discussion and computations below, we predict the resolution of the spectrometer, both as $E/\Delta E$ and as the mass at which $\Delta m=1$ is just resolved.

The timing uncertainty in the acceleration and transport of the secondary electrons depends on their initial energy distribution, the acceleration voltage, the distance over which the acceleration

occurs, and the length of the drift region between the acceleration grid and the electron detector. As all of the distances in the problem are made smaller and the voltages larger, the timing uncertainty due to the initial energy distribution of secondary electrons from the start foil decreases; however, mechanical and electrical considerations limit the ultimate size and voltage that can be achieved. The actual timing calculations are done using the trivial kinematic formulas from classical physics, which are exact for this calculation.

The time required for an electron to travel from the start foil to the end of the acceleration region is computed by solving the quadratic

$$d = \frac{a t^2}{2} + v_0 t = \frac{q_e E}{2 m_e} t^2 + \sqrt{2 T_0 / m_e} t = \frac{q_e V_0}{2 m_e d} t^2 + \sqrt{2 T_0 / m_e} t$$

where d is the distance from the foil to the accelerating grid, V_0 is the acceleration voltage, T_0 is the initial kinetic energy of the electrons and m_e and q_e are the electron mass and charge, respectively.

This can be more conveniently recast in natural units with $q_e=1$, $m_e = 511 \text{ keV}/c^2$, and T_0 expressed in eV to yield

$$\frac{V_0 c^2}{2 (m_e c^2) d} t^2 + \sqrt{\frac{2 T_0}{m_e c^2}} t - d = 0$$

Let the solution of this equation, obtained by the quadratic formula, be designated t_1 . The drift time between the accelerating grid and the detector can be computed from the total kinetic energy of the electron. The energy after acceleration will be $T=T_0+V_0$ (in eV) and the drift speed will be

$$v_d = c \sqrt{\frac{2 (T_0 + V_0)}{m_e c^2}} \text{ and the flight time, } t_2, \text{ will be } t_2 = \frac{l}{v_d}$$

where l is the distance between the grid and the detector. Then, $t \equiv t_1+t_2$ is the total electron flight time and $t(T_0=0)-t(T_0=\text{max secondary energy})$ is our estimate of the timing spread attributable to the secondary electron energy distribution. The more conventional technique of expanding a Taylor series to get $\frac{\partial t}{\partial T_0}$ doesn't work well here since $\frac{\partial t_1}{\partial T_0}$ is infinite at $T_0=0$.

If we assume an initial energy spread of 20 eV for the secondary electrons, an acceleration distance of 1 cm, an acceleration voltage of 2 kV, and a drift path of 20 cm, the total timing uncertainty is 110 ps. The actual electron flight time, including acceleration, is 8.3 ns. The assumption of a 20 eV secondary electron energy spread is probably conservative; it is likely to be smaller. In Table 1, we use a 150 ps total timing resolution δt_e .

The precision in measuring the scattered particle's flight time is also limited by the uncertainty in the energy loss of the particle in the foil used to generate the start pulse. This uncertainty contains two terms, one due to the intrinsic variation in energy loss known as straggling, the other due to variations in the foil thickness. For the foils we are using ($1 \mu\text{g}/\text{cm}^2$ of carbon), we estimate for 50 keV deuterons a total energy loss of about 590 eV, with a variation due to straggling of about 132 eV. The uncertainty due to variations in the thickness of the foil can be estimated at 5% of the total energy loss, based upon the manufacturer's guarantee of uniformity of the foils. Adding the two uncertainties in quadrature yields a final estimate for the resolution for the detector. As can be seen in table 1, the resolution $E/\Delta E$ can approach 400, and is above 300 for many beams. If this resolution is achieved, it will be unprecedented for charge-state-independent detection of particles in this energy range and will allow extremely high quality backscattering spectra to be collected. Some features of this table are important to highlight. First, note the cross section for 100 keV deuterons on gold is $7.6 \times 10^{-6} \text{ \AA}^2$; for comparison, the cross section for 2 MeV He is $6.8 \times 10^{-8} \text{ \AA}^2$, a factor of 100 smaller. Another important feature is the very high value for the unit mass separation limit, m_1 , that can be realized using heavy ions. For a Li beam at 300 keV (which will be routinely available with our accelerator), we predict a unit mass separation at masses as high as 80 u. This is extremely difficult, if not impossible, to do using conventional RBS or even heavy-ion RBS at the normal energies used with Si surface barrier detectors.

Conclusion

Time-of-flight Medium Energy Ion Scattering promises to be a technique capable of providing unprecedented sensitivity and resolution for surface analysis. It will provide detailed structural information in conjunction with channeling and blocking techniques. Because of the large scattering cross-section, lower total beam fluences will be required and surface damage induced by the analyzing beam will be minimized. In addition, it will provide better resolution and simpler operation than pulsed-beam time-of-flight measurements, since it is very difficult to perform pulsed-beam worked with resolution much better than 1 nanosecond.

Acknowledgement

Support for this project has been provided by the School of Engineering, the College of Arts and Science, and the University Research Council at Vanderbilt University.

Table 1

Table 1						
m	z	E(keV)	E/ ΔE	m_1	E_B	$\sigma (10^{-8} \text{\AA}^2)$
1.	1.	25.	230.	28.	28.	9663.
1.	1.	50.	290.	32.	56.	2942.
1.	1.	100.	301.	32.	111.	806.
1.	1.	200.	253.	29.	225.	206.
2.	1.	50.	338.	48.	58.	2754.
2.	1.	100.	400.	52.	114.	768.
2.	1.	200.	351.	49.	230.	197.
4.	2.	300.	370.	71.	364.	311.
6.	3.	300.	328.	82.	385.	606.
10.	5.	1000.	322.	105.	1386.	135.
12.	6.	1000.	312.	114.	1435.	180.
16.	8.	1000.	265.	122.	1569.	262.
28.	14.	3000.	283.	167.	5350.	69.
35.	17.	4000.	281.	187.	7643.	49.

TABLE 1: Predicted resolution and sensitivity of the detector for various beam species: m =mass of the scattered particle, z =charge of scattered particle, $E(\text{keV})$ =energy of scattered particle, $E/\Delta E$ =resolution of detector, m_1 =the highest target nuclide mass for which $\Delta m=1$ should be resolvable, E_B =the incoming beam energy required to produce a scattered particle of energy $E(\text{keV})$ from a target nucleus of mass m_1 , $\sigma(\text{Au})$ =the cross section, in \AA^2 , for scattering a particle of energy E_B from an Au nucleus at 135° ; provided for comparison. These cross sections are computed from the ZBL universal potential¹⁶ to include corrections for non-Rutherford scattering.

Figure 1 Caption

Schematic of time-of-flight detector design, showing a) the Mark I prototype design and b) the Mark II design.

References

- ¹ H-J. Grossmann and L.C. Feldman, Materials Analysis with High Energy Ion Beams Part I: Rutherford Backscattering, *ibid.*, p. 26.
- ² W-K. Chu, James W. Mayer and M-A. Nicolet, **Backscattering Spectrometry**, (Academic Press, New York, 1978) Chap. 2.
- ³ T.M. Buck, "Neutralization Behavior in Medium Energy Ion Scattering", in **Inelastic Ion-surface Collisions**, ed. N.H. Tolk, J.C. Tully, W. Heiland and C.W. White (Academic Press, New York, 1977) 47.
- ⁴ W.C. Turkenburg, H.H. Kersten, B.G. Colenbrander, A.P. de Jongh and F.W. Saris, "Experimental Parameters for Quantitative Surface Analysis by Medium Energy Ion Scattering", *Nucl. Instr. and Methods* **138** (1976) 271.
- ⁵ A. van Wijngaarden, B. Miremadi and W.E. Baylis, "Energy Spectra of keV Backscattered Protons as a Probe for Surface-Region Studies", *Can. J. of Physics* **49** (1971) 2440.
- ⁶ A. Feuerstein, H. Grahmann, S. Kalbitzer and H. Oetzmann, "Rutherford Backscattering Analysis with Very High Depth Resolution Using an Electrostatic Analyzing System" in **Ion Beam Surface Layer Analysis**, O. Meyer, G. Linder, and F. Kappeler, eds., (Plenum Press, New York, 1976) 471.
- ⁷ R.G. Smeenk, R.M. Tromp, H.H. Kersten, A.J.H. Boerboom and F.W. Saris, "Angle Resolved Detection of Charged Particles with a Novel Type Toroidal Electrostatic Analyzer", *Nucl. Instr. and Methods* **195** (1982) 581.
- ⁸ G. Gabor, W. Schimmerling, D. Greiner, F. Bieser and P. Lindstrom, "High Resolution Spectrometry for Relativistic Heavy Ions", *Nucl. Instr. and Methods* **130** (1975) 65.
- ⁹ J.D. Bowman and R.H. Heffner, "A Novel Zero Time Detector for Heavy Ion Spectroscopy", *Nucl. Instr. and Methods* **148** (1978) 503.

-
- 10 A. Chevarier, N. Chevarier and S. Chiodelli, "A High Resolution Spectrometer Used in MeV Heavy Ion Backscattering Analysis", Nucl. Instr. and Methods **189** (1981) 525.
 - 11 A. Chevarier and N. Chevarier, "Time of Flight Spectrometer in Heavy Ion Backscattering Analysis", Nucl. Instr. and Methods **218** (1983) 1.
 - 12 J. P. Thomas, M. Fallavier, D. Ramdane, N. Chevarier and A. Chevarier, "High Resolution Depth Profiling of Light Elements in High Atomic Mass Materials", Nucl. Instr. and Methods **218** (1983) 125.
 - 13 A. Chevarier, N. Chevarier, M. Stern, D. Lamouche, P. Clechet, J.R. Martin and P. Person, "Heavy Ion Rutherford Backscattering Analysis Used to Study the Alloyed Metal/GaAs Interface", Nucl. Instr. and Methods **B13** (1986) 207.
 - 14 P. Person, A. Chevarier, N. Chevarier, P. Clechet, D. Lamouche, J.R. Martin and M. Stern, "Rutherford Backscattering Analysis of GaAs-Oxide Interface", Nucl. Instr. and Methods **B15** (1986) 425.
 - 15 J.P. Thomas, M. Fallavier and A. Ziani, "Light Elements Depth-Profiling Using Time-of-Flight and Energy Detection of Recoils", Nucl. Instr. and Methods **B15** (1986) 443.
 - 16 J. F. Ziegler, J. P. Biersack, and U. Littmark, *The Stopping and Ranges of Ions in Solids* (Pergamon Press, New York, 1985) Chapter 2.

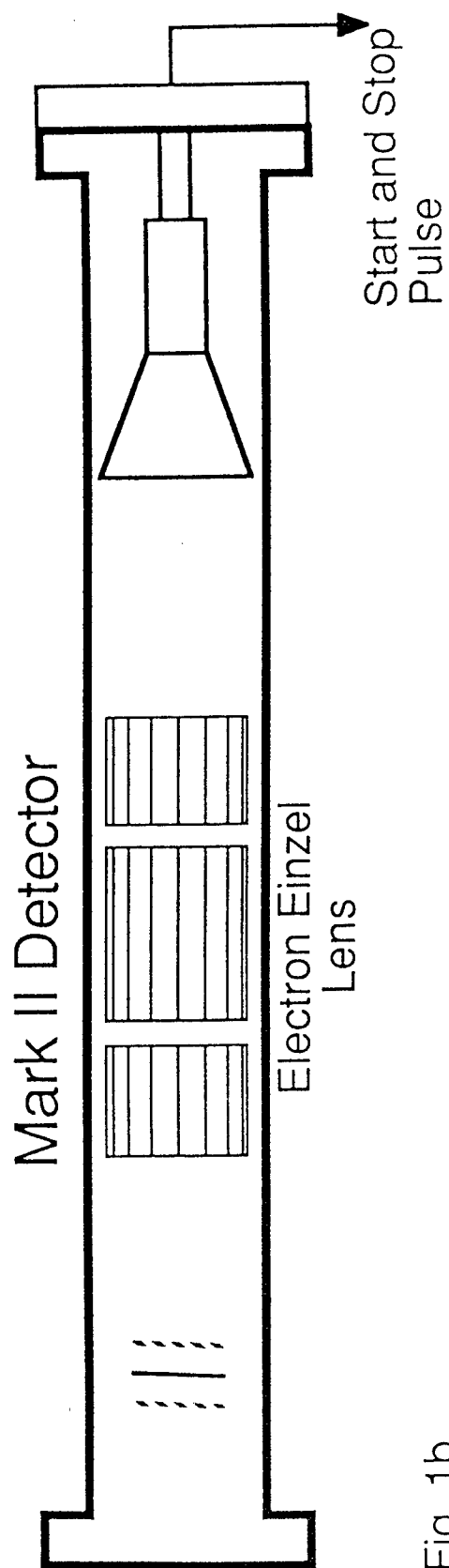
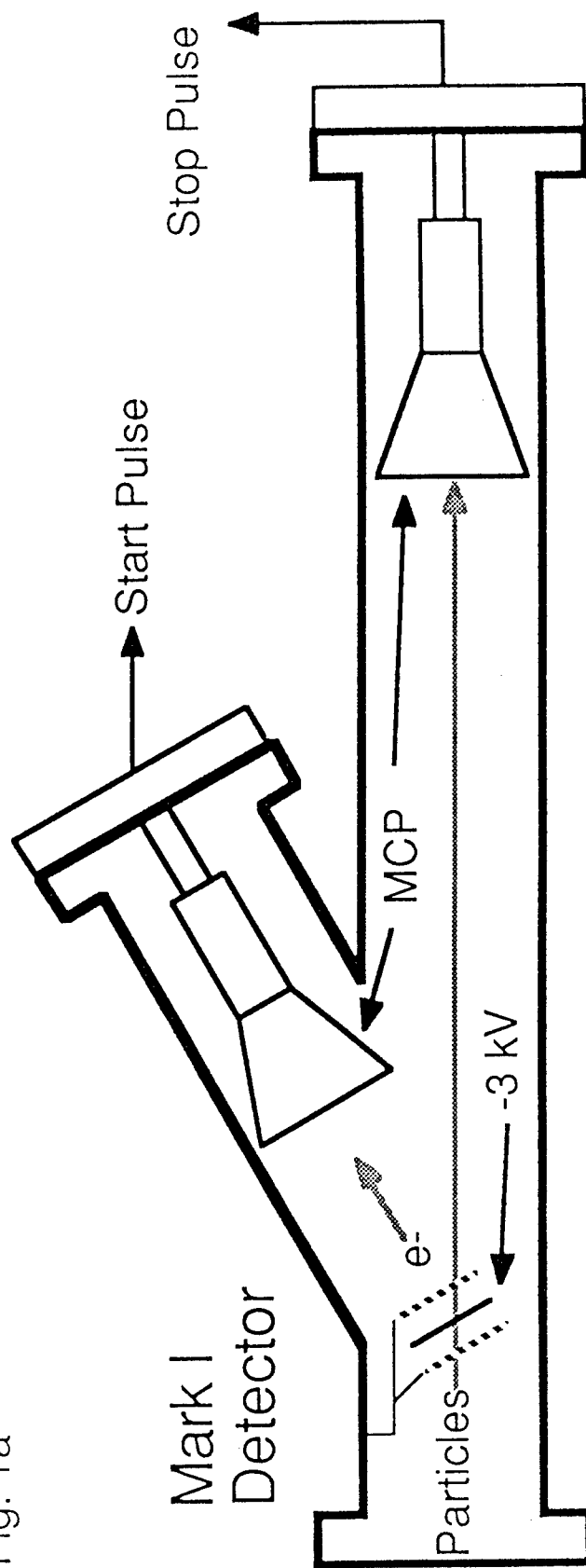


Fig. 1b

Fig. 1a



SURFACE ELECTRON SPECTROSCOPY

ROYAL ALBRIDGE / SALIM BANNA
Center for Atomic and Molecular Physics at Surfaces
Vanderbilt University, Nashville, TN

One of the goals of the experimental and theoretical efforts of CAMPS research is to determine the means by which energy incident on either a clean or overlayered surface is adsorbed, partitioned and localized in ways that result in a number of phenomena such as desorption and sputtering. Our experimental measurements have consisted primarily of visible and/or infrared spectra recorded by grating spectrometers looking at, or just in front of, the surface; and recently we have expanded this effort by the addition of an ultraviolet spectrometer. We are now adding the capability of recording electron and electron energy - loss spectra. The new equipment consists of three 106° spherical-sector ($r = 3.5$ cm) electrostatic spectrometers, which have an energy resolution of 10 meV at 2 eV and are bakable to 450° C. These spectrometers will provide the means by which four types of electron spectra can be measured: Auger-, photoelectron-, electron energy loss- and electron emission-spectra.

Auger electrons are produced when the surface is irradiated with electrons or photons; the resulting spectra provide qualitative information regarding the composition of the surface. Photoelectron spectra provide a special type of qualitative analysis because not only do the positions of the peaks identify the elements, but also small shifts in the positions of the peaks indicate the chemical environment in which the elements reside. An electron energy-loss spectrum is recorded by a high-resolution electron spectrometer when a highly monochromatized beam of electrons is reflected from the surface. The incident beam of electrons loses energy to various types of excitation of the surface and its adsorbates and this energy loss is recorded by the high-resolution spectrometer. This technique requires two electron monochromators: one to create the incident beam and one to record the reflected beam. In our work these three types of spectra will be used to determine the composition of the surface and the nature of its overlayers. Since such information is essential to all surface studies, these techniques will be widely used. For example, our studies of grazing-incidence and tilted-foil neutralization, which involves both pure and overlayered surfaces, require a complete and detailed analysis of the nature of the surfaces and their overlayers. Also, electron energy loss spectra may help shed light on the nature of the surface and its adsorbates in our studies of molecular species that reside on surfaces.

The spectroscopies discussed above will be used primarily as analytical tools to characterize surfaces before, during and after the primary experiments. The primary experiments themselves consist of the excitation of surfaces by particles or photons and these excitations will in most cases cause the emission of electrons; hence during the primary experiment the recording of electron emission spectra, as well as photon emission spectra, is essential if all channels of energy partitioning are to be investigated. Furthermore, the final states of species leaving a surface can be determined in part by electron processes such as the Auger effect and the emission of secondary electrons. Therefore a complete bookkeeping of energy partitioning and a complete analysis of modes of final-state production require that electron emission spectra as well as electromagnetic spectra be recorded. For example, our efforts to deduce the mechanisms by which final states are produced when M^* and M^0 desorb from alkali halides will be facilitated by the recording of electron spectra.

We conclude that our capability to record electron spectra will greatly enhance our ability to deduce the micro-scale dynamics of surface processes. We plan for the new equipment to be operational in April of 1989.

Interactions of Hyperthermal Ions at Metal Surfaces

B.H. Cooper, D.M. Goodstein, G.A. Kimmel, R.L. McEachern

Laboratory of Atomic and Solid State Physics

Cornell University, Ithaca, NY 14853

Abstract

We are investigating the interactions of hyperthermal energy ions with clean and adsorbate-covered metal surfaces. In this summary we present energy spectra for 56eV to 4keV Na^+ scattered in-plane from Cu(110) along the $\langle 1\bar{1}0 \rangle$ and $\langle 001 \rangle$ azimuths. The measured spectra are compared to classical trajectory simulations to extract information about scattering trajectories and scattering potentials for the hyperthermal Na^+ beams. We have also investigated the neutralization of scattered potassium beams from Cu(110) with Cs overlayers. These results are compared to a model of resonant charge transfer at surfaces.

I. INTRODUCTION

The types of interactions which occur when an energetic atom or ion beam encounters a surface are varied, and are determined in large part by the incident beam energy. Traditionally, most experiments that measure energy and angular distributions of the scattered particles have used either neutral thermal beams, which diffract from the corrugated potential of the whole surface, or higher (kiloelectronvolt) energy beams, whose interaction with the surface can be described as classical sequential binary collisions between the incident ion and individual surface atoms. Between these two extremes is the important and relatively unexplored hyperthermal energy regime (incident energies below 500 eV).^{1,2}

We are investigating hyperthermal energy ion scattering from clean and adsorbate-covered metal surfaces. In this summary we compare experimental spectra of Na^+ scattered from Cu(110) to simulations using a computer code that calculates classical trajectories. From such comparisons we extract information about the ion-surface interaction potentials and trajectories.

Using K^+ scattered from Cu(110) with low coverages of Cs adsorbates, we have also investigated electron transfer processes which result in neutralization of the scattered particles. These data are compared to a model of resonant charge transfer at surfaces.

In section II we give a brief description of the experimental procedure. Results are presented in section III as a series of expanded figure captions. Section III is intended to give an overview of some of our major experimental findings, all of which are reported elsewhere with additional data and discussion. References are given where appropriate. We conclude with a brief summary.

II. EXPERIMENTAL PROCEDURE

These experiments were performed in a UHV scattering chamber which has been described in detail elsewhere.³ The alkali ion beams are produced by thermal emission from a hot alkali-embedded tungsten source.⁴ The ions are mass-selected with a Wien filter. A 90° spherical electrostatic analyzer is used to accurately monitor the energy of

the beam and to reject any neutral particles produced by the source. The energy of the beam on target can be varied from approximately 10 eV to several keV.⁵ For the energy region between 100 eV and 400 eV the beam on target had a current of several nanoamps in a 2-3 mm diameter beam spot, and an energy spread characteristic of the thermal source (less than 0.5 eV). The half-angle divergence of the beam was less than 2°.

Scattered ions are detected with a rotatable 180° spherical electrostatic analyzer with an energy resolution of 1% and an angular acceptance of 1° half-angle. The Cu(110) sample was mounted on a manipulator with three degrees of rotation, allowing us to detect ions scattered into any outgoing direction except those excluded by the finite size of the detector and beam lenses. For the results summarized in this paper, the spectra were measured with the beam and detector aligned for in-plane scattering along the $\langle 1\bar{1}0 \rangle$ and $\langle 001 \rangle$ azimuths of the Cu(110) crystal. The total scattering angle and incident beam angle relative to the crystal normal were accurate to 0.1°. LEED and ion scattering were used to align the scattering plane to within $\pm 0.5^\circ$.

The Cu crystal was routinely cleaned by 500 eV Ar⁺ sputtering followed by annealing at 550°C. An SAES getter was used to deposit Cs adsorbates for the charge transfer measurements. The Cs coverage was calibrated using Auger. The work function of the cesiated surface was measured using the LEED system in a retarding field configuration. The spectra were carefully monitored for sputter damage by the incident beam. The doses were kept small between anneals in order to avoid depositing alkalis on the surface from the incident beam. More details of this procedure are reported elsewhere.⁶

III. RESULTS

As stated in the introduction, all of the results discussed here are reported elsewhere in more detail. In this section we summarize our major experimental findings as a series of expanded figure captions.

Figure 1

Figure 1 shows a series of energy spectra for Na⁺ scattered from the Cu(110) surface

along the $\langle 1\bar{1}0 \rangle$ and $\langle 001 \rangle$ azimuths.⁷ The vertical axis is scattered intensity. For each spectrum the intensity is arbitrarily normalized and offset for clarity. The horizontal axis is the energy of the scattered ions E divided by the energy of the incident ions E_0 . The spectra have been corrected for the $1/E$ transmission function of the spherical analyzer. The incident beam energy varies from 56 eV to 4 keV. In all cases a 90° specular scattering geometry is used (see figure 1).

Figure 1 shows the atomic positions on the Cu(110) surface. The $\langle 1\bar{1}0 \rangle$ and $\langle 001 \rangle$ azimuths have different spacings along the chains of atoms and between adjacent chains of atoms. Spacings between atoms are 3.61\AA and 2.55\AA for the $\langle 001 \rangle$ and $\langle 1\bar{1}0 \rangle$ azimuths, respectively.

The two sets of energy spectra demonstrate that ion scattering trajectories are very sensitive to surface structure and beam energy. Looking first at the spectra for the $\langle 1\bar{1}0 \rangle$ azimuth, we can describe the energy spectra as follows. Note first that the second layer chains of atoms are exposed on the fcc(110) surfaces. For incident ion energies of 400 eV and below most of the detected ions in figure 1 have scattered from the second layer chains of atoms, after having undergone "focused scattering" trajectories. A simple explanation of focusing can be obtained by considering the different impact parameters that will result in in-plane scattering. Impact parameters located precisely along either top layer or second layer chains of atoms will scatter in-plane. For top layer scattering, where there is no focusing, an impact parameter slightly off the chain will experience out-of-plane forces and scatter away from the detector. For second layer scattering, the ion experiences small angle collisions with the top layer atoms in adjacent chains, both on the incoming and outgoing parts of the trajectory. For impact parameters slightly off the second layer chains, these small angle collisions involve out-of-plane forces that focus the particle toward the second layer chain on the incoming trajectory and toward the scattering plane on the outgoing trajectory. The range of impact parameters that will result in focused in-plane scattering depends on the surface geometry and the interaction potentials that describe the scattering.

The higher energy peaks ($E/E_0 \lesssim 0.64$) in the $\langle 1\bar{1}0 \rangle$ spectra are primarily from quasi-double scattering events. These are ions that scatter through two roughly equal angle

collisions from adjacent atoms in the chains. The lower energy peaks ($E/E_0 \gtrsim 0.46$) are from quasi-single scattering events. The slight shift in E/E_0 as the incident energy is decreased results from the behavior of the focused single trajectories. These focused trajectories scatter from the tails of the potentials of first layer atoms on the incoming and outgoing trajectories. As the beam energy is lowered the ions become increasingly sensitive to the long range part of the potential and scatter more strongly from the first layer atoms. For a fixed total scattering angle, this reduces the principal scattering event from a second layer atom, which results in less energy loss.

In the $\langle 001 \rangle$ azimuth, at 1 keV and below the scattering is also primarily from second layer chains. The higher energy peaks are from quasi-double scattering events. The lower energy peaks are due to quasi-single scattering. Unlike the $\langle 1\bar{1}0 \rangle$ spectra, the top layer singles and the second layer focused singles are separately resolved for beam energies of 400 eV and lower. The value of E/E_0 for the focused single peak is also seen to vary dramatically with incident beam energy, ranging from ≈ 0.46 for 4 keV Na^+ to 0.57 for 56 eV Na^+ . This trend, which was not observed in the $\langle 1\bar{1}0 \rangle$ spectra, results from the fact that the atomic chains are much closer together in the $\langle 001 \rangle$ azimuth than in the $\langle 1\bar{1}0 \rangle$ azimuth. The interaction with the first layer atoms is thus much stronger for focused trajectories in the $\langle 001 \rangle$ azimuth, which causes the trajectory to be strongly dependent on the incident beam energy.

These trajectories are analyzed in more detail elsewhere.⁷

Figure 2

In order to model the scattering at hyperthermal energies, an interaction potential must be used that can reproduce the strong energy dependent focusing effects observed in the spectra presented in figure 1. Figure 2 shows the agreement between measured and simulated spectra for the 100, 200, and 400 eV Na^+ beams. The simulations are classical trajectory calculations⁸ using a potential constructed from a sum of Na^+/Cu diatomic potentials calculated in the Hartree-Fock approximation, plus an added image potential that depends only on perpendicular distance from the surface. The only adjustable parameter

in the potential is the depth of the image well at $z=0$ (3eV). Thermal vibrations of the Cu surface atoms and the oscillatory relaxation of the Cu(110) surface were included.⁹

We have found similar agreement using Hartree-Fock potentials to model K^+ scattering from Cu(110).¹⁰ Other experimental studies of hyperthermal alkali scattering report agreement between experiment and simulation using Hartree-Fock-Slater potentials.^{11,12}

Figure 3

Figure 3a shows the 100, 200, and 400 eV Na^+ spectra for the $\langle 001 \rangle$ azimuth with simulations using two interaction potentials. One is the same potential described in figure 2. The other is constructed from a sum of ZBL Na/Cu pair potentials.¹³ The ZBL potential has been used to give good agreement with scattering data for keV ions.¹⁴

Figure 3b shows a comparison of the Hartree Fock and ZBL pair potentials for separations of 0.6 to 2.0 Å. Note that these two potentials are similar for small separations, but deviate from one another at separations on the order of 1-1.5 Å. An ion scattering from a second layer chain of atoms will sample the potential tails of the first layer atoms at similar distances. Figure 3a shows that the focused scattering from Cu(110) is very sensitive to the tails of the pair potentials used in the simulations.

Figure 4

Figure 4 shows a series of energy spectra for 90° specular scattering of 100 eV K^+ ions from Cu(110) along the $\langle 1\bar{1}0 \rangle$ azimuth.⁶ The vertical axis is the scattered ion intensity, which has not been corrected for the $1/E$ dependence of the analyzer transmission function. The solid curve in figure 4a is for scattering from the clean Cu(110) surface. Each of the dashed curves corresponds to the spectrum measured from the Cu(110) surface with a different coverage of Cs adsorbates. In each spectrum the same incident K^+ dose is used. The work function measured for the different Cs coverages is given in the inset to figure 4a. The scattered K ion intensity is approximately zero for a work function of 3.13 eV, which corresponds to a Cs coverage of $\theta \lesssim 1/10$. The decrease in the scattered ion intensity can be attributed to the Cs-induced increase in the neutralization probability of the scattered

potassium by resonant electron transfer.¹⁵

Each spectrum from figure 4a is normalized by its integrated intensity and plotted in figure 4b. Figure 4b shows that the neutralization probability is independent of the velocity of the scattered ion. Furthermore, there are no new peaks apparent in the spectrum as the Cs coverage increases. There are several reasons for this. First the Cs coverages are very low and therefore very few of the ions scatter directly from adsorbates. Second, the energy for quasi-single scattering off a cesium adsorbate lies within the quasi-double peak of the copper substrate. Also, if local variations in the electrostatic potential from the Cs overlayer are important in the charge transfer process, one would expect ions scattering from areas around the adsorbate sites to be preferentially neutralized and thus not detected.

Figure 5

Figure 5a is a plot of the intensity of scattered K^+ (for 100 eV incident energies) as a function of the measured work function. The vertical axis corresponds to the integrated counts in an energy spectrum (with Cs adsorbates) divided by the integrated counts in the clean surface spectrum (no Cs adsorbates). The horizontal axis gives the measured work function for the Cs overlayer of the corresponding energy spectrum. Note that there is a plateau in the data at small Cs coverages (work functions $\lesssim 4.5$ eV). This plateau is also observed for similar measurements using 400 eV and 1000 eV incident energies, which are plotted in figure 5b. We have also measured the intensity decrease for different scattering geometries using K^+ beams, and for different energies using Li^+ beams.⁶

If one assumes that resonant charge transfer is the principal mechanism for neutralizing the scattered potassium, the data in figure 5 can be compared to a standard model for charge transfer.¹⁵ In this model the surface is treated as jellium, and the metal electrons occupy the states of the jellium potential well. The electron density falls off exponentially with distance outside the jellium edge. The Hamiltonian outside the surface corresponds to an atomic potential. Charge transfer is assumed to occur between the atomic ionization level and the metal states of the same energy. When the ion is far from the metal surface, an electron bound to the ion has a well-defined energy which corresponds

to the atomic ionization potential. As the ion approaches the surface this electronic level shifts and broadens due to hybridization with the metal electrons. Far from the surface the energy shift has the classical $1/4z$ dependence, where z represents the distance from the surface. Close to the surface this shift must be calculated by considering the interaction of the atomic and metal electrons in detail. Resonant electron transfer from the metal to the K can occur if the potassium ionization level is resonant with filled states in the metal at some distance from the metal surface z_c (the "crossing distance"), which depends on the work function. The probability that transfer does occur depends on the width of the ionization level at z_c and the velocity of the ion perpendicular to the metal surface on the outgoing trajectory.

If the only important effect of the Cs adsorbate layer is to shift the work function of the surface, then the ionization probability P^+ is expected to vary as $P^+ \propto \exp(-\Delta(z_c)/\alpha v_\perp)$, where $\Delta(z_c)$ is the width of the resonance at the level crossing, α characterizes the exponential dependence of the level width Δ with separation z , and v_\perp is the velocity of the scattered ion perpendicular to the surface. The two dashed curves in figure 5a show the calculated P^+ values for the two v_\perp values given in the inset (which correspond to the two peaks in the measured K^+ energy spectra), with values of Δ and α taken from the literature. The solid curve in figure 5a shows the calculated P^+ with Δ and α chosen to give a best fit to the data.

Figure 5a shows that these data cannot be modeled by assuming that the only relevant effect of the Cs adsorbate layer is to shift the work function by the measured amount. This is consistent with the notion that the level crossings for the K ionization level are located a few Å outside the Cs/Cu surface. At these distances the local electrostatic potential induced by the Cs adsorbates is inhomogeneous, and these lateral variations must be included to reproduce the data. Similar results have been found by Geerlings, et al.¹⁶ Recent calculations by Nordlander and Tully¹⁷ have produced good agreement with Geerlings' data. Nordlander and Tully have calculated the widths and positions for the alkali electronic levels and included lateral variations in the electrostatic potential from the alkali adsorbates.

IV. SUMMARY

We have measured energy spectra of 90° specular scattering of 56 eV to 4 keV Na^+ from Cu(110). For the 100 eV, 200 eV, and 400 eV beams, comparison of experimental spectra with classical trajectory simulations shows that most of the detected ions have scattered from second layer chains of atoms. There are strong focusing effects observed in the scattering which determine how peaks in the energy spectra shift as the incident beam energy is varied. Scattering potentials constructed from sums of Na^+/Cu pair potentials calculated within the Hartree-Fock approximation give excellent agreement between measured and calculated energy spectra.

Electron transfer processes at surfaces were investigated by measuring the scattered K^+ intensities from Cu(110) with Cs overlayers. The ion intensity decreased with increasing Cs coverage, and was essentially zero for $\theta \approx 1/10$. This intensity decrease was attributed to a Cs-induced increase in the resonant charge transfer probability. Since the charge transfer has a high probability to occur at ion-surface separations of a few Å, lateral variations in the Cs-induced electrostatic potential must be considered to explain the data.

V. ACKNOWLEDGMENTS

David Adler, Bengt Kasemo, and Jim Sethna are acknowledged for stimulating discussions. Ernie Behringer and Chris DiRubio provided valuable assistance in collecting the data.

This work has been supported by the Air Force Office of Sponsored Research (grant no. AFOSR-88-0069) and by the National Science Foundation (grant. no. NSF-DMR-8451979). The simulations were done on the Production Supercomputer Facility of the Center for Theory and Simulation in Science and Engineering which is funded, in part, by the National Science Foundation, New York State, and IBM Corporation.

References

- ¹E. Hulpke and K. Mann, Surf. Sci. **133**, 171 (1983).

²A.D. Tenner, K.T. Gillen, T.C.M. Horn, J. Los, and A.W. Kleyn, Phys. Rev. Lett. **52**, 2183 (1984).

³R.L. McEachern, D.L. Adler, D.M. Goodstein, G.A. Kimmel, B.R. Litt, D.R. Peale, and B.H. Cooper, Rev. Sci. Instrum., in press.

⁴D.R. Peale, D.L. Adler, B.R. Litt, and B.H. Cooper, Rev. Sci. Instrum., in press.

⁵D.L. Adler and B.H. Cooper, Rev. Sci. Instrum. **59**, 137 (1988).

⁶G.A. Kimmel, D.M. Goodstein, and B.H. Cooper, J. Vac. Sci. Technol., in press.

⁷R.L. McEachern, D.M. Goodstein, and B.H. Cooper, to be published.

⁸D.M. Goodstein, S.A. Langer, and B.H. Cooper, J. Vac. Sci. Technol. A **6**, 703 (1988).

⁹M. Copel, T. Gustafsson, W.R. Graham, and S.M. Yalisove, Phys. Rev. B **33**, 8110 (1986).

¹⁰D.M. Goodstein, R.L. McEachern, and B.H. Cooper, to be published.

¹¹P.J. van den Hoek, A.D. Tenner, A.W. Kleyn, E.J. Baerends, Phys. Rev. B **34**, 5030 (1986).

¹²T.C.M. Horn, Pan Haochang, P.J. van den Hoek, and A.W. Kleyn, Surf. Sci. **201**, 573 (1988).

¹³J.P. Biersack and J.F. Ziegler, in *Ion Implantation Techniques*, Springer Series in Electrophysics Vol. 10, edited by H. Ryssel and H. Glawischnig (Springer-Verlag, Berlin, 1982).

¹⁴S.H. Overbury and D.R. Huntley, Phys. Rev. B **32**, 6278 (1985).

¹⁵R. Brako and D.M. Newns, Surf. Sci. **108**, 253 (1981).

¹⁶J.J.C. Geerlings, L.F.Tz. Kwakman, and J. Los, Surf. Sci. **184**, 305 (1987).

¹⁷P. Nordlander and J.C. Tully, to be published.

Figure 1

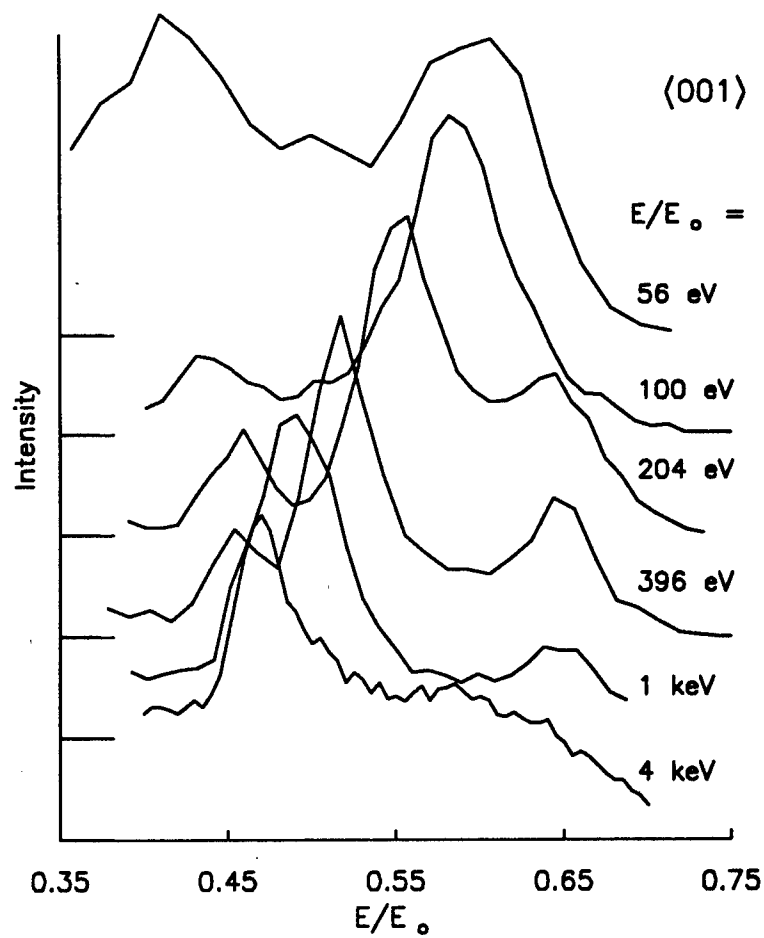
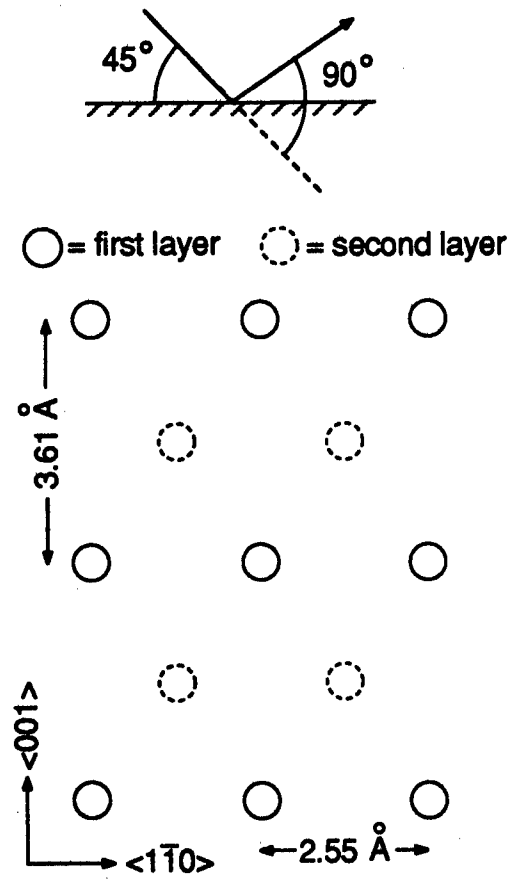
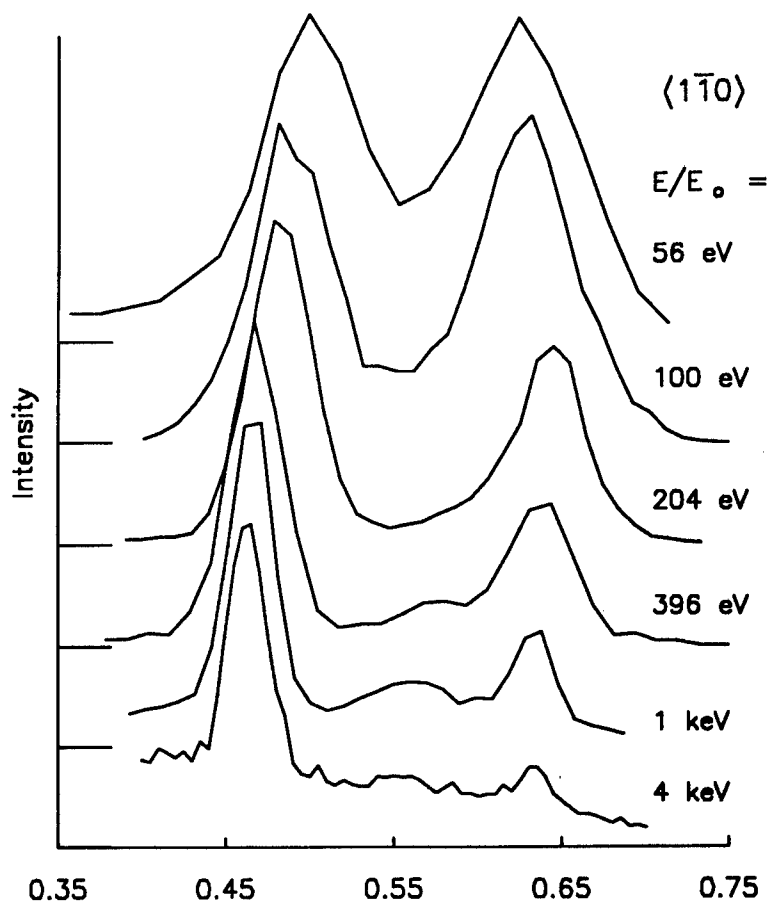


Figure 2

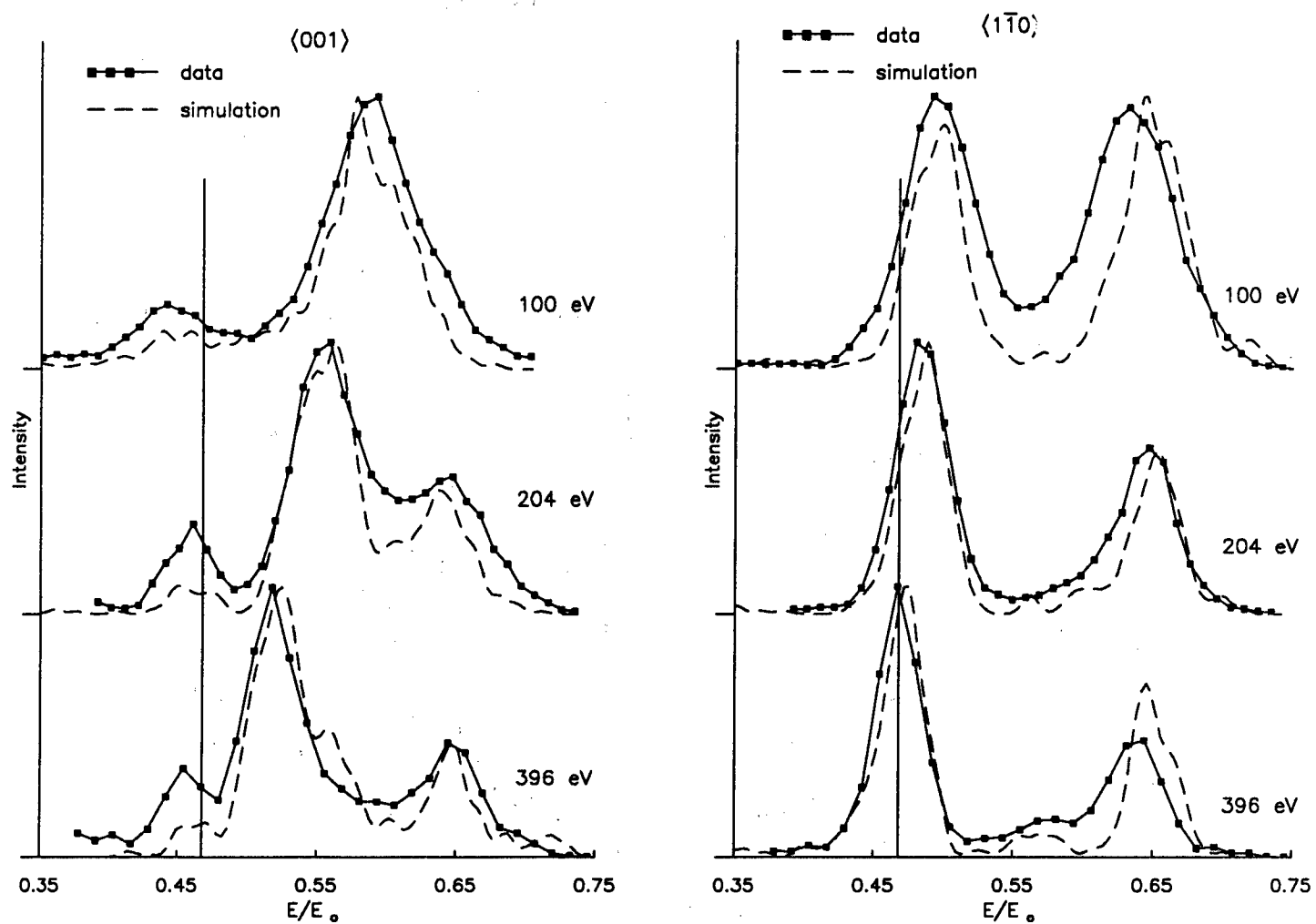


Figure 3a

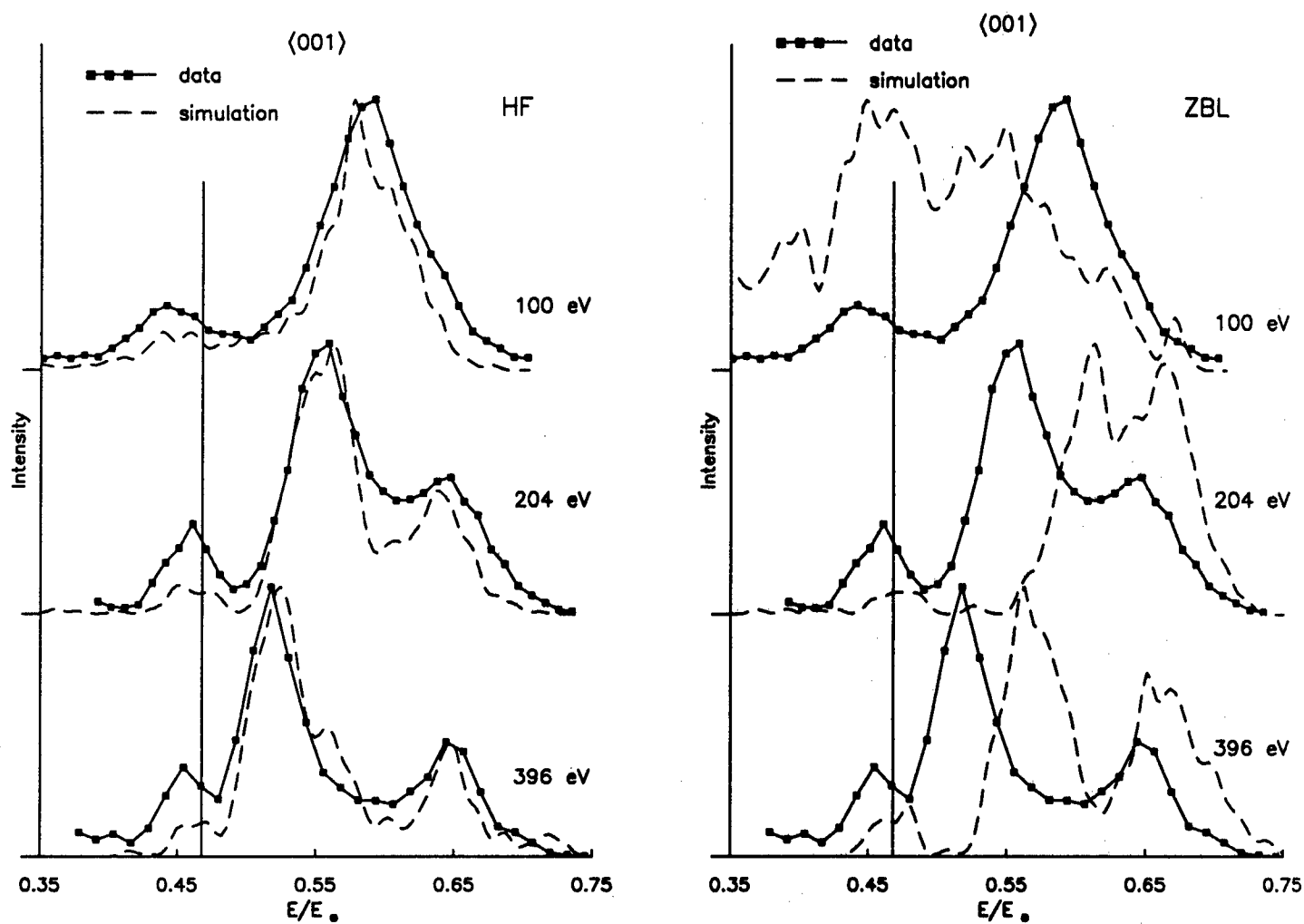


Figure 3b

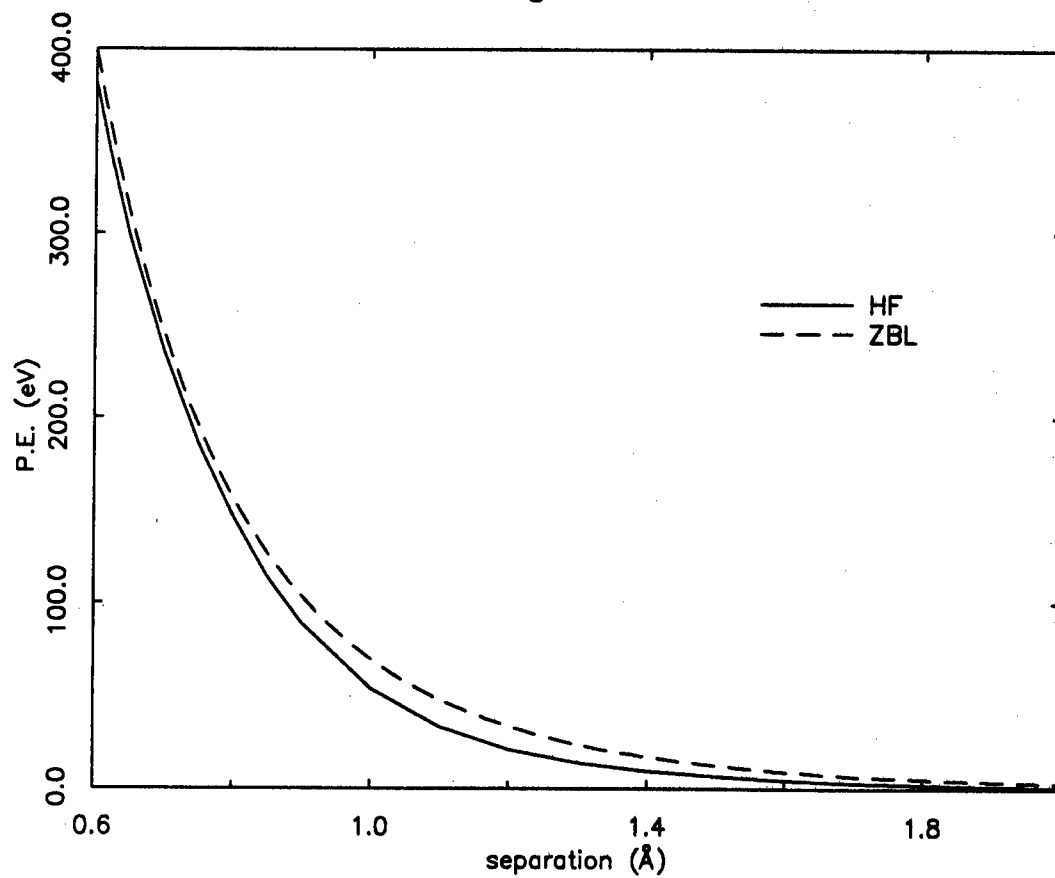


Figure 4a

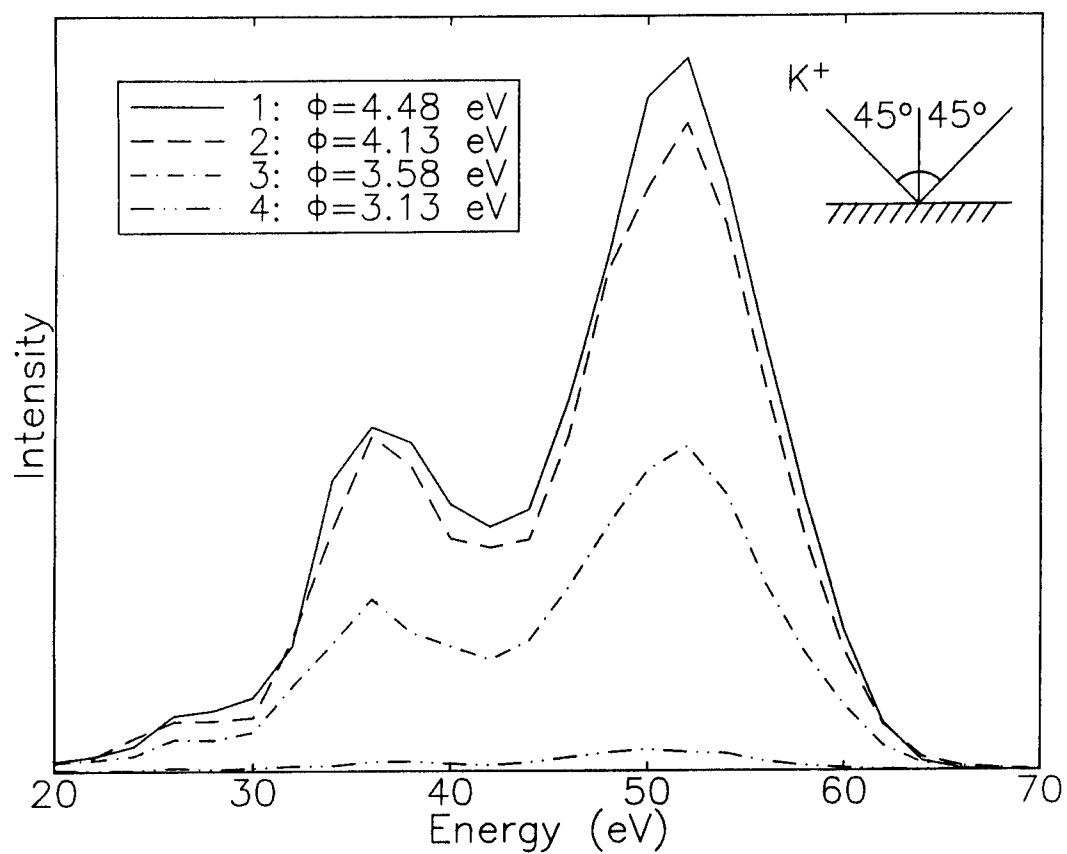


Figure 4b

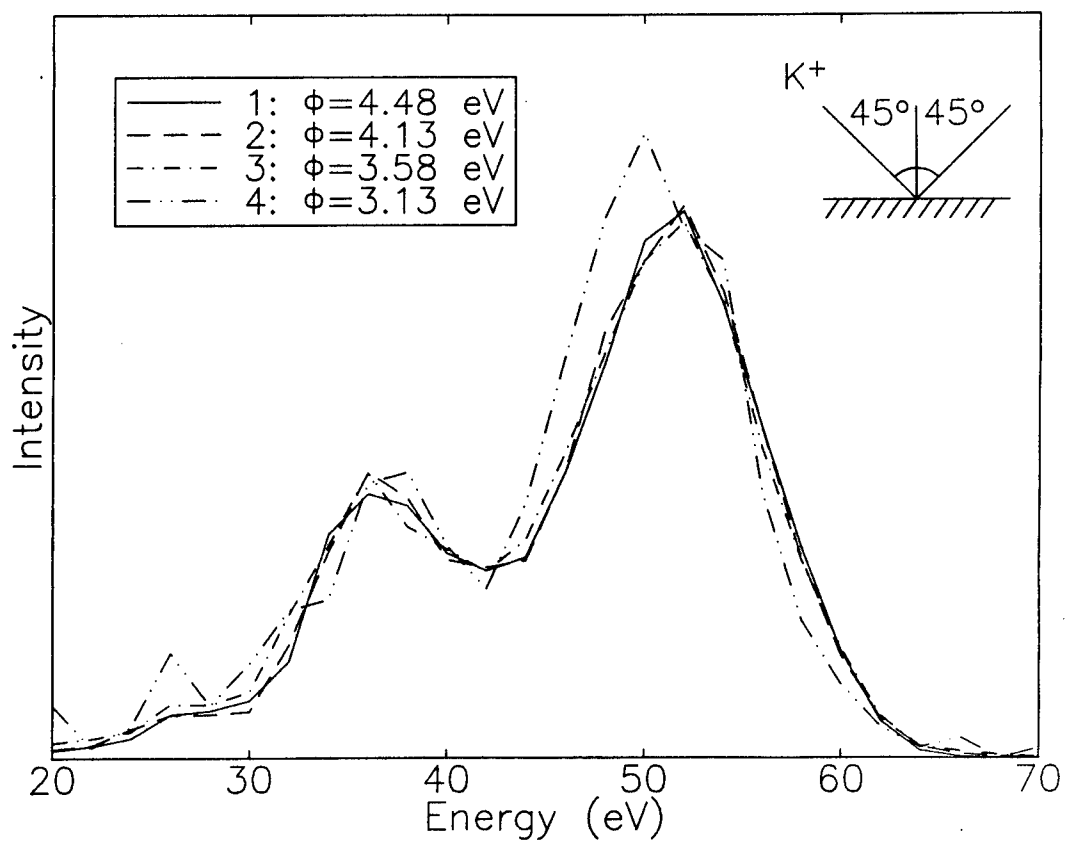


Figure 5a

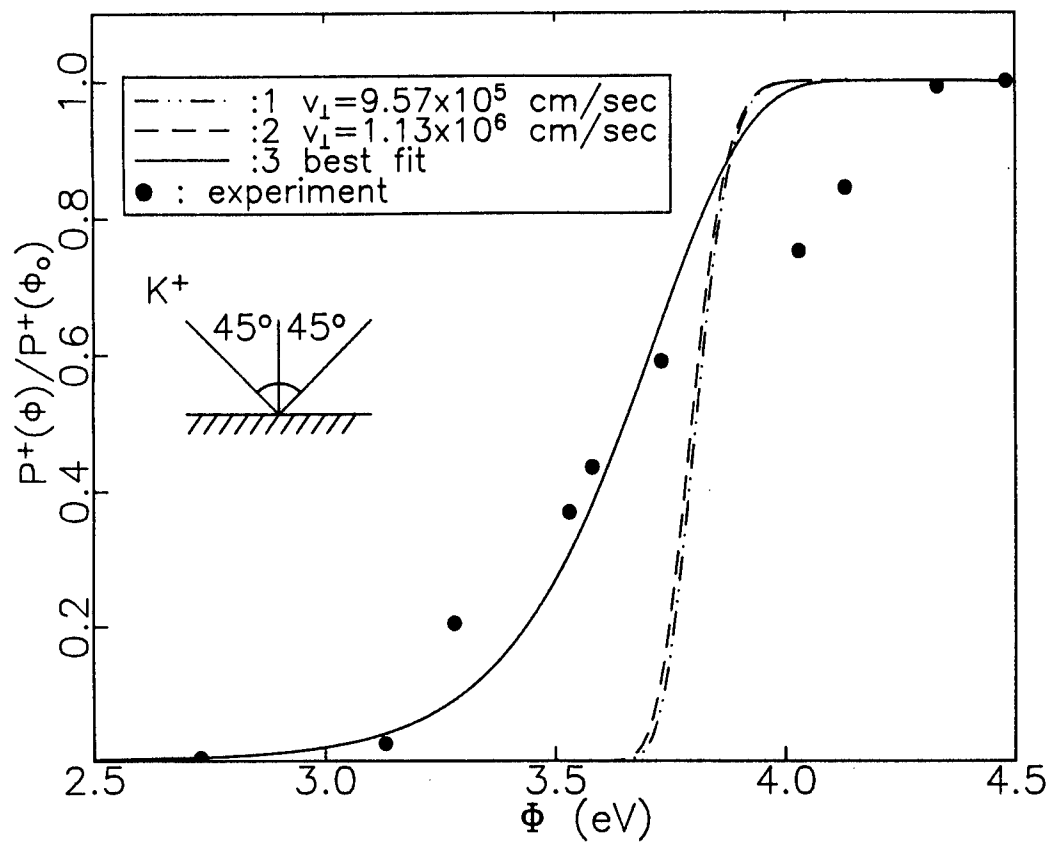
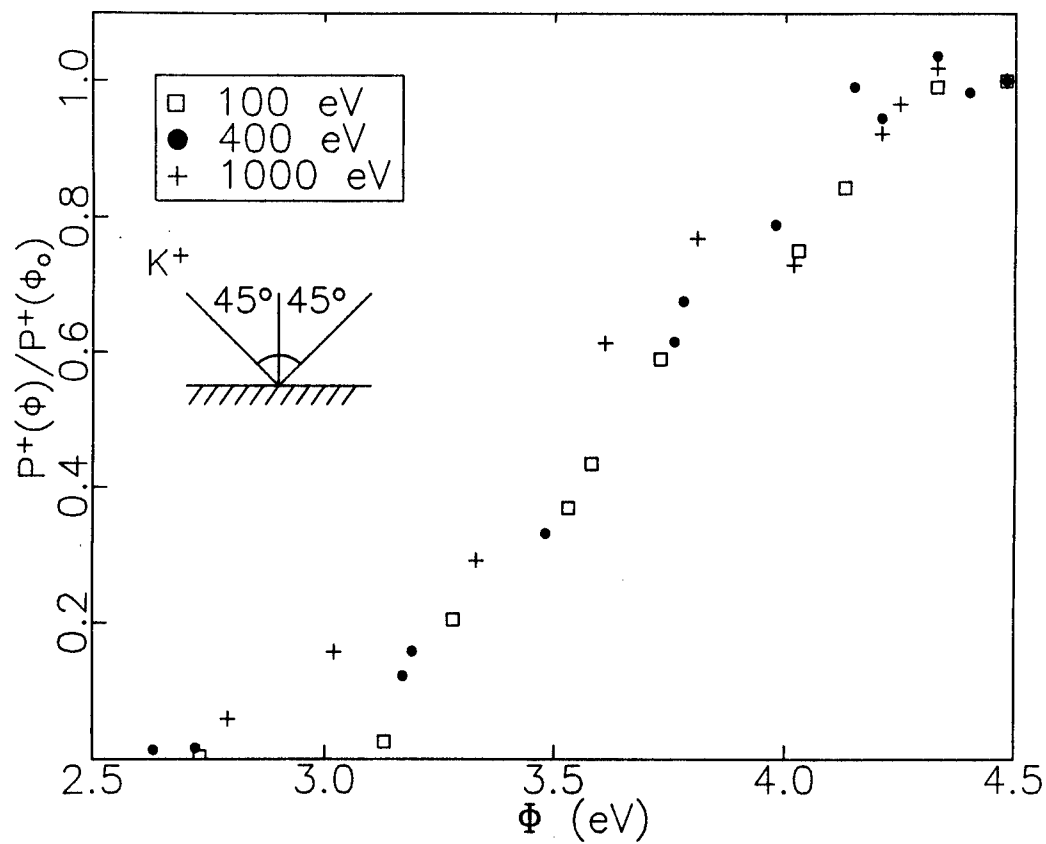


Figure 5b



On the Validity of Reduced Potential Curves*

by

Joel Tellinghuisen

Department of Chemistry and Center for Atomic and Molecular Physics at Surfaces
Vanderbilt University, Nashville, TN 37235

ABSTRACT

The idea of a universal potential function for the dependence of interaction energies of systems of particles on some distance parameter has long tantalized molecular physicists. Such a "magic potential" would relieve experimentalists and theorists of a considerable amount of work, allowing them to focus their efforts on the determination of only three (or perhaps four) fundamental parameters for each system. Recently Ferrante *et al.* [Phys. Rev. Lett. **50**, 1385 (1983)] claimed to have found such a universal relationship, applicable to interactions in diatomic molecules, bulk metals, bimetallic interfaces, and gas-solid interfaces. On the other hand, Graves and Parr [Phys. Rev. A **31**, 1 (1985)], examined the spectroscopic properties of 150 diatomic molecules and challenged the conclusions of Ferrante, *et al.* In the present work, a number of well-known diatomic potentials are examined on a *global* scale. For these systems the truth lies somewhere between the extreme conclusions of the above-mentioned works: Used judiciously, reduced potentials *do* have much to offer, particularly in "ignorance" situations.

I. INTRODUCTION

In molecular physics, potential energy functions are all-important for theoretical description of the properties of systems of particles. Not surprisingly, considerable effort has been expended toward obtaining "good" potential energy functions. For two-particle systems experiencing central forces, the Schrodinger equation is separable; and the desired potential energy function depends on a single variable, the separation R of the particles. Neglecting small effects such as magnetic interactions, the potential energy curve $U(R)$ then provides all of the information about the energy levels of the system.

In the early days of the new quantum mechanics, attempts to define molecular potentials centered on closed-form expressions containing 3-5 parameters which could be adjusted to match the observed energy levels.^{1,2} Dunham³ gave a more general semiclassical treatment based on an expansion in the variable $(R - R_e)/R_e$, where R_e is

* adapted from "Reduced Potential Energy Curves for Diatomic Molecules," by J. Tellinghuisen, S. D. Henderson, D. Austin, K. P. Lawley, and R. J. Donovan, Phys. Rev. A (in press).

the internuclear distance at the minimum of the potential. About the same time Klein⁴ derived the equations which have become the basis for the widely used RKR (Rydberg-Klein-Rees) method for inverting spectroscopic data to obtain potentials. Although Klein's derivation was also semiclassical, it has been found to yield potentials which are remarkably reliable quantally as well.⁵

Although the problem of obtaining reliable diatomic potentials might be considered solved, there has persisted through the years a search for "the magic potential" -- the Holy Grail of spectroscopy. The motivation for this search is unassailable: If only a few spectroscopic properties were required to define an entire potential curve, experimentalists and theorists alike would be relieved of a considerable part of their working burden. Indeed there *are* intriguing regularities among the spectroscopic constants of diatomic molecules which suggest an underlying simplicity.^{6,7} Finally, certain parametric potentials lead to reduced equations of state for describing bulk properties of matter -- and such reduced equations of state are also much sought after.

Since actual two-particle interaction potentials span vibrational frequencies and binding energies which range over ~ 3 orders of magnitude, the search for the magic potential translates into a quest for a suitable prescription for a *reduced potential*. One such prescription has been used by Jenc for over two decades to describe trends relatable to periodic table locations of the combining atoms.⁸ More recently Rose, Ferrante, and Smith have claimed discovery of a universal binding energy curve applicable to metals and bimetallic interfaces,⁹ chemisorption,¹⁰ and diatomic molecules.¹¹ These same authors have also explored the implications of this universal relationship for metallic bonding¹² and for equations of state of metals.¹³ In extolling the virtues of their simple reduction scheme, they have laid strong claims: "Thus there is a single binding-energy relation for all these seemingly diverse systems. . . There is an underlying simplicity in nature that has not been recognized heretofore."¹¹

The problem with universality is that, like beauty, it is to a large extent in the eye of the beholder: If one anticipates factor-of-two agreement in plotted reduced potentials but observes 10% agreement, one is pleasantly surprised and impressed. On the other hand the same result constitutes disappointment in the face of 1% expectations. In particular, diatomic spectroscopists demand a higher standard of performance in a universal potential than do solid-state and surface scientists, since the precision with which interaction potentials can be determined is much lower in the phenomena investigated by the latter group. While the comparisons displayed by Ferrante, Rose, and Smith indeed show good pictorial agreement, the consistency is far from perfect; and one might reasonably ask whether such universality is no more than a trick of display.

From a spectroscopic perspective, Graves and Parr¹⁴ have challenged the assessment of Ferrante *et al.*, showing that certain predictions of the reduced potential model are

not borne out in observed spectroscopic constants. Without being so presumptuous as to claim discovery of the Holy Grail, we wish to suggest that the criteria used by Graves and Parr to evaluate the reduced potential concept are not the whole story, and that regularities which appear when reduced potentials are examined over a large range of reduced distance are not adequately predicted by parameters which are related to the first few derivatives of the potential at its minimum. For example Fig. 1 illustrates the reduced potentials of nine molecular states, plotted according to the simple prescription discussed in refs. 11 and 14 (see below). Admittedly, we have chosen these nine for their approximate agreement; but note that the quantities plotted in the inset do not coalesce in a single point, as would be required for satisfaction of the reduced potential model according to the test adopted by Graves and Parr. Moreover, we have found cases where two states share virtually identical A and B values but display *discordant* reduced potentials. Finally, even where reduced potentials are in poor agreement, their repulsive branches are often in quite good agreement. This behavior can be useful in approximating unknown potentials¹⁵ and is only revealed through comparisons of the potentials themselves (eg. Fig.1), being totally obscured in quantities based on a limited set of spectroscopic parameters (eg. inset to Fig. 1).

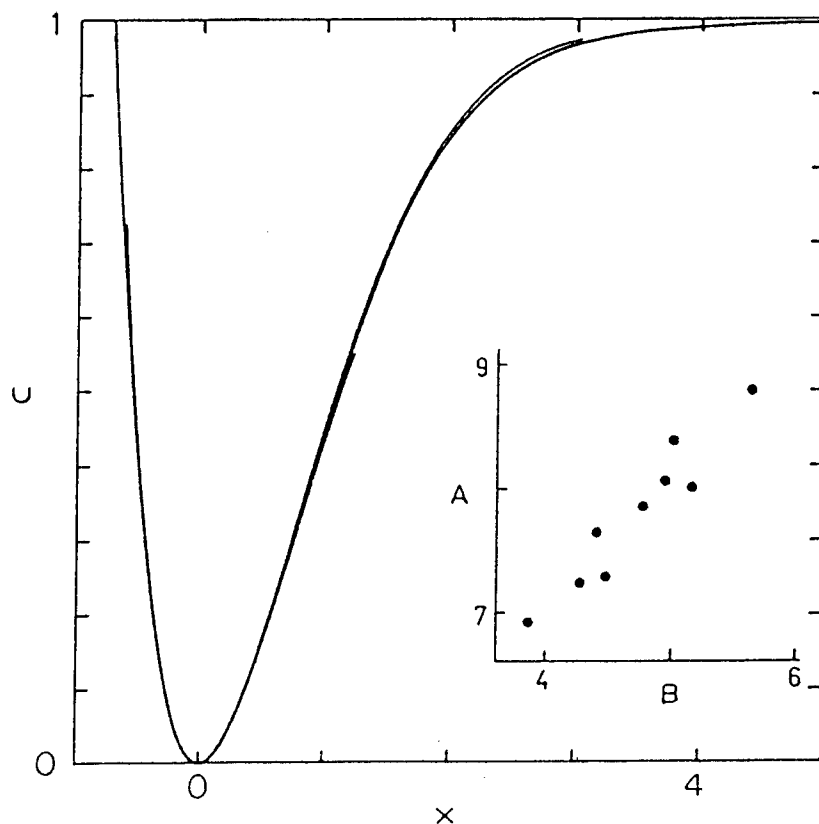


Figure 1: Reduced potentials for $\text{Cl}_2(X)$ (to $u = 0.97$), $\text{ICl}(X)$ (0.99), $\text{N}_2(A)$ (0.57), $\text{N}_2(X)$ (0.54), $\text{O}_2(X)$ (0.73), $\text{P}_2(X)$ (0.53), $\text{S}_2(X)$ (0.57), $\text{Se}_2(X)$ (0.40), and $\text{Te}_2(X)$ (0.43).

II. THE SCALED POTENTIAL

If the potential energy $U(R)$ is expanded in a Taylor series about its minimum, the term quadratic in $(R-R_e)$ is generally taken to be the lead term, yielding the harmonic oscillator approximation,⁶

$$U(R) \simeq k_e (R - R_e)^2 / 2 = 2\pi^2 \mu c \omega_e^2 (R - R_e)^2 / h, \quad (1)$$

where k_e is the force constant, μ the reduced mass, c the speed of light, h Planck's constant, and ω_e the vibrational frequency. Both U and ω_e are expressed in the customary spectroscopic units of cm^{-1} . The harmonic approximation is only a crude representation of the vibrational levels of diatomics, so at least one anharmonicity correction is needed to adequately represent even the lowest bound levels,

$$G_v = \omega_e(v + 1/2) - \omega_e x_e(v + 1/2)^2. \quad (2)$$

The harmonic oscillator also has no defined dissociation limit. However, we might naively seek to obtain a scaled potential by dividing U by the dissociation energy \mathcal{D}_e , obtaining

$$u \equiv U(R)/\mathcal{D}_e = x^2, \quad (3)$$

where

$$x \equiv (2\pi^2 c \mu / \mathcal{D}_e h)^{1/2} \omega_e (R - R_e). \quad (4)$$

The definitions of Eqs. (3) and (4) ensure that all potentials will agree at least near their minima. This is in fact the approach taken by Ferrante *et al.*¹¹ The present definition of the reduced distance is the same as the argument in the Morse potential function and its variants and extensions,¹ as discussed by Graves and Parr.¹⁴ In terms of this reduced distance, and for our reference energy of zero at the potential minimum, the reduced Morse function is

$$u = (1 - \exp(-x))^2. \quad (5)$$

For their comparisons of 150 diatomic ground states, Graves and Parr defined the quantities Δ , a_1^2 , and a_2 . In terms of the usually available spectroscopic constants, these quantities are, to a very good approximation,^{1,3}

$$\Delta = \omega_e^2 / (4B_e \mathcal{D}_e), \quad (6)$$

$$a_1^2 = [1 + (\omega_e x_e / 6B_e^2)]^2, \quad (7)$$

$$a_2 = 5a_1^2/4 - 2\omega_e x_e / 3B_e, \quad (8)$$

If the scaling hypothesis were rigorously correct, the quantities a_1^2/Δ and a_2/Δ -- which we define as $A/10$ and $B/10$, respectively -- should be constant and independent of species for a group of potentials which follow the universal reduced potential $u = F(x)$.

For the 150 cases examined in ref. (14) this was far from the case, though the plots of A vs B did show a tantalizing near-linear behavior, suggesting the need for an adjustable parameter in the reduced potential.

III. RESULTS AND DISCUSSION

We have examined the reduced potential curves of some 35 diatomic molecular states, plotted according to the simple definition of Eqs. (3) and (4). The examples include both ground and excited states of a number of molecules and were chosen because the potentials are well defined over a sizable fraction of the well depth in most cases. The potentials studied included the 25 examined in ref. (15), updated and augmented as follows: $\text{Li}_2(X)$,¹⁶ $\text{K}_2(X)$,¹⁷ $\text{Cs}_2(X)$,¹⁸ $\text{NaK}(X)$,¹⁹ $\text{Te}_2(X)$,²⁰ $\text{F}_2(X)$,²¹ $\text{ICl}(X)$,²² $\text{ICl}(A')$,²³ $\text{ICl}(A)$,²⁴ $\text{XeF}(X)$,²⁵ $\text{Br}_2(A)$,²⁶ $\text{Br}_2(B)$,²⁷ $\text{P}_2(X)$.²⁸

Figure 2 shows the ground states of five alkali dimer molecules and H_2 . The latter and the Morse curve itself are significantly different, but the five alkali molecules share a "nearly common" reduced ground-state potential. Here as in Fig. 1, the plot of A vs B is nearly linear, but the actual values of A and B vary by factors of 2-3.

Figure 3 displays the ground states of four halogen molecules. The degree of universality is reduced at large x , by comparison with Fig. 2, but again the reduced curves show good "eyeball" consistency. And again the linear A vs B dependence is noted.

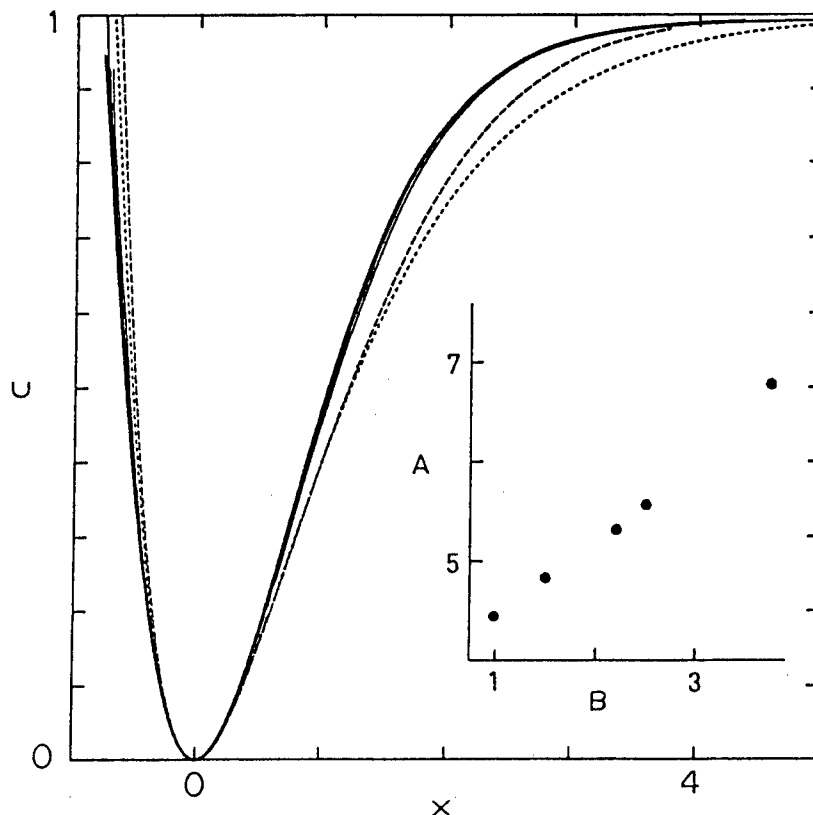


Figure 2: Reduced potentials for alkali dimer ground states (solid curves), $\text{H}_2(X)$ (coarse dash), and Morse function (fine dash). In the inset the points are for, from left to right: Cs_2 , K_2 , NaK , Na_2 , and Li_2 .

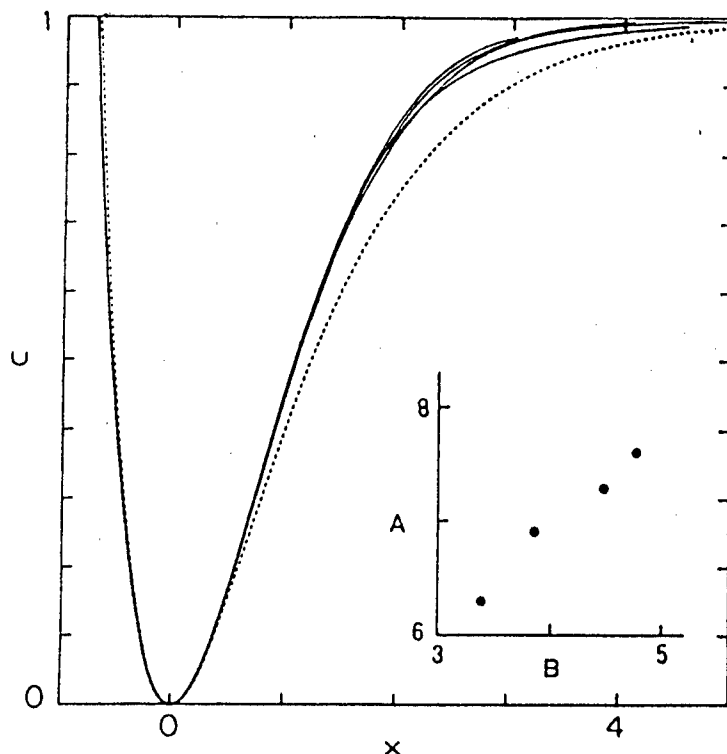


Figure 3: Halogen ground states with Morse function (dashed) for comparison. At $x = 2.8$, the curves are for, top to bottom: Cl_2 , ICl , F_2 , and I_2 . Left to right, the points in the inset represent I_2 , ICl , Cl_2 , and F_2 .

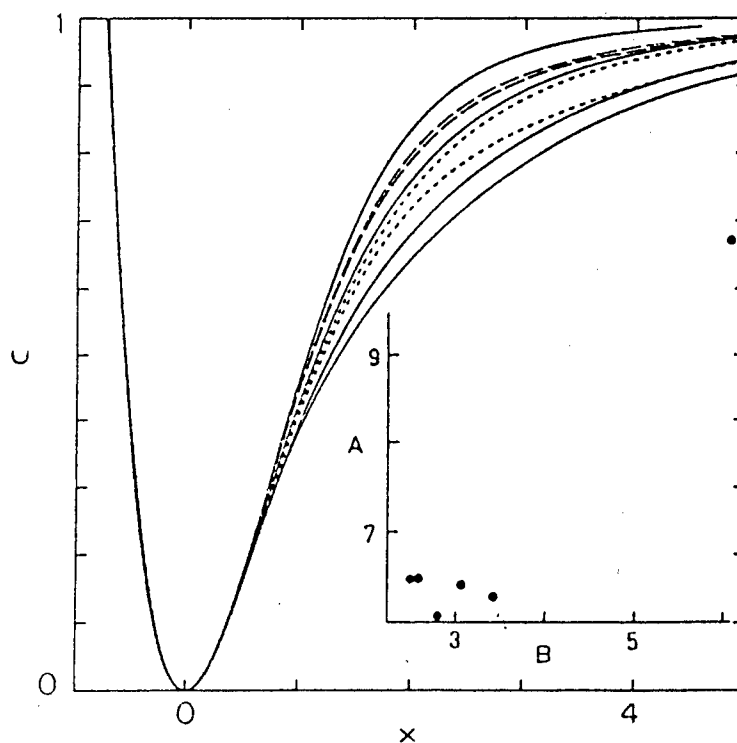


Figure 4: Halogen states. At $x = 3$, reading top to bottom, the solid curves are for $\text{I}_2(X)$, B , A' , and A ; the broad dashed curves for $\text{ICl}(A')$ and A ; and the fine dashed curves for $\text{Br}_2(B)$ and A . In the inset the one point at large A and B is for $\text{Br}_2(A)$, while the points for $\text{I}_2(A')$ and A have negative B values are off scale.

Several electronic states of different halogens are compared in Fig. 4. The attractive branches are now grossly different, although the repulsive branches coincide remarkably well. In this case the points plotted in the inset show a fairly tight grouping near $A = 6.5$, $B = 3$. This grouping may indicate similarities in the reduced potentials near their minima but is of little value in predicting the course of the curves at large x .

Results for four van der Waals molecules and XeF are illustrated in Fig. 5. Here there are sizable differences on both branches of the potential. The near-linear A vs B dependence is regained, but again the clustering of points near the middle of the inset is a misleading predictor of the reduced potentials on the large scale.

Figure 6 shows changes that occur in homonuclear diatomics going across a period in the atomic table. We have also included the ground states of CO and SiO, and it is interesting to note the level of *disagreement* between these two (which are mutually consistent) and the isoelectronic N_2 and P_2 (see also Fig. 1). Again a linear dependence between A and B is suggested, and in this case some close-lying points *do* represent closely similar reduced potentials (eg. CO(X) and SiO(X), and Cl₂(X) and P₂(X)).

In his reduced potential method, Jenc has given a slightly more complicated recipe for the reduced distance ρ ,⁸

$$\begin{aligned}\rho &= (R - Z)/(R_e - Z) \\ Z &= [1 - \exp(-R/\rho_{ij})]\rho_{ij}\end{aligned}\tag{9}$$

where ρ_{ij} solves

$$\rho_{ij} \times [1 - \exp(-R_e/\rho_{ij})] = R_e - (3.96\mathcal{D}_e/k_e)^{1/2}.\tag{10}$$

We have calculated Jenc reduced potentials for the alkali dimers included in Fig. 2. Results are shown in Fig. 7. The Jenc potentials for this group of molecules show considerably less agreement in the attractive branch; however the agreement in the repulsive branch is actually better than in Fig. 2.

Given the occurrence of pictorial similarity in the reduced potentials, one may rightly ask what is the quantitative significance of agreement at the level of the reduced potentials depicted in, for example, Figs. 1-3. To address this question we have conducted the following computational experiment: We used the reduced potential for Cl₂(X) together with the experimental \mathcal{D}_e , ω_e , and R_e values for ICl(X) (Figs. 1 and 3) to regenerate an approximate potential for the latter. Then we solved numerically²⁹ for the eigenvalues and rotational constants B_v for a range of levels in ICl(X) and compared the results with the known values.²² Figure 8 shows that the error in the calculated quantities is less than 0.5% for almost all levels. For the vibrational energy G_v , that translates into shifts of 80-90 cm⁻¹ for levels near $v = 50$. While such an error is intolerable in a spectroscopic experiment, we predict that it is considerably smaller than would result from any similar test employing, for example, an *ab initio* potential for ICl; and the latter potential will be significantly harder to obtain.

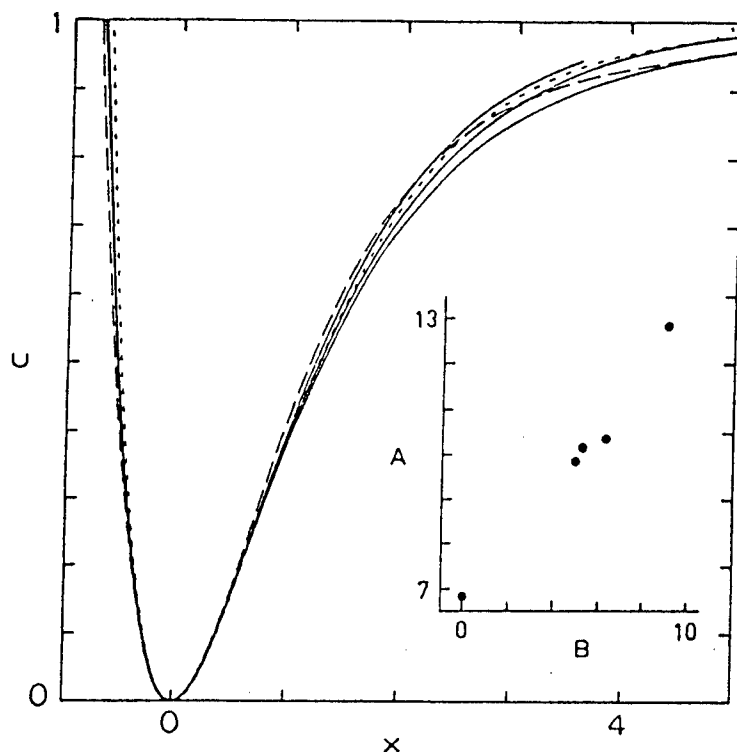


Figure 5: Van der Waals molecules and XeF. Top to bottom at $x = 3$, the solid curves are for NaAr, Ca₂, and Ar₂, while the dashed curves represent Mg₂ and XeF. Left to right, the points in the inset represent XeF, Ca₂, Ar₂, NaAr, and Mg₂.

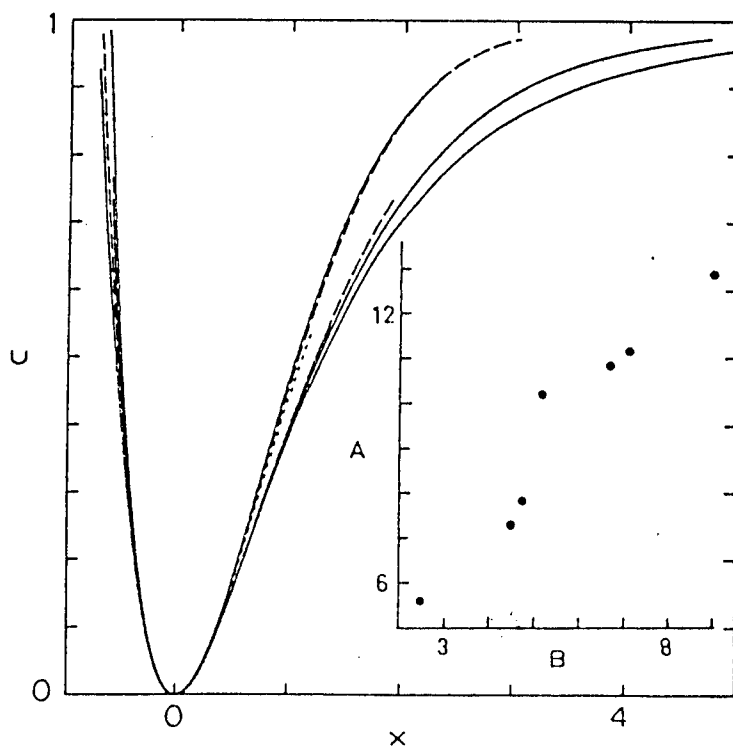


Figure 6: Periodic trends in ground states. Left to right on the attractive branches at $u = 0.6$, the solid curves represent Na₂, Mg₂, and Ar₂, while the dashed curves are for Cl₂ and CO. The curve for SiO coincides with the latter, and the fine dashed curve represents P₂. Left to right in the inset: Na₂, Cl₂, P₂, Ar₂, CO, SiO, Mg₂.

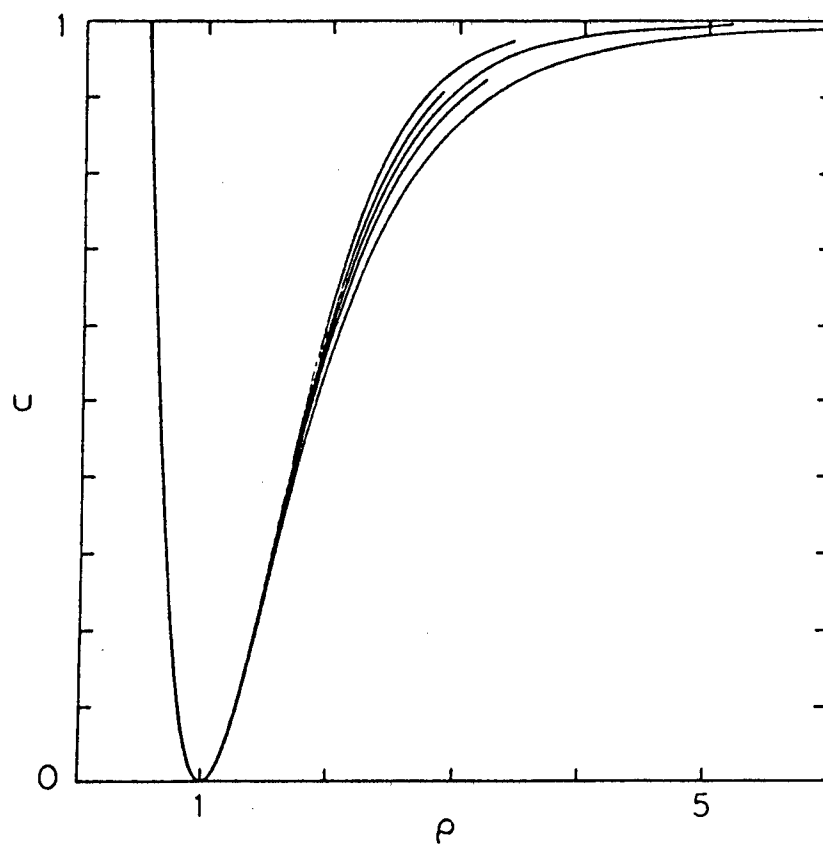


Figure 7: Reduced potentials for alkali dimers of Fig. 2 obtained using the Jenc scheme (see text).

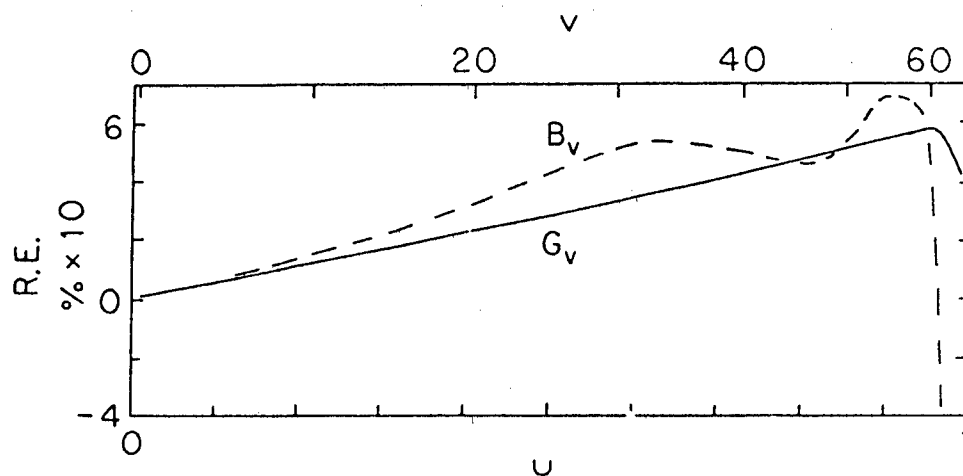


Figure 8: Relative errors (R.E.) in the G_v and B_v values for $\text{ICl}(X)$ calculated using the reduced potential for $\text{Cl}_2(X)$ to produce the potential for ICl . The plotted quantity is $(\text{calculated} - \text{experimental}) / \text{experimental}$.

IV. CONCLUSION

The scaled potentials of analogous electronic states in chemically similar diatomic molecules can show surprising similarity over the full range of the bound well. On the other hand parameters based on experimental estimates of the third and fourth derivatives of the potential at R_e are not very reliable predictors for either agreement or disagreement of the reduced potentials, when the latter are examined away from the region of the minimum. The near-linear dependence of the particular combinations of these parameters employed by Graves and Parr¹⁴ is intriguing and may suggest, as these authors noted, that one additional appropriately defined parameter may yield a better reduction scheme. However the double exponential function, used in ref. (14) to illustrate this idea, cannot fill the bill for most of the states examined in the present work, because the A and B values lie below the range spanned by this potential form.

Used judiciously, reduced potentials can provide good "ignorance" guesses for unknown potentials. For such an application one requires preferably at least two known analogous potentials for similar molecules, and D_e , R_e , and ω_e for the unknown state. Knowledge of the latter parameters might seem to beg the question; however it often happens that these quantities are determined well from an analysis of low-lying v levels in a state (together with other information for D_e), leaving most of the state in question undetermined. For such cases the reduced potential can aid in extrapolating the potential to higher energies. It is not clear whether the simple reduction prescription given by Eqs. (3) and (4) in the present work will yield the same kinds of systematic trends exploited by Jenc with his reduction scheme.⁸ However, the comparison of Figs. 2 and 7 suggests that for the purpose of guessing an unknown potential, the present scheme is both simpler and more reliable.

ACKNOWLEDGMENT

This work was supported in part by the Air Force under contract AFOSR-F49620-86-C-0125 and by the Natural Science Fund of the Vanderbilt University College of Arts and Science. The work was initiated when the first author was at the University of Edinburgh, the beneficiary of a British Science and Engineering Research Council Fellowship.

REFERENCES

1. Y. P. Varshni, *Rev. Mod. Phys.* **29**, 664 (1957).
2. D. Steele, E. R. Lippincott, and J. T. Vanderslice, *Rev. Mod. Phys.* **34**, 239 (1962).
3. J. L. Dunham, *Phys. Rev.* **41**, 713, 721 (1932).
4. O. Klein, *Z. Phys.* **76**, 226 (1932).
5. A. W. Mantz, J. K. G. Watson, K. Narahari Rao, D. L. Albritton, A. L. Schmeltekopf, and R. N. Zare, *J. Mol. Spectrosc.* **39**, 180 (1971).
6. G. Herzberg, *Spectra of Diatomic Molecules* (Van Nostrand Reinhold, New York, 1950).
7. R. F. Borkman and R. G. Parr, *J. Chem. Phys.* **48**, 1116 (1968).
8. F. Jenc, *Adv. At. Mol. Phys.* **19**, 265 (1983).
9. J. H. Rose, J. Ferrante, and J. R. Smith, *Phys. Rev. Lett.* **47**, 675 (1981).
10. J. R. Smith, J. Ferrante, and J. H. Rose, *Phys. Rev. B* **25**, 1419 (1982).
11. J. Ferrante, J. R. Smith, and J. H. Rose, *Phys. Rev. Lett.* **50**, 1385 (1983).
12. J. H. Rose, J. R. Smith, and J. Ferrante, *Phys. Rev. B* **28**, 1835 (1983).
13. F. Guinea, J. H. Rose, J. R. Smith, and J. Ferrante, *Appl. Phys. Lett.* **44**, 53 (1984).
14. J. L. Graves and R. G. Parr, *Phys. Rev. A* **31**, 1 (1985).
15. J. Tellinghuisen and S. D. Henderson, *Chem. Phys. Lett.* **91**, 447 (1982).
16. K. K. Verma, M. K. Koch, and W. C. Stwalley, *J. Chem. Phys.* **78**, 3614 (1983).
17. J. Heinze, U. Schuhle, F. Engelke, and C. D. Caldwell, *J. Chem. Phys.* **87**, 45 (1987).
18. M. Raab, H. Weickenmeier, and W. Demtroder, *Chem. Phys. Lett.* **88**, 377 (1982).
19. A. J. Ross, C. Effantin, J. d'Incan, and R. F. Barrow, *Mol. Phys.* **56**, 903 (1985).
20. R. F. Barrow and K. K. Yee, *Acta Phys. Hung.* **35**, 239 (1974).
21. E. A. Colbourn, M. Dagenais, A. E. Douglas, and J. W. Raymonda, *Can. J. Phys.* **54**, 1343 (1976).
22. J. C. D. Brand and A. R. Hoy, *J. Mol. Spectrosc.* **114**, 197 (1985).
23. J. C. D. Brand, D. Bussieres, and A. R. Hoy, *J. Mol. Spectrosc.* **113**, 388 (1985).
24. J. A. Coxon and M. A. Wickramaaratchi, *J. Mol. Spectrosc.* **79**, 380 (1980).
25. P. C. Tellinghuisen and J. Tellinghuisen, *Appl. Phys. Lett.* **43**, 898 (1983).
26. J. A. Coxon, *J. Mol. Spectrosc.* **41**, 548 (1972).
27. R. F. Barrow, T. C. Clark, J. A. Coxon, and K. K. Yee, *J. Mol. Spectrosc.* **51**, 428 (1974).
28. J. Brion, J. Malicet, and M. F. Merienne-Lafore, *Can. J. Phys.* **55**, 68 (1977).
29. J. Tellinghuisen, *Adv. Chem. Phys.* **60**, 299 (1985).

COMPARISON OF THE DESORPTION BY 9 KeV N₂⁺ AND 4.5 KeV N⁺ ON SILICAS*

P.W. Wang (a)(b)(c), R.F. Haglund, Jr.(b)(c), D.L.Kinser (a) (c), N.H. Tolk (b).(c), and R.A. Weeks (a) (c)

(a) Department of Materials Science and Engineering (b) Department of Physics and Astronomy, (c) Center for Atomic and Molecular Physics at Surfaces, Vanderbilt University, Nashville, TN 37235

ABSTRACT

Same energy density and same number of nitrogen nuclei have been used to bombard the high-purity silicas. Preliminary results show the different intensities of desorbed silicon and sodium from surface between 9 KeV N₂⁺ and 4.5 KeV N⁺ ions. Possible reasons of different yields of silicon atoms and sodium atoms will be discussed.

INTRODUCTION

Desorption is a very complicated phenomenon due to many physical and chemical processes are going on in a very short time during the impact of the incoming energetic particles on the substrate surface. Energy of the incoming particle was absorbed by the substrate and dissipated through available pathways such as atomic collisions and electronic transitions. The redistribution of the energy results in the desorption of the particles from substrate, the recoil of the primary particles, light emitted from the de-excitation process of the excited absorbed atoms, luminescence from the near-surface bulk, and formation of the excitons and defects.

Our recent results of high-purity silicas irradiated by 9 KeV He⁺ show that the electronic transition process is a dominant pathway to dissipate the absorbed energy [1]. The electronic energy deposited in the near-surface bulk is rechanneled primary into luminescence and the desorption of the particles from the surface as shown in our previous reports [2-4].

In this paper, we report our preliminary results on the different sputtering yield of silicon atoms induced by same energy density and number of nitrogen nuclei on silicas.

EXPERIMENTAL

Samples we used were Type III and IV [5] high-purity synthetic silicas. Samples were Spectrosil and Spectrosil WF purchased from Thermal American Fused Quartz Co., and Suprasil 1 and Suprasil W1 were made by Heraeus Inc.

Samples were cut to 1.8 cm x 0.5 cm x 0.1 cm in size and then cleaned by the procedures described in our previous report [2]. Samples were mounted on a sample holder and then inserted into the ultra-high vacuum chamber. The pressure in the UHV chamber was low, 10^{-8} to 10^{-9} torr at room temperature during measurements.

Each sample was bombarded by N_2^+ and N^+ . The desorption due to the de-excitation of the desorbed species from the surface were monitored in situ by an optical detect system during measurement [6]. The geometry of the sample position with respect to the optical detect system was kept the same during N_2^+ and N^+ bombardment.

In order to keep same number of nuclei strike on the surface, the flux of N^+ was kept twice as N_2^+ ions. Since N_2^+ also has twice energy as N^+ does, same energy density and same number of nitrogen nuclei strike the silica surface.

RESULTS

Desorption spectra from Spectrosil, Spectrosil WF, Suprasil 1 and Suprasil W1 were monitored in situ during 9 KeV N_2^+ and 4.5 KeV N^+ bombardment in ultra-high vacuum as shown in Fig. 1 to 4. Part (a) and (b) in all figures indicate the desorption spectrum induced by N_2^+ and N^+ respectively. Fig. 1 (a) is a typical spectrum which contains a broad spectral luminescence and a few sharp lines which come from the excited atoms. The excited-atom spectra show contributions from silicon (the first order lines at 2516 Å and 2882 Å and the second-order lines at twice those wavelengths), two still unidentified contaminants (around 4000 Å and 4500 Å), and sodium excited states (5890 Å) which are easily sputtered by N^+ ions. It is clear indicated in these four figures that for the same energy density and same number of nitrogen nuclei, N_2^+ sputtered more silicon atoms from silica surfaces than N^+ and sodium atoms are effectively sputtered by N^+ than N_2^+ .

DISCUSSION

The 9 KeV N_2^+ and N^+ bombarding silica can be categorized to the linear cascade sputtering [7,8] where the sputter yield can be expressed as

$$Y = \Lambda F_D \quad (1)$$

where Y is the sputter yield, Λ is a material constants and the other, and F_D is the deposited energy at the sputtered surface [9]. Λ is a function of atomic density and the surface binding energy of the target. For the deposited energy F_D can be written as

$$F_D = \alpha N S_n = \alpha (dE/dx)_n \quad (2)$$

where α is a function of the mass ratio and ranges between 0.2 and 0.4 [10], N is the atomic density of the target, S_n is the nuclear stopping cross section, and $(dE/dx)_n$ is the energy loss of the incoming particle due to atomic collision.

Since one 9 KeV N_2^+ ion is dissociated to two 4.5 KeV N^+ ions right on the impact with the silica surface, one 9 KeV N_2^+ ion is equivalent to two 4.5 KeV N^+ ions for the sputtering. That is to say that one 9 KeV N_2^+ ion should have same sputter yield as two 4.5 KeV N^+ ions have because one 9 KeV N_2^+ ion has same quantities of Λ and F_D as two 4.5 KeV N^+ ions do. But this is not what the observed spectra showed. The observed spectra showed that for the same energy density and same number nitrogen nuclei, the sputter yield of silicon atom is higher by N_2^+ ions bombardment and the sputter yield of sodium atom is higher by N^+ ions bombardment.

These results clearly indicate that some other features are not included in sputter yield equation (1). In equation (1) only nuclear energy loss, $(dE/dx)_n$, has been considered and the electronic excitation and ionization are neglected. The electronic transitions can produce the excitons which can lead to the displacement of the atoms and the bond breaking in the target through the relaxation [11]. Another important point is that is any chemical reactions (bond formation) between incoming particles and the target atoms? Indeed nitrogen atoms can form bridging nitrogen structure, $Si-N-Si$, and NO_2 molecules in amorphous SiO_2 film as reported by Friebele et al [12].

The plausible explanation for N_2^+ has higher sputter yield for silicon is perhaps due to the size effect in which N_2^+ is larger than N^+ ion so that N_2^+ can easily knock out silicon atoms from the silica surface. However, the higher sputter yield of sodium atoms for N^+ may ascribed to the electronic excitations and chemical reactions.

The real reasons for different sputter yields of silicon and sodium atoms under same energy density and same number of nitrogen nuclei bombardment are not clear, but in order to understand the sputter process on silica surface size effect, electronic transitions and chemical reactions must be considered.

ACKNOWLEDGEMENT * This work was supported by Naval Research Laboratory under contract N00014-86-C2546.

REFERENCE

- [1] P. W. Wang et al. to be published.
- [2] P. W. Wang, R. F. Haglund, Jr., L. T. Hudson, D. L. Kinser, M. H. Mendenhall, N. H. Tolk, and R. A. Weeks, in: Third International Workshop on Desorption Induced by Electronic Transitions, Springer Series in Surface sciences Vol. 13, eds. R.H. Stulen and M.L. Knotek, Springer-Verlag, Berlin, 1988, p. 288-294.
- [3] P. W. Wang, R. F. Haglund, Jr., D. L. Kinser, M. H. Mendenhall, N. H. Tolk, and R. A. Weeks, J. of Non-Crys. Solids, 102, (1988) 288--294.
- [4] P. W. Wang, R. F. Haglund, Jr., D. L. Kinser, H. Mogul, N. H. Tolk, and R. A. Weeks, in : Second International Conference on The Effects of Modes of Formation on the Structure of Glasses, Trans Tech., Switzerland, 1988, p. 463.
- [5] G. Hetherington, J. British Ceramic Society, 3, 595(1966).
- [6] H.C. Mogul, R.A. Weeks, R.F. Haglund, Jr., D.L. Kinser, N.H. Tolk, and P.W. Wang, J. Vac. Sci. Technol. A6, (1988) 1428-1434.
- [7] P. Sigmund, in: Inelastic Ion-surface Collisions, eds. N.H. Tolk et al., Academic Press, New York, 1977, p. 121.
- [8] P. Sigmund, Appl. Phys. lett., 27 (1975) 52.
- [9] P. Sigmund, Phys. Rev., 184 (1969) 383, 187 (1969) 768.
- [10] P. Sigmund, in: Sputtering by Particle Bombardment I, ed. R. Behrisch, Springer-Verlag, New York, 1981, Chapter 2.
- [11] T. Tanaka, T. Eshita, K. Tanimura and N. Itoh, Crys. Latt. Defects and Amorphous Mat., 11 (1985) 221.
- [12] E.J. Friebele, D.L. Griscom and T.W. Hickmott, J. Non-crys. Solids, 71 (1985) 351.

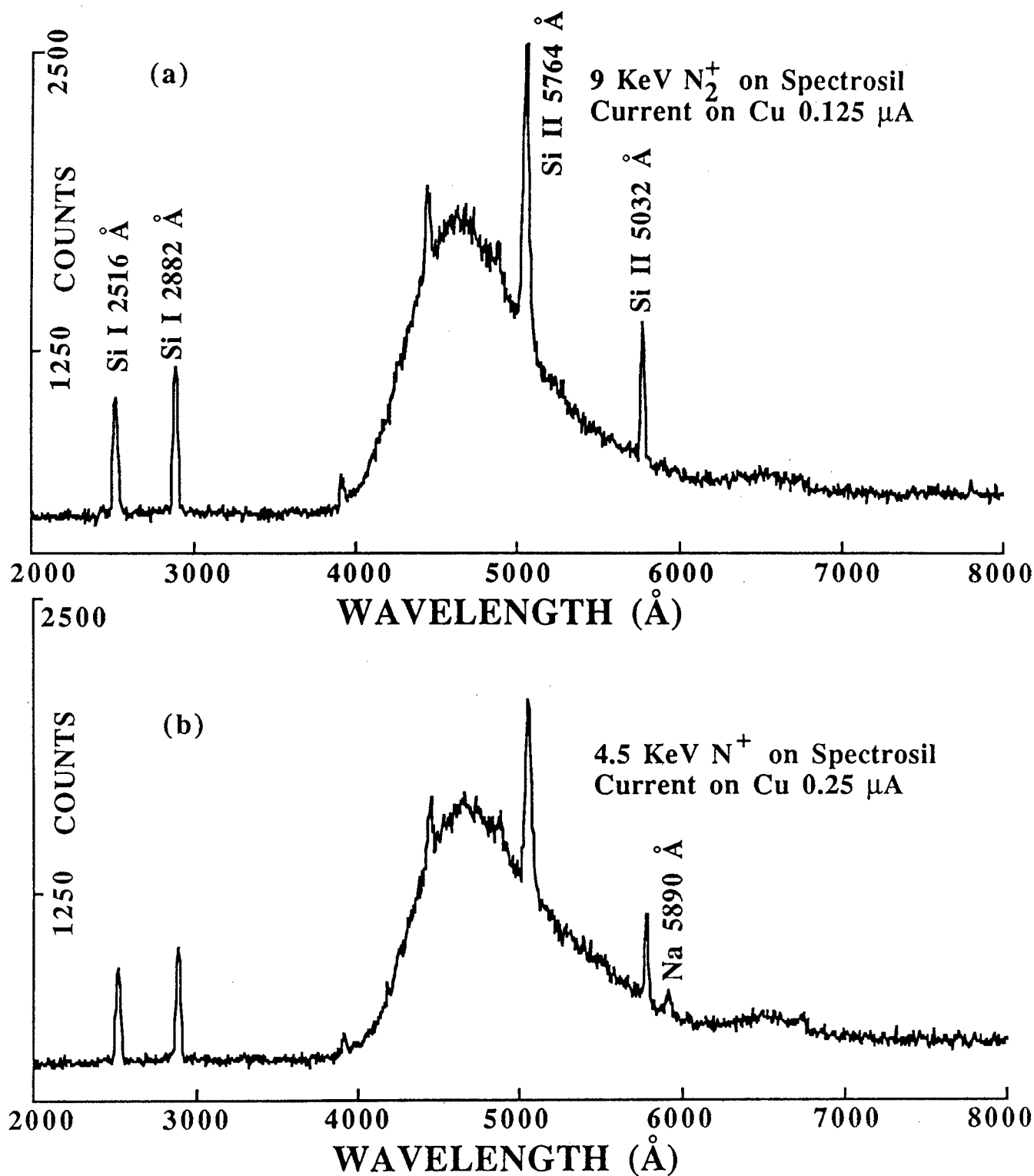


Figure 1. Spectra of Spectrosil bombarded by same energy and number of nitrogen nuclei. Desorbed silicon atoms are more by N_2^+ (a) than N^+ (b) but sodium desorbed only by N^+ .

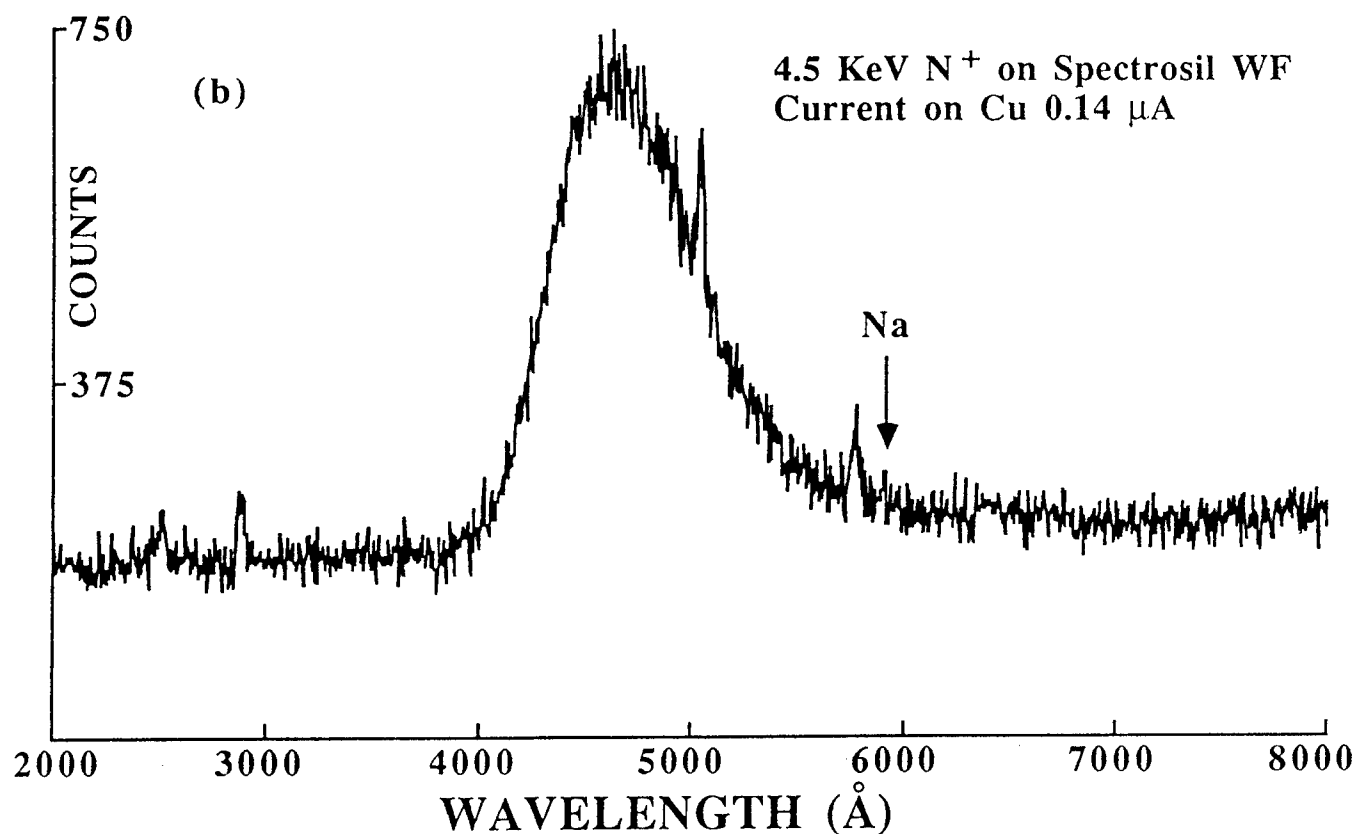
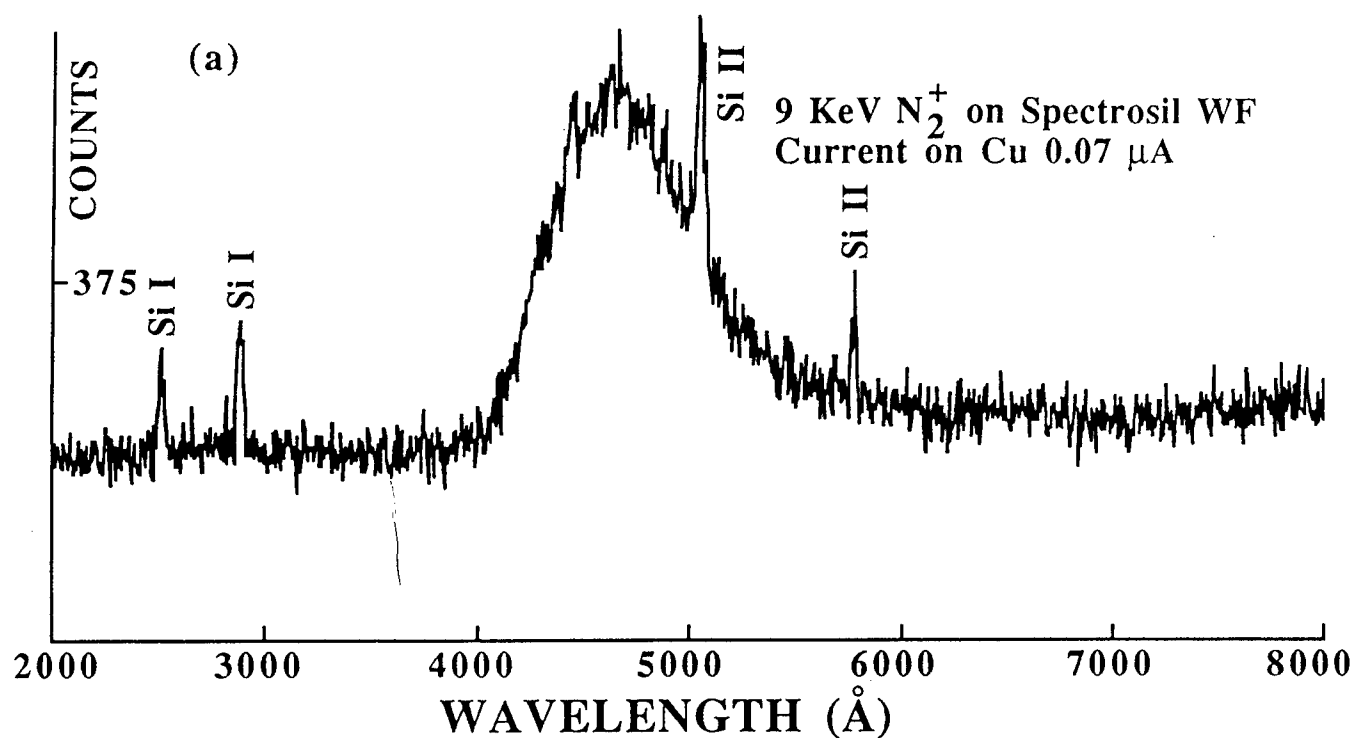


Figure 2. Same number and energy density nitrogen nuclei, N_2^+ sputtered more silicon atoms (a) than N^+ (b). A little sodium line is observed in (b).

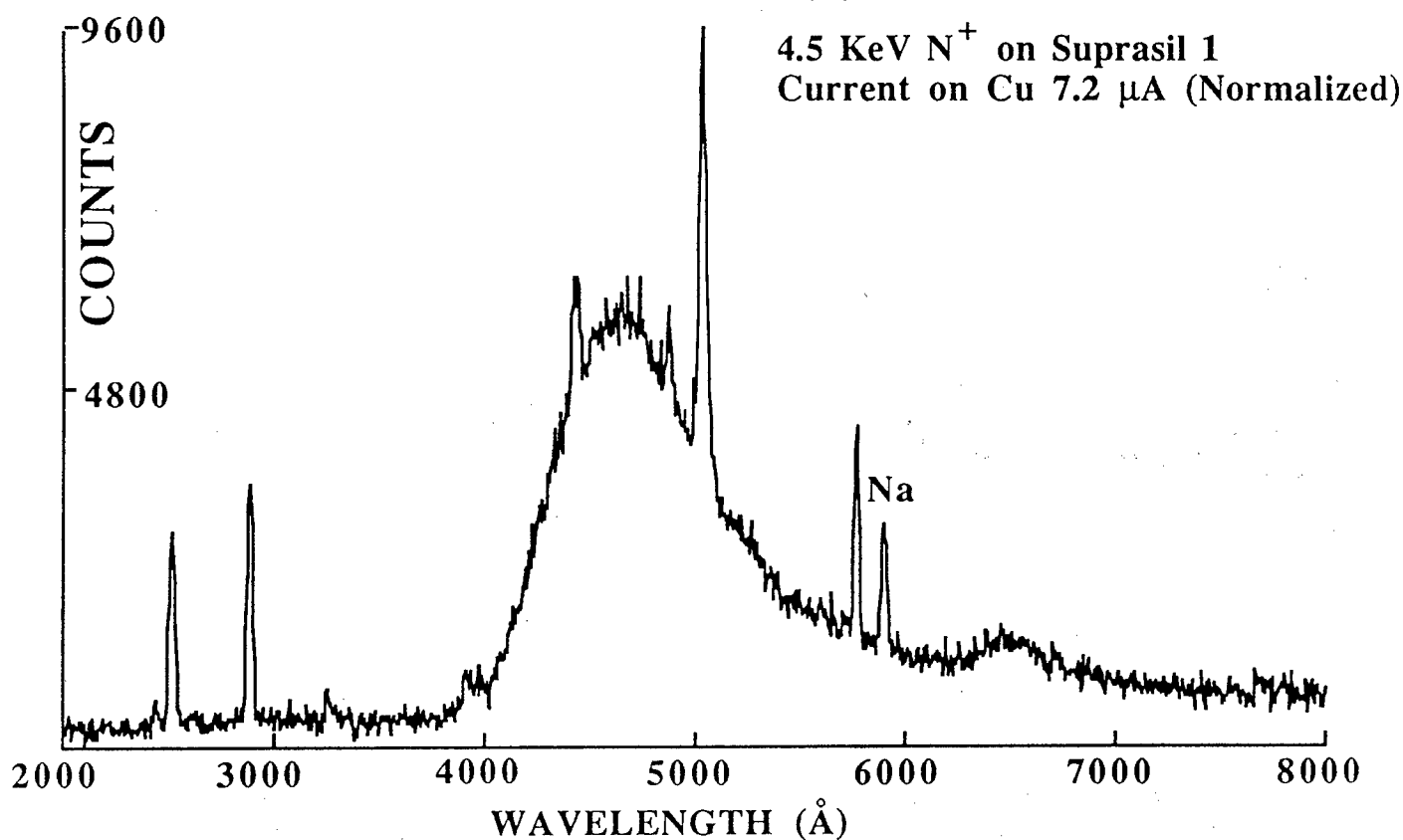
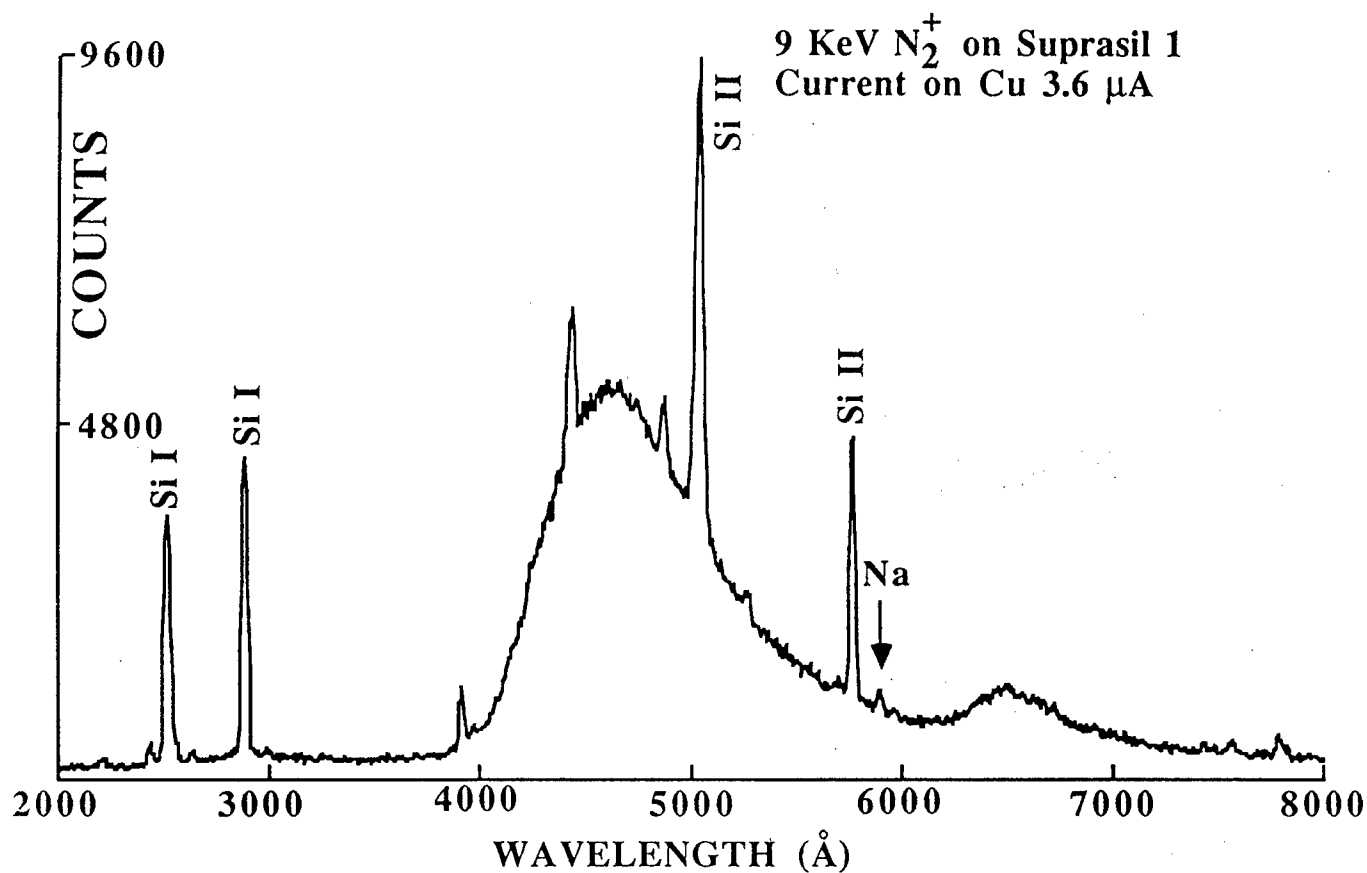


Figure 3. N_2^+ is more effective to desorb silicon atoms from Suprasil 1 but N^+ knocks out more sodium atoms.

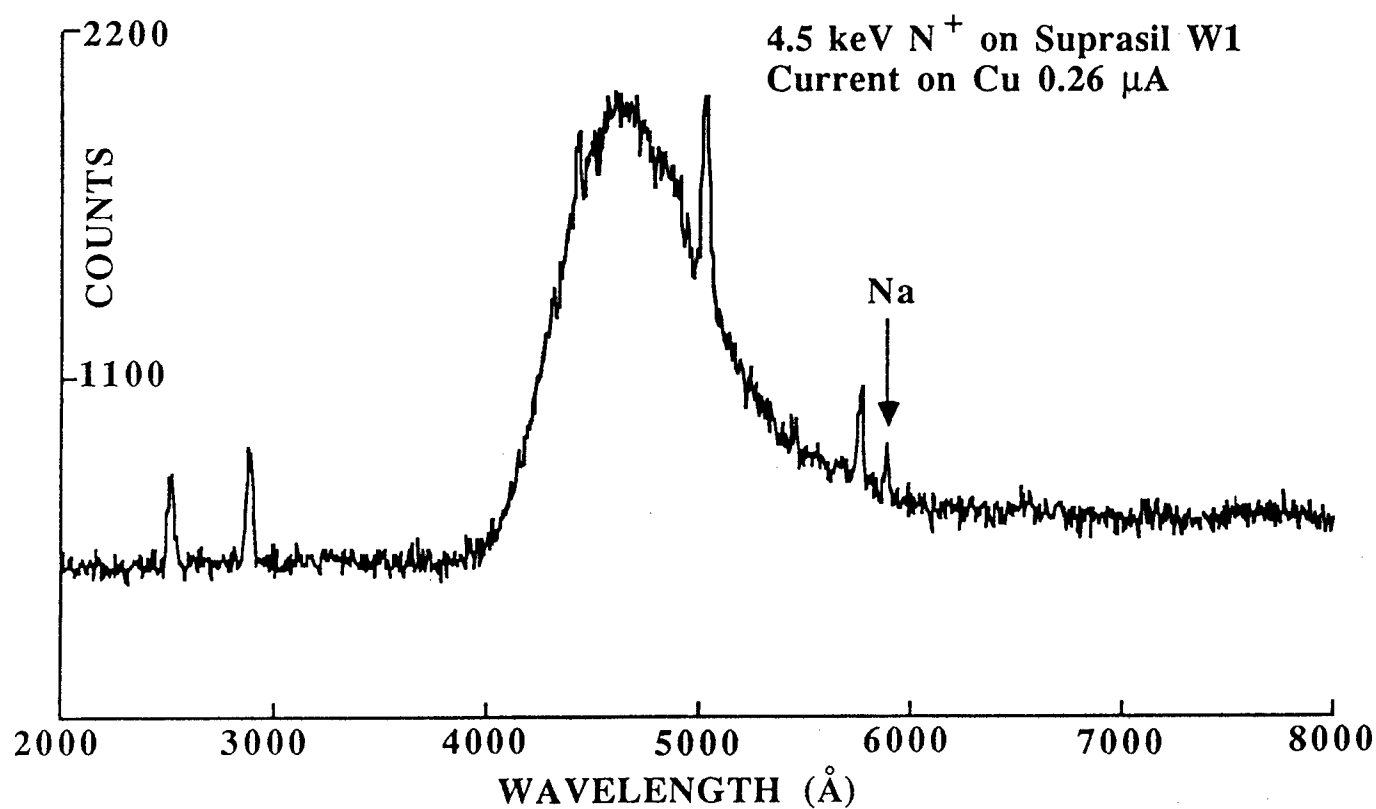
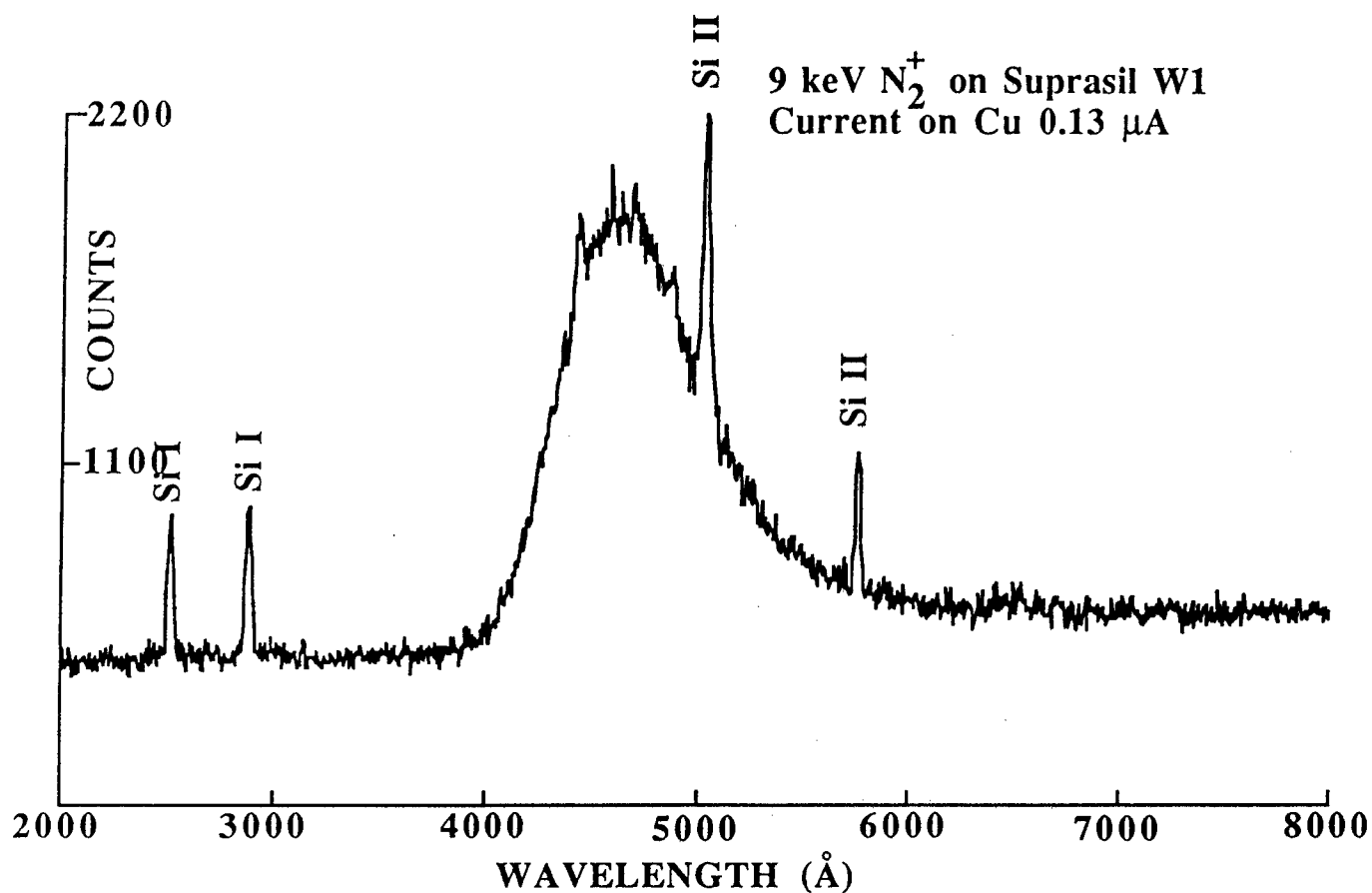


Figure 4. N_2^+ knocked out more silicon atoms than N^+ on Suprasil W1 and N^+ sputtered sodium atoms.

Secondary Electron Excitation as a Possible Mechanism for Shuttle Glow

P. H. Bunton, R. F. Haglund, Jr., J. Rose and L. J. Wang

Center for Atomic and Molecular Physics at Surfaces

Vanderbilt University, Dept. of Physics and Astronomy, Box 1807-B, Nashville, TN 37212

A number of recent studies have pointed to secondary electron emission as a factor in the production of excited states of atoms and molecules following irradiation of surfaces. We have observed some correlations between secondary electron emission and excited atom radiation in photon-stimulated desorption experiments, and believe this may be a factor which needs to be taken into account in studies of excited atoms and molecules on or near surfaces in low earth orbit.

I. Introduction

The problem of glow of spacecraft in low earth orbit has been discussed in many papers and will not be reviewed here.¹ Also, a few commendable mechanisms for shuttle glow have been proposed that are at least plausible and do a fair job of accounting for the glow observations.² A particularly insightful paper by I. L. Kofsky and J. L. Barrett (*Planet. Space Sci.*, Vol. 34, No. 8 (1986) pps. 665-681) pointed out that perhaps too much attention had been paid to the energy of the incident oxygen atoms and not enough to the chemistry of recombination on surfaces. They point out that the incident oxygen serves to condition the surface resulting in recombination of adsorbed molecules which are emitted in excited states. It is the purpose of this paper to discuss the relationship of electron yield from an irradiated surface and the existence of excited atomic

states above that surface, *i.e.*, we will examine the possibility that the existence of glow is consistent with the desorption of ground state neutral particles under combined ultraviolet and particle irradiation which are then excited by electrons which are also emitted during the course of irradiation (For brevity these electrons will be termed secondary electrons even though the term is usually reserved for electrons resulting from electron irradiation). Note that this is not the same as previously proposed plasma mechanisms as those mechanisms relied on ambient electrons rather than those emitted from the material.

The results which will be referred to herein are not necessarily obtained from "spacecraft materials" but from materials with simpler structures that nonetheless one has reason to believe behave in a manner similar to the materials of interest. This requires some justification other than the fact that they are the materials with which we are accustomed to working. The results presented here were obtained mostly from alkali-halides; the primary justification for using insulators to model a spacecraft surface lies in the fact that the surface probably is not a metal but a metal oxide. If one can understand the mechanisms responsible for excited particles above these comparatively simple materials, perhaps generalizations can be extended to more complex surfaces.

II. Plausibility Argument

The first step in showing that secondary electron excitation is a possible mechanism for space glow involves showing that the ground state neutrals needed are likely to be available and that indeed secondary electrons are likely to excite them. It is known that for alkali-halides ground state neutral particles surpass excited states or ions as the dominant means of erosion under UV, electron, ion, and neutral irradiation by at least two orders of magnitude.³ A likely mechanism for their desorption has been proposed which is to some extent independent of the irradiating species

as it only requires as a first step the production of excitons in the crystal.⁴ (The excitons become self trapped and then decay into an F center H center pair. The H center begins a focused collision sequence leading to halogen desorption; the F center defuses to the surface where it neutralizes an alkali ion leading to the emission of a neutral ground state alkali in thermal equilibrium with the surface.) In short one does not need to account for the presence of ground state particles in front of the shuttle surface; they will be there due to desorption from the metal oxide insulator surface under combined ultraviolet and atomic oxygen bombardment (or in fact any incident radiation with enough energy to produce excitons). It has also been proposed that the yield of excited state alkalis from alkali halides under electron irradiation is due to secondary electron excitation.⁵

Figure 1 shows the yield of excited Na from uncleaned NaCl during ultraviolet irradiation as a function of incident photon energy. The excited sodium in front of the surface was monitored by observing its deexcitation radiation with a McPherson 218 spectrometer and photomultiplier tube. When these data are compared with secondary electron yields from NaCl under synchrotron irradiation over the same photon energy range (See R. Haensel, *et al*, *Physical Review Letters*, Vol. 23, No.

Photon Stimulated Desorption
Yield of Na* from NaCl

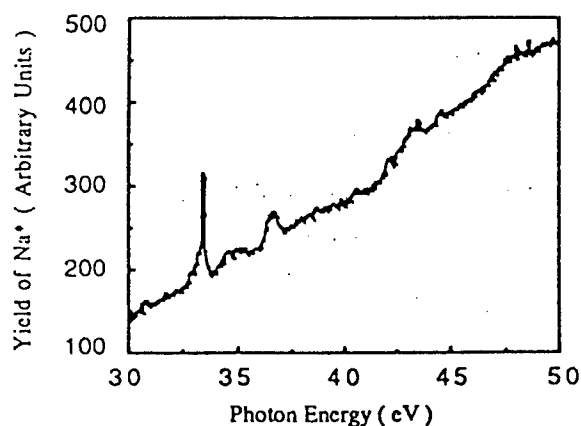


Figure 1 : Yield of excited Na (denoted by Na*) from NaCl during irradiation by 30 - 50 eV ultraviolet light.

10 (8 Sept. 1969) pps. 530-532 for the photoelectron spectra.), it is immediately evident that the two curves have the same structure giving strong evidence for the excited Na being due to secondary electron excitation. Of course alternatively the two processes may be due to the photon

absorption following the same general structure as can be seen in the same reference. For further evidence that the excited Na emission is due to secondary electrons see reference 5 and for the opposing view see reference 6.

The next important point to be made in support of secondary electron excitation is that the presence of oxygen would probably enhance the process. Figure 2 shows secondary electron yield as a function of oxygen pressure for Ar^+ incident on Ni. Note the strong enhancement of secondary electron yield as the pressure increases. If a corresponding process occurs for NaCl and assuming that the Na^* is due to secondary electrons, one would expect the yield of Na^* to increase as a function of partial pressure of oxygen. Figure 3 shows the yield of Na^* as a function of oxygen pressure under 0-order synchrotron irradiation. Again the data were taken at the Synchrotron

Change in Electron Yield from Ni as Oxygen is Introduced.

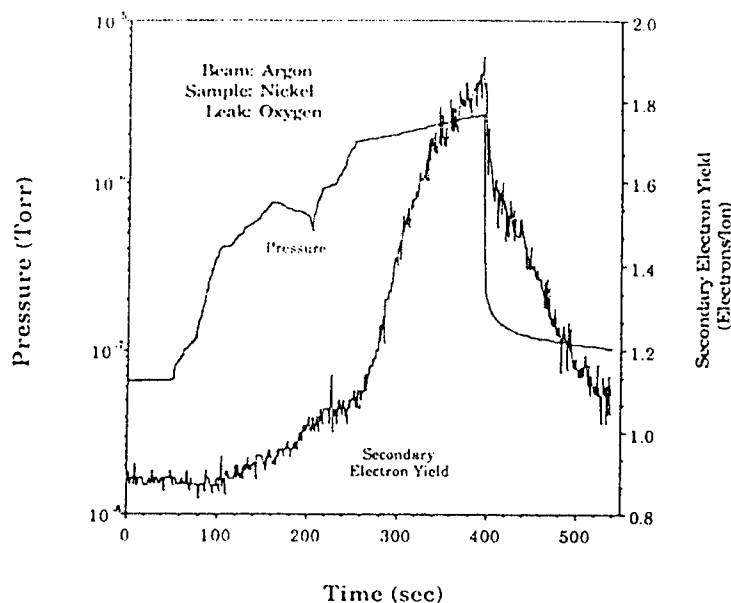


Figure 2: Change in electron yield from nickel under argon bombardment as oxygen is introduced.

Photon Stimulated Desorption Yield of Na^* from NaCl Dosed with Oxygen

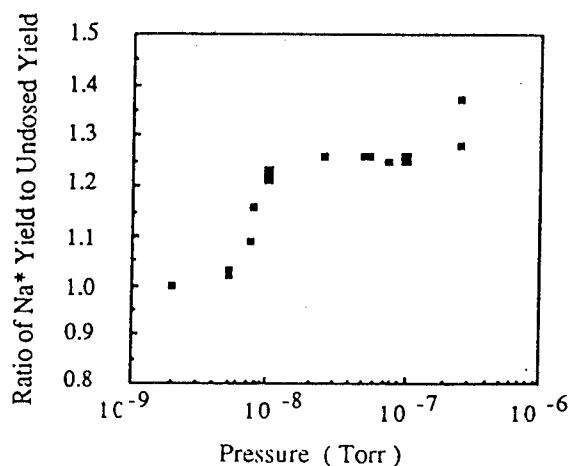


Figure 3 : Increase in excited Na yield from NaCl under 0-order synchrotron irradiation as oxygen is introduced. Error bars have not been determined.

Radiation Center with the same geometry as described above. In these cases the sample was cleaned by heating to ~ 500 C. The data were then obtained by observing the deexcitation radiation while maintaining a given partial pressure of molecular oxygen and irradiating with 0-order synchrotron light. Each point represents net counts obtained by scanning the spectrometer across the Na D doublet. The important point is that the yield of Na* does increase as suggested.

Here is a summary of the above discussion:

- * On alkali-halides ground state neutral desorption prevails.
- * On nickel the presence of O on the surface (due to dissociated O₂) increases the yield of electrons under ion irradiation.
- * With NaCl the excited states seem to track the electron yield.
- * On NaCl the presence of oxygen increases the yield of Na* under UV irradiation.
(Perhaps another case of the electron yield increasing due to the oxygen.)

These observations by no means prove but at least make plausible the following sketch of glow in the low earth orbital environment:

- * Incident particles striking the shuttle adsorb and release energy to the surface.
- * By a somewhat radiation-independent mechanism based on the formation of excitons which then produce point defects, ground state neutral molecules are desorbed.
- * The presence of oxygen on the surface enhances the yield of electrons under UV and particle irradiation.
- * The electrons excite the desorbed ground state neutrals resulting in glow.

The above discussion is admittedly vague; for example, what ground state neutrals are excited? Two candidates for the source of the glow are NO or NO₂.⁸ If enough of either exists in the shuttle bay to account for the glow; it merely needs an excitation mechanism. A proposed and possibly even correct mechanism is formation of excited NO or other molecules by recombination on the surface followed by desorption.⁹ If one takes secondary electron excitation into account, the molecule need not be excited prior to desorption. The NO (or almost any molecule you care to propose) could be excited into higher vibrational levels after desorption. This excitation mechanism would perhaps be termed a gas phase or even plasma process. T. G. Slanger (*Geophysical Res. Lett.*, Vol. 13, No. 5, p. 431) has argued based on geometrical considerations that plasma processes are not a viable option. However, processes due to secondary electron excitation would be at least as directional as emission of excited states from the surface and perhaps more so due to the angular dependences of the ground state molecular emission and the secondary electron emission being folded together.

This mechanism is in agreement with one other bit of data based on flight experiments, that is, the failure to find any correlation between erosion rates and glow intensity. Taking secondary electron excitation into account would imply that one should actually try to correlate the glow to the electron yield rather than the mass yield. If glow is indeed due primarily to secondary electron excitation then efforts to prevent it should concentrate on materials that have low secondary electron yields which can most likely be translated into high band gaps. Admittedly some data exist which would seem to contradict this. E. Murad (*Physics of Space Plasmas*, Vol. 6) reports that carbon cloth and anodized aluminum seem to glow less than the insulators MgF₂ and polyethylene. However, we have not located sufficient data to make an accurate comparison of the electron yields from those materials. Also, with so much oxygen striking the surfaces under

consideration one has to wonder if the conductors are not actually converted to metal oxides.

III. Experimental Description and Results

The above considerations led us to propose the following experiment. Four alkali halide samples were irradiated with ultraviolet radiation from the Vanderbilt-SRC 6-meter TGM beamline at the University of Wisconsin's Synchrotron Radiation Center. Desorption of excited alkali atoms were monitored by detecting the deexcitation radiation with a McPherson 218 spectrometer and a photomultiplier tube. *Simultaneously*, photoelectrons were monitored by biasing a piece of stainless steel near the sample at 9 V and recording the resultant current with an electrometer and analog to digital convertor. Since the excited state and photoelectron data were taken simultaneously, no normalization to incident photon flux was necessary. Also, any doubt that differences in energy spectra might be due to sample history or improper energy calibration can be ruled out. It should also be pointed out that the data were reproducible for different counting times.

Figure 4 shows both photoelectron yield and excited K yield from KCl and KBr under UV irradiation. Both striking similarities and differences can be observed immediately. Toward the higher photon energies the spectra look remarkably similar; however, the electrons exhibit a pronounced peak at lower energies which is not so evident for the excited K. This difference at lower photon energy could be due to one or more of at least three possibilities. First, the photoelectrons may not have sufficient energy to cause excitation of K. Second, perhaps the incident photon energy is low enough that comparatively few ground state K atoms are emitted.

Yield of Excited K and Photoelectrons from KCl Irradiated with Ultraviolet Light

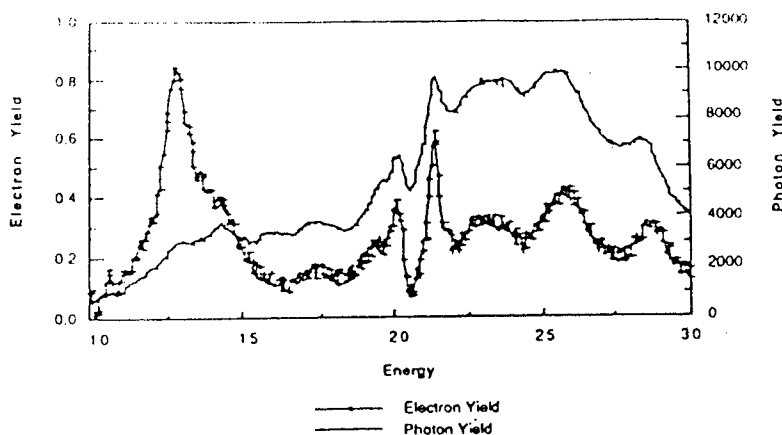
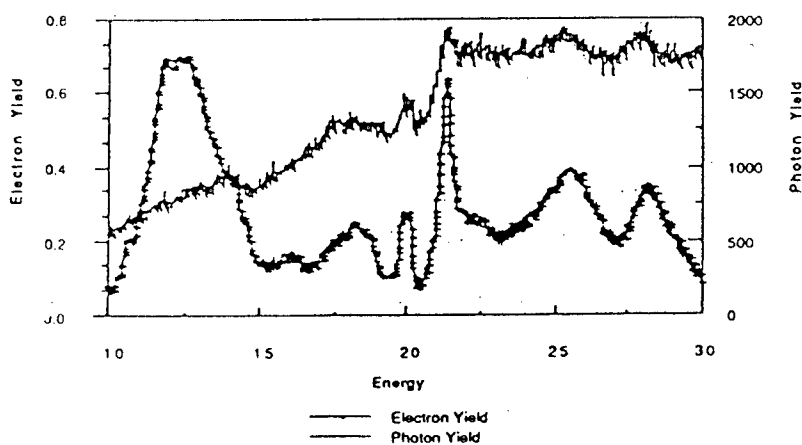


Figure 4 : Simultaneous yields of photoelectrons and excited K atoms from KCl and KBr under 10 - 30 eV ultraviolet light irradiation. Units for electron and excited state yields are arbitrary. Excepting the large photoelectron peak at lower energies, the electron and excited state yields look very similar.

Yield of Excited K and Photoelectrons from KBr Irradiated with Ultraviolet Light



Finally, the excited K may not be due to the electrons at all in that energy regime.

Further evidence that the photoelectrons are not the only source of excited particles above alkali halide surfaces is shown in figure 5. Again both excited atom and photoelectrons were monitored simultaneously but this time for LiF and NaCl targets. The scans were taken across

peaks in the energy spectra that have been attributed to core exciton formation based on absorption studies. *Note that the photoelectron and the excited atom peaks are shifted slightly in energy.* The shifts are admittedly small but reproducible. If the excited states were being produced by electron excitation, the peaks would be in the same place. It is worth noting that if the data had not been taken *simultaneously*, the shifts would have gone unnoticed due to their small magnitude relative

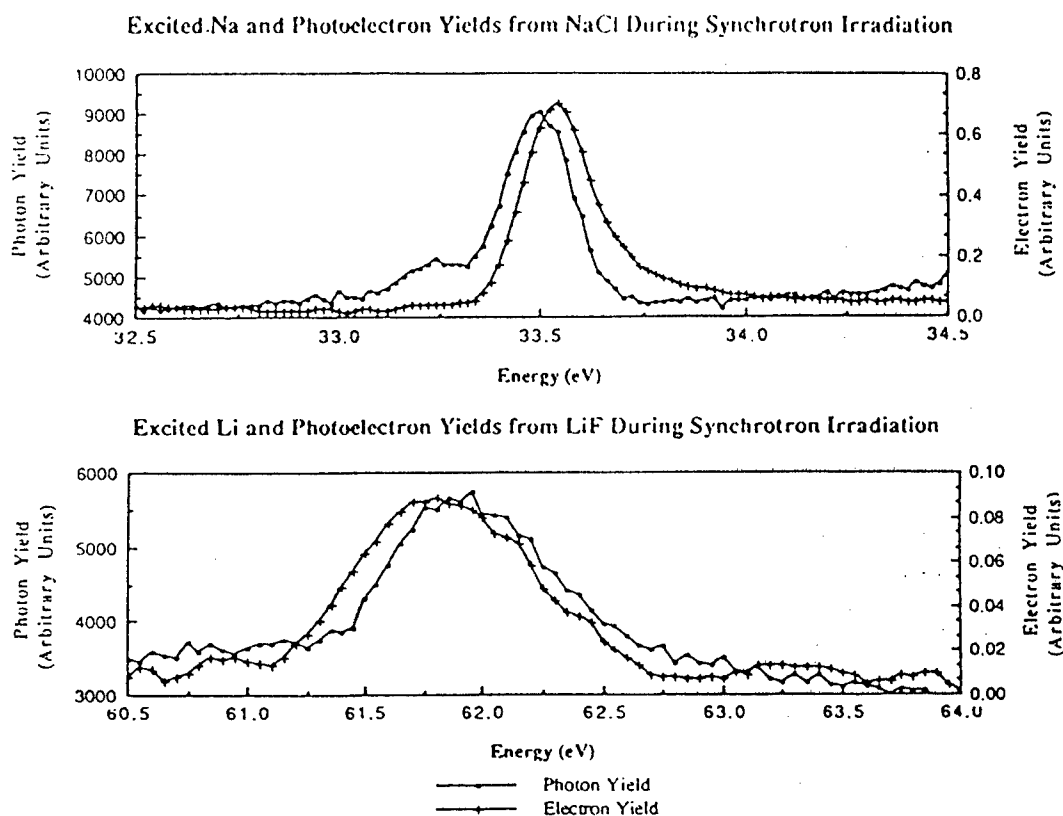


Figure 5: Simultaneous yields of photoelectrons and excited alkali atoms from NaCl and LiF. Note that the electron and excited atom peaks are shifted in opposite directions for the two crystals.

to the monochrometer resolution at the slit widths used. Furthermore, note that for LiF and NaCl the shifts are in opposite directions. This indicates that they are not due to some sort of systematic

error in the measurement technique as that would result in shifts in the same direction. These data indicate that in at least some cases the excited states and the electrons both result from processes that require as a precursor step the formation of core excitons. The shifts would then indicate that the excitons responsible are formed at either different depths relative to the crystal surface or perhaps at slightly different locations on the surface.

IV. Conclusion

At least for alkali halide crystals it can be concluded that while secondary electron emission is a plausible contributor to deexcitation radiation above surfaces, it is not the only source of radiation. Simultaneous yields of photoelectrons and excited particles under ultraviolet irradiation show enough similarities to indicate that photoelectrons are probably at least partially responsible for the excited state atom yield. However, sufficient differences exist to indicate that the electrons are not the only source. Rather indications are that the photoelectrons and the excited states emitted from alkali halide surfaces during irradiation by photons of the energies considered here may both be due to processes that first require the formation of core excitons. One cannot rule out the possibility that many of the excited atoms are due to photoelectron excitation; however, one can with some certainty say that they are not the only source. In order to make a definitive statement one would also need to measure ground state yields simultaneously. This is a much more difficult experiment as it requires the use of laser induced fluorescence to detect the ground states. As regards "space materials" all that can be said at the moment is that while electron excitations should be considered as contributing to glow, based on experiments with "simple" materials there is no reason to expect that they are the only source.

Acknowledgements

N. Tolk of Vanderbilt University was a help in motivating and discussing these measurements. D. P Russell and D. L. Harper, also of Vanderbilt, took the data on nickel. R. Rosenberg of the Synchrotron Radiation Center was also a great help in acquiring and understanding these data.

References

1. See for example M. R. Torr, *Geophys.Res.Lett.*, **10** No. 2, 114-117 (Feb. 1983); S. B. Mende, *et al*, *Geophys.Res.Lett.* **10** No. 2, 122-125 (Feb. 1983); R. G. Albridge, *et al*, *Nucl. Inst. Meth. Phys. Res.* **B18**, 582-586 (1987); B. D. Green, *et al*, *Planet. Space Sci.* **34** No. 9 , 879-887 (1986); B.D. Green and E. Murad, *Planet. Space Sci.* **34** No. 2 219-224 (1986).
2. B. D. Green, *et al*, *Planet. Space Sci.*, **34**, No. 9, 879-887 (1986); I. L. Kofsky and J. L. Barrett, *Planet. Space Sci.*, **34**, No. 8, 665-681 (1986); T. G. Slinger, *Geophy. Res. Lett.* **13**, No. 5 431-433 (1986); B. D. Green, *Geophys. Res. Lett.* **11**, No. 6, 576-579 (June, 1984).
3. N. G. Stoffel, *et al*, *Phys.Revi. B* **32**, No. 10, 6805-6808 (15 Nov. 1985); R. F. Haglund, *et al*, *Nucl. Inst. Meth. Phys. Res.* **B13**, 525-532 (1986).
4. G. M. Loubriel, *et al*, ; R. F. Haglund, *et al*, *Nucl. Inst. Meth. Phys. Res.* **B13**, 525-532 (1986).

5. R. E. Walkup, *et al*, Phys. Rev. Lett. **57**, No. 17 2227-2230 (27 Oct. 1986).
6. R. F. Haglund, *et al*, Nucl. Inst. Meth. Phys. Res., **B13** 525-532 (1986).
7. R. Haensel, *et al*, Phys. Rev. Lett. **23** No. 10, 530-532 (8 Sept. 1969) pps..
8. B. D. Green and E. Murad, Planet. Space Sci. 219-224 (1986).
9. B. D. Green, W. T. Rawlins and W. J. Marinelli, Planet. Space Sci. **34** No. 9, 879-887 (1986).

UV Responses in GeO₂ Glasses

Robert H. Magruder, III, Donald L. Kinser

John M. Jackson and Robert A. Weeks

Department of Materials Science and Engineering

Vanderbilt University

Nashville, TN 37235

Abstract:

The fusion temperature (T_ϕ), the oxygen partial pressure (P_{O_2}) during melting, and the quenching rate from T_ϕ all influence the optical absorption around 245 nm in glassy GeO₂. The 245 nm absorption was substantially reduced by exposure to UV radiation. Recovery of the absorption occurred with thermal annealing. These observations are consistent with the assumption that the defect responsible for the optical absorption is an oxygen vacancy. The hypothesis of detrapping of the specie which bleaches the oxygen deficient absorption is consistent with the assignment of the trapped specie to be an electron or hole.

Introduction

The optical absorption of glasses has been observed to be modified by UV radiation since the early work of Faraday¹ in 1824. Similar phenomena have been observed in a number of glasses. The research reported here is concerned with the UV absorption in high purity GeO₂ glasses. The UV absorption band at 245 nm (5.06 eV) was first reported by Garino-Canina² who noted that increasing the glass fusion temperature increased the magnitude of the absorption. He also used this absorption peak to monitor the diffusion of oxygen³ in the GeO₂ glass at temperatures of approximately 400°C. Cohen and Smith⁴ reported bleaching of the UV absorption at 244.5 nm by exposure to "UV radiation" in GeO₂ glasses whose preparation was inadequately described. The UV spectral data was extended to ~50 nm by the reflection measurements of Pajasova.⁵ The glasses used for these measurements were prepared by differing melting techniques. Subtle reflectivity differences are evident in these data. To our view, these differences arise from preparation conditions.

We have recently reexamined⁶ Pajasova's results and conclude that the oxygen deficiency leads to spectral features related to those of metallic germanium. Vergano and Uhlmann⁷ utilized the UV absorption of the 245 nm band to characterize the extent of nonstoichiometry in glasses whose crystallization behavior they were studying. They noted that deviations in stoichiometry to the metal rich side of stoichiometry led to increases in crystallization rate which they attributed to decreases in viscosity. Kordas et al^{8,9} have shown that the intensity of two paramagnetic states observed in GeO₂ glasses is dependent upon the temperature, T_ϕ , at which their glass melts were equilibrated.

Experimental Procedure

Our glasses were prepared as previously described.¹⁰ The glasses were melted and equilibrated at T_ϕ 's ranging from 1450 to 1650°C using electronic grade GeO₂ in 40 ml platinum crucibles. The samples were cooled in the crucible at measured cooling rates of approximately 5°C/sec from T_ϕ to 400°C. Samples with cooling rates from the T_ϕ temperatures of 0.2°C/sec and approximately 10⁶°C/sec were obtained by cooling the melt in the furnace by shutting off the furnace and by splat cooling, respectively. The splat cooling was accomplished by heating a premelted glass with an oxygen-natural gas torch at temperatures T_ϕ ~1700°C. After a short period of time, a drop formed which then fell through a photocell activating two solenoid driven stainless-steel anvils. Samples prepared by this technique were disks approximately 2.5 cm in diameter and 0.5-1 mm thick. Typical neutron activation analyses of glasses melted for this work are reported in reference 10. Samples were removed from the crucible by core drilling a cylinder from the crucible and slicing samples perpendicular to the axis of the resulting cylinder. Samples were cut and polished

using petroleum lubricants with a final polishing abrasive of 0.25 micron diamond powder. Two samples were prepared for each measurement with thicknesses ranging from 100 to 300 microns. Sample thicknesses were measured to an accuracy of 10% in an optical microscope by noting the stage travel between focus on opposite surfaces, and correcting by the index of refraction (1.605).

Optical measurements in the 350 nm (3.54 eV) to 200 nm (6.2 eV) range were made using a Cary 14 dual beam spectrometer with the thinner sample of the pair placed in the reference beam and the other in the sample beam. This technique eliminated reflection losses which interfere with measurements of large absorption coefficients.

Samples were bleached by exposure to radiation from a 400 watt quartz envelope low pressure mercury vapor lamp at a distance of approximately 5 cm from the lamp. A high velocity air jet was directed at the sample during exposure so as to avoid heating of the sample during exposure. The measured intensity of UV radiation at the sample location averaged 1.7 milliwatts/cm² during the exposures. Thermal annealing was conducted in an air atmosphere furnace with temperature regulation of $\pm 10^\circ\text{C}$.

Results

Figure 1 presents the absorption coefficients as a function of photon energy for $T_\phi = 1650$, 1550, 1450, 1350, and 1200°C. The 5.06-eV (245-nm) absorption band reported by Garino-Canina^{2,3} and Cohen and Smith⁴ is clearly present in each of the glasses examined. The complete absorption band in the $T_\phi = 1650$ and 1550°C samples is unresolved because of the high optical density in the region of the peak. The peak of the 5.06-eV (245-nm) band is resolved in glasses with $T_\phi < 1450^\circ\text{C}$. For these glasses, adequate response of the spectrometer was observed down to ~ 5.6 eV (215 nm) in agreement with previous work.^{3,4} We were able to calculate as reported¹⁰ previously the activation energy for this peak as 2.3 ± 0.1 eV. The 5.06 eV peak is seen to decrease with T_ϕ for $T_\phi \leq 1450^\circ\text{C}$ and the low energy side is seen to decrease with decreasing T_ϕ for all samples.

Figure 2 shows the results of samples fused at 1650° and cooled at rates of 0.2 and 5°C and samples with fusion temperatures estimated at $1700 \pm 50^\circ\text{C}$ which had cooling rates of approximately 10^6°C/sec . While the data from the splat cooled samples has a large scatter, in all cases the absorption on the low energy side is greater than for samples cooled at lower rates.

Figure 3 gives the results obtained from glasses with $T_\phi = 1550^\circ\text{C}$ equilibrated in atmospheres with $P_{\text{O}_2} = 0.2$ and 2.0 and glasses with $T_\phi = 1450^\circ\text{C}$ equilibrated in atmospheres $P_{\text{O}_2} = 0.2$ and 1.0. The effect of increasing oxygen partial pressure is to decrease the optical absorption associated with the 5.06 eV (245 nm) peak.

The optical absorption spectra of a glass fused and equilibrated at $T_{\phi}=1450^{\circ}\text{C}$ for a series of exposures to UV radiation are shown in Figure 4. The unirradiated spectra displays the prominent absorption peak at 245 nm (5.06 eV) which is substantially identical to the peak in Figure 1 for $T_{\phi} = 1450^{\circ}\text{C}$. Exposure of this glass to UV radiation for times up to 31.2 days (76 joules/cm²) leads to a substantial depression of the 245 nm absorption. Subsequent exposure up to 94.1 days (230 joules/cm²) leads to no subsequent detectable decrease. Hence the bleaching process saturates without complete removal of the shoulder on absorption bands at lower wavelength. Similar responses were observed in the glasses prepared with T_{ϕ} 's of 1550 and 1650°C.

The absorption spectra were fitted by assuming that the 245 peak is Gaussian in shape and the absorption at lower wavelengths is fitted by the exponential (Ae^{-Bx}). This function is that appropriate for an absorption edge, i. e. band to band transition. The resulting Gaussian equation, describing the 245 nm band, was then reduced using Samakula's equation and the assumption that the oscillator strength is unity to give a defect concentration responsible for the observed absorption. These defect concentrations as a function of UV exposure are plotted as a function of log UV exposure in Figure 2. Assuming that $\ln n = a \ln t$, the slope decreases monotonically with increasing T_{ϕ} . The slope of the defect concentration in the $T_{\phi} = 1450^{\circ}\text{C}$ glass has a much larger slope than the corresponding $T_{\phi}=1550$ or 1650°C glasses. The probable error, resulting from the spectroscopy measurement errors propagated through the above described data reduction technique are largest in the data for the $T_{\phi}=1650^{\circ}\text{C}$ glass. The typical error for that case is shown on the 1650°C data. The saturation of the optical absorption with UV exposure is evident at the largest dose in the 1450 and 1550°C glasses. A decrease is observable in the $T_{\phi} = 1650^{\circ}\text{C}$ glass although the errors are large compared to the decrease in n after the largest exposure time. The data for the $T_{\phi}=1450$ and 1550°C glasses indicate that the bleaching process is completed for the longest exposure time.

The effect of isochronal anneals of glasses exposed to saturation UV dose is to increase the intensity of the 245 nm absorption band. The concentration of the defect responsible for the 245 nm band grows with thermal anneals as is shown in Figure 3. Assuming that $\ln n/n_0 \propto 1/kT$ the slope of the concentration versus isochronal annealing temperature is greatest for the $T_{\phi}=1450^{\circ}\text{C}$ and decreases with increasing T_{ϕ} . The concentration of defects present in the unirradiated glasses are shown as an asymptote in each case. The concentration of defects after annealing is less than the initial concentration for annealing temperatures up to 300°C. The cumulative annealing time for a sample annealed at 300 C was 15 hours. Diffusion of oxygen into the sample during annealing may have occurred. This diffusion produces an irreversible decrease in intensity of the 245 nm band as described by Garino-Canina.³

Discussion

From the behavior of the 245 nm band with T_ϕ and partial pressure of oxygen over the melt liquid, we have previously concluded that an oxygen vacancy complex is responsible for this band. The behavior of this oxygen defect was determined to be more complex than a simple oxygen vacancy. The concentrations of defects calculated using Samakula's equation were found to exhibit Arrhenius behavior with T_ϕ . The lower T_ϕ and higher oxygen vapor pressure result in smaller numbers of oxygen vacancies. Hence the strength of this 245 nm absorption can be controlled by T_ϕ and P_{O_2} . In addition the quenching rate also has a marked effect on the 245 nm absorption. Increasing the quench rate succeeds in quenching in concentration more characteristic of the T_ϕ . However, no cooling rate will preserve the vacancy concentration characteristic of T_ϕ . The fact that samples with a range of T_ϕ can be quenched to room temperature at constant rate and subsequently display concentrations which are Arrhenius with T_ϕ indicates that a constant fraction of these defects was quenched in each sample.

The bleaching or reduction in the intensity of the 245 nm absorption peak shown in Figure 4 indicates that the UV radiation is either populating or depopulating an electronic state associated with oxygen deficient sites in the glass. This bleaching response is evident in glasses equilibrated at 1450, 1550 and 1650°C.

Results of observations of the bleaching measurements on each of the glasses are summarized in Figure 5 which displays the logarithm of the absorption center concentration as a function of bleaching time. The absorption center concentration as a function of bleaching time for the 1450°C glass appears to fall with UV exposure at a faster rate than the glasses equilibrated at 1550 or 1650°C. This more rapid decrease may arise from differing bleaching kinetics or from the fact that the 1450°C glass is more transparent to the UV radiation as seen from Figure 1 thus permitting a larger fraction of the absorbing sites to be activated. We have not been successful in modeling the phenomena to distinguish between these two possible explanations because of the polychromatic light used in the experiments.

The isochronal annealing results of bleached samples shown in Figure 6 indicate that the concentration of defect sites responsible for the 245 nm absorption has undergone approximately $1/e$ of its annealing at temperatures of approximately 180°C. This suggests that kT at 180°C or ~ 0.04 eV is the approximate height of the barrier between the bleached and unbleached state. We suggest that a charge is excited by UV radiation from an unidentified site within the glass and is trapped at the oxygen deficient site. This trapping reduces the absorption at 245 nm. Subsequent annealing processes thermally detrap this charge and it diffuses back to its original position.

We have examined the normalized thermal annealing process for each of the three glasses and, after normalization, the behavior of each of the glasses is identical within experimental error

limits. The barrier height determined by assuming a constant rate of heating (actually a series of isochronal anneals at incremental increasing temperatures) and a delta function distribution of traps is 0.044 eV.¹¹ This indicates that the thermal detrapping process, for glasses equilibrated during melting at differing temperatures T_ϕ , is identical with a barrier height of 0.044 eV. Thus we conclude that similar defect sites are involved in thermal removal of bleaching in all three glasses.

The process which gives rise to the rate determining step in thermal annealing of the bleached defect appears to be electronic because of its low activation energy. The activation energy for oxygen diffusion in these glasses has been determined to be 1-1.2 eV^{3,12} thus the bleaching process does not involve oxygen diffusion.

Conclusions:

1. The T_ϕ , atmosphere P_{O_2} and quenching rate dependencies of the 5.06 eV (245 nm) absorption peak in GeO_2 glasses are consistent with an oxygen vacancy or complex of vacancies causing the absorption.
2. Thermal detrapping of the specie which bleaches the oxygen deficient absorption center at 245 nm in GeO_2 glasses indicates that the trap depth is 0.044 eV.
3. The activation energy for detrapping suggests that the trapped specie is an electron or hole.

Acknowledgements

The authors gratefully acknowledge the financial support of the US Army Research-Durham under contract number DAAG29-84-K-0143.

References

1. M. Faraday, "Sur la Coloration produite par la lumiere, dans une espece particuliere de carreaux de vitres", *Annale de Chimie et de Physiq*, 25, 99-102, 1824.
2. V. Garino-Canina, *C. R. Acad. Sci.* 247, 593 (1958).
3. V. Garino-Canina, *C. R. Acad. Sci.* 248 1319 (1959).
4. A. J. Cohen and H. L. Smith, *J. Phys. Chem. of Solids* (Pergamon, NY 1958), Vol. 7, pp. 301-306.
5. L. Pajasova', *Czech. J. Phys. B* 19, 1265 (1969).
6. N. M. Ravindra, R. A. Weeks and D. L. Kinser, "Optical Properties of GeO_2 ", *Phys. Rev. B*, 36 6132-6134 (1987).
7. P. J. Vergano and D. R. Uhlmann, *Phys. Chem. Glasses* 11, 30 (1970).

8. G. Kordas, R. A. Weeks and D. L. Kinser, J. Appl. Phys. 54, 5394 (1983).
9. G. Kordas, R. Weeks, and D. L. Kinser, Glastech. Ber. 56K, 141 (1983).
10. J. M. Jackson, M. E. Wells, G. Kordas, D. L. Kinser, R. A. Weeks and R. H. Magruder, III, "Preparation effects on the UV optical properties of GeO₂ Glasses", J. Appl. Phys, 58, 2308-2311, 1985.
11. R. J. Borg and G. J. Dienes, An Introduction to Solid State Diffusion, pp 228 ff., Academic Press, NY, 1988.
12. M. Wells, Master's Thesis, Vanderbilt University, 1983.

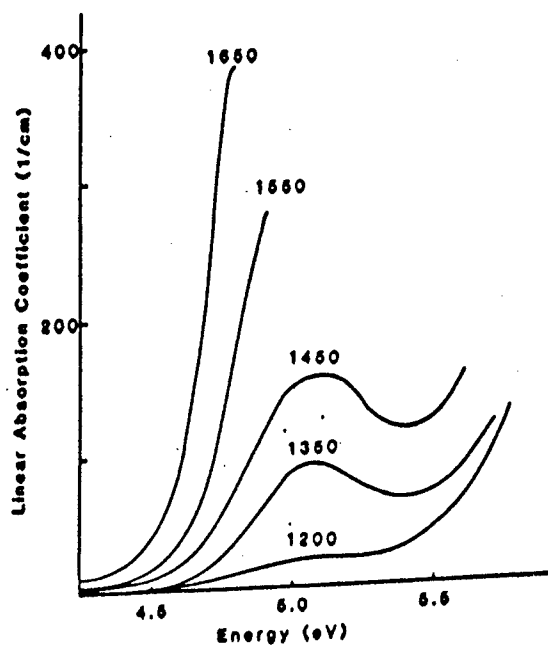


Figure 1. Linear absorption coefficient in GeO₂ glass as a function of photon energy for 1200°C < T_φ < 1650°C, P_{O2} = 0.2 atm and cooling rate 5°C/sec.

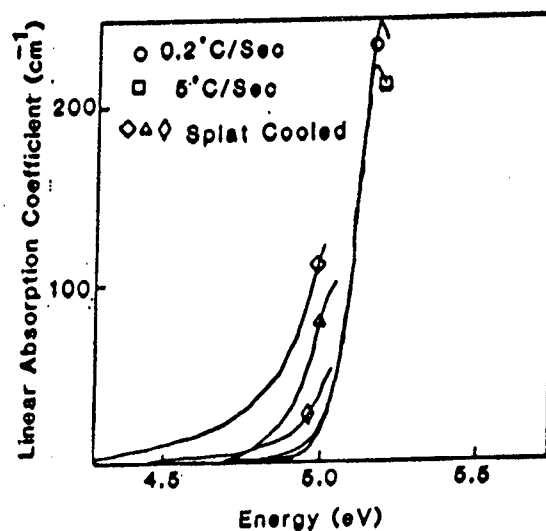


Figure 2. Linear absorption coefficient vs photon energy for GeO₂ glass of T_φ = 1650°C, P_{O2} = 0.2 atm cooled at different rates as noted.

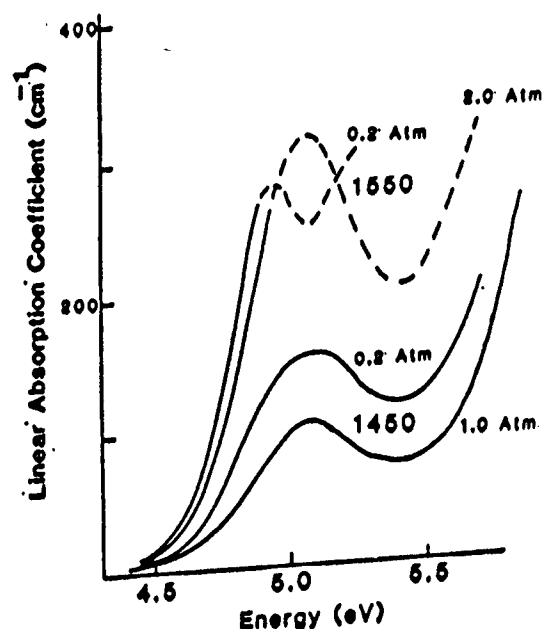


Figure 3. Linear absorption coefficient vs photon energy in GeO_2 glass $T_\phi = 1450$ and 1550°C at oxygen partial pressures as noted with cooling rate of $5^\circ\text{C}/\text{sec}$.

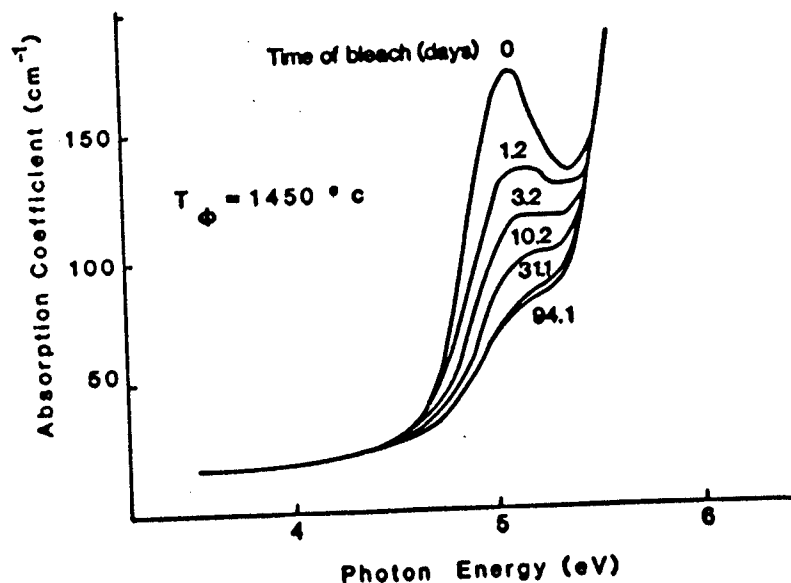


Figure 4. Absorption coefficient (α) as a function of energy for bleaching times from zero to 94.1 days (zero to 230 joules/ cm^2) for a glass with $T_\phi = 1450^\circ\text{C}$.

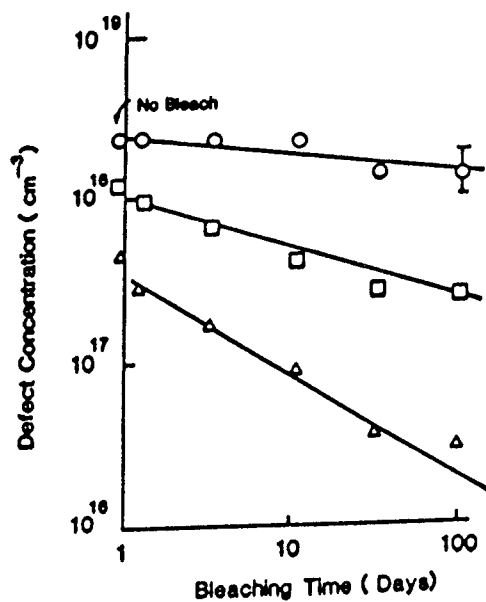


Figure 5. Defect concentration as a function of UV bleaching time for glasses with $T_\phi = 1450, 1550, 1650^\circ\text{C}$.

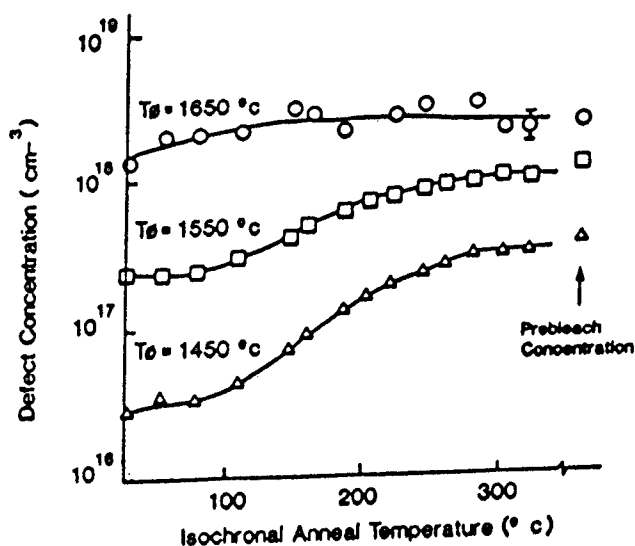


Figure 6. Defect concentrations as a function of annealing temperature for 1 hr isochronal anneals.

The Role of Microstructure in Determining Critical Currents in 1:2:3 High Temperature Polycrystalline Superconductors

J.D. Stark, R.H. Magruder, III and D.L. Kinser
Materials Science and Engineering Department
Vanderbilt University, Nashville, TN 37235

Quantitative microscopy techniques were used to characterize the microstructures of samples of varying grain sizes. The measured critical current densities, J_c , were found to rise linearly with $1/d^3$ (d = median grain diameter). This effect of grain size on the critical current density is modeled as a percolation-type process. The percolation pathway is composed of weakly-linked, Josephson-coupled grains.

I. INTRODUCTION

Bednorz and Müller¹ inspired an unprecedented number of reports on high temperature superconductor (HTSC) materials. This paper focusses on the relationship between critical current and microstructure of the 123, Y-Ba-Cu HTSC materials.

The physical picture of polycrystalline ceramic superconductors is one of good superconducting grains separated by weak links. Although the cause of these weak links is not well understood, the general consensus is that they are intergranular Josephson junctions. These weak links limit the critical current density, J_c , in the polycrystalline materials. This limit on J_c is a major problem in fabricating devices from these materials. There are several reports in the literature which report increasing J_c by melt-textured growth², grain alignment³ and improving the chemical purity of the material⁴.

Larbelieuter, et al.⁵, have shown from magnetic data that the current flow in their material follows a very tortuous path.

This indicates a large amount of decoupling of good superconducting region and thus a percolation controlled conduction process.

Critical current and grain size data from the literature are difficult to compare due to the differing processing conditions and measurement techniques. There are reports in the literature that decreasing grain size results in increasing critical current. Nakahara, et al.⁶, found that smaller grain size leads to increasing J_c , however, they changed sintering conditions to achieve grain size variation. Chiang, et al.⁷, reported increasing J_c with decreasing grain size but used different powder processing and sintering conditions. It is thus difficult to compare the reported critical current densities with respect to grain size because in each case other processing parameters were also changed. The objective of this paper is to determine the relationship between critical current and grain size while maintaining other processing variables constant.

II. EXPERIMENTAL PROCEDURE

Samples of $\text{YBa}_2\text{Cu}_3\text{O}_{9-x}$ superconductors were prepared by mixing stoichiometric amounts of the starting materials¹ BaCO_3 , CuO , and Y_2O_3 and calcining in air at 950°C for 24 hrs. The mixture was ground and calcined three times. After the third grinding the powder was separated according to particle size using sieves with openings of $150\ \mu\text{m}$, $75\ \mu\text{m}$, and $38\ \mu\text{m}$. The different size powders

¹ACS Reagent Grade Materials.

were then each pressed into pellets at a pressure of 4500 psi and sintered in an oxygen atmosphere at 955°C for 20 hrs.

Samples were cut, weighed, coated with paraffin and reweighed. Archimedes density measurements were performed on these samples using water with a wetting agent to minimize the formation of bubbles on the samples.

Samples were cut, mounted and polished for examination in the SEM. Quantitative microscopy was performed on scanning electron micrographs taken of the samples at a magnification of 350X. The average grain size was determined by measuring the maximum dimension of at least 70 grains and then determining the mean and standard deviation. The median grain size was determined by plotting the distribution of these measured grain sizes for each sample. The grain boundary surface area per unit volume, S_v , was determined by the linear intercept technique.⁸

Conductivity measurements were made using the four probe method and a closed cycle helium refrigerator unit with temperature controller. The transition temperature ranges were determined using the 10%-90% method.⁵

Critical current measurements were made on samples which were mounted on alumina substrates and necked. Indium electrodes were applied to the sample and the four probe technique was used. Critical current measurements were made while samples were immersed in a liquid nitrogen bath. The measured current did not exceed 2 amps and there was no evidence of joule heating. The superconductivity criterion was dictated by the 10 μ V sensitivity of the voltmeter that was used.

III. RESULTS

The results of the critical current measurements, grain size, transition temperature and density measurements made in this work are presented in Table 1. The transition temperature breadth, ΔT_c , were measured and observed to be approximately 3 K in all samples. Transition temperatures for the material as prepared were $93 \text{ K} \pm 4 \text{ K}$. The densities of the samples fell in the range 4.02 g/cm^3 to 4.40 g/cm^3 which is 64% to 70% of the theoretical density. The measured grain size distributions are presented in Figures 1a to 3a. The grain size distribution for the smallest grain size sample is much tighter than is that of the coarser samples. Samples sintered from powders where $d < 38 \text{ }\mu\text{m}$ and $38 \text{ }\mu\text{m} < d < 75 \text{ }\mu\text{m}$ show grains which are greater than the original powder size thus evincing grain growth during sintering. Representative scanning electron micrographs of the three types of samples examined are presented in Figures 1b to 3b.

The critical current measurement results as a function of $1/d^3$ (d = median grain diameter) are shown in Figure 4 for samples employing identical processing variables but differing particle size. The critical current results of Jin, et al.², who used similar processing conditions and reported a grain sizes between $5 \text{ }\mu\text{m}$ and $10 \text{ }\mu\text{m}$ are plotted in Figure 5 with our results. These plots strongly suggest a $J_c \propto 1/d^3$ relationship.

The successful application of quantitative microscopy techniques to determine particle sizes requires an assumption (commonly spherical) of the grain shape. If the shape changed

among the samples employed here then the relationship of grain boundary area to grain diameter would necessarily change. The measured grain boundary area as a function of grain diameter cubed is plotted in Figure 6. The linearity of this plot is evidence that the grain shape does not change amongst the samples examined.

IV. Discussion

A number of other reports^{2,3,7} of increasing critical current with decreasing grain size have appeared but these results not been obtained from samples prepared with identical thermal processing. We have achieved a limited range of grain sizes while maintaining equivalent processing as Table 1 indicates. Jin, et al.², reported critical current measurements on samples prepared by a technique similar to ours and these results fit the $J_c \propto 1/d^3$ relationship established by our results.

The electronic behavior of granular superconductors has been successfully modeled as a percolation process.⁹ Hence, it seems appropriate to model the behavior of the polycrystalline ceramic superconducting materials in a similar manner. Larbalestier, et al.⁹, have concluded that, "the grains or subsection of the grains are almost totally decoupled from each other", based upon magnetic measurements. They continue, "In a percolation model, the critical current, I_c , is determined entirely by a very small, good quality contact".

Bulk superconductivity, as determined by a resistance measurement, requires that the current flow intergranularly as well as intragranularly. Our observations suggest that additional pathways, arising from additional grains present, result in a higher number of superconducting pathways thus permitting a higher critical current. This observation suggests a percolation process in a network of good superconducting grains connected by weak links. The current will be limited by the establishment of a cluster of size sufficient to span the distance between the electrodes. This cluster will consist of a series of weak links of varying strength depending on the quality of the contacts (i.e., contact area, distance between grains, crystallographic mismatch, etc). The current carrying capacity of a path will depend on the weakest of the weak links. As the number grains per unit volume is increased, two things happen. The surface area available to form good contacts between adjacent grains increases thus increasing the probability of creating a path of maximum strength weak links. Second, an increase in the number of grains increases the probability that a pathway of maximum strength weak links exists by allowing more possible paths.

Clem, et al.¹⁰, have given the following expression for the critical current density, J_c , due to tunneling between grains for the weak links of the Josephson junction type:

$$J_c = J_0 = I_0/A \text{ and } I_0(T) = [\pi \Delta^2(T)]/[4eR_n k_B T_c]$$

where A is the cross sectional area of the grain, I_0 is the

Ambegaokar-Baratoff¹¹ expression for the critical current near T_c , $\Delta(T)$ is the temperature-dependent gap parameter, R_n is the normal-state tunneling resistance of a junction, and k_B is the Boltzmann constant. The maximum current will depend on the weakest of the links in a connected cluster. The more grains per unit volume the greater the probability of a quality contact at the weakest link. This corresponds to a lower value of R_n and, therefore, a larger value of J_c in the above equation. It is not surprising that J_c scales with surface area and the number of grains per unit volume. Because of this observation, and the greater total surface area for increased contact, we would expect the limit of the increase in J_c to be determined by the intra-crystal film material. The percolation model will fail when the size of the grain approaches the coherence length. As we increase the number of possible paths in the cluster we expect the probability of achieving this pathway to increase.

V. CONCLUSIONS

1. Critical current density is increased with decreasing grain size with a functional relationship of $J_c \propto 1/d^3$ where d is the median grain diameter.
2. A percolation model can describe the physical behavior of critical current and grain size.
3. The percolation model predicts an increasing critical current with decreasing grain size until grain size is on the order of the coherence length.

References

1. J.G. Bednorz and K.A. Müller, Z. Phys. B64, 189 (1986).
2. S. Jin, R.C. Sherwood, T.H. Tiefel, R.B. van Dover, G.W. Kammlott, M.E. Davis, R.A. Fastnacht, S. Nakahara, M.F. Yan, and D.W. Johnson, Jr., Mat. Res. Soc. Symp. Proc. 99, 773 (1988).
3. S. Jin, T.H. Tiefel, R.C. Sherwood, M.E. Davis, R.B. van Dover, G.W. Kammlott, R.A. Fastnacht, and H.D. Keith, Appl. Phys. Lett., 52(24), 2074 (1988).
4. J.E. Blendell and M.D. Vandin, Preprint to be published.
5. D.C. Larbalestier, S.E. Babcock, X. Cai, M. Daeumling, D.P. Hampshire, T.F. Kelly, L.A. Lavanier, P.J. Lee and J. Seuntjens, HTSC Mat. Mech. SC, Interlaken (Switzerland) Feb. 29 - Mar. 4, 1988.
6. S. Nakahara, G.J. Fisanick, M.F. Yan, R.B. van Dover, T. Boone, and R. Moore, J. Crystal Growth 85, 639 (1987).
7. Y.M. Chiang, J.A.S. Ikeda, and A. Roshko, Am. Cer. Soc. Symp., (Cincinnati, Spring 1988), Preprint to be published.
8. R.T. DeHoff and F.N. Rhines, Quantitative Microscopy, (New York, McGraw-Hill (1968)).
9. G. Deutscher, O. Entin-Wohlman, S. Fishman, and Y. Shapira, Phys. Rev. B 21(11), 5041 (1980).
10. J.R. Clem, B. Bumble, S.I. Raider, W.J. Gallagher, and Y.C. Shih, Phys. Rev. B 35(13), 6637 (1987).
11. V. Ambegaokar and A. Baratoff, Phys. Rev. Lett. 10, 486 (1963); 11, 104(E) (1963).

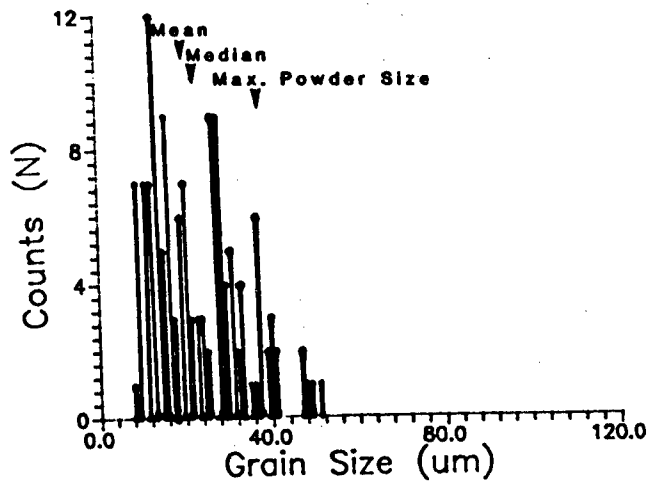
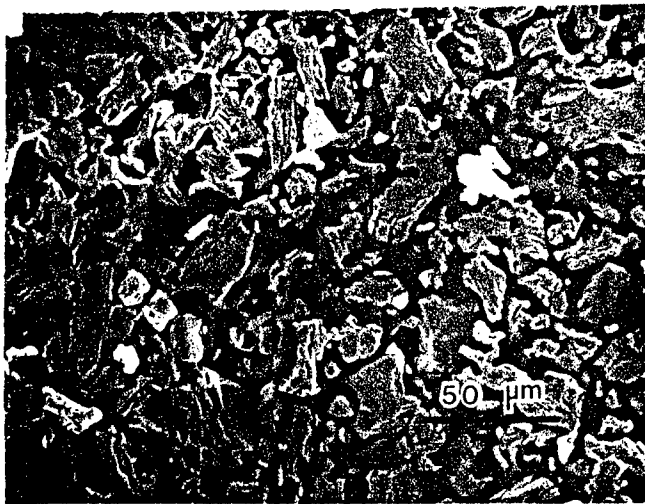


Figure 1. (a) SEM micrograph of sample sintered from powder -400 mesh screen size ($38\text{ }\mu\text{m} < d$) and (b) Grain size distribution for same sample.

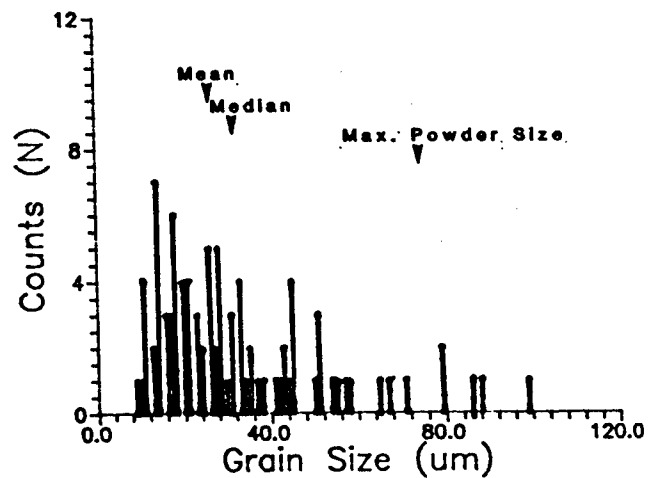


Figure 2. (a) SEM micrograph of sample sintered from powder -200+325 mesh screen size ($45\text{ }\mu\text{m} < d < 75\text{ }\mu\text{m}$) and (b) Grain size distribution for same sample.

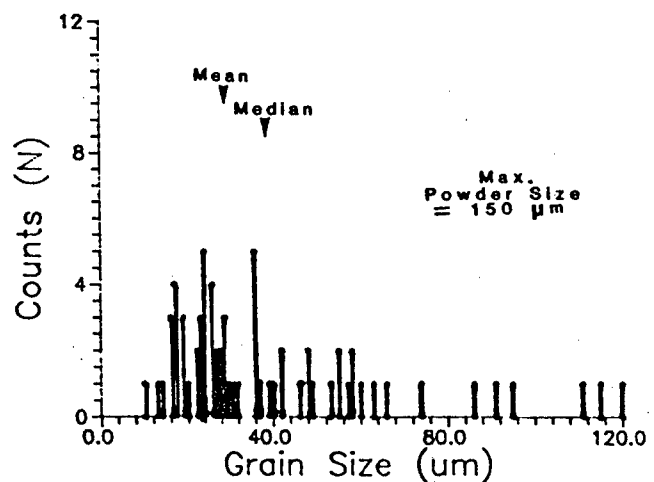


Figure 3. (a) SEM micrograph of sample sintered from powder -100+200 mesh screen size ($75\text{ }\mu\text{m} < d < 150\text{ }\mu\text{m}$) and (b) Grain size distribution for same sample.

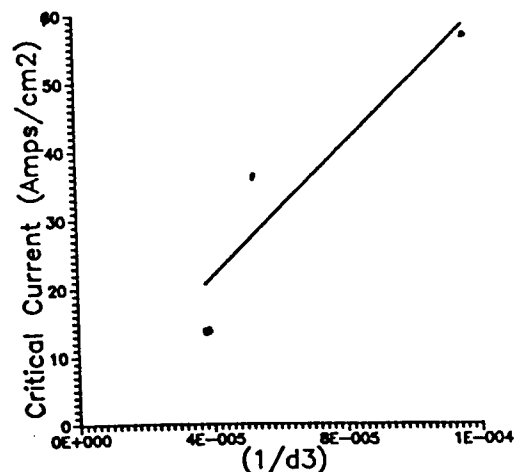


Figure 4. Graph showing the linearity of critical current density, J_c , as related to $1/d^3$ for samples shown in Figures 1-3.

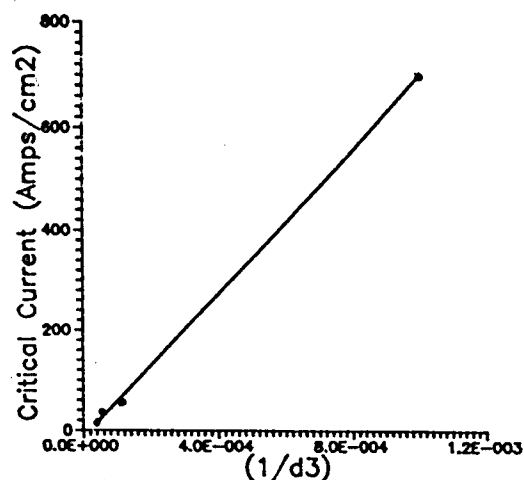


Figure 5. Graph showing critical current density, J_c , vs. $1/d^3$ for data from this study combined with data from Jin, et al.²

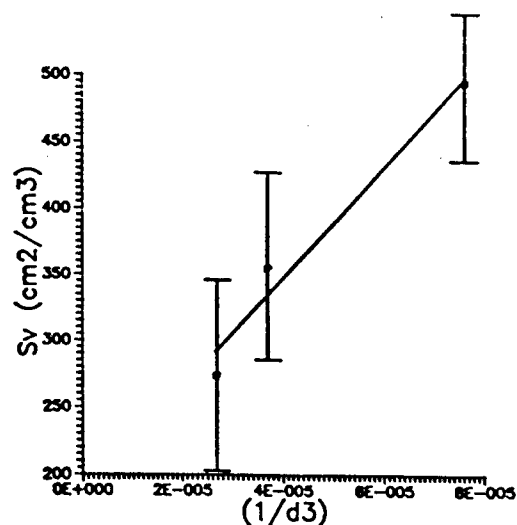


Figure 6. Graph showing the linearity of grain boundary surface area, S_v , in relation to $1/d^3$.

Table 1. Summary of Results

Grain Size				Archimedes Density		
Powder (μm)	Median (μm)	Mean (μm)	σ_{n-1} (μm)	S_v (cm^2/cm^3)	I_c (A/cm^2)	ρ (g/cm^3)
d < 38	20.5	23.0	10.2	492	57.0	4.02
45 < d < 75	26.5	32.1	19.2	356	36.5	4.40
75 < d < 150	29.5	39.0	24.8	274	14.0	4.32

ION IMPLANTATION MODIFICATION OF THE SURFACE REGION OF SILICA

G. Whichard, R. A. Weeks, and J. D. Stark
Vanderbilt University, Nashville, TN 37235

ABSTRACT

Transition metal ions (Ti^+ , Cr^+ , Mn^+ , and Fe^+) were implanted into high purity silica to modify the magnetic and optical properties of the surface region. The refractive index of the surface region increases with increasing ion implantation dose. Optical absorption bands, due to radiation damage, are superimposed on the low energy tail of an absorption band. The electron paramagnetic resonance (EPR) spectra show vastly different magnetic characteristics as a function of transition metal ion specie. The EPR studies also indicate that the ion modified surface region contains a mixture of magnetic phases.

INTRODUCTION

Ion implantation is a materials processing technique that can be used to modify the surface region of glasses by varying the chemical composition and creating structural changes in the substrate surface [1,2,3] for applications such as integrated optics, waveguides, and coatings [4]. Ion implantation provides for control of the dopant concentration and thickness of the ion modified surface region. Ion implantation into high purity silica substrates reduces the interference from impurities, thus, the modification of the surface is attributed to the implanted ions only. Transition metal ions were selected for implantation because of the interesting optical and magnetic properties that result from elements with less than full 3d electronic shells [2,5]. The data summarized shows that the ion modified surface region produced by transition metal ion implantation into amorphous silica substrates are novel materials.

PROCEDURE

Ti, Cr, Mn, and Fe ions, in the +1 charge state, were implanted at 160 keV and $4 \mu\text{A}/\text{cm}^2$, into high purity amorphous silica (Spectrosil) substrates to doses ranging from 0.5×10^{16} to 6×10^{16} ions/ cm^2 .

The depth profiles of the implanted ions were measured by ion backscattering techniques using a 2 MeV $^4\text{He}^+$ incident ion beam. The sample surface was at normal incidence to the probing $^4\text{He}^+$ ion beam and the detector was placed at an angle of 165° .

Electron paramagnetic resonance (EPR) spectra of the transition metal ion implanted samples were measured at 9.75 GHz. The spectra were recorded at various orientations of the implanted surface with respect to the applied magnetic field and over a temperature range from 500 K to 9 K.

Optical spectra were measured between 1.0 eV and 6.5 eV in a double beam spectrophotometer. Reflection losses and substrate absorption were compensated for by placing a virgin substrate in the reference beam.

Ellipsometry, which is a technique that analyzes the change in phase and ellipticity of light reflected from a film-substrate interface [6], was used to measure the refractive index and thickness of the ion modified surface layer. Ellipsometric data was measured using a wavelength of 632.8 nm and a 50° angle of incidence. The data was analyzed using a computer program developed by the National Bureau of Standards [7] and assuming the refractive index of the modified surface layer was constant. This model is labeled the "single layer model" [8].

RESULTS

A schematic of a sample containing an ion modified surface region is shown in figure 1. The implanted transition metal ion depth profiles, determined by ion backscattering techniques, are independent, within experimental error, of each ion specie. The depth profiles are Gaussian in shape with a full width at half maximum (FWHM) of approximately $0.14 \mu\text{m}$. The maximum ion concentration is $0.11 \pm 0.01 \mu\text{m}$ from the surface for all samples.

Electron Paramagnetic Resonance (EPR) spectra of the samples exhibit different magnetic characteristics as a function of ion specie. Figure 2 compares the intensities of the EPR signal, at room temperature, for Cr, Mn, and Fe samples implanted with a dose of 6×10^{16} ions/cm². The Fe signal is approximately 40 times greater than the Mn signal and no signal from implanted Cr ions is observed. A sample implanted with titanium, to a dose of 6×10^{16} ions/cm², exhibits an intense E' signal superimposed on the Ti spectrum as shown in figure 3. The E' signal can be resolved in the Fe, Mn, and Cr implanted samples but not with spectrometer parameters similar to those used in figure 3. Manganese implanted samples contain spectral components associated with the implanted Mn ions and the E' center. The temperature dependence of the resonance field, line width, and signal intensity is shown in figure 5 for a Mn implanted sample, and in figure 6 for an Fe implanted sample. The Fe implanted samples contain an E' center spectral component and an orientation dependent signal due to the implanted ion. Only the E' center spectrum has been observed in the Cr implanted samples.

The optical absorption spectra of the Cr, Mn and Fe implanted samples, measured over an energy range of 1.0 eV to 6.5 eV, have three absorption features resolved at energies greater than 2.5 eV. These absorption features are a band at 5.0 eV, an inflection at 5.8 eV, and the low energy tail of an absorption band centered at approximately 7.15 eV.

The refractive indices of the Cr, Mn, and Fe modified surface layers, as measured by ellipsometric techniques, are plotted in figure 6 as a function of implantation dose [8]. Although the small changes in the refractive indices of the samples, at doses less than 3×10^{16} ions/cm² are within the magnitude of the experimental error, the refractive indices tend to increase with increasing implantation dose for these samples. The Ti implanted samples show a slight decrease in refractive index at lower doses and a slight increase in the refractive index at the higher doses [9]. The ellipsometric thickness of the modified surface layers is $0.14 \pm 0.01 \mu\text{m}$. This thickness, based on the single layer model is the same within experimental error for all ions and doses studied.

DISCUSSION

The backscattering profiles of the implanted ions are Gaussian in shape. The depth of maximum ion concentration and the FWHM are equal, within experimental error, for each ion specie.

The only EPR signal observed in the Cr implanted samples is the radiation induced E' damage center. Line broadening and saturation behavior of the E' signal indicates a spin interaction between the E' center and the implanted Cr ions. The implanted Cr ions do not exhibit an EPR signal, however a Cr³⁺ EPR signal is reported in glasses doped with Cr₂O₃ [10].

The EPR spectra of the Ti implanted sample contains two components, a line broadened signal attributed to the implanted ion and an E' center signal. The intensity ratio of the E' signal to the Ti signal is much greater than the ratio of the E' signal to the Mn and Fe signal intensities in samples implanted with equal doses.

The Mn EPR signal is independent of the orientation of the implanted surface with respect to the laboratory magnetic field indicating the absence

of long range magnetic order. The behavior of the Mn EPR signal, as a function of temperature in ion implanted silica, is similar to the behavior reported for spin glasses [11,12,13]. This indicates that implantation of Mn in silica produces a spin glass structure.

The Fe EPR signal varies with the orientation of the implanted surface with respect to the laboratory magnetic field, as observed in previous studies [1,14]. This angular anisotropy indicates the presence of long range magnetic order in the plane of the sample surface. This long range ordering increases with decreasing temperature.

The EPR signals discussed above account for only a small fraction of the total number of implanted ions. The temperature dependence of the Mn and Fe EPR signals do not follow a Boltzmann distribution for paramagnetic systems. The rate of increase in the signal intensities, with implantation dose, is greater than expected for a paramagnetic system, indicating the presence of short range magnetic interactions. An order of magnitude greater rate of increase in the EPR signal intensity with dose is observed in the Fe samples as compared to the Mn samples and is attributed to the long range interactions which are present in the Fe samples and absent in the Mn samples. The implanted Cr ions, and the major fraction of the Mn ions not observed in the spin glass state, may contain randomly oriented spins, without long range interactions, that are in another magnetic state, i.e. speromagnetic [11].

The optical absorption, measured as extinction coefficient, is related to the number of ions implanted per cm^2 . The absorptions for each sample are not proportional to the implantation dose, however, the optical absorption spectra for a given dose are similar in shape for all ion species. This similarity in shape, combined with the lack of absorption between 1.0 eV and 2.5 eV, suggests that the absorption spectra are due primarily to radiation damage effects. Previous work [15], on ion implantation, has characterized five distinct absorption bands in the 2 eV to 6.5 eV range attributed to radiation damage; the three presently observed bands at 5.0 eV, 5.8 eV, and 7.15 eV and two additional bands at 4.8 eV and 5.3 eV. Using these five bands, with FWHM and peak positions fixed, and allowing only the peak amplitude to vary, a good fit to the measured optical spectra of the Cr, Mn, and Fe ion implanted silica samples is obtained at all doses. This fit is shown in figure 7 for a Cr implanted sample. The intensities of the five bands necessary for a good fit to the data vary with ion specie and dose.

The refractive indices of the Cr, Mn, and Fe ion implanted surface regions increase with increasing implantation dose for each ion specie. For an implantation dose of 6×10^{16} ions/ cm^2 the magnitude of the refractive index increases with increasing atomic mass of the implanted ion. The behavior of the refractive index of the Ti implanted samples, as compared to the Cr, Mn, and Fe implanted samples, may result from a greater difference in atomic radius and electronic structure [9]. The thickness of the implanted layer determined by ellipsometry is consistent with that obtained by backscattering techniques. A single layer model, which assumes a constant ion concentration from the surface to the ellipsometric depth, was developed to represent the ion modified surface region. The single layer model is a good approximation of the ion implanted region in that the total number of ions in the single layer model is within 10% of the total number of implanted ions measured by ion backscattering [8]. The ion modified surface region is actually more complex than a single layer because the concentration of the implanted ion changes with depth from the surface and the radiation induced damage varies with depth. Refractive index changes of 2% in ion implanted silica have been associated with radiation induced network damage [15,16,17,]. The magnitude of the refractive index changes due to the implanted transition metal ions indicate an ion contribution in addition to the refractive index

change due to the radiation damage.

CONCLUSIONS

The implantation of Ti^+ , Cr^+ , Mn^+ , and Fe^+ ions into high purity silica results in a modified surface layer with optical and magnetic properties different from those produced by introducing the ions by other methods.

The depth profiles of the Ti, Cr, Mn, and Fe ion implanted silica show that the implanted ion distribution is essentially the same for each ion specie.

The intensities of the absorption bands in the optical spectra of the samples studied are not linearly related to the implantation dose. The same bands are observed in each implanted sample but their relative intensities are ion specific.

The refractive index of the ion modified surface layer increases with increasing implantation dose for implanted Cr, Mn, and Fe ions. The refractive index change with increasing implantation dose is related to the atomic mass of the implanted ion [8].

The different magnetic behaviors of the Ti^+ , Cr^+ , Mn^+ , and Fe^+ ion implanted surface regions are a result of the different magnetic interactions associated with the implanted species. A fraction of the implanted Mn ions are in a spin glass state. Some of the implanted Fe ions are in both an ordered planar structure and a ferromagnetic phase. The remainder of the implanted Mn and Fe ions, and possibly all of the Cr ions are in a speromagnetic state. The surface region of high purity silica modified by transition metal ion implantation contains mixed magnetic systems.

REFERENCES

1. R. A. Weeks, M. C. Silva, G. Kordas, D. L. Kinser, J. Martinelli, and B. R. Appleton, Mater. Res. Soc. Symp. Proc. 85, (1985) 59.
2. R. A. Weeks, G. Whichard, G. Kordas, and B.R. Appleton, XIV Intl. Congr. on Glass (1986) 236.
3. A. R. Baly and P. D. Townsend, J. Phys. D: Appl. Phys. 6, (1973) 1115.
4. N. N. Gerasimenko and G. M. Tseitlin, Rad. Effects. 49, (1980) 141.
5. J. D. Stark, R. A. Weeks, G. Whichard, D. L. Kinser, and R. A. Zuhr, J. Non-Cryst. Solids 95 & 96, (1987) 685.
6. R. J. Archer, Manual on Ellipsometry, Gaertner Scientific Corp., Chicago, (1968).
7. F. L. McCrackin, National Bureau of Standards Technical Note 479, (1969). software supplied by Deane Chandler-Horowitz.
8. G. Whichard, H. C. Mogul, R. A. Weeks, J. D. Stark, and R. Zuhr, to be published in Proc. Mater. Res. Soc., April (1988).
9. H. C. Mogul, results to be published.
10. F. Gan and H. Liu, J. Non-Cryst. Solids 95 & 96, (1987) 61.
11. K. Moorjani and J. M. D. Coey, Magnetic Glasses, Elsevier Science Publishing Co., New York, (1984).
12. J. Ferre, J. Pommier, J. P. Renard, and K. Knorr, J. Phys. C: Solid St. Phys., 13, (1980) 3697.
13. J. P. Jamet, J. C. Dumais, J. Seiden, and K. Knorr, J. Mag. and Mag. Materials, 15-18, (1980) 197.
14. D. L. Griscom, J. J. Krebs, A. Perez, and M. Treilleux, Nuclear Instru. Meth. Phys. Res. B32, (1988) 272.
15. M. Antonini, P. Champagni, P. N. Gibson, and A. Manara, Radiation Effects, 65, 41 (1982) 281.
16. R. L. Hines and R. Arndt, Phys. Rev. 119, 2 (1960) 623.
17. E. Schineller, R. Flam, and W. Wilmot, J. Opt. Soc. 58, 9, (1968) 1171.
18. A. R. Bayly, Rad. Effects, 18, (1973) 111.

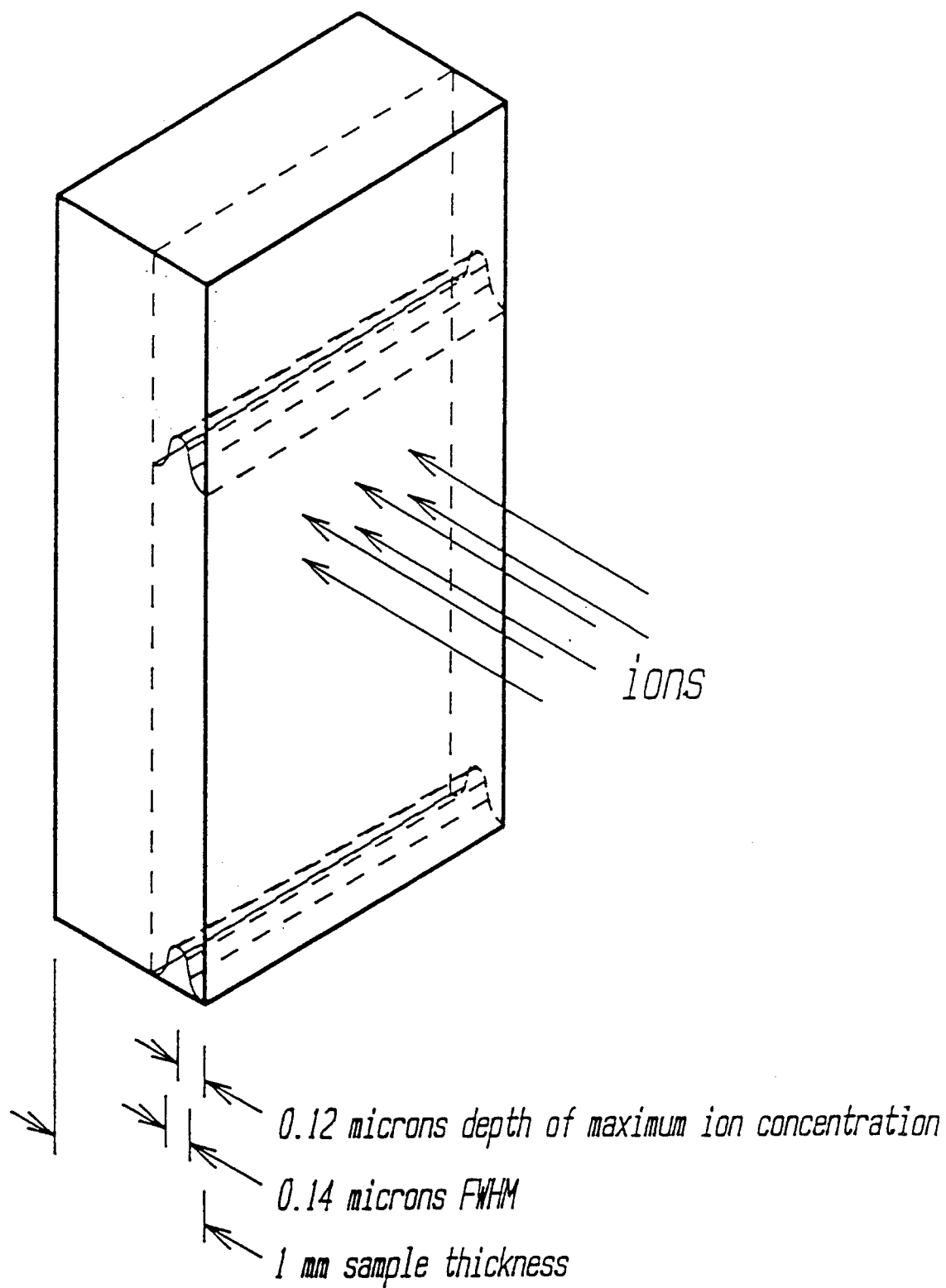


Figure 1. Schematic of an amorphous silica substrate with an ion implantation modified surface layer. The concentration profiles of the implanted ions are approximately Gaussian with depth.

TRANSITION METAL ION IMPLANTED SILICA

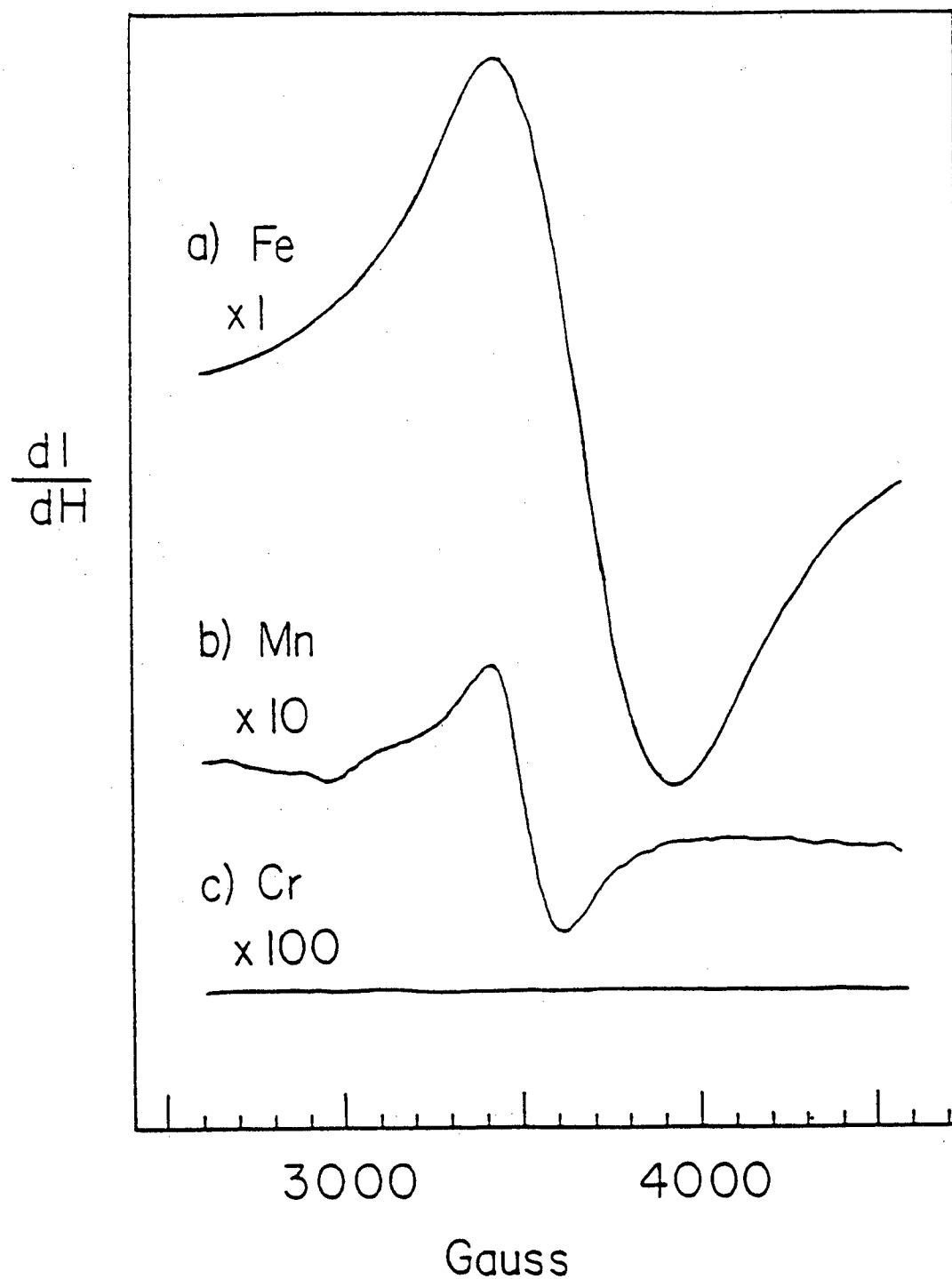


Figure 2. Comparison of the intensities of the EPR signals, at room temperature, for silica implanted with Fe, Mn, and Cr ions to a dose of 6×10^{16} ions/cm². The data scale for the Mn sample is a factor of 10 greater than the Fe scale, and the Cr scale is larger than the Fe scale by a factor of 100.

Ti ION IMPLANTED SILICA

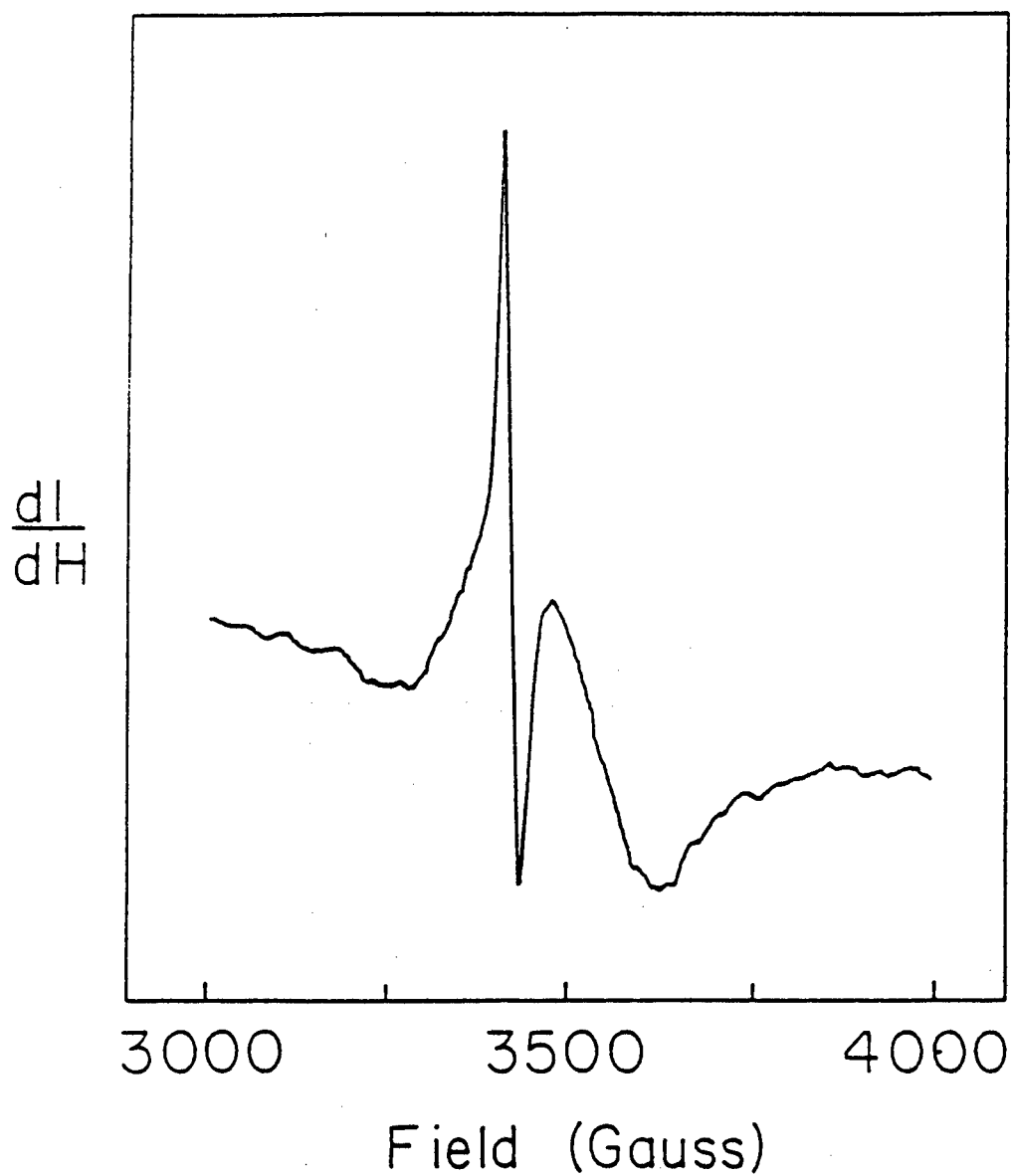


Figure 3. The EPR spectrum of a sample implanted with 6×10^{16} Ti³⁺ ions/cm². The broad spectral component is due to the implanted ion and the sharp spectral component is the E' center.

TEMPERATURE DEPENDENCE OF Mn EPR SIGNAL

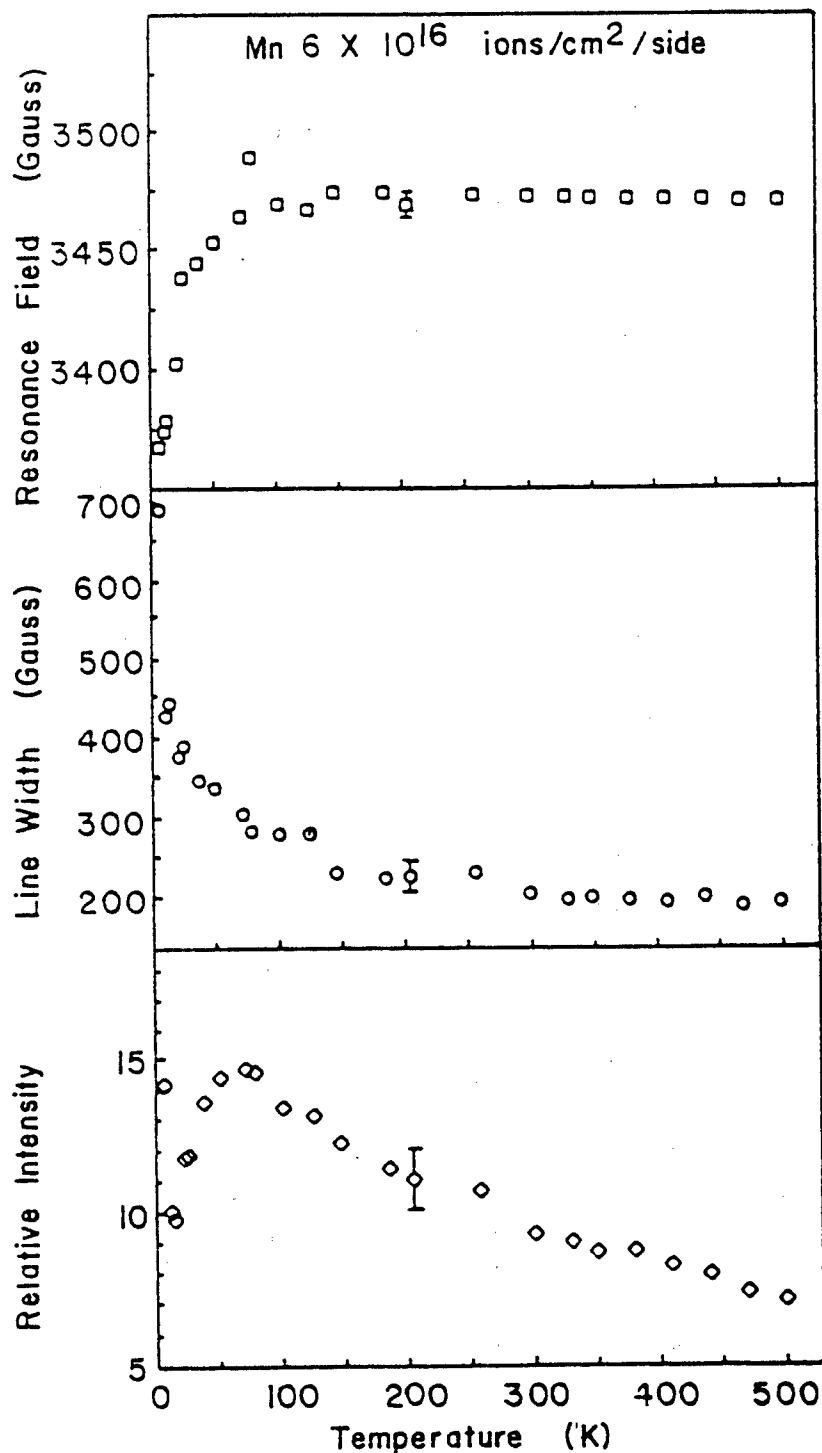


Figure 4. The temperature dependence of the resonance field, line width, and relative intensity of a silica sample implanted with 6×10^{16} Mn⁺ ions/cm².

TEMPERATURE DEPENDENCE OF Fe EPR SIGNAL

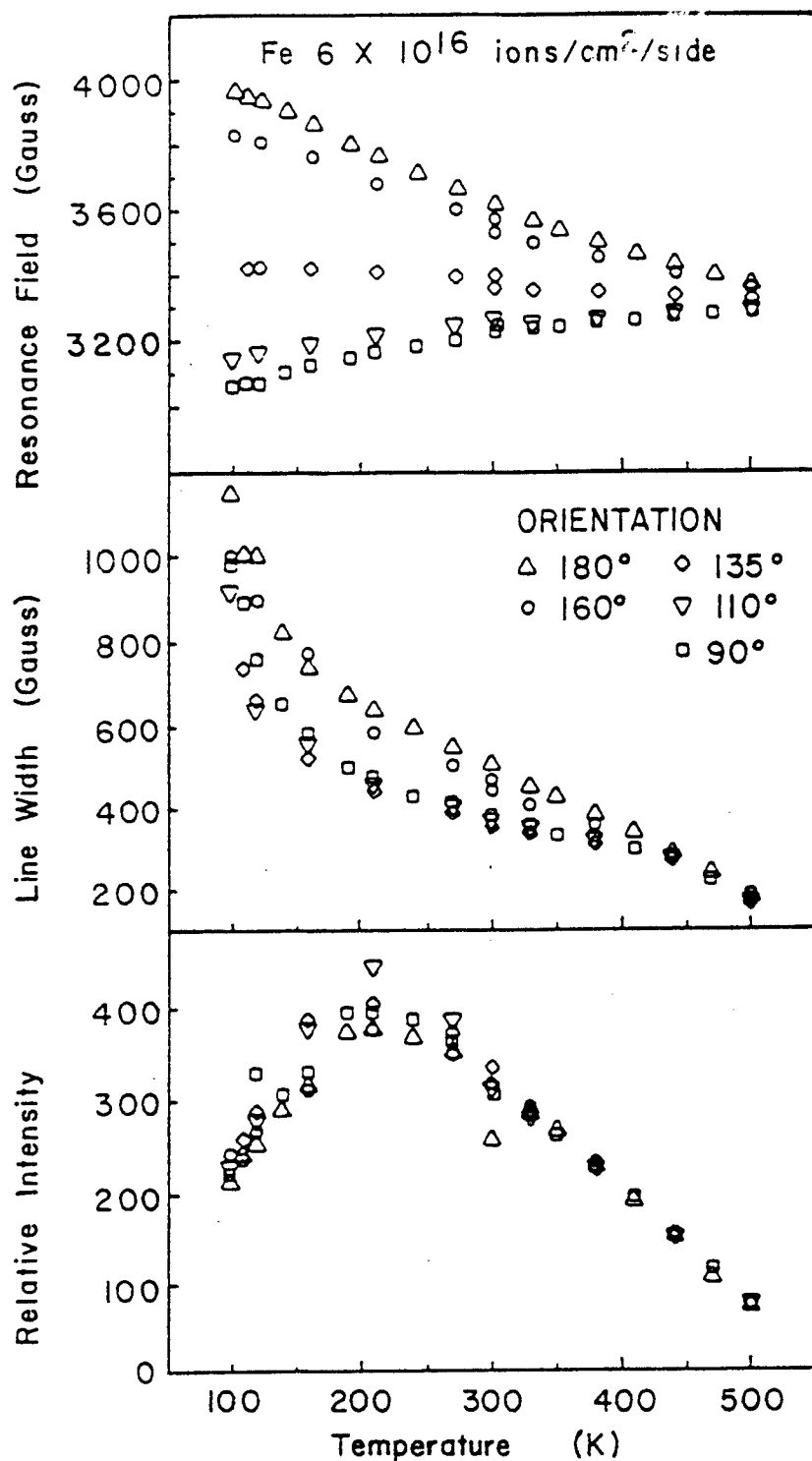


Figure 5. The temperature dependence of the resonance field, line width, and relative intensity of a silica sample implanted with 6×10^{16} Fe⁺ ions/cm². An orientation of 180° corresponds to the implanted surface perpendicular to the laboratory magnetic field and 90° corresponds to the implanted surface parallel to the laboratory field. The relative error in the measurements is approximately the magnitude of the data symbols.

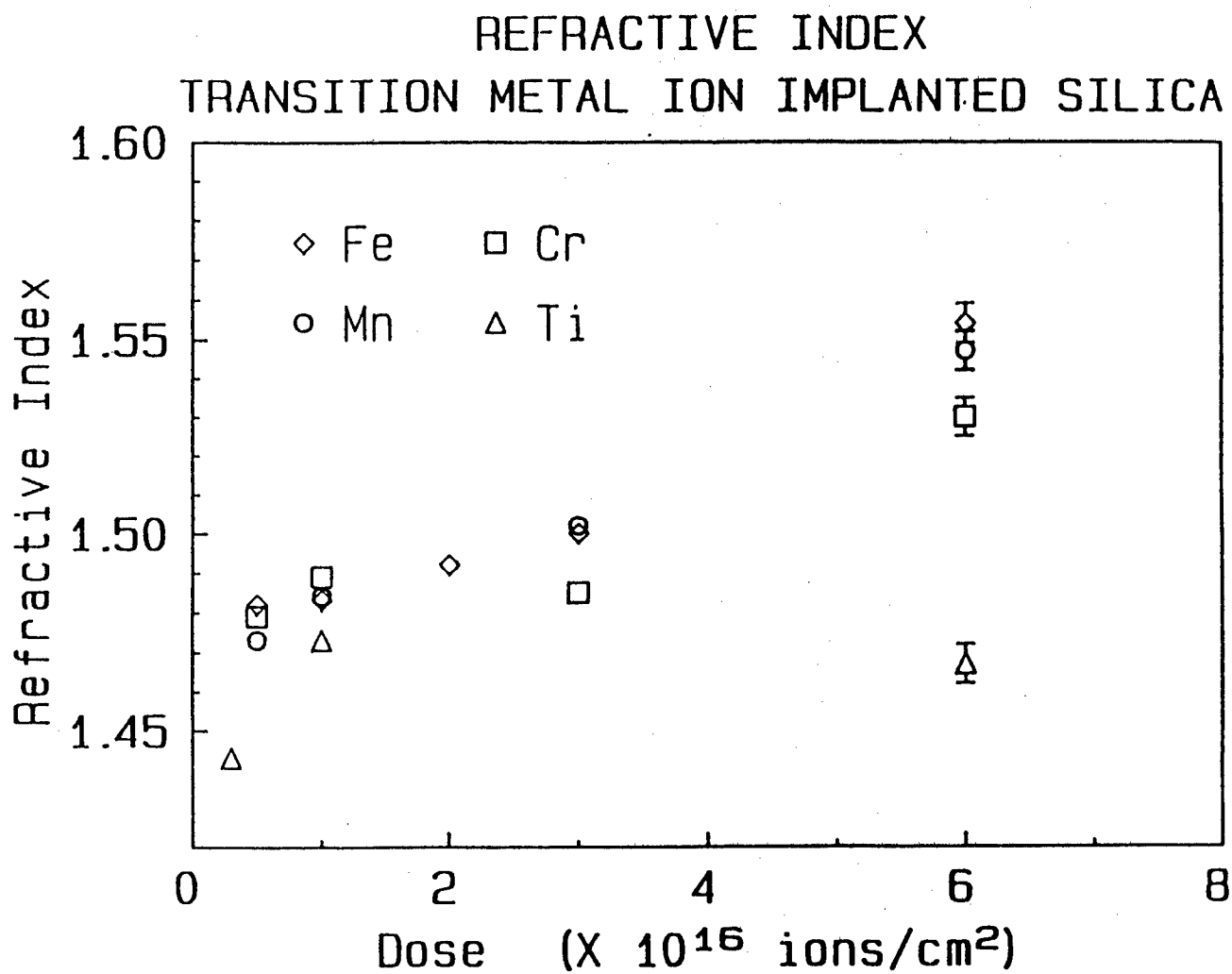


Figure 6. The refractive index of the ion modified surface, measured by ellipsometry, as a function of the implantation dose.

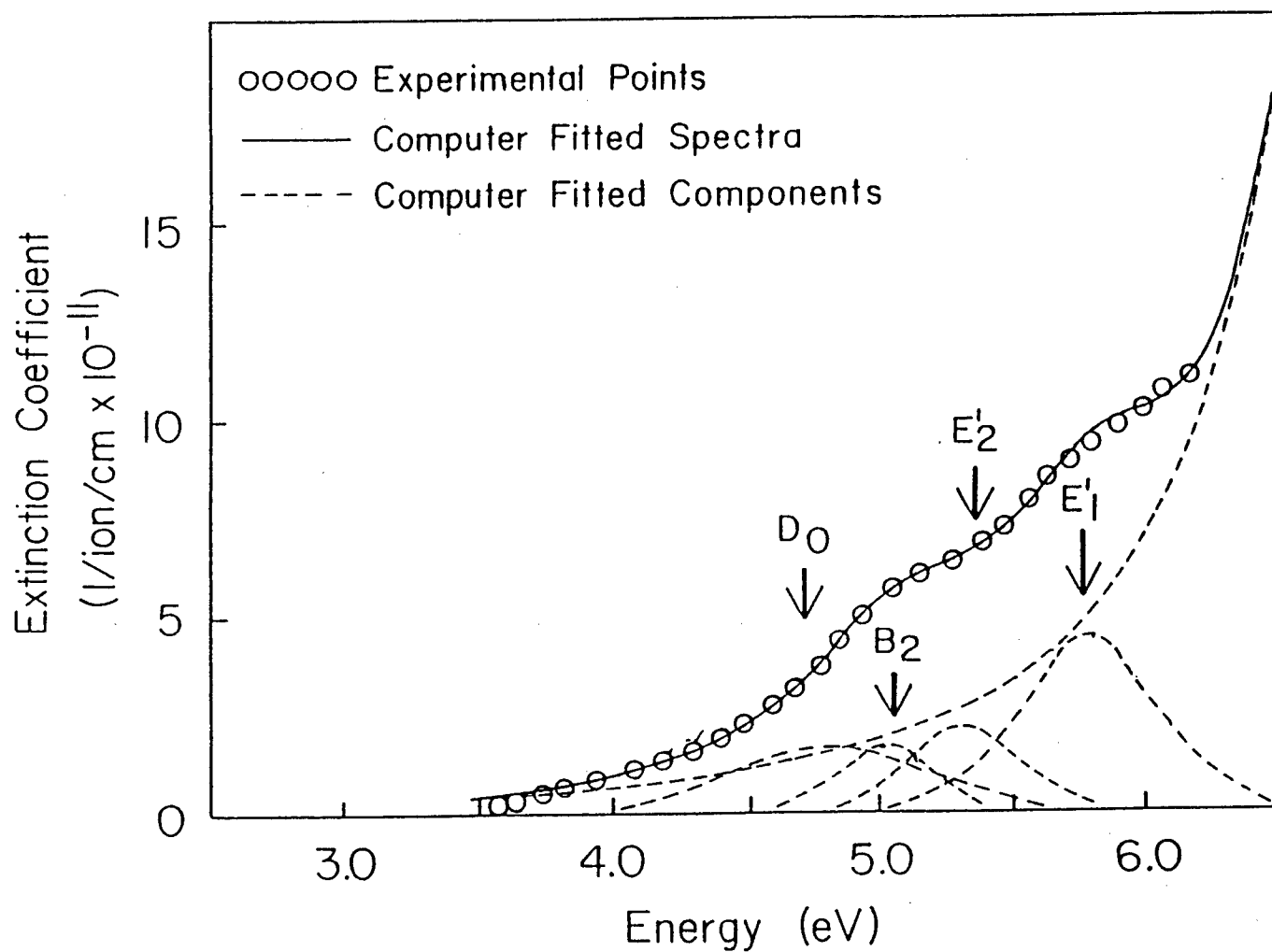


Figure 7. Comparison of a computer fitted spectrum with a measured optical absorption spectrum. The FWHM and peak positions of the spectral components are fixed. The peak amplitudes are varied to match the measured data.

CN Excited Neutral Desorption from KCl Surfaces

Jun Xu, M. Mendenhall, N. Tolk
L. Hudson, D. Russell, J. Tellinghuisen

Center for Atomic and Molecular Physics at Surface
Department of Physics and Astronomy
Vanderbilt University
Nashville, TN 37235

We present first measurements of CN excited neutral molecules desorbed from KCl surfaces. We have observed CN $B^2\Sigma^+ \rightarrow X^2\Sigma^+$ 0-0, 0-1, and 1-1 transitions. The energy dependent yields of CN transitions vary markedly with that observed from CN⁻ center fluorescence yields. This opens strong experimental and theoretical interest in the relationship between CN⁻ center fluorescence, which exists in KCl bulk, and CN neutral desorption, which may represent the diffusion of the CN⁻ center diffusion to the surface. A theoretical analysis based on the idea that the CN desorption yield comes from the energy primarily deposited on the surface and the CN⁻ fluorescence yield comes from the energy primarily deposited in the bulk shows generally trends similar to the CN and CN⁻ energy dependent yields. We have scanned CN $B^2\Sigma^+ \rightarrow X^2\Sigma^+$ 0-0 and 1-1 transitions with high resolution. The profiles of the transitions are definitely different from the transitions observed in gas phase CN. This change may represent the interaction between the surface and the molecule.

1. Introduction

Bombardment of alkali halides by energetic beams of electrons or photons have been observed to result in the emission of optical radiation from excited molecules and atoms desorbed from single crystal surfaces and from excited CN⁻ centers in the bulk. The investigation of the interaction processes involves three basic interests: (a) the mechanisms responsible for these desorptions, (b) transformation and competition of incident energy between surface and bulk excitations, (c) and the relationship of the surface desorption and bulk diffusion processes.

Molecular desorption from alkali halide surfaces is a powerful tool in the investigation of the interaction between the surfaces and molecules. The most remarkable aspect is that diatomic molecules can provide detailed information since they include electronic, vibrational and rotational transitions. By investigating the difference of emissions from molecules desorbed from surfaces in excited states and that of gas-phase studies, we can directly get surface information. For example, from the change of band distributions of OH desorbed from surfaces we may learn the change of the surface state population [1]. The CN neutral molecule desorption is of special interest since it might have a connection with the CN⁻ center, which exists in the bulk. If the surface CN comes from the reneutralization of the CN⁻ center diffused from bulk to surface, we can investigate the competition process of incident energy between CN⁻ diffusion and CN⁻ center radiation.

This paper is the first report of CN neutral desorption from KCl surfaces. We have observed CN $B^2\Sigma^+ \rightarrow X^2\Sigma^+$ 0-0, 0-1 and 1-1 transitions. We have measured its energy dependence which is different from that measured from CN⁻ center optical emissions. We have scanned the 0-0 transition with high resolution and found that the profile is definitely different from the transition of gas phase CN.

2. Experimental Setup

The experimental setup as shown in Fig.1 consists of a UHV chamber with a base pressure of 6.5×10^{-11} T. An electron gun was used to create the incident beam in the energy range 6 eV to 300 eV. A potassium chloride (KCl) crystal, cleaved in air and cleaned by heating to 400°C in vacuum, was mounted with the (100) face normal to the electron beam. A 0.3 meter scanning monochromator with 1200/mm and 2400/mm grating is used to collect photons at 90° to the beam direction. The spectrometer is driven by a stepping motor from a CAMAC crate attached to a Macintosh computer.

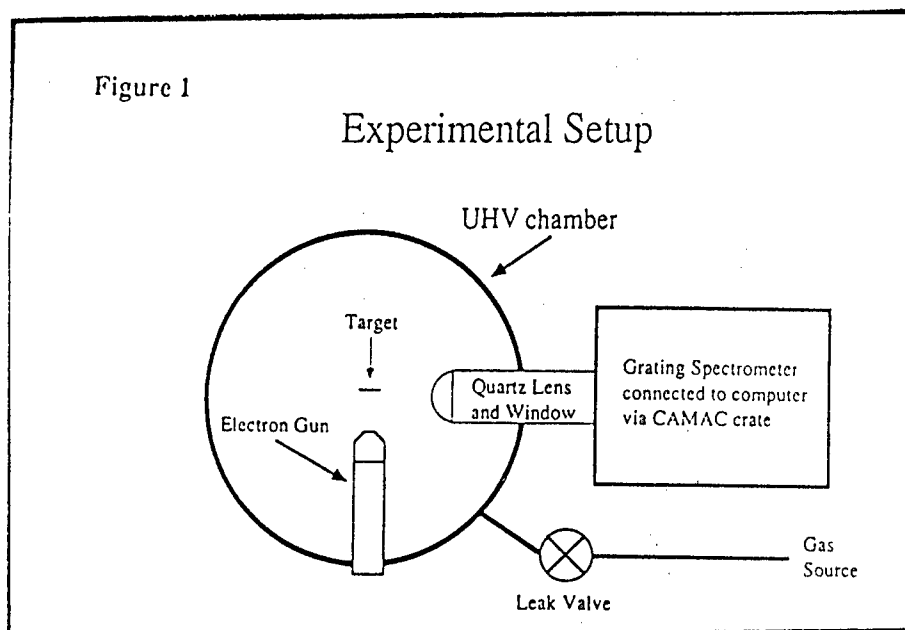


Fig. 1 Experimental Setup

3. Results

3-1. Identification of spectra Three general classes of emitted radiation are found: (a) molecular radiation from desorbed molecules, such as CN excited neutral and OH excited neutral radiations; (b) discrete line radiation from desorbed atoms, for example the hydrogen Balmer lines and the line of potassium; (c) broadband optical radiation arising from the solid, for example radiation band of CN⁻ center and the KCl bulk luminescence. The methods for the identification of spectra are comparing the electronic, vibrational and rotational structure with that identified in gas phase studies, e.g. wavelength positions and Franck-Condon factors. In this experiment, we observed the following transitions as numbered in Fig. 2:

- 1) CN⁻ electronic transition [2],
- 2) OH $A^2\Sigma^+ \rightarrow X^2\Pi$ 0-0 transition in first order,
- 3) CN neutral $B^2\Sigma \rightarrow X^2\Pi$ 0-0 transition,
- 4) CN neutral $B^2\Sigma \rightarrow X^2\Pi$ 0-1 transition,

- 5) Hydrogen Balmer β transition,
- 6) CN^- electronic transition in second order,
- 7) $\text{OH } A^2\Sigma^+ \rightarrow X^2\Pi$ 0-0 transition in second order,
- 8) Hydrogen Balmer α transition, and
- 9) K^* transition.

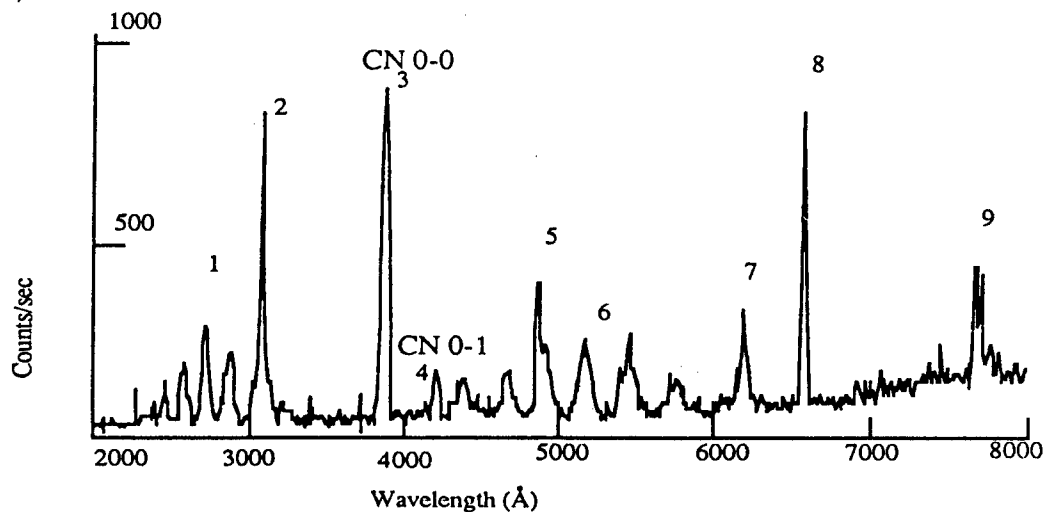


Fig. 2 Optical Emission from KCl under electron beam irradiation

Fig. 3 shows emissions of CN neutral $B^2\Sigma \rightarrow X^2\Pi$ 0-0, 0-1 and 1-1 transitions.

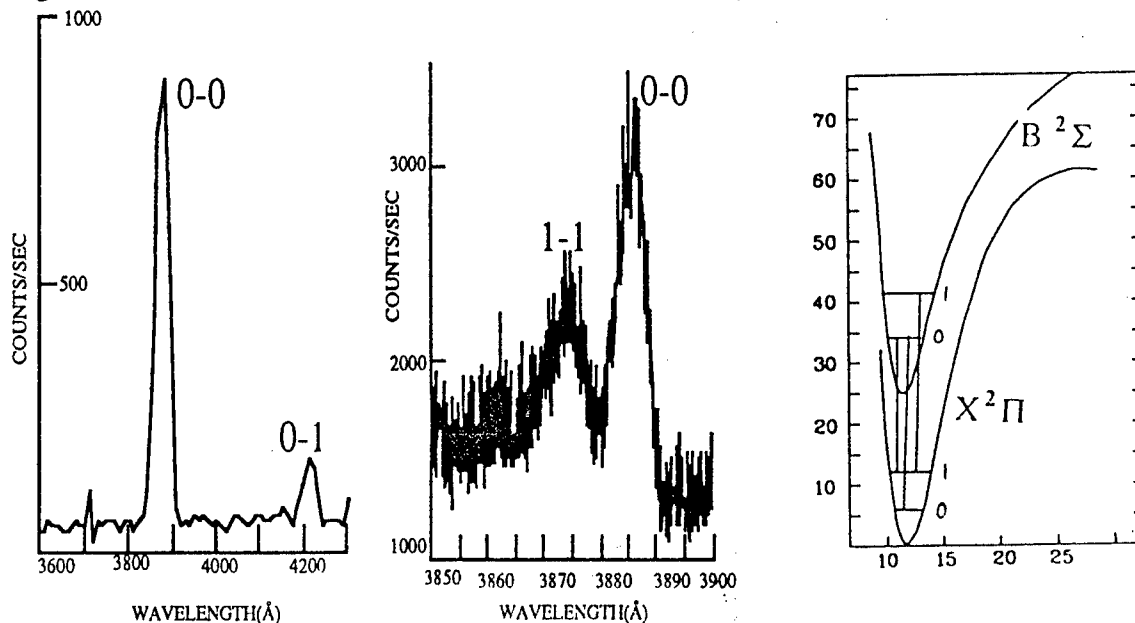


Fig.3 (a) $B^2\Sigma \rightarrow X^2\Pi$ 0-0, 0-1 Emission, (b) $B^2\Sigma \rightarrow X^2\Pi$ 0-0, 1-1 Emission

When aligning optics to both bulk and near surface region, we observed radiation from molecules and atoms plus solid radiation. When aligning optics just to the bulk region, we only observed CN^- center radiation and the KCl bulk luminescence. This suggests that CN neutral

radiation comes from the surface, like the well-known hydrogen Balmer lines, OH molecule and potassium radiations.

3-2 CN neutral / CN⁻ Energy Dependence We started at 70 eV since at lower incident electron energies the KCl crystal may exhibit effects attributed to charging. Fig.4 demonstrates relative photon yields at different incident energies of electrons with the z-axis corresponding to counts, y-axis corresponding to energy of electron beam and the x-axis corresponding to wavelength.

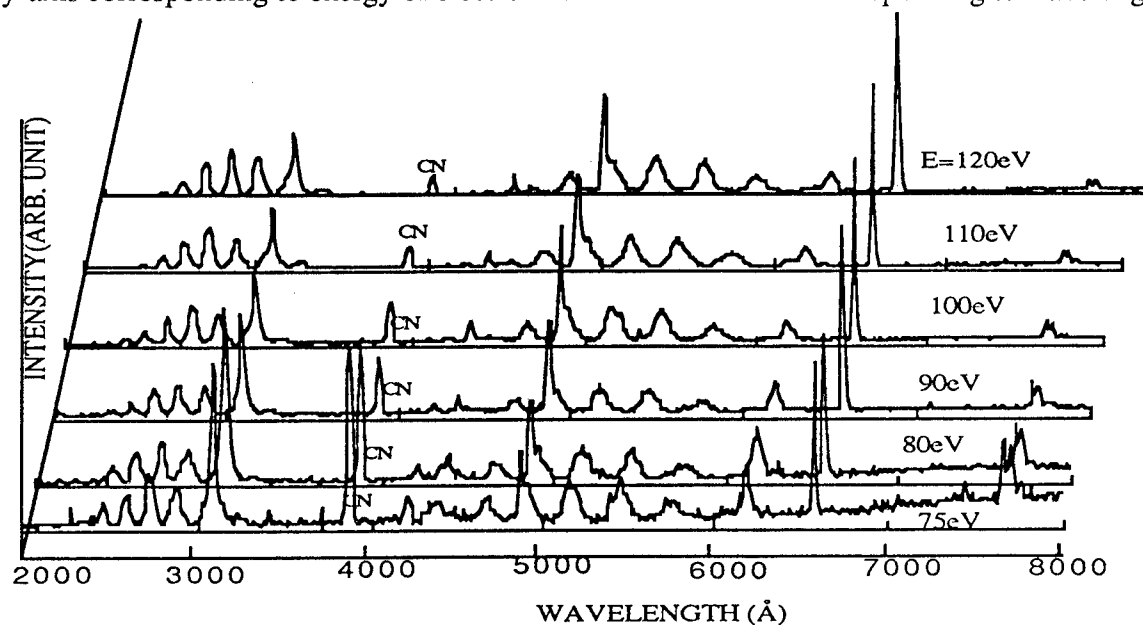


Fig. 4 Experimental Relative Photon Yield at Different Energies

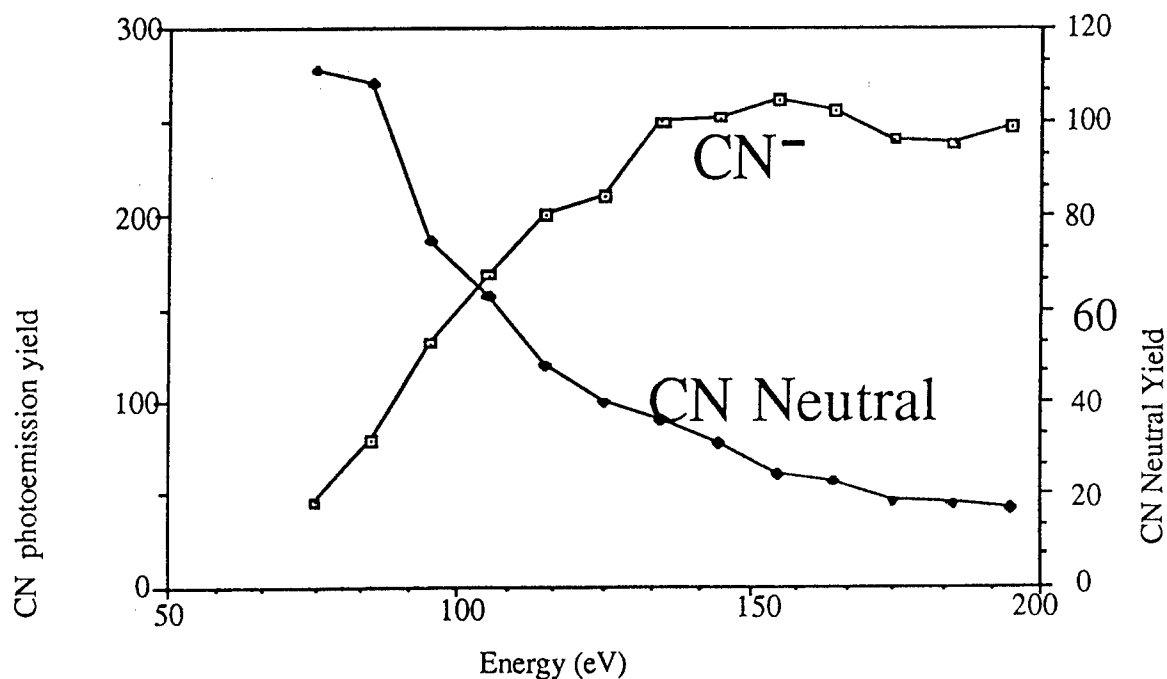


Fig. 5 CN Neutral/CN⁻ Center Energy Dependence

The 3883Å peak and 4216Å peak are CN $B^2\Sigma^+ \rightarrow X^2\Sigma^+$ 0-0, 0-1 emissions respectively. Fig.5 shows CN $B^2\Sigma^+ \rightarrow X^2\Sigma^+$ 0-0 and CN⁻ fluorescence energy dependences, which are the normalized to incident electron beam current. It shows that CN neutral yield dominants at lower energies and CN⁻ fluorescence is dominant at higher energies. The CN $B^2\Sigma^+ \rightarrow X^2\Sigma^+$ 0-1 radiation has the same result as 0-0 radiation. This dramatic inverse relation suggests that at lower energy the competition probability of CN⁻ center diffusion is bigger than CN⁻ center optical radiation, then the CN⁻ centers diffuse to the surface and are reneutralized to form CN excited neutral.

3-3 High Resolution Spectrum The Fig.6 shows the high resolution scan of CN $B^2\Sigma^+ \rightarrow X^2\Sigma^+$ 0-0 and 1-1 transitions. In our experiment with the presence of surface, the peaks are wider compared to that observed in purely gas phase studies. The structure of the band lacks the sharp band head apparent in the spectrum from Ref.[2] seen for gas phase emission. The change of emission structure suggests two possible interactions between the surface and the molecule: (a) since the surface state presence, the capture probability of molecular electrons by the surface varies with different molecular states. (b) since the symmetry is broken by the surface, the selection rule of the molecular transitions will be changed.

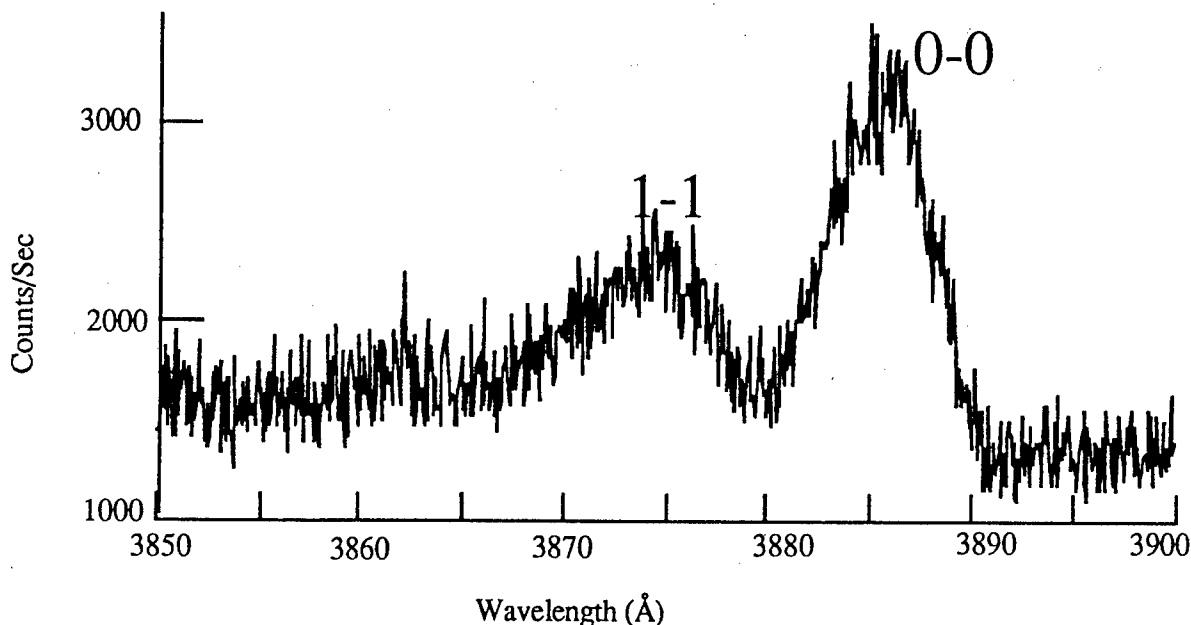


Fig.6 CN $B^2\Sigma \rightarrow X^2\Pi$ 0-0, 1-1 High Resolution Scan

4. Energy Deposition Model

The simplest model for the idea that the CN signal represents surface phenomena and the CN⁻ signal represents bulk phenomena is that the CN and CN⁻ signals be proportional to the amount of energy deposited in the surface and the bulk regions respectively. The energy deposition curve generally used in low energy electron studies is shown in Fig. 7. With E being

the electron energy and R the range of the electron

$$\int_0^R H(x) dx = E \quad (1)$$

and from Ref. [3]

$$R = \beta E^2 \quad (2)$$

$$\frac{g_1}{g_2} = h \quad (3)$$

$$g_2 = \frac{2E}{(1-hf)R} \quad (4)$$

$$h=0.5, f=0.2, \beta=1.25 \times 10^{-3} \text{ Å}/(\text{eV})^2$$

Selecting the surface region to be the first atomic layer we define the energy deposited on the surface as

$$E(x_0) = \int_0^{x_0} H(x) dx \quad (5)$$

where $X_0 = 7.6 \text{ Å}$ for KCl. Then the energy deposited in the bulk is $E - E(x_0)$. Plots comparing CN to $E(x_0)$ and CN^- to $E - E(x_0)$ are given in Fig.8. The normalization is selected to fit the highest energy points. Although these fits are far from ideal the basic trends are the same. The use of a continuum model for the energy deposition is a possible source of the discrepancy since the lower energy is range of energy deposition is on the order of a lattice spacing. The CN^- center diffusion may involve the CN desorption.

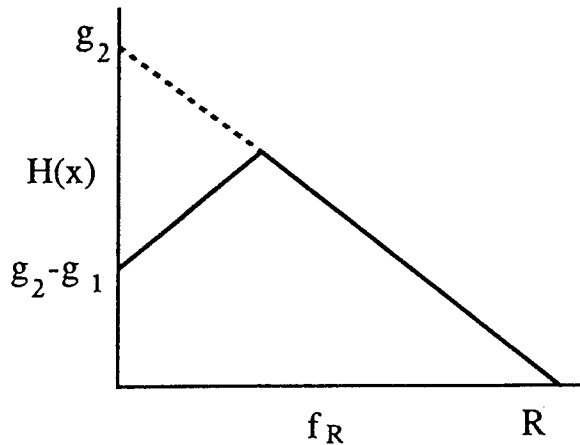


Figure 7

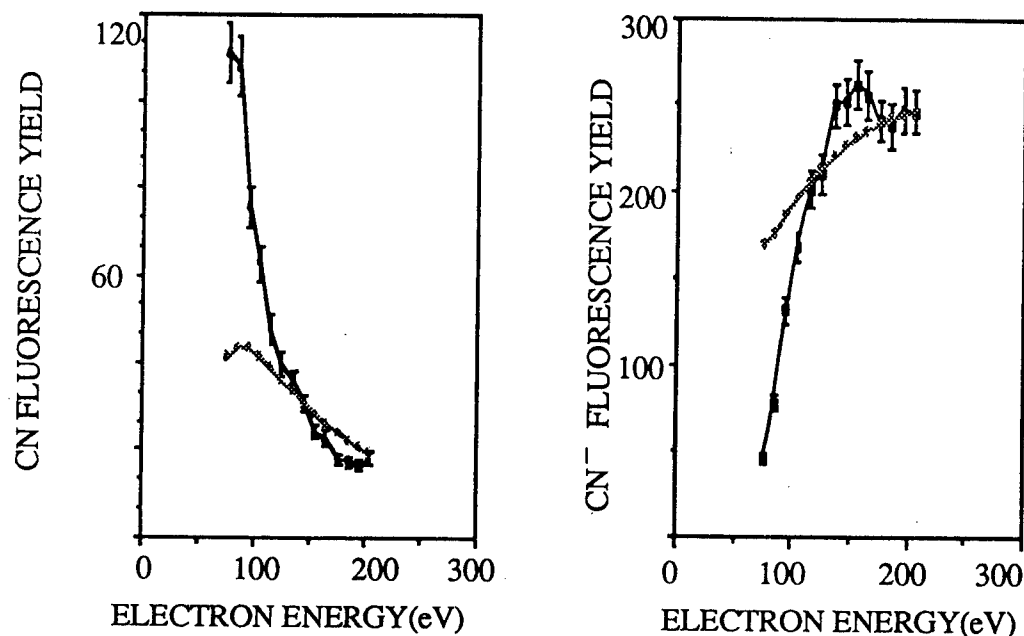


FIG. 8 THE ENERGY DEPOSITION MODEL

5. Conclusions

In conclusion, the $\text{CN } B^2\Sigma^+ \rightarrow X^2\Sigma^+ 0-0, 0-1$ and $1-1$ transitions is the first evidence that we observed CN excited neutral molecule desorption from KCl single crystal surfaces. The energy dependent yields of CN transitions vary inversely with that observed from CN^- center fluorescence yields. This reverse relation suggests that at lower energy the competition probability of CN^- centers diffuse to the surface and are reneutralized to form CN excited neutral. A theoretical model based on the idea that the CN desorption yields come from the energy deposited on the surface and the CN^- center fluorescence yields come from the energy deposited in the bulk shows general trends similar to the CN and CN^- energy dependent yields.

The profiles of the $\text{CN } B^2\Sigma^+ \rightarrow X^2\Sigma^+ 0-0$, and $1-1$ transitions with high resolution are definitely different from the transition observed in gas phase CN. This change suggests two possible events happened with presence of the surface: (a) since the surface state presence, the capture probabilities of molecular electrons by the surface vary with different molecular states. (b) since the symmetry is broken by the surface, the selection rules of the molecular transitions are changed. The discover of the CN excited neutral desorption is just opening a door. We have lots of further works needed to be done, e.g. time reserved CN desorption, high resolution scan at lower temperature and thermal effects of CN desorption.

References

- [1] M. Mendenhall et.al., ICACS XII V.12
- [2] Brocklehurst et.al., IAMS 9 (1970)
- [3] Y Al Jammal, et. al., J. Phy. C Vol.6, 247(1973)

Anisotropic neutralization by thin-foil transmission

Douglas L. Harper, Royal G. Albridge, Dwight P. Russell,
Philip M. Savundararaj, Norman H. Tolk

*Department of Physics
Center for Atomic and Molecular Physics at Surfaces
Vanderbilt University
Nashville, TN 37235*

We report preliminary measurements of the properties of anisotropically excited atomic hydrogen created by the transmission of 10 to 25 keV protons through 5 to 25 $\mu\text{g}/\text{cm}^2$ amorphous carbon foils. Excited hydrogen atoms are produced by electron-exchanges between atoms on the surface of the foil and the proton beam following transmission of the protons through the foil. Our interest is to carefully control the local electronic structure of the exit surface of the foil by coating it with various electronegative and electropositive adsorbates, and to study the influence of these changes on the properties of the final states. The dependence of the final atomic states on the adsorbate coverage will provide a means for monitoring the electron transfer process at surfaces.

I. INTRODUCTION

The transmission of energetic ions through thin-foils is followed by the transfer of electrons from the atoms on the exit surface of the foil to the emerging ions, which results in the production of excited atomic states. These final states have an anisotropic distribution of electrons due to the reduced symmetry of the beam-foil interaction.¹ This anisotropy is manifest in the polarization and angular distribution of the light emitted as the excited state decays to a state with lower energy. Measurements of the polarization of the emitted light can provide information about the atomic state of the electron at the instant of pickup.

In order to better understand the mechanisms involved in ion-surface electron-exchange interactions, we have made measurements of the polarization of light emitted following the transmission of protons through thin amorphous carbon foils. The basic objective of this experiment was to determine how the electronic structure of the surface influenced the electron-exchange process and the properties of the final states. We altered the local electronic environment of the exit surface of the foil

by dosing it with a thin layer of an alkali and measured the change in polarization due to the surface modification. The preliminary results presented here show that the beam-foil method is sensitive to changes in the electronic properties of the foil surface and it is an informative probe the electron-transfer process at surfaces.

II. EXPERIMENTAL TECHNIQUE AND DATA ANALYSIS

The source of excitation in this experiment was a momentum analyzed beam of protons produced by a Colutron ion source. The protons had a well defined kinetic energy that could range from 10 to 25 keV. The proton beam entered an ultra-high vacuum chamber (ambient background pressure $\sim 10^{-9}$ Torr) where it impinged on a very thin foil of amorphous carbon. The foils were prepared by vacuum evaporation of spectrographically pure graphite.² A typical foil surface density used was 10 $\mu\text{g}/\text{cm}^2$ which corresponds to a thickness of approximately 400 Ångstroms. The surface densities and thickness uniformities are accurate to within $\pm 10\%$. Figure 1 shows the geometry of the beam-foil interaction. The beam defines the z-axis

and passes through the center of the foil. The foil holder can be rotated about an axis perpendicular to the beam so that the normal to the foil makes an angle α with the beam.

Following transmission through the foil, the protons acquire an electron from the surface and form an excited hydrogen atom. The light emitted as these hydrogen atoms decay to a lower energy level is measured by a spectrometer whose image is a vertical slit 2 mm wide centered on the beam a few millimeters downstream of the foil. Figure 2 shows the optical radiation emitted following the passage of 15 keV protons through a $10 \mu\text{g}/\text{cm}^2$ carbon foil.

The basic observation in this experiment was the polarization of the light emitted in the Balmer-alpha transition at 656.3 nm by the foil excited atoms. The polarization was determined by measurements of the reduced Stokes parameters:

$$\frac{M}{I} = \frac{I_{0^\circ} - I_{90^\circ}}{I_{0^\circ} + I_{90^\circ}} \quad \frac{C}{I} = \frac{I_{45^\circ} - I_{135^\circ}}{I_{45^\circ} + I_{135^\circ}}$$

$$\frac{S}{I} = \frac{I_{\text{RCP}} - I_{\text{LCP}}}{I_{\text{RCP}} + I_{\text{LCP}}}$$

M/I , C/I , and S/I . In the above definitions, each I refers to the intensity of light measured in the particular polarization state identified by the subscript.³ The subscripts RCP and LCP stand for right- and left-hand circular polarization respectively, and the numbers represent linear polarization along angles referred to the beam axis as shown in Figure 1. A rotating linear polarizer was used to measure the linear polarization as a function of the angle of inclination from the beam. From this measurement the linear Stokes parameters M/I and C/I were extracted. A quarter-wave plate was inserted in front of the linear polarizer to measure the net circular polarization fraction, S/I .

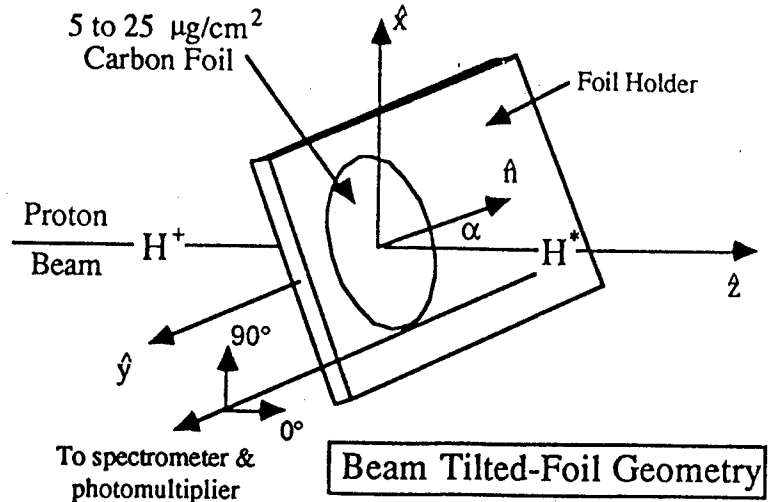


Figure 1: A schematic diagram of the beam tilted-foil experimental arrangement. The proton beam strikes the foil at an angle α with respect to the foil normal. Measurements of the polarization are made downstream of the foil.

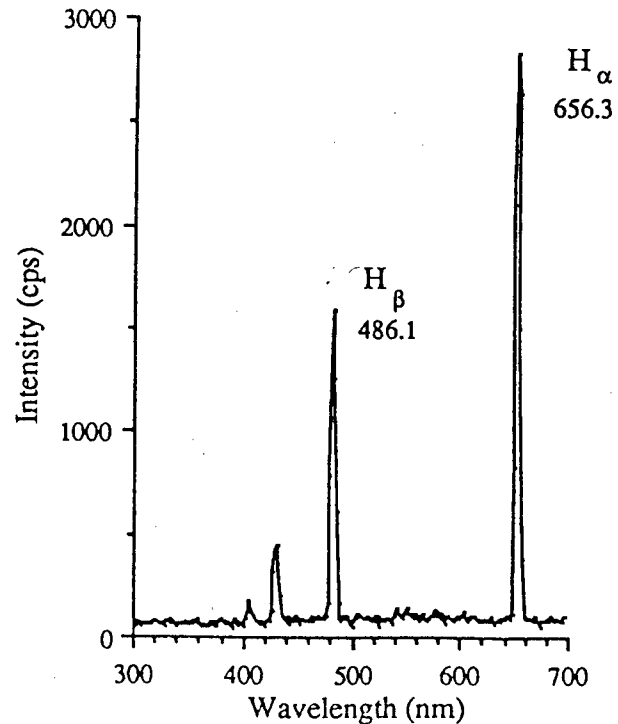


Figure 2: The Balmer series radiation emitted following the transmission of 15 keV protons through a $10 \mu\text{g}/\text{cm}^2$ carbon foil. The strong Balmer- α signal at 656.3 nm was used for all subsequent polarization measurements.

III. EXPERIMENTAL RESULTS

As mentioned earlier, the neutralization of energetic ions by transmission through thin foils results in an anisotropic distribution of electrons in the excited species as is indicated by the polarization of the collision-induced radiation. Figure 3 shows the dependence of the Stokes parameters, which characterize the polarization, on the foil tilt angle for 17 keV protons transmitted through a $15 \mu\text{g}/\text{cm}^2$ carbon foil. The cylindrical symmetry about the beam

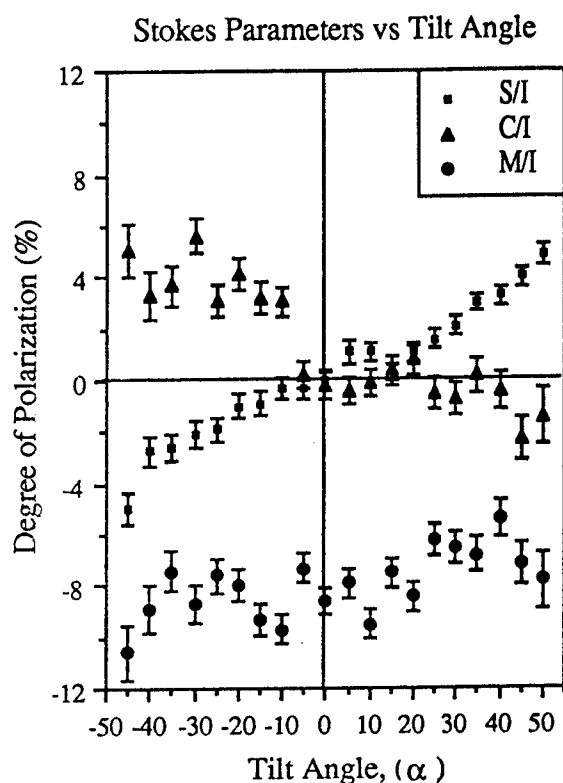


Figure 3: The dependence of the Stokes parameters as a function of the tilt angle α for a 17 keV proton beam transmitted through a $15 \mu\text{g}/\text{cm}^2$ carbon foil.

and reflection symmetry through any plane containing the beam inherent in the interaction of an ion-beam incident normally on a thin-foil results in the production of aligned atomic states, which emit partially linearly polarized light.⁴ For the interaction shown in Figure 3, the alignment at normal incidence is shown by the high absolute value of

M/I at $\alpha=0^\circ$. The cylindrical symmetry of the collision geometry is broken when the foil is tilted at an oblique angle with respect to the beam axis, resulting in the production of oriented atomic states.⁵ Such states emit partially circularly polarized light. The orientation as a function of tilt angle is shown in Figure 3 where S/I depends on α in a sinusoidal fashion.

Figure 4 shows the results of studies made to test the influence of modifying the local electronic structure of the foil exit surface on the final state. The linear Stokes parameter M/I was measured repeatedly for 17 keV protons transmitted through a $9.9 \mu\text{g}/\text{cm}^2$ carbon foil, and found to have a mean value of $-8.2 \pm 0.3\%$. The exit surface of the foil was then modified by dosing to a visibly thick layer of lithium from an SAES doser. Subsequent measurements of the polarization showed that the alignment of the system was shifted by a statisti-

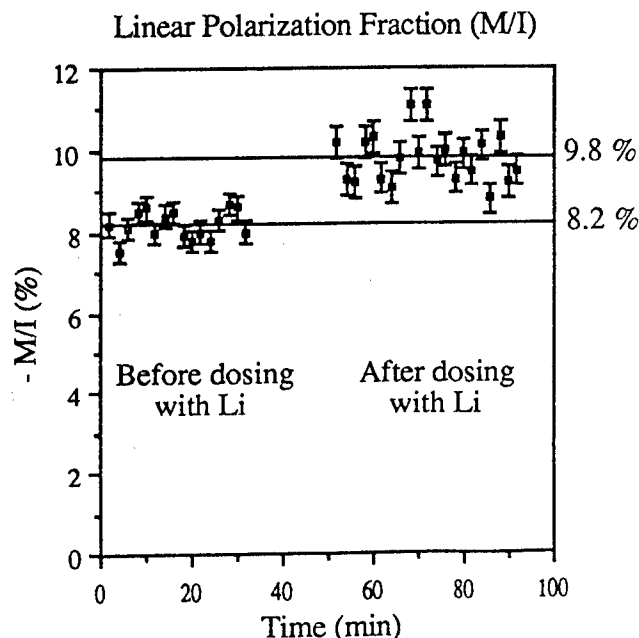


Figure 4: The linear Stokes parameter M/I as a function of time for 17 keV protons transmitted through a $9.9 \mu\text{g}/\text{cm}^2$ carbon foil before and after dosing the exit surface of the foil with lithium. The modification of the local electronic environment of the surface altered the final state.

cally significant amount. The value of M/I after dosing was found to be $-9.8 \pm 0.6\%$. The modification of the local electronic structure of the exit surface of the foil altered the final state.

IV. CONCLUSION

The preliminary results presented here suggest that the presence of adsorbates on the exit surface of the foil plays a crucial role in determining the final states of the proton-foil electron-exchange interaction. Further measurements are necessary in order to quantify the effects of overlayers on ion-surface interactions and to develop models which describe the mechanisms that lead to the observed final states.

Future directions include using a higher energy accelerator to increase the beam energy to a regime where energy straggling and scattering of the beam by the foil are significantly reduced. Also, plans are underway for progressing from amorphous carbon foils to single crystal silicon films.

ACKNOWLEDGEMENTS

This work was supported by the University Research Initiative of the Air Force Office of Scientific Research, Contract No. F49620-86-C-0125DEF, by Martin Marietta Michoud Contract No. A71205, and by the Acurex Contract No. F33615-85-C-5063 Project No. 8505.

¹H.G. Berry, L.J. Curtis, D.G. Ellis, and R.M. Schectman, "Anisotropy in the beam-foil light source," *Phys. Rev. Lett.* **32**(14), 751-4 (1974).

²The foils used were acquired from the Arizona Carbon Foil Co.

³W.A. Shurcliff, *Polarized Light* (Harvard, Cambridge, 1962) p. 21.

⁴H.G. Berry, "Orientation and alignment in beam tilted-foil spectroscopy," in *Inelastic Ion-Surface Collisions*, edited by N.H. Tolk, J.C. Tully, W. Heiland, and J.C. White (Academic Press, New York, 1977) p. 309.

⁵H. Winter, "Contribution of surface and bulk to the orientation of beam-foil excited He I $3p^3P$," *Nucl. Instrum. Methods* **202**, 241-5 (1982).